Physical Drivers of Seasonal Variability in the tropical Angolan Upwelling System

Dissertation

zur Erlangung des Doktorgrades

der Mathematisch-Naturwissenschaftlichen Fakultät
der Christian-Albrechts-Universität zu Kiel

vorgelegt von

Mareike Körner

Kiel, Januar 2024

Erster Gutachter: Prof. Dr. Peter Brandt
Zweiter Gutachter: Prof. Dr. Stephan Juricke

Tag der mündlichen Prüfung: 18.03.2024
Zum Druck genehmigt: 18.03.2024

Abstract

The eastern boundary regions of the Atlantic and Pacific oceans host highly productive ecosystems. These upwelling systems play a key role in supporting marine biodiversity, local and global fisheries, and biogeochemical cycles. Consequently, it is of high interest to understand the processes driving these systems. This thesis focuses on one of these highly productive ecosystems - the tropical Angolan upwelling system (tAUS). Conditions in the tAUS undergo strong seasonal modulations, where many characteristics exhibit variability on semi-annual and annual time scales. The lowest sea surface temperature (SST), highest primary productivity, and lowest along-shore wind are found in austral winter during the main upwelling season. Interestingly, and in contrast to other upwelling systems, the productivity signal cannot be explained by local wind-driven upwelling. Possible forcing mechanisms of the productivity signal are connected to equatorial dynamics via the propagation of coastal trapped waves (CTWs). The tAUS is thus an ecosystem influenced by both remote and local processes.

This thesis focuses on understanding the physical drivers of the seasonal and interannual variability in the tAUS, particularly in SST and primary productivity. The analyses conducted within this thesis are mostly based on observational datasets. Additionally, the results are compared with output of a regional ocean model. The observational data includes shipboard measurements as well as satellite products. The shipboard measurements comprise an extensive ocean turbulence dataset. This dataset provides, for the first time, insights into turbulent heat and nitrate fluxes in the tAUS.

In the tAUS, waters are colder directly at the coast than further offshore. Both SST and the cross-shore SST gradient exhibit a seasonal cycle. A seasonal mixed layer heat budget is calculated to identify atmospheric and oceanic causes for heat content variability. The results show that the seasonal cycle in SST is mainly controlled by surface heat fluxes and turbulent heat loss at the base of the mixed layer. The net surface heat flux warms the coastal ocean more strongly than the offshore region and thus acts to dampen cross-shore SST differences. Ocean turbulence data shows that turbulent mixing across the base of the mixed layer is an important cooling term. This turbulent cooling, being strongest in the shallow shelf regions, explains the observed negative cross-shore temperature gradient. The seasonal cycle of the cross-shore SST gradient exhibits semi-annual variability, likely linked to tidal mixing acting on changing background stratification associated with the passage of CTWs.

The primary productivity in the tAUS peaks in late austral winter. Analyses of observational data and the output of a regional ocean model reveal that the seasonal productivity maximum is due to the combined effect of CTWs and elevated tidal mixing on the shelf. During austral winter, the passage of an upwelling CTW displaces the nitracline upward by more than 50 m. Thereby, nitrate-rich waters spread onto the shelf, where elevated vertical mixing causes a nitrate flux into the surface mixed layer. High-mode CTWs play an important role in the upward and onshore transport of nitrate-rich waters.

The interannual variability of the productivity maximum in the tAUS is strongly correlated with the amplitude of the upwelling CTW. Consequently, it is of high interest to investigate dynamical factors controlling the characteristics of the CTW as their strength controls the amount of primary production in the tAUS. Regression analyses suggest that the timing and amplitude of the austral winter upwelling CTW in tAUS are influenced by variability in different regions. The timing of the CTW is mostly influenced by variability in the equatorial region and along the southern African coast. Here, weaker equatorial easterlies from April to July lead to a late arrival of the upwelling CTW. The amplitude of the CTW is influenced by variability in the eastern equatorial Atlantic and in the central South Atlantic, a region characterizing the strength of the South Atlantic anticyclone. A cooling in the eastern equatorial Atlantic four to three months before the arrival of the CTW causes stronger zonal winds, leading to a stronger austral winter upwelling CTW. In general, the results suggest that the timing and amplitude of the upwelling CTW in the tAUS during austral winter are predictable on seasonal time scales.

Overall, this thesis enhances our understanding of the seasonal to interannaul dynamics in the tAUS. The results of this thesis show that CTWs, near-coastal mixing, and surface heat fluxes are essential processes to explain the seasonal variability of SST and productivity in the tAUS. A key result is the proposed mechanism explaining the austral winter productivity peak, based on the combined effect of CTWs and near-coastal mixing. This result not only advances process understanding in the tAUS but also suggests a potential predictability of productivity in the region.

Zusammenfassung

Die östlichen Randgebiete des atlantischen und pazifischen Ozeans beherbergen hochproduktive Ökosysteme. Diese Auftriebssysteme spielen eine Schlüsselrolle bei der Erhaltung der marinen Artenvielfalt, der lokalen und globalen Fischerei und der biogeochemischen Kreisläufe. Es ist daher von großem Interesse, die Prozesse, die diese Systeme antreiben, zu verstehen. Diese Doktorarbeit konzentriert sich auf eines dieser hochproduktiven Ökosysteme: das tropische angolanische Auftriebssystem (tAUS). Die Bedingungen im tAUS sind starken saisonalen Schwankungen unterworfen, wobei viele Merkmale halbjährliche und jährliche Variabilitäten aufweisen. Die niedrigste Meeresoberflächentemperatur (SST), die höchste Primärproduktivität und der schwächste küstenparallele Wind werden im Südwinter während der Hauptauftriebszeit gemessen. Interessanterweise, und im Gegensatz zu vielen anderen Auftriebssystemen, kann das Produktivitätssignal nicht durch lokalen windgetriebenen Auftrieb erklärt werden. Mögliche Antriebsmechanismen für das Produktivitätssignal sind mit dynamischen Prozessen am Äquator verbunden. Windveränderungen am Äquator können Kelvinwellen auslösen, die am östlichen Rand Küsten-Kelvinwellen (CTWs) auslösen, welche sich polwärts ausbreiten. Somit wird das tAUS nicht nur von lokalen Prozessen beeinflusst, sondern ist auch eng mit der äquatorialen Dynamik verbunden.

Diese Doktorarbeit beschäftigt sich mit dem physikalischen Antrieb der saisonalen und interannuellen Variabilität im tAUS. Insbesondere werden die Variabilität der SST und der Primärproduktion untersucht. Die im Rahmen dieser Arbeit durchgeführten Analysen basieren größtenteils auf Beobachtungsdaten sowie auf Vergleichen mit numerischen Ozeanmodellen. Die Beobachtungsdaten beinhalten umfangreiche Messungen, die während Forschungsfahrten aufgezeichnet worden sind. Es wurden unter anderem zahlreiche Turbulenzmessungen durchgeführt, welche zum ersten Mal Erkenntnisse über turbulente Wärme- und Nitratflüsse im tAUS liefern.

Im tAUS ist die SST direkt an der Küste das ganze Jahr über kälter als weiter weg von der Küste. Sowohl die SST als auch die Stärke des SST-Gradienten quer zur Küste weisen saisonale Schwankungen auf. In dieser Arbeit wird ein Wärmebudget der durchmischten Deckschicht berechnet. Mit diesem Budget können atmosphärische und ozeanische Ursachen für die Variabilität des Wärmeinhalts analysiert werden. Die Ergebnisse zeigen, dass der SST-Jahresgang hauptsächlich durch Oberflächenwärmeflüsse und durch Abkühlung aufgrund von vertikaler Vermischung erklärt wird. Die Oberflächenwärmeflüsse erwärmen den küstennahen Ozean stärker als den küstenfernen und dämpfen so die räumlichen SST-Unterschiede. Turbulenzdaten zeigen, dass die vertikale Vermischung an der Unterkante der durchmischten Deckschicht ein wichtiger Prozess ist. Die Abkühlung, die durch diese Vermischung hervorgerufen wird, ist in flachen Schelfregionen am stärksten. Diese küstennahe Vermischung kann den beobachteten negativen SST-Gradient quer zur Küste erklären. Die Särke des SST-Gradienten weist halbjährliche Schwankungen auf, die wahrscheinlich durch eine konstante Vermischung aufgrund von Gezeitenenergie hervorgerufen wird, die auf die sich ändernde Schichtung einwirkt.

Die Primärproduktivität im tAUS erreicht ihr Maximum im Südwinter. Beobachtungsdaten und Daten eines regionalen Ozeanmodells zeigen, dass das saisonale Produktivitätsmaximum durch den Effekt von CTWs und Vermischung durch Gezeitenenergie auf dem Schelf erklärt werden kann. Während des Südwinters verschiebt eine Auftriebs-CTW den maximalen Nitratgradienten um mehr als 50 m nach oben. Dadurch wird nitratreiches Wasser auf den Schelf transportiert. Auf dem Schelf führt eine starke Vermischung zu einem erhöhten Nitratfluss in die durchmischte Deckschicht. Hochbarokline CTWs spielen eine wichtige Rolle bei der vertikalen Verschiebung des maximalen Nitratgradienten sowie bei dem Transport von nitratreichem Wasser auf den Schelf.

Die zwischenjährliche Variabilität des Produktivitätsmaximums im tAUS korreliert stark mit der Amplitude der Auftriebs-CTW. Aufgrund ihrer hohen Bedeutung für die Primärproduktion ist es daher von großem Interesse zu untersuchen, welche Faktoren die Variabilität der Auftriebs-CTW beeinflussen. Regressionsanalysen deuten darauf hin, dass Zeitpunkt und Amplitude der Auftriebs-CTW von der Variabilität in jeweils verschiedenen Regionen beeinflusst werden. Der Zeitpunkt der CTW wird hauptsächlich durch Variabilität in der äquatorialen Region und entlang der südafrikanischen Küste beeinflusst. Hier führen schwächere äquatoriale Ostwinde von April bis Juli zu einem späten Eintreffen der Auftriebs-CTW. Die Amplitude der CTW wird sowohl von der Variabilität im östlichen Äquatorialatlantik als auch von der Stärke des südatlantischen Hochdruckgebiets im zentralen Südatlantik beeinflusst. Eine Abkühlung im östlichen Äquatorialatlantik drei bis vier Monate vor der Ankunft der CTW führt zu stärkeren zonalen Winden und damit zu einer stärkeren Auftriebs-CTW. Im Allgemeinen deuten die Ergebnisse darauf hin, dass Zeitpunkt und Amplitude der Auftriebs-CTW im tAUS während des Südwinters auf saisonalen Zeitskalen vorhersagbar sind.

Diese Doktorarbeit trägt zu einem besseren Verständnis der saisonalen und zwischenjährlichen Dynamiken im tAUS bei. Die Ergebnisse dieser Arbeit zeigen, dass CTWs, küstennahe Vermischung und Oberflächenwärmeflüsse wesentliche Prozesse sind, um den Jahresgang der SST und der Primärproduktivität im tAUS zu erklären. Ein zentrales Ergebnis der Arbeit ist der gefundene Mechanismus, der das saisonale Produktivitätsmaximum während des Südwinters erklärt. Dieser Mechanismus beruht auf dem kombinierten Effekt aus CTWs und küstennaher Vermischung. Dieses Ergebnis trägt nicht nur zum verbesserten Verständnis der dynamischen Prozesse im tAUS bei, sondern deutet auch auf eine mögliche Vorhersagbarkeit der Produktivität in der Region hin.

Contents

Abstract I

Zusammenfassung III

1 Introduction 1
- 1.1 Background conditions in the tAUS 2
- 1.2 Seasonal variability 3
- 1.3 Interannual variability and long-term changes 6
- 1.4 Large-scale dynamics 7
- 1.5 Mixing and small-scale processes 12
  - 1.5.1 Internal waves 13
  - 1.5.2 Turbulence and fluxes 14
  - 1.5.3 Small-scale processes in the tAUS 16
- 1.6 Motivation & Outline 17

2 Seasonal cycle of sea surface temperature in the tropical Angolan upwelling system 19
- 2.1 Abstract 20
- 2.2 Introduction 20
- 2.3 Data 23
  - 2.3.1 Shipboard measurements 23
  - 2.3.2 Mooring data 24
  - 2.3.3 Satellite and reanalysis data 25
- 2.4 Methods 26
  - 2.4.1 Mixed layer heat budget 26
  - 2.4.2 Uncertainty estimation 28
- 2.5 Results 29
  - 2.5.1 Surface heat fluxes 30
  - 2.5.2 Mean horizontal advection 30
  - 2.5.3 Turbulent heat loss at the base of the mixed layer 32
  - 2.5.4 Mixed layer heat budget 35
- 2.6 Summary and discussion 37
- 2.7 Appendix A: Comparison of satellite and reanalysis data to moored observation 41
  - 2.7.1 Surface heat fluxes 42
  - 2.7.2 Horizontal velocities 44
  - 2.7.3 Surface temperatures 45

3 CTWs and tidal mixing control primary production in tAUS 48
- 3.1 Abstract 49
- 3.2 Introduction 49
- 3.3 Results 52
  - 3.3.1 Seasonal changes in nitrate and density 52

3.3.2 Upward nitrate supply by vertical mixing 57
3.3.3 Interannual variability of productivity in the tAUS 59
3.4 Discussion 61
3.5 Materials and Methods 65
3.5.1 Hydrographic, oxygen and nitrate data 65
3.5.2 Satellite data 65
3.5.3 Mooring data 66
3.5.4 Calcualting nitrate concentration from oxygen 66
3.5.5 Calculating mean sections from observations 67
3.5.6 Turbulent nitrate fluxes 67
3.5.7 Theoretical coastal trapped wave modes 68
3.5.8 Regional Ocean model Configuration 68
3.5.9 Integrated wind-driven upwelling 69
3.5.10 Different time periods of observation 69
3.6 Supplementary Materials 71

4 Strength and timing of remotely forced Angolan coastal upwelling in austral winter 82
4.1 Abstract 83
4.2 Introduction 83
4.3 Results 85
4.3.1 Interannual variability of the austral winter SLA minimum in the tAUS 85
4.3.2 Timing of the SLA minimum 86
4.3.3 Amplitude of the SLA minimum 88
4.3.4 Temporal evolution of the equatorial connection 90
4.4 Discussion 91
4.5 Methods 94
4.5.1 Satellite/Reanalysis data 94
4.5.2 Determining timing and amplitude of SLA minimum 94
4.5.3 Regression analysis 95
4.6 Supplementary Materials 96

5 Summary, Discussion & Outlook 99
5.1 Summary & Discussion 99
5.2 Outlook 103

References 110

Publication list 127

1 Introduction

The ocean covers over 70% of the surface of the Earth and is home to a variety of different ecosystems. The existence of nearly all marine ecosystems relies on photosynthesis. For photosynthesis, the availability of light and nutrients is crucial. Large parts of the sunlit ocean are limited in the availability of nutrients thus primary productivity is low. Notable exceptions are found along the eastern boundaries of the Atlantic and Pacific Oceans, known as eastern boundary upwelling systems (EBUS). Here, physical processes bring up nutrient-rich waters from below, inducing high primary productivity. While the EBUS cover only about 1 % of the surface area of the world ocean, they produce about 20 % of the global fish catch (Kämpf and Chapman, 2016). Because of their importance in global productivity and biogeochemical cycles, it is of high interest to understand the mechanisms shaping these systems, especially under exposure to climate variability and climate change. The characteristics and physical drivers of upwelling are very diverse among the EBUS. This thesis focuses on one of these ecosystems - the tropical Angolan upwelling system (tAUS).

The tAUS is a highly productive ecosystem that is of great socio-economic importance for local communities (Hutchings et al., 2009; Sowman and Cardoso, 2010; FAO, 2022). About 25 % of the total animal protein of the Angolan population is supplied by fishing which is of high importance for the economic security of Angola (FAO, 2022). The main exploited resources in the tAUS include sardinellas, horse mackerel, demersal sparid fish, and deep-sea crab (Kirkman et al., 2016).

Many characteristics of the tAUS exhibit a strong seasonal cycle. The highest productivity, the lowest sea surface temperatures (SST) and the strongest cross-shore SST gradient are found in late austral winter (Brandt et al., 2023). In contrast to other EBUS, the upwelling signal in austral winter cannot be explained by local wind-driven upwelling (Berrit, 1976; Picaut, 1983; Ostrowski et al., 2009). Instead, previous studies discussed whether the seasonal cycle in productivity is connected to equatorial dynamics (Ostrowski et al., 2009; Tchipalanga et al., 2018a; Brandt et al., 2023). However, the mechanisms controlling the productivity in the tAUS are still not fully resolved yet (Brandt et al., 2023).

Understanding processes influencing conditions in the tAUS is vital for predicting variability and assessing potential future changes within these systems, e.g., due to anthropogenic influences. This is of interest for local communities as well as on global scales, as upwelling systems play a key role in global biogeochemical cycles, climate, and supporting marine biodiversity (Kämpf and Chapman, 2016). Note in this context that state-of-the-art climate models have difficulties to realistically simulate EBUS and their variability (Richter, 2015; Kurian et al., 2021; Farneti et al., 2022). The tAUS is no exception to this, on the contrary, one of the strongest warm biases is present in the southeastern tropical Atlantic (Farneti et al., 2022). Consequently, it is crucial to advance process understanding and improve prediction skills.

The tAUS is an ecosystem with strong seasonal modulations shaped by both local and remote influences. The physical mechanisms driving the seasonal cycle are identified in this thesis, aiming to contribute towards a better understanding of the tAUS and tropical upwelling systems. The tAUS as well as some important concepts are introduced in more detail in this chapter. Chapter 1.1 describes the background conditions in the tAUS. In chapter 1.2 the seasonal modulations of conditions in the tAUS are described.

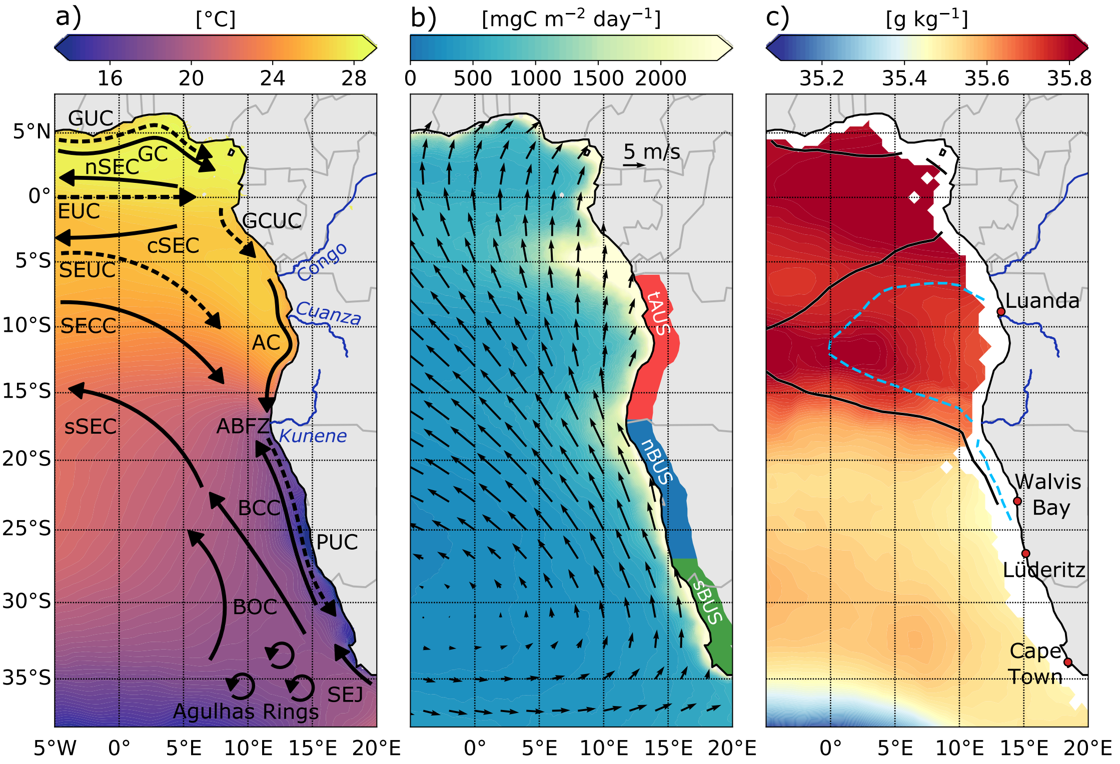

Figure 1.1: *Mean background conditions and circulation schematic for the eastern boundary upwelling system of the South Atlantic.* ***(a)*** *Sea surface temperature in the eastern tropical and subtropical South Atlantic with circulation schematic superimposed,* ***(b)*** *net primary production surface wind vectors superimposed, and* ***(c)*** *absolute salinity on the potential density surface $\sigma_\theta = 26.3\ kg\ m^{-3}$. In (a), surface (solid arrows) and thermocline (dashed arrows) current branches shown are the Guinea Undercurrent (GUC), the Guinea Current (GC), the Equatorial Undercurrent (EUC), the northern, central and southern branches of the South Equatorial Current (nSEC, cSEC, and sSEC), the South Equatorial Undercurrent (SEUC), the South Equatorial Countercurrent (SECC), the Gabun-Congo Undercurrent (GCUC), the Angola Current (AC), the Poleward Undercurrent (PUC), the Benguela Offshore and Coastal Currents (BOC and BCC), and the shelf-edge jet (SEJ). Also marked in (a) is the Angola-Benguela Frontal Zone (ABFZ) at about 17°S. In (b) the latitude range of the three subregions, the tropical Angolan and the northern and southern Benguela upwelling systems (tAUS, nBUS, sBUS). In (c), the 70 $\mu\ kg^{-1}$ oxygen concentration contours at 130 m depth (light blue dashed line) and at 250 m depth (black line) are included. The figure is adapted from Brandt et al. (2024), check reference for information on the data used in this figure.*

Innterannual variability and long-term changes are introduced in chapter 1.3. In chapter 1.4 theoretical aspects of equatorial dynamics and coastal trapped waves are introduced. Chapter 1.5 presents mixing and small-scale processes. Finally, the motivation and outline of this thesis are presented in chapter 1.6.

1.1 Background conditions in the tAUS

Angolan waters are situated south of the Congo River outflow at 6°S and north of the Angola-Benguela Frontal Zone (ABFZ) located at about 17°S (Fig. 1.1a). The ABFZ separates the tAUS from the cold waters of the Benguela upwelling system. Meteorologically, the tAUS is located on the northeastern flank of the South Atlantic Anticyclone (SAA). Consequently, in the tAUS southerly alongshore winds blow throughout the year. The winds are substantially weaker than in the permanently wind-driven Benguela upwelling system to the south (Fig. 1.1b).

The main large-scale circulation feature of the tAUS is the poleward flowing Angola Current (Fig. 1.1 (Kopte et al., 2017; Siegfried et al., 2019; Brandt et al., 2024). The Angola Current connects the equatorial Atlantic with the coastal upwelling systems of Angola and Benguela. Its core is situated at about 50 m depth and its mean southward transport is $\sim 0.32\,Sv$ (Kopte et al., 2017). The Angola current is a wind-driven current thought to be set up by the local near-coastal wind stress curl (Tchipalanga et al., 2018a).

Waters in the tAUS are characterized by tropical stratification, with warm and fresh waters above cold and saltier waters (Mohrholz et al., 2008; Kopte et al., 2017; Tchipalanga et al., 2018a; Roch et al., 2021). Precipitation, the Congo River at 6°S and the Cuanza River at 9°S are the main sources of freshwater (Brandt et al., 2023). The water mass below the warm and fresh surface waters consists mainly of the cold, hypoxic, nutrient-rich South Atlantic Central Water (SACW) (Mohrholz et al., 2008; Ostrowski et al., 2009; Kopte et al., 2017; Tchipalanga et al., 2018a). The SACW is formed in the center of the subtropical gyre and is transported north towards the equator via the North Brazil Current. From the equator, the SACW is transported to Angola via the Equatorial Undercurrent and subsequently by the Gabon-Congo Undercurrent (Wacongne and Piton, 1992) and the Angola Current (Kopte et al., 2017) (Fig. 1.1a). Additional sources of SACW are the South Equatorial Undercurrent and the South Equatorial Counter Current (Siegfried et al., 2019) (Fig. 1.1a). It is low in oxygen as consumption reduces oxygen concentration over a long transient time from its forming region (Karstensen et al., 2008).

In the South Atlantic, an eastern boundary oxygen minimum zone is present between the equator and about 20°S (Fig. 1.1c). The core of the oxygen minimum is located at about 400 m depth (Karstensen et al., 2008). The presence of the oxygen minimum can be explained by the concept of shadow zones (Luyten et al., 1983). In the area of the SAA, waters in the surface layer are subject to wind-induced Ekman pumping. The subducted water parcels are advected equatorward and westward. Through this advection, weakly ventilated shadow zones form along the eastern boundary.

1.2 Seasonal variability

Conditions in the tAUS undergo strong seasonal modulations (Brandt et al., 2023). This chapter introduces the seasonal variability of some characteristics in the tAUS. In the following, I will focus on the seasonal changes in circulation, hydrographic conditions, wind, and productivity. Additionally, potential drivers of upwelling in the tAUS are discussed.

The tAUS is closely connected to equatorial dynamics. Wind fluctuations at the equator can trigger equatorial Kelvin waves (EKWs), which propagate eastward. Upon reaching the eastern boundary, part of their energy is transformed into westward propagating equatorial Rossby waves, and part of their energy transforms into poleward propagating coastal trapped waves (CTWs) (Moore, 1968; Moore et al., 1978; McCreary, 1976; Polo et al., 2008). To analyze the presence of CTWs in the tAUS, sea level anomaly (SLA) data can be utilized. Upwelling CTWs exhibit a depression in sea level, while downwellling CTWs are associated with an elevation in sea level. Note that in chapter 1.4 equatorial and CTW dynamics are introduced in greater detail.

Connected with the passage of CTWs, SLA data averaged at the Angolan coast reveal a strong seasonal cycle (Fig. 1.2 & 1.3). Throughout the year, the signals of two upwelling and two downwelling CTWs are visible (Schouten et al., 2005; Lazar et al., 2006; Polo et al., 2008; Rouault, 2012; Ostrowski et al., 2009; Tchipalanga et al., 2018a) First, the signal of a downwelling CTW peaking in February is visible. Subsequently, an upwelling CTW peaks in July. A secondary, weaker downwelling wave is visible in October/November followed by a secondary much weaker upwelling wave, which can be seen in December/January. Consequently, the seasonal cycle of SLA in the tAUS can be described as a superposition of annual and semi-annual harmonics.

The passage of CTWs affects the variability of the Angola Current. On seasonal time scales, the Angola Current exhibits annual and semi-annual variability. Southward velocity maxima are found in March/April and September/October respectively (Kopte et al., 2017; Awo et al., 2022). Kopte et al. (2018) found that the remote equatorial forcing plays an important role in the variability of the Angola Current using a shallow-water model. Thus, despite being a wind-driven current, the variability of the Angola Current is largely influenced by CTW dynamics (Bachèlery et al., 2016b; Kopte et al., 2017, 2018).

Hydrographic conditions within the tAUS undergo distinct seasonal changes (Ostrowski et al., 2009; Kopte et al., 2017; Tchipalanga et al., 2018a). Large differences are visible when comparing conditions between late austral summer and austral winter. During late austral summer, warm and fresh waters occupy the surface ocean and a subsurface salinity maximum is visible, while during austral winter, colder and more saline water prevails (Kopte et al., 2017; Tchipalanga et al., 2018a; Brandt et al., 2023). Furthermore, observation reveals that isopycnals bend downward towards the coast in late austral summer and upward in austral winter, thus showing evidence of downwelling and upwelling (Tchipalanga et al., 2018a; Brandt et al., 2023). Looking at changes throughout the year reveals a semi-annual cycle in the vertical isopycnal movements that can be associated with the passage of the CTWs (Kopte et al., 2017; Rouault, 2012).

Salinity changes in the surface waters are influenced by changes in freshwater input and circulation. The Congo River outflow at 6°S is a major freshwater source for this region. In the mean, the river plume is located towards the offshore and the northern region of 6°S (Awo et al., 2022). Biannual intrusion of freshwater into tAUS in February-March and October-November from the north can be observed (Kopte et al., 2017; Lübbecke et al., 2019; Awo et al., 2022; Martins and Stammer, 2022). Observations show waters with salinity below $35\,psu$ reach 11°S in February in the climatological mean. The biannual intrusion of freshwater into the tAUS is in phase with the seasonal strengthening of the Angola Current, resulting in a semi-annual cycle in SSS in the tAUS (Awo et al., 2022).

Contrary to SSS, the seasonal cycle of SST in the tAUS undergoes no distinct semi-annual cycle (Fig. 1.2a). The lowest SSTs are found in August, when temperatures at the coast are on average 20.1 °C (averaged between 17°S and 6°S within 1° distance to the coast). The highest SSTs are present in March (27.4 °C). A mixed layer heat budget derived at a mooring location at 6°S, 8°E shows that surface temperatures at this location are controlled mainly by surface heat fluxes and vertical turbulent entertainment (Scannell and McPhaden, 2018).

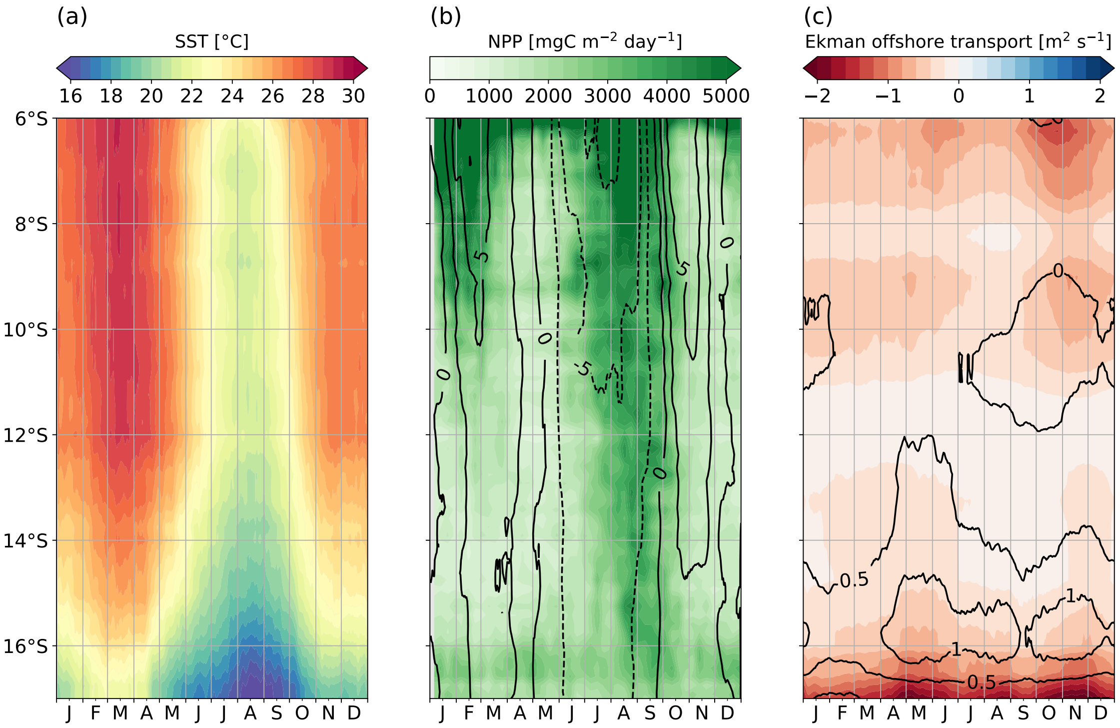

Figure 1.2: *Seasonal hovmöller plots along the Angolan coast.* ***(a)*** *Seasonal cycle of SST.* ***(b)****Seasonal cycle of net primary production (NPP) (colors) and SLA (black contour lines).* ***(c)*** *Seasonal cycle of Ekman offshore transport (colors) and wind stress curl driven upwelling (black contour lines). SST data from 1993-2022 was used (https://doi.org/10.48670/moi-00168). SLA data is from Copernicus (https://doi.org/10.48670/moi-00148) and was linearly detrended before producing this figure. SLA data from 1993-2022 was used. NPP data from 2003-2022 is used from ocean productivity site (http://orca.science.oregonstate.edu/1080.by.2160.8day.hdf.epple y.m.chl.m.sst.php). Wind data from ERA5 from 1993-2022 is used (https://doi.org/10.24381/cds.adbb2d47). NPP, SLA and wind stress curl driven upwelling were averaged within 1° distance from the coast. Ekman offshore transport is the zonal transport in the nearest grid point to the coast.*

The primary productivity in the tAUS undergoes a distinct seasonal cycle (Fig. 1.2b). A peak in productivity along the Angolan coast is visible in late austral winter. Furthermore, a secondary weaker peak, which is restricted to the northern tAUS, is visible in January/February. Thus, the seasonal cycle in productivity can be seen as a superposition of annual and semi-annual harmonics. Additionally, Fig. 1.2b shows the high productivity throughout the year at the the Congo River outflow at 6°S. The high productivity of the Kuene upwelling cell south of 16 °S is also visible, which marks the boundary to the Benguela upwelling system (Brandt et al., 2023).

Fig. 1.2b shows that the productivity peaks occur about a month after the passage of seasonal upwelling CTWs. As the occurrence of upwelling CTWs and productivity peaks is in phase, previous studies suggested that productivity in the tAUS is controlled by thermocline movements induced by CTWs (Ostrowski et al., 2009; Tchipalanga et al., 2018a; Brandt et al., 2023).

In literature, upwelling is often associated with the upward movement of water parcels driven by winds (Kämpf and Chapman, 2016). The reason for that is that most permanent upwelling systems in the world, like the Benguela upwelling system to the south of the tAUS, are driven by wind (Kämpf and Chapman, 2016). Wind-driven upwelling can be forced either by alongshore wind stress inducing offshore Ekman transport or by a cyclonic curl in the wind stress. In the tAUS, weak southerly alongshore winds blow throughout the year (Fig. 1.1a). The seasonal cycle is weak, with slightly enhanced winds in April and calmer winds in austral summer. Fig. 1.2c shows that the seasonal maxima of offshore Ekman transport as well as the wind curl-driven upwelling are disjoint from the maxima in net primary productivity. This underlines that upwelling in the tAUS is not driven by local winds (Berrit, 1976; Picaut, 1983; Ostrowski et al., 2009).

A look at the seasonal modulations in the tAUS suggests that productivity is connected to the passage of CTWs. However, how the upwelling CTWs control productivity is still not fully resolved (Brandt et al., 2023). In this context, note that an upward movement of the thermocline alone is unable to explain the near-coastal cooling and the upward nutrient supply. Gill and Clarke (1974) portrayed upwelling in a linear model as the raising of the thermocline at the coast with no change in the water mass properties at the surface. Near-surface mixing has been discussed as an important mechanism to cool surface water and enhance nutrient concentrations (Brink, 1983). See chapter 1.5 for an introduction to mixing and small-scale processes.

In the tAUS, the seasonal environmental changes lead to seasonal migration patterns of pelagic fish (Boely and Fréon, 1980; Ostrowski, 2007). Ostrowski (2007) found that the strong seasonal modulation of conditions in the tAUS impacts the preferred habitats of small pelagic fish. During downwelling phases, conditions for spawning and grazing are poor, leading to southward migration (Boely and Fréon, 1980; Ostrowski, 2007). During upwelling phases, high primary productivity is found in shallow waters in the tAUS, leading to favorable conditions in shallow waters along the Angolan coast (Ostrowski, 2007).

1.3 Interannual variability and long-term changes

Next to seasonal variability, variability on longer time scales is also important in the tAUS. The strongest mode of variability on interannual time scales are extreme warm and cold events, so-called Benguela Niños and Niñas (Shannon et al., 1986; Imbol Koungue et al., 2019). These events occur along the Angolan and Namibian coasts and peak typically between March and May (Rouault et al., 2007; Lübbecke et al., 2010; Imbol Koungue et al., 2019; Illig et al., 2020). Thus, these events peak mostly during the main downwelling season in the tAUS and play a minor role in the variability of biological productivity during the main upwelling season in late austral winter. Nevertheless, they can have severe impacts on regional climate, rainfall (Rouault et al., 2003; Hansingo and Reason, 2009), the distribution of oxygen and nutrients (Bachèlery et al., 2016a), and thus ecosystem productivity (Gammelsrød et al., 1998; Boyer et al., 2001; Ostrowski et al., 2009; Blamey et al., 2015). The forcing of Benguela Niños and Niñas has been mainly related to remotely forced CTWs inducing changes in the thermocline depth leading to SST anomalies (Florenchie et al., 2003; Rouault et al., 2007, 2018; Bachèlery et al., 2016b; Lübbecke et al., 2010; Imbol Koungue et al., 2019). Bachèlery et al. (2020) found that 71% of Benguela Niños and Niñas can be related to remote forcing. Local atmospheric forcing also plays an important role in generating and modulating these extreme events (Hu and Huang, 2007; Polo et al., 2008; Richter et al., 2010; Lübbecke et al., 2019; Illig et al., 2020). For instance, Lübbecke et al. (2019) showed that enhanced freshwater input into the surface ocean contributed to the surface warming during the 2016 extreme warm event.

In addition to the extreme events occurring in the tAUS, the tAUS is also subject to climate warming. Global SSTs show warming trends in response to increasing atmospheric greenhouse gas concentrations, which is projected to continue ((IPCC) Intergovernmental Panel on Climate Change, 2023). In the eastern equatorial Atlantic and in the tAUS, this warming trend is higher than the global average ((IPCC) Intergovernmental Panel on Climate Change, 2023). Furthermore, in recent decades, ocean stratification has increased, especially in the tropical oceans (Yamaguchi and Suga, 2019; Li et al., 2020). Roch et al. (2021) observed a strong increase in stratification in the Angola-Benguela Area (ABA) over the Argo period.

The SST variability in the tropical Atlantic is subject to variability as well (Tokinaga and Xie, 2011; Servain et al., 2014; Prigent et al., 2020b,a, 2023). Prigent et al. (2020b) found a shift in SST variability at the equator after the year 2000 associated with a weakening in the Bjerknes feedback and stronger net heat flux damping. The variability in SST in the ABA reduced associated with less influence of the equatorial remote forcing on the region and a strengthening of local atmospheric forcing (Prigent et al., 2020a). Sobral Verona et al. (2023) showed in historic CMIP6 model runs a decline in tropical Atlantic variability since the 1970s in response to a warming climate. However, the results of Sobral Verona et al. (2023) also highlight high multidecadal variability in tropical Atlantic variability, potentially linked to Atlantic Meridional Oscillation, which exhibits increased equatorial variability in negative phases (Martín-Rey et al., 2018). Around the same time that SST in the tropical Atlantic exhibited a shift in variability, the variability of El Niño/Southern Oscillation (ENSO) changed as well (Lübbecke and Mcphaden, 2014; Li et al., 2019; Hu et al., 2020). This is important to note, as ENSO influences tropical Atlantic variability (Chang et al., 2006; Latif and Grötzner, 2000).

Looking at future projections, the SST variability in the tropical Atlantic is expected to decrease in response to climate warming (Crespo et al., 2022; Deppenmeier, 2022; Prigent et al., 2023). At the equator, the variability of Atlantic Niño is projected to weaken, attributed to a decoupling of subsurface and surface processes (Crespo et al., 2022; Deppenmeier, 2022). Similarly, in the ABA, SST variability is projected to decrease, especially during the peak season of interannual SST variability (Prigent et al., 2023). Note that in the last few years, variability at the equator and in the ABA picked up again, with major warm events recorded in 2019 and 2021 (Richter et al., 2022; Illig and Bachèlery, 2023; Lee et al., 2023). This underlines that further work is needed to understand the future of tropical Atlantic variability and how this affects the dynamical connection between the equatorial region and the tAUS.

1.4 Large-scale dynamics

Chapter 1.2 & chapter 1.3 showed that the equatorial-forced CTWs play an important role for the tAUS. In this chapter, the theoretical concepts behind equatorial and CTW dynamics are introduced.

In general, the equator acts as a waveguide for disturbance in the vicinity of it due to the Coriolis force being zero there (Matsuno, 1966; Gill, 1982). There are four primary types of linear equatorial trapped waves: Poincaré, Rossby, Yanai, and Kelvin waves. In a stratified ocean, the equatorial waves have distinct vertical structures. These structures depend on the stratification and can be analysed with the concept of vertical normal modes (see Gill (1982) for a theoretical derivation). In general, low baroclinic modes have less complex vertical structures and propagate faster than high baroclinic waves.

For the tAUS, equatorial Kelvin waves (EKWs) are of high importance. EKWs are characterized by eastward propagation, are non-dispersive, and have a constant phase speed. The phase speed corresponds to the gravity wave speed of the particular baroclinic mode (Gill, 1982). Upon reaching the eastern boundary, part of its energy is reflected into a westward propagating equatorial Rossby wave and part is transferred into poleward propagating CTWs (Moore, 1968; Moore et al., 1978; McCreary, 1976; Polo et al., 2008). While propagating along the continental shelf, CTWs affect the water-coloumn density (Wang and Mooers, 1976). This deformation of the local density field affects the steric height. Consequently, CTWs can be observed in SLA data (Polo et al., 2008; Rouault, 2012). An upwelling CTW leads to an uplift of the main thermocline, which results in a negative SLA, and vice versa for a downwelling CTW.

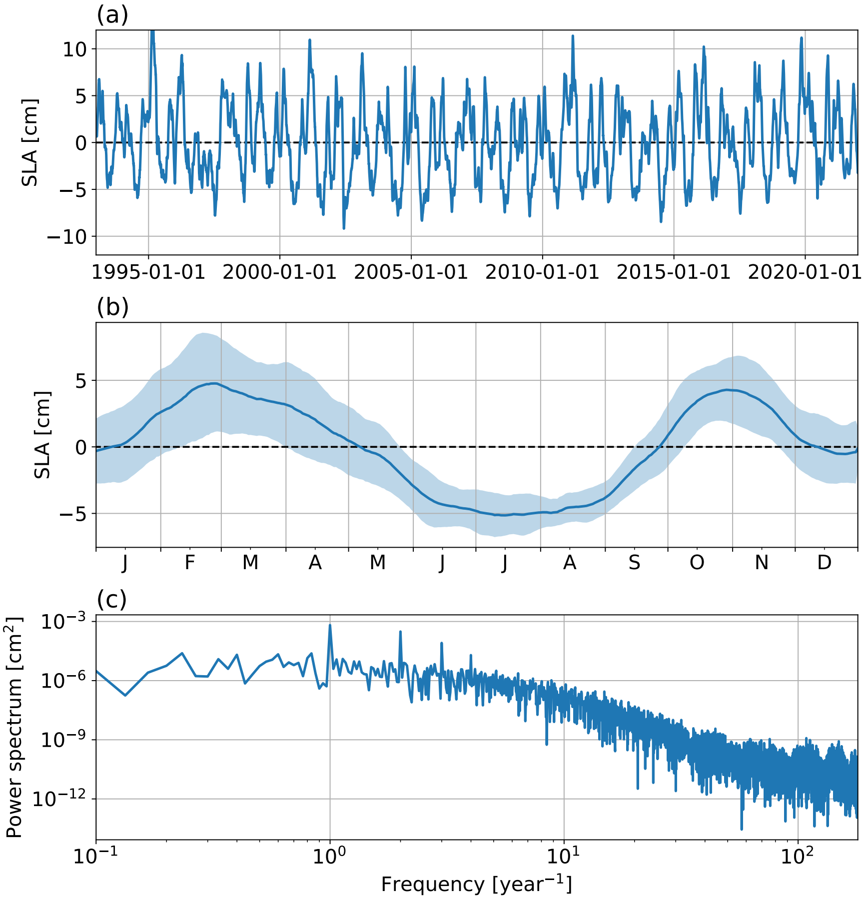

Figure 1.3: *Temporal variability of spatially averaged SLA in the tAUS. SLA data is averaged between 6°S and 17°S within 1° distance to the coast.* ***(a)*** *Time series of SLA between 1993 and 2022.* ***(b)*** *The seasonal cycle of SLA is calculated from the time series shown in (a). Shading gives the standard deviation.* ***(c)*** *Peridogram of the time series of SLA in the tAUS, calculated from the time series shown in (a). SLA data is from Copernicus (https://doi.org/10.48670/moi-00148) and was linearly detrended before producing this figure.*

Chapter 1.2 showed that the seasonal cycle of SLA in the tAUS can be described as a superposition of annual and semi-annual harmonics as two upwelling and two downwelling CTWs propagate along the Angolan coast throughout the year. Fig. 1.3 shows that annual and semi-annual variability are the dominant time scales of variability of SLA in the tAUS. The dominance of these time scales can be explained by considering the dominant wind forcing at the equator. At the equator, the winds show a seasonal cycle driven by the meridional mitigation of the intertropical convergence zone. The seasonal cycle of zonal wind stress can be described as a superposition of the annual and semi-annual harmonics as well. However, the annual signal is much stronger, with a distinct peak in boreal summer. Despite the relatively weak semi-annual wind forcing, an enhanced semi-annual signal in velocity at the equator is found. The relative enhancement of the semi-annual cycle can be attributed to equatorial basin modes (Philander and Pacanowski, 1981; Thierry et al., 2004; Ding et al., 2009; Brandt et al., 2016; Kopte et al., 2018). Equatorial basin modes are low-frequency standing equatorial modes consisting of an eastward propagating EKW and a westward propagating Rossby wave (Cane and Moore, 1981). The oscillation period of the gravest basin mode of a particular baroclinic mode is

$$T = \frac{4L}{c_n} \tag{1.1}$$

with L being the basin width and c_n the phase speed of the baroclinic mode n. Thus, with a particular combination of frequency and basin width, the resonance effect can lead to strong oscillation despite relatively weak forcing. In the Atlantic, the gravest basin mode of the second baroclinic mode is in resonance with the semi-annual wind forcing (Thierry et al., 2004; Ding et al., 2009; Brandt et al., 2016). The annual cycle is associated with the gravest basin mode of the fourth baroclinic mode, which is excited by the resonance of this mode with the annual wind forcing (Brandt et al., 2016). This resonance effect of the annual and semi-annual cycle is the reason why we find enhanced variability in the tropical Atlantic on these time scales.

The peridogram of the SLA time series exhibits clear peaks at annual and semi-annual time scales. Additionally, the spectrum reveals peaks of variability with 90- and 120-day periods (Fig. 1.3c). These peaks of intraseasonal CTWs can be associated with remote forcing as well (Imbol Koungue and Brandt, 2021). The signal of CTWs with a 90-day period is associated with zonal wind fluctuations in the eastern equatorial Atlantic. The 120-day signal can be attributed to the second equatorial basin mode of the second baroclinic mode (Imbol Koungue and Brandt, 2021).

CTWs are an important dynamical feature of the tAUS shaping conditions on different time scales. The characteristics of CTWs vary and depend on the forcing, the local shelf geometry, and the stratification. CTWs can be separated, analogous to vertical normal modes of equatorial waves, into distinct CTW modes. Much of the theory of CTWs was developed in the 1970s and 1980s (see Brink (1991) for a review). These theoretical concepts developed then are still widely used today when discussing CTWs (e.g. Illig et al. (2018b); Lüdke et al. (2020); Poli et al. (2022)). Although the excitement of CTWs by equatorial waves was discussed as well (Moore, 1968; Moore et al., 1978; McCreary, 1976), most of the theoretical groundwork was developed and discussed in the context of CTWs excited by alongshore wind fluctuations (Brink, 1991). Note that the concepts hold regardless of their excitement mechanisms.

CTWs exist with various length and frequency scales. For the topics discussed in this thesis, CTWs with frequencies smaller than the inertial frequency are of interest. These waves fall into "long wave" approximations, which assume that alongshore scales are large compared to across-shore scales. In the following, the CTW modes for this "long wave" approximation are derived (follwing e.g. Brink (1982, 1989); Wang and Mooers (1976); Chapman (1987); Huthnance (1978)). To derive the CTW modes, a linear, inviscid, continuously stratified ocean is considered. The bottom topography does not change in the alongshore direction, the stratification is horizontally uniform, and the Boussinesq approximation is applied. Given these assumptions the equations of motion reduce to:

$$-fv = -\frac{1}{\rho_0}p_x \tag{1.2}$$

$$v_t - fu = -\frac{1}{\rho_0}p_y \tag{1.3}$$

$$0 = -p_z - g\rho' \tag{1.4}$$

$$0 = u_x + v_y + w_z \tag{1.5}$$

$$0 = \rho'_t + w\overline{\rho}_z \tag{1.6}$$

where u, v, w are the onshore, alongshore and vertical velocities, p is the pressure perturbation, g the gravitational acceleration, and f the Coriolis parameter. The density is treated as $\rho = \rho_0 + \overline{\rho}(z) + \rho'(x, y, z, t)$ with $|\rho'| \ll \overline{\rho} \ll \rho_0$, f. The subscripts denotes partial derivation.

The solution to this can be found by reducing Eq. 1.2 - 1.6 to a single equation in terms of pressure:

$$0 = p_{xxt} + f^2\left(\frac{p_z}{N^2}\right)_{zt} \tag{1.7}$$

where N^2 is the buoyancy frequency. Solution to Eq. 1.7 can be found for a slowly varying medium by expanding p in terms of the free CTW modal structure $F_n(x, z)$ and their amplitude Φ_n:

$$p(x, y, z, t) = \sum_{n=1}^{\infty} F_n(x, z)\Phi_n(y, t) \tag{1.8}$$

Eq. 1.7 then becomes the following eigenvalue problem:

$$0 = (F_n)_{xx} + f^2\left(\frac{(F_n)_z}{N^2}\right)_z \tag{1.9}$$

which is subject to the following boundary conditions:

(a) free surface: $0 = g(F_n)_z + N^2F_n$ at $z = 0$

(b) No flow through the bottom: $(F_n)_z + N^2h_xf^{-2}[(F_n)_x + fc_n^{-1}F_n] = 0$ at $z = -h(x)$

(c) No flow though the coast: $0 = fc_n^{-1}F_n + (F_n)_x$ at $x = 0$

(d) Coastal trapping: $F_n \to 0$ as $x \to \infty$

where the phase speed c_n is the eigenvalue of this problem.

Modal structures are orthonormal subject to

$$\delta_{nm}D_n = f^{-1}\left[\int_{-h}^{0} F_n F_m|_{x=0} + \int_{-h}^{\infty} h_x F_n F_m|_{x=-h}\right] \tag{1.10}$$

where δ_{nm} is the Kronecker delta. D_n sets the magnitude of the cross-product. Thus, choosing D_n sets the normalization of the CTW modes. Brink (1989) showed that this should not be done arbitrary, and $D_n = 1$ has to be chosen to ensure energy conservation.

Solution to Eq. 1.9 can be found iteratively based on a resonance approach (Wang and Mooers, 1976; Brink, 1982). In this approach, for a fixed wavenumber, the frequency is varied until free-mode resonance is reached. Brink and Chapman (1987) developed a toolbox to perform this iteration, which is also used in this thesis in a modified version. Once the solution to Eq. 1.9 is found the structure functions of the cross- and alongshore velocity as well as the density can be derived.

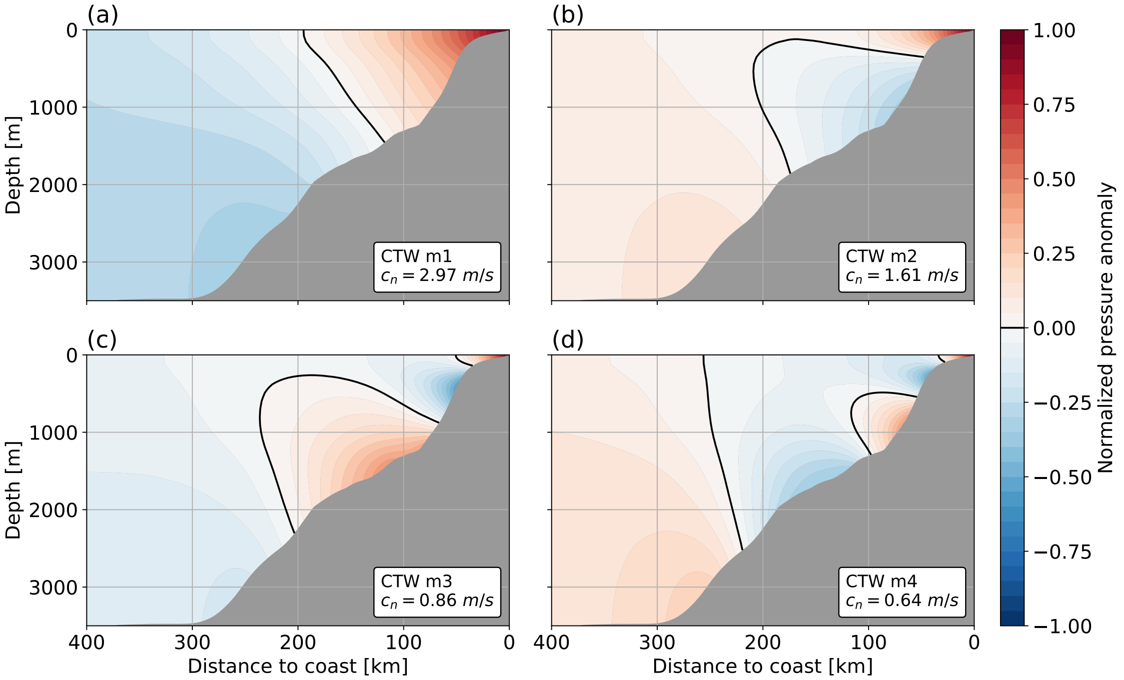

Figure 1.4: *Theoretical structure functions of pressure perturbation of the first four CTW modes at 11°S. The fields are normalized to the maximum pressure perturbation of each mode. The associated phase speed of each mode is given in the lower right corner. The black line marks the zero line. The structure functions were calculated using a modified version of the toolbox of Brink and Chapman (1987), observed mean N^2, and GEBCO topography (for details see Chapter 3).*

Based on the derived CTW modes, some properties of the waves can be discussed. Lower CTW modes have larger cross-shelf structures and propagate faster than higher mode CTWs (see example in Fig. 1.4). In general, following the theory, the modal structure of the n^{th}-order CTW has n zero crossing(s) in the pressure perturbation field at the sloping shelf (Illig et al., 2018b). Note that small topographic features can lead to numerical errors, resulting in pockets of reversed sign in CTW pressure structures at the coast (Brink and Chapman, 1987; Illig et al., 2018b). The evaluation of the dimensionless Burger number, S, is one way to quantify the relative importance of the latitude, the stratification, and the slope of the topography for the modal structure

$$S = \left(\frac{N_0 H}{f L}\right)^2 \tag{1.11}$$

where H, N_0, and L are typical values of depth, buoyancy frequency, and cross-shelf horizontal scale (Huthnance, 1978; Brink, 1991, 2006; Illig et al., 2018b). For small S, the flow of the CTW tends to be faster and more barotropic. For large S, flow tends to be slower and more baroclinic. Consequently, steep topographic slopes and stronger stratification are associated with more baroclinic structures (Illig et al., 2018b). Additionally, increasing the stratification increases the frequency at the same wavenumber (Brink, 1991).

The main mechanism for the decay of CTWs is friction (Brink, 1991). Note that friction does not act equally upon the modal structures, as frictional efficiency is much higher in shallow waters. Consequently, frictional effects can alter the modal structures (Brink, 1991; Romea and Allen, 1984; Brink, 2006). How frictional effects affect the modal structures is not straightforward and depends on the shelf geometry, stratification, latitude, and the presence of a mean flow (Romea and Allen, 1984; Brink, 2006). Romea and Allen (1984) find that for slopes where the Rossby radius is large compared to the slope width (typical for low latitude) offshore and vertical phase lags are induced and onshore flow is generated.

CTW modes are a powerful concept to characterize these kind of waves. However, when comparing the theory to observations, some aspects have to be kept in mind. Deriving modal structures for the "long wave" case makes some assumptions. One is that the topography does not change in the alongshore direction. This is far from reality considering the drastic changes in the topography and many seamounts off the coast of Angola. A horizontal uniform stratification is assumed to derive the CTW modes, which is also not the case off the coast of Angola (Tchipalanga et al., 2018a). Furthermore, the effect of friction, turbulent boundary layers, and fronts on the modal structures is complex and can alter the modal structures (Brink, 1991).

1.5 Mixing and small-scale processes

Variability in the ocean happens on various time and spatial scales. These scales range from millennial and basin-wide to seconds and millimeters. These motions are not independent but connected through an energy cascade. Energy input into oceans at large scales cascades towards small scales. The smallest end of the time and space scales are occupied by turbulent motion. Turbulent motion are of interest at global scales to understand the global ocean energy budget and overturning circulation (Sandström, 1908; Munk and Wunsch, 1998; Ferrari and Wunsch, 2009; Kunze, 2017; Whalen et al., 2020). Additionally, turbulence is also very important, as it potentially mixes waters with different characteristics and is thus important for the distribution of heat and solutes like nutrients. Consequently, turbulence is important for the tAUS as it may play a vital role in the near-coastal cooling and upward nutrient supply.

1.5.1 Internal waves

Internal waves are an ubiquitous feature of the stratified ocean. They play an important role in the cascade of energy to turbulent motion, as turbulent motion can be induced by breaking internal waves. The internal wave field can be excited by various factors: wind, geostrophic currents, and tides (Whalen et al., 2020). As tides are thought to be the most important energy source of the internal wave field at the continental slope/on the shelf in the tAUS (Zeng et al., 2021), this aspect is the focus of the following.

Tides supply roughly $1TW$ of energy to the global internal wave field (Whalen et al., 2020). The barotropic tides are generated through the gravitational interaction between the Moon, the Sun, and the Earth (Garett and Kunze, 2007). Barotropic tides have a uniform depth structure. Part of the barotropic tidal energy generates internal tides through interaction with topography by pushing stratified fluid over sloping seafloor (Wunsch and Gill, 1976; Baines, 1982; Whalen et al., 2020). The generated internal tide can have different vertical structures. Generally, high-mode internal tides are more dissipative and often induce turbulence in close proximity to the topography where they were generated (Ledwell et al., 2000; Polzin, 2004). In the contrary, low-mode internal tides can propagate over large distances and induce turbulence far away from their generation site (Ray and Mitchum, 1996; Nash et al., 2004; Zhao et al., 2016).

The interaction of the barotropic and low-mode internal tides with the continental slope/shelf can lead to a complex internal wave field (Lamb, 2014). One important factor that helps predict the behavior of incident waves approaching a slope is the ratio between the topographic slope and the internal wave characteristic slope,

$$\alpha = \frac{s_{topo}}{s_{wave}} = \frac{\partial H/\partial x}{\left[(\omega^2 - f^2)/(N^2 - \omega^2)\right]^{1/2}} \tag{1.12}$$

where H is the water depth, x is the cross-slope distance, ω is the frequency of the wave, f is the inertial frequency, and N is the buoyancy frequency. α is the criticality, where $\alpha < 1$ indicates subcritical conditions where waves approaching the slope are transmitted onshore. If $\alpha > 1$, the conditions are supercritical, and waves are reflected back. If $\alpha \approx 1$, linear wave theory breaks down, leading to nonlinear effects, wave breaking, and turbulence (Legg and Adcroft, 2003; Dauxois et al., 2004; Hall et al., 2012). The criticality α shows how wave-topography interactions depend on shelf geometry, the frequency of the wave, stratification, and latitude.

The internal wave field on continental shelves is often composed of waves of many frequencies and wave lengths (Nash et al., 2004; Lamb, 2014). Commonly observed in coastal shelf systems are nonlinear internal waves (NLIWs) (Apel, 2002). NLIW can have various characteristics. One form of NLIWs is internal solitary waves (ISW) (see Fig. 1.5 for ISW observed on the Angolan shelf). These waves often form from weakly nonlinear internal tides, which steepen and form strongly nonlinear ISW packages (Jackson et al., 2012). The internal tides and ISW on continental shelves may be locally (Shroyer et al., 2010a) or remotely generated (Nash et al., 2012). ISW are capable of transporting mass through trapped cores or through Stokes drift (Huthnance, 1995; Lamb, 2014). Consequently, they can play an important

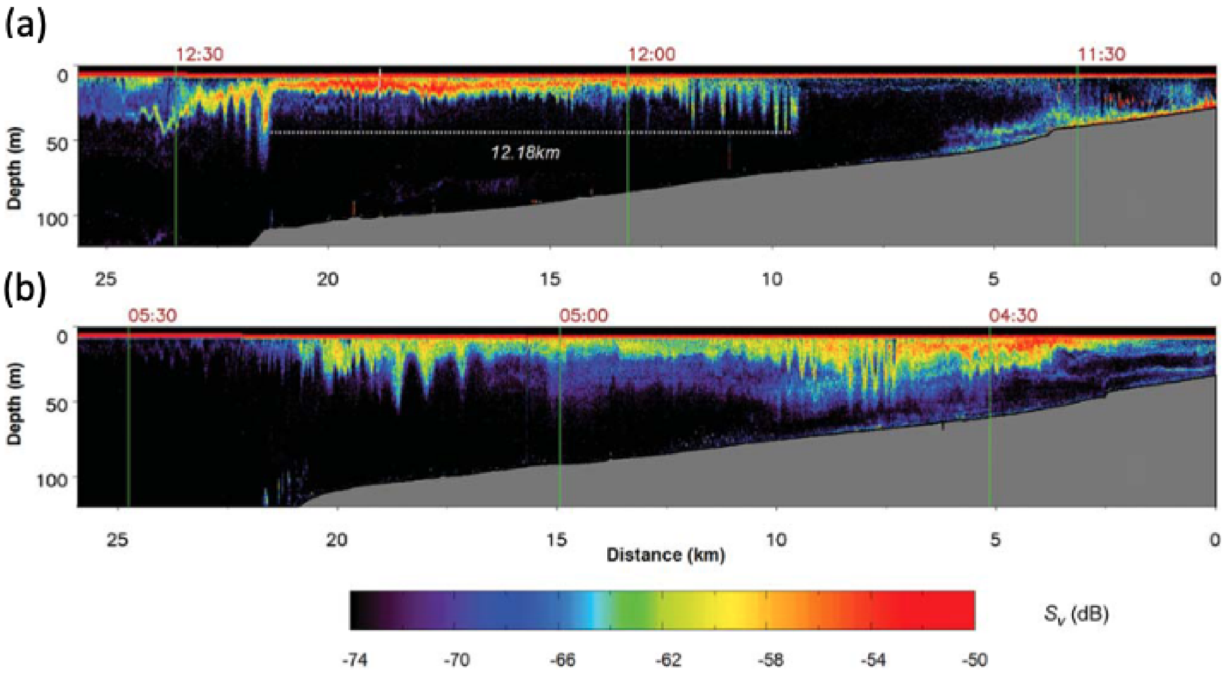

Figure 1.5: *Echosounder images measured across the Angolan shelf. Dates and times (UTC) of the observations are:* ***(a)*** 5^{th} *August 1998, 11:21–12:37; and* ***(b)*** 7^{th} *August 2001, 04:15–05:34. The colour scale depicts volume-backscattering strength Sv (dB). Figure is adapted from Ostrowski et al. (2009)*

role in the lateral exchange of water in the cross-shelf direction (Huthnance, 1995). Furthermore, the breaking of ISW and internal waves in general can induce turbulent motion, which potentially play an important role in the near-coastal cooling and upward nutrient supply. In the next chapter, these turbulent motion and fluxes are introduced.

1.5.2 Turbulence and fluxes

One of the last steps of the energy cascade from large scales to small scales is turbulence. But what exactly is turbulence? According to Thorpe (2005), "no really precise, robust, unambiguous or clear definition of what is meant by turbulence has [...] been devised ." He goes on that, "turbulence is generally accepted to be an energetic, rotational and eddying state of motion that transpires to produce dispersion of material and to transfer heat and solutes at rates far higher than those of molecular processes alone" (Thorpe, 2005).

Turbulence can be induced by internal waves cascading to small scales, where shear and convective instabilities can lead to wave breaking (Van Haren, 2015; Thorpe, 2018; Whalen et al., 2020). Breaking internal waves create turbulent kinetic energy (TKE). The TKE either dissipates into heat or works against the ocean density gradient (Osborn, 1980; Whalen et al., 2020).

One reason why we care about turbulence motion is because of the turbulent fluxes it induces. As mentioned by Thorpe (2005), turbulent fluxes transfer heat and solutes at rates far higher than those of molecular processes alone. However, it's crucial to recognize that, at their core, turbulent fluxes rely on molecular processes. Molecular diffusion occurs because particles move randomly and undirected in above absolute zero temperatures (Einstein, 1905). Considering a fluid with a concentration gradient, while the movement of one particle is random, the interaction of several particles leads to equilibration of the concentration gradients. Thus, molecular diffusion increases the entropy of a system and is an irreversible process. Molecular diffusion is inherently slow. Turbulent fluxes operate at far higher rates as turbulent motions add external force to vigorously stir the fluid.

Molecular diffusion can be mathematically described by Ficks law,

$$\mathbf{J} = -D \nabla \phi \tag{1.13}$$

where $\mathbf{J}$ is the diffusion flux vector of the variable ϕ and D is the diffusivity (Fick, 1855). Fick's law shows that diffusion depends on two variables: the concentration gradient and the diffusivity. Turbulent fluxes can be described similarly by replacing the diffusivity D with the eddy diffusivity K (Taylor, 1935). Consequently, to determine turbulent fluxes in the ocean, we need to know two key aspects: concentration gradients and turbulent eddy diffusivity. Measuring concentration gradients is pretty straightforward and can often be measured directly. Determining the turbulent eddy diffusivity is more complex as it cannot be measured directly and because turbulent motion is highly variable on small temporal and spatial scales.

Eddy diffusivity can be defined differently, e.g. the diapycnal diffusivity, K_ρ, is the diffusivity perpendicular to isopycnals. Analogously, K_T, the diathermal diffusivity, is the diffusivity perpendicular to isotherms, and the diahaline diffusivity, K_S, is defined perpendicular to isohalines (Gregg et al., 2018). Estimating K from measurable quantities presents a challenge, and various approaches exist. One approach determining the diapycnal diffusivity is based on the shear variance,

$$K_\rho = \Gamma \epsilon N^{-2} \tag{1.14}$$

where ϵ is the dissipation rate of TKE and Γ is the mixing efficiency (Osborn, 1980). ϵ can be estimated from microstructure shear measurements. When assuming isotropy, ϵ and shear are connected through

$$\epsilon = 7.5\ \nu \int E_{du/dz}(k) dk \tag{1.15}$$

where ν is the dynamic viscosity of seawater and $E_{du/dz}(k)$ is the shear wavenumber spectrum. The shear spectra can be determined from the airfoil shear sensors attached to the microstructure probes (Hummels et al., 2014). To account for variance loss due to the limited resolution in wavenumber space, the spectra are fitted to the universal Nasmyth spectrum (Wolk et al., 2002).

The eddy diffusivity also depends on the mixing efficiency. The mixing efficiency is the ratio of the net change in potential energy to the energy expended in producing mixing (Gregg et al., 2018). Essentially, it represents the fraction of TKE that is effectively utilized for mixing water. Gregg et al. (2018) pointed out by reviewing observational, laboratory, and numerical studies fundamental gaps in our knowledge concerning the mixing efficiency. The mixing efficiency is unlikely constant and seems to be dependent on various factors, including the stratification and the turbulent regime (Shih et al., 2005; Gregg et al., 2018). Many studies find that $\Gamma = 0.2$ is a good choice for many turbulent processes and background conditions. Gregg et al. (2018) propose to choose $\Gamma = 0.2$ until further understanding is achieved in this important aspect of ocean mixing. Because of the uncertainties in mixing efficiency and the the fact that ϵ is lognormally distributed (Davis, 1996), it is desirable to estimate turbulent fluxes averaged over many observations. Ideal datasets encompass samples of many mixing events at varying intensities and ages. It is important to note that mixing efficiency tends to decrease in weakly stratified waters, although the specifics of this decrease remain uncertain (Gregg et al., 2018). Consequently, estimating eddy diffusivity in low-stratified waters, such as the mixed layer, should be avoided.

1.5.3 Small-scale processes in the tAUS

In the tAUS, a region with generally low winds, the biggest energy source for the local internal wave field is assumed to be tide topography interaction (Zeng et al., 2021). In the tAUS, the continental slope/shelf region between 200 and 500m is critical or supercritical with respect to the M2 tide (Fig. 1.6c) (Zeng et al., 2021). In this depth range, the largest portion of the internal tide energy is generated. While some of that energy was found to be dissipated locally or further offshore, a substantial amount propagates onshore and dissipates in shallow waters near the coast, which leads to near-coastal surface cooling (Zeng et al., 2021) (Fig. 1.6).

The absence of a seasonal cycle in the barotropic tide indicates a relatively constant tidal energy influx to the Angolan shelf throughout the year. But what is the situation on the shelf? Eq. 1.12 shows that the interaction of internal waves with topography also depends on stratification. Stratification in the tAUS undergoes a semi-annual cycle (Kopte et al., 2017). How does the internal wave field change throughout the year?

Shipboard acoustic backscatter images show the presence of tidally generated ISWs on the Angloan shelf (Ostrowski et al., 2009) (Fig. 1.5). The ISW packages propagate from the shelf break towards the coast. Ostrowski et al. (2009) found that the trains of ISWs are more developed and stronger during the upwelling phases, where stratification is weaker, than during the downwelling phases. This led to the theory that the seasonal change in stratification could alter the tide-topography interaction such that more tidal energy is available for mixing on the Angolan shelf during the upwelling phases. How the interaction of tide and topography changes with changing stratification in the tAUS was investigated by using a MITgcm model set up by Zeng et al. (2021). They found that the characteristics of the internal wave field in the tAUS vary with varying background stratification. However, the spatially averaged generation, onshore flux, and dissipation of internal tide energy are weak. This means that throughout the year, roughly the same amount of energy is available for mixing in shallow waters. However, the energy available for mixing acts on seasonally different background stratification, leading to different effects of mixing. The model shows stronger cooling of surface waters during times of weak stratification. This can be explained when considering that the eddy diffusivity is anti-proportional to the stratification($K_\rho \sim N^{-2}$). Consequently, mixing is more effective with weak background stratification even when the energy available for mixing is constant. This underlines the complex relationship between tidal forcing, background stratification, and the resulting impact on the conditions in the tAUS.

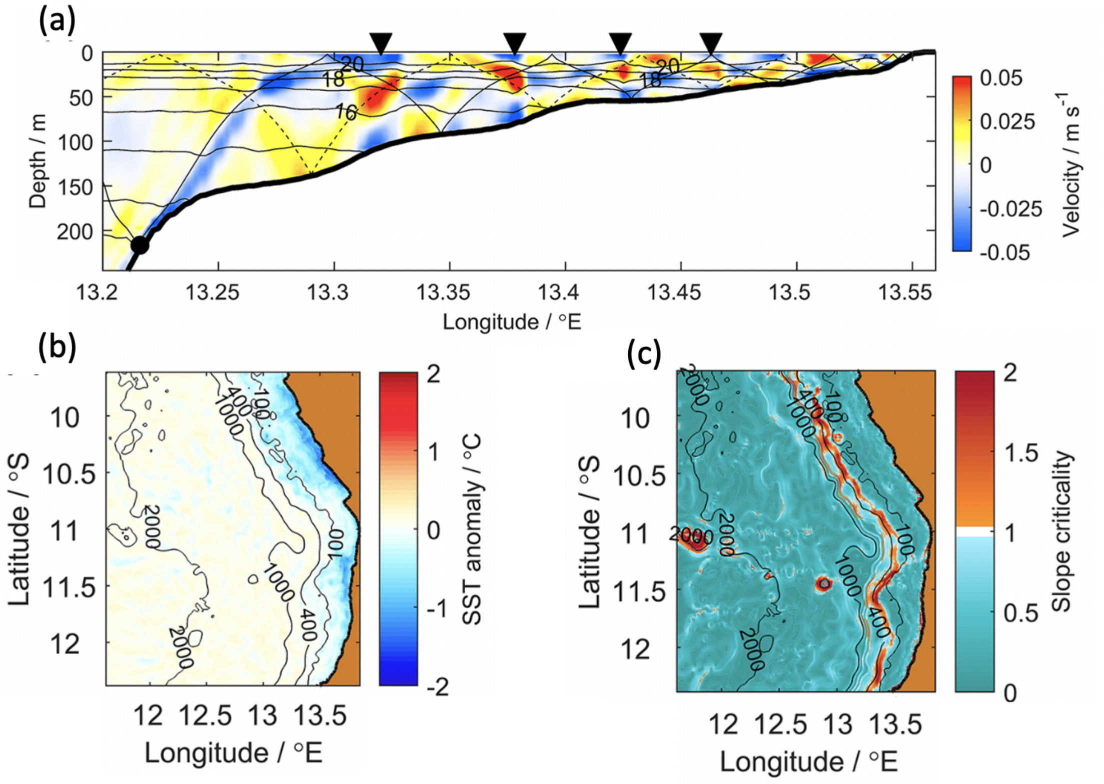

Figure 1.6: *Model results simulating tide-topography interaction at the Angolan shelf.* ***(a)*** *Cross-shore baroclinic velocity anomaly along a cross-shelf section at 11°S after 20 tidal cycles. Solid horizontal lines are isotherms. Overlaid black solid lines originating at the critical point (black dot) are primary M2 tidal beams, allowing reflections at the surface and at the bottom. The dashed lines are secondary M2 tidal beams, starting at another generation point further offshore.* ***(b)*** *SST anomaly after 20 tidal cycles.* ***(c)*** *Slope criticality for M2 tide. Figure adapted from Zeng et al. (2021), the reader is referred to this publication for more information. The results shown here are from case 0 which uses the climatological July stratification.*

Small-scale processes play an important role for the tAUS. The results of the model set up by Zeng et al. (2021) showed that tidally induced mixing leads to a cooling near the coast (Fig.1.6b). Furthermore, Ostrowski and Bazika-Sangolay (2016) showed how pelagic fish aggregations can be located inshore of a shallow front induced by internal wave breaking. Additionally, the role of mixing has been discussed for upward nitrate supply (Ostrowski et al., 2009; Brandt et al., 2023), although it has not been explicitly investigated so far.

1.6 Motivation & Outline

The eastern boundaries of the tropical Atlantic and Pacific Oceans are hot spots of primary production and marine life. These tropical upwelling systems play a key role in supporting marine biodiversity, global fisheries, and biogeochemical cycles (Kämpf and Chapman, 2016). It is thus of high interest to understand the processes that drive these systems. A high process understanding is fundamental to predicting variability and to assessing possible future changes within these systems, e.g., due to climate warming.

The tAUS is one of these highly productive tropical upwelling systems. As shown in this chapter, the characteristics of the tAUS are shaped both by local as well as remote factors. The tAUS is closely linked to equatorial dynamics via the propagation of CTWs (Polo et al., 2008; Rouault, 2012). Conditions in the tAUS show strong seasonal modulations with dominant variability on annual and semi-annual time scales (Brandt et al., 2023). The dominance of these time scales is connected to the prevailing wind forcing in the equatorial Atlantic and to the basin resonance, relatively enhancing the semi-annual cycle (Philander and Pacanowski, 1981; Thierry et al., 2004; Brandt et al., 2016).

Great progress has been made in understanding the dynamics in the tAUS, however, open questions remain. One central question concerns the mechanism controlling productivity in the tAUS. Similar to other tropical upwelling systems, wind stress maxima and productivity maxima are disjoint in the tAUS (Thomas et al., 2001, 2012). In the tAUS, the seasonal cycle of productivity is thought to be connected to the passage of CTWs (Ostrowski et al., 2009; Tchipalanga et al., 2018a; Brandt et al., 2023). However, how the CTWs control productivity in the tAUS is not resolved. Further open questions concern the seasonal variability of SST. In the tAUS, SST directly at the coast is lower than further offshore throughout the year. The lowest SST and the strongest cross-shore SST gradient are found in austral winter during the main upwelling season (Brandt et al., 2023). It is thus of interest to analyze if similar processes drive the seasonal variability in SST and productivity. A greater understanding of the processes driving the seasonal cycle in SST is further of interest, as the southeastern tropical Atlantic is subject to a warm bias in SST in global climate models (Richter, 2015; Kurian et al., 2021; Farneti et al., 2022). Consequently, a deeper understanding of seasonal variability in this region might contribute towards a better representation of the tAUS in climate models.

The work presented in this thesis focuses on the dynamics behind the seasonal variability in the tAUS. To do so, mostly observational data is used, including shipboard measurements as well as satellite products. The shipboard datasets include over 8000 conductivity-temperature-depth (CTD) and oxygen profiles collected in the tAUS. Furthermore, over 700 microstrucutre profiles provide insights into turbulent heat and nitrate fluxes in the tAUS. Combining these extensive observational datasets allows for in-depth analyses of the dynamics in the tAUS on various spatial and temporal scales. The thesis aims at contributing towards answering the following questions:

- What physical drivers shape the seasonal variability in the tAUS?
- What controls the year-to-year variability of the main upwelling season in the tAUS?

This thesis is structured as follows: chapters 2 through 4 contain individual manuscripts that are either already peer-reviewed and published in scientific journals, are accepted for publication, or are in the final stage of preparation for submission. In chapter 2 a study on the seasonal cycle of SST is presented. A study about the mechanism behind the main productivity peak is presented in chapter 3. Chapter 4 presents a study on the year-to-year variability of the characteristics of the austral winter upwelling CTW. Finally, chapter 5 summarizes and discusses the results before giving an outlook.

2 Seasonal cycle of sea surface temperature in the tropical Angolan upwelling system

The seasonal cycle of sea surface temperatures (SST) in the trocial Angolan upwelling system (tAUS) exhibits annual variability. In the tAUS, throughout the year, SST is colder directly at the coast than further offshore. The seasonal cycle of the cross-shore temperature gradient shows variability on semi-annual time scales. The study presented in this chapter analyzes the drivers behind the seasonal cycle of SST both in the coastal and offshore regions of the tAUS. To do so, a mixed layer heat budget is calculated based on satellite and in situ data. The mixed layer heat budget allows for an analysis of the oceanic and atmospheric drivers of heat content change. Furthermore, differences in the processes between the near-coastal and offshore regions can be evaluated.

The manuscript was published in *Ocean Science* in January 2023.

Körner, M., Brandt, P., and Dengler, M. (2023), Seasonal cycle of sea surface temperature in the tropical Angolan Upwelling System, Ocean Sci., 19, 121–139, https://doi.org/10.5194/os-19-121-2023.

The candidate designed the study, and carried out the analysis of observational, reanalysis, and satellite data products, produced all figures, and authored the manuscript from the first draft to the final published version.

2.1 Abstract

The Angolan shelf system represents a highly productive ecosystem. Throughout the year the sea surface is cooler near the coast than further offshore. The lowest sea surface temperature (SST), strongest cross-shore temperature gradient, and maximum productivity occur in austral winter when seasonally prevailing upwelling-favourable winds are weakest. Here, we investigate the seasonal mixed layer heat budget to identify atmospheric and oceanic causes for heat content variability. By using different satellite and in situ data, we derive monthly estimates of surface heat fluxes, mean horizontal advection, and local heat content change. We calculate the heat budgets for the near-coastal and offshore regions separately to explore processes that lead to the observed SST differences. The results show that the net surface heat flux warms the coastal ocean stronger than further offshore, thus acting to damp spatial SST differences. Mean horizontal heat advection is dominated by meridional advection of warm water along the Angolan coast. However, its contribution to the heat budget is small. Ocean turbulence data suggest that the heat flux, due to turbulent mixing across the base of the mixed layer, is an important cooling term. This turbulent cooling, being strongest in shallow shelf regions, is capable of explaining the observed negative cross-shore temperature gradient. The residuum of the mixed layer heat budget and uncertainties of budget terms are discussed.

2.2 Introduction

The coastal waters off Angola host a highly productive ecosystem of great socio-economic importance for local communities: the tropical Angolan Upwelling System (tAUS) (Sowman and Cardoso, 2010; FAO, 2022). The Congo River outflow at 6°S forms the northern boundary of the tAUS. To the south the Angola-Benguela Frontal Zone located between 15°S and 18°S separates the warm surface waters of the tAUS from colder water further south (Fig. 2.1a). The tAUS is characterized by lower Sea Surface Temperatures (SSTs) near the coast compared to further offshore throughout the year (Fig. 2.1a). In austral winter we find the lowest SSTs, the strongest negative cross-shore SST gradient as well as the maximum in primary productivity in the tAUS (Fig. 2.2) (Tchipalanga et al., 2018a; Zeng et al., 2021; Awo et al., 2022). Thus, understanding the drivers of heat content changes in the upper ocean in the tAUS might be important for the understanding of productivity as well. Additionally, it is also of larger-scale importance due to the remote impact of the southeastern tropical Atlantic on tropical climate (Xu et al., 2014).

The circulation in the tAUS is dominated by the Angola Current (Fig. 2.1a) whose core is located at around 50 m depth. The Angola Current transports warm water poleward along the Angolan continental slope and shelf. The transport is weak (0.32 SV) and subject to variability on different time scales (Kopte et al., 2017). Past studies showed that the variability is connected to equatorial dynamics via the propagation of equatorial and coastal trapped waves (CTWs) and to local forcings (Bachèlery et al., 2016b; Kopte et al., 2017; Illig et al., 2018b). The Angola Current is fed via the Equatorial Undercurrent, the South Equatorial Undercurrent, and the South Equatorial Countercurrent with South Atlantic Central Water (Kopte et al., 2017; Tchipalanga et al., 2018a; Siegfried et al., 2019). In the Angola-Benguela

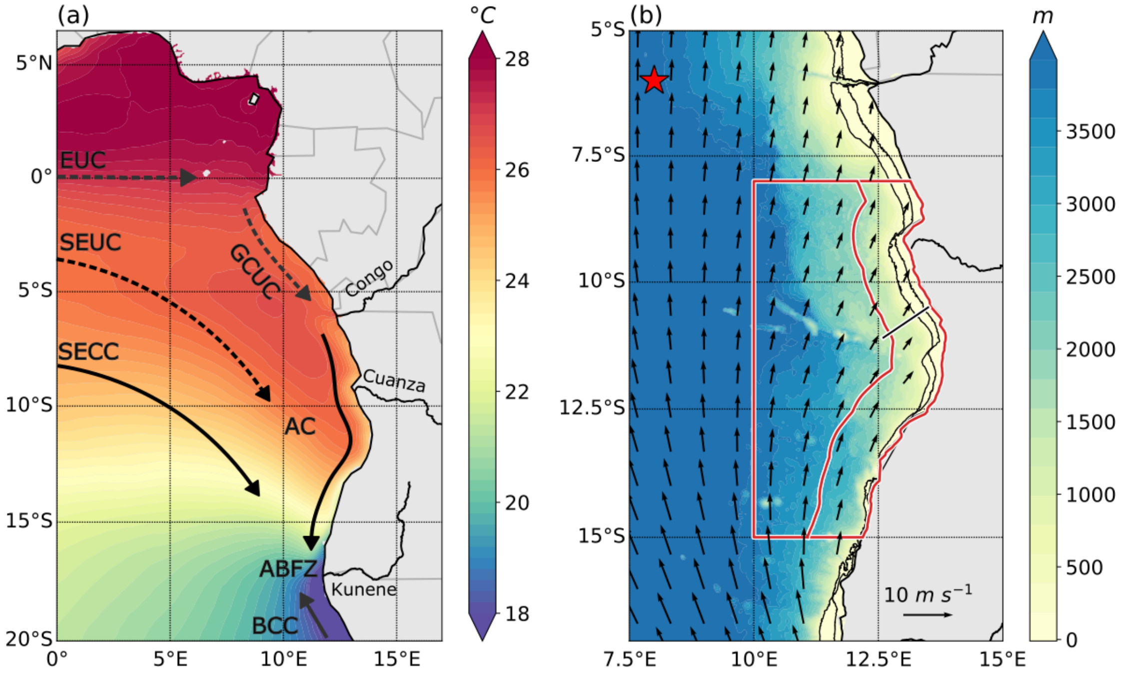

Figure 2.1: *(a) Mean Sea Surface Temperature (SST) (colours) and schematic circulation in the southeastern tropical Atlantic. Solid arrows indicated pathways of surface currents, dashed arrows of subsurface currents. Currents displayed here are the Equatorial Undercurrent (EUC), the Gabon Congo Undercurrent (GCUC), the South Equatorial Undercurrent (SEUC), the South Equatorial Countercurrent (SECC), the Angola Current (AC), and the Benguela Coastal Current (BCC). Additionally, the position of the Angola-Benguela Frontal Zone (ABFZ) is marked. (b) Topography (colours) and mean wind field (arrows) off the coast of Southwest Africa. Black lines mark the 75 m and 175 m isobath. Red boxes show the extent of the coastal and offshore boxes. Red star marks the position of the PIRATA-SEE mooring. Black line shows the 11°S section.*

Frontal Zone, the poleward Angola Current meets the northward Benguela Coastal Current (Shannon et al., 1987; Siegfried et al., 2019) (Fig. 2.1a).

The surface waters in the tAUS are characterized by warm tropical conditions (Tchipalanga et al., 2018a; Awo et al., 2022) (Fig 1a). In austral winter the lowest SSTs are observed (Fig. 2.2). The SST at the coast can then drop below 21°C (Fig. 2). Highest temperatures are found in austral autumn when coastal SSTs reach 28°C (Fig. 2.2) (Awo et al., 2022). In contrast to other eastern boundary upwelling systems, the changes in surface temperatures, cross-shelf temperature gradient, and productivity in the tAUS cannot be explained by local wind-driven upwelling (Ostrowski et al., 2009). On average, the winds in tAUS are southwesterly and substantially weaker than in the Benguela upwelling system further south (Fig. 2.1b). They have a weak seasonal cycle with a minimum in upwelling-favourable winds during the upwelling season in austral winter (Ostrowski et al., 2009; Zeng et al., 2021).

Changes in upper ocean heat content in the tAUS can be affected by the passage of remotely forced CTWs. The CTWs have a signal in sea level anomaly (SLA). Analysing SLA data in the tAUS reveal the passage of four CTWs per year (Rouault, 2012). In March a downwelling CTW propagates along the Angolan coast followed by an upwelling CTW in June-July. In October a second downwelling CTW arrives at the Angolan coast followed by a weak upwelling wave in December-January (Tchipalanga et al., 2018a). Thus, the upwelling season coincides with the presence of an upwelling CTW at the Angolan

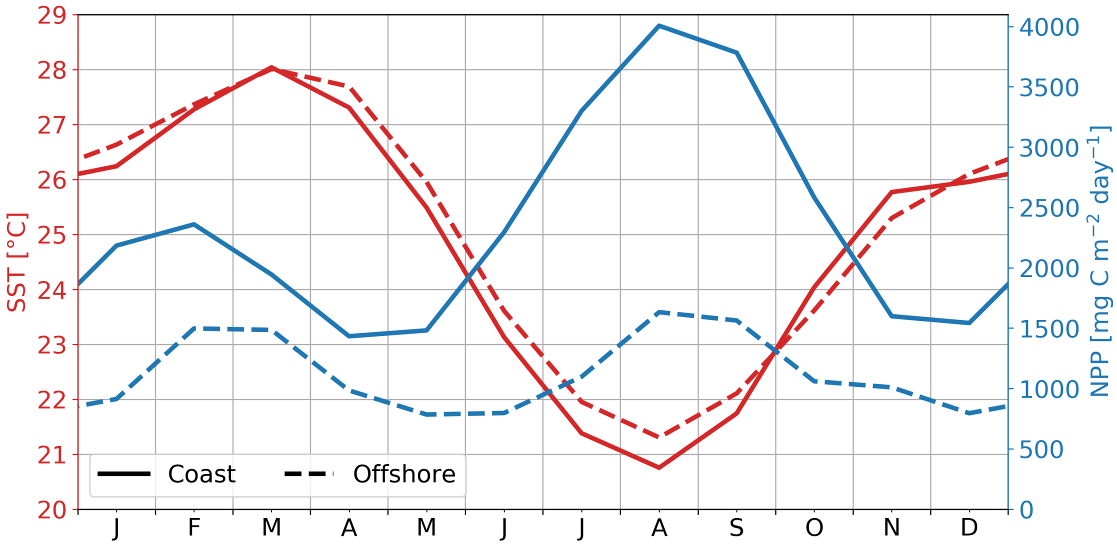

Figure 2.2: *Seasonal cycle of SST (red) and net primary production (blue) averaged over the coastal box (solid lines) and offshore box (dashed lines) shown in Fig. 2.1b.*

coast. However, the vertical movement of the thermocline alone is unable to explain the near-coastal cooling and the upward nutrient supply during austral winter. In this context, the role of mixing induced by internal tides has been discussed (Ostrowski et al., 2009; Tchipalanga et al., 2018a; Zeng et al., 2021). Zeng et al. (2021) showed in a recent model study that seasonal variations in the spatially-averaged generation, onshore flux, and dissipation of internal tide energy are weak. Due to the seasonal variation in stratification, however, turbulent mixing driven by internal tides is more effective in reducing the SST during the upwelling season.

The sea surface salinity (SSS) undergoes a distinct seasonal cycle in the tAUS (Awo et al., 2022). In October/November and in February/March freshwater intrudes into the northern part of the tAUS (Kopte et al., 2017; Lübbecke et al., 2019; Awo et al., 2022). A recent model study (Awo et al., 2022) suggests that the freshening is controlled by meridional advection via the Angola Current, with the Congo River as an important freshwater source. Vertical advection and mixing at the base of the mixed layer (ML) were found to counteract this freshening (Awo et al., 2022).

The stratification in the tAUS is controlled by the passage of CTWs as well as the changes in salinity and temperature (Kopte et al., 2017; Tchipalanga et al., 2018a). The stratification undergoes a semi-annual cycle with strong stratification near the surface during the passage of the downwelling CTW and surface freshening in February/March and October/November (Kopte et al., 2017; Tchipalanga et al., 2018a; Awo et al., 2022).

The southeastern tropical Atlantic is subject to a warm bias in SST in global climate models (Richter, 2015; Kurian et al., 2021; Farneti et al., 2022). The reasons for the warm bias are still under debate. Some studies suggest that the origin of the bias lies in the representation of the atmosphere. Here excessive shortwave radiation due to a poor representation of clouds (Huang et al., 2007), an atmospheric moisture bias (Hourdin et al., 2015; Deppenmeier et al., 2020) or errors in the wind forcing (Voldoire et al., 2019; Richter and Tokinaga, 2020; Kurian et al., 2021) have been discussed. The role of the correct representation of ocean dynamics has also been suggested as the source of the bias (Xu et al., 2014). In this context, Deppenmeier et al. (2020) show that enhancing turbulent vertical mixing in ocean models helps to reduce the error.

Previous studies investigated the ML heat budget in the southeastern Atlantic Ocean to identify atmospheric and oceanic drivers of heat content variability (Scannell and McPhaden, 2018; Foltz et al., 2019; Deppenmeier et al., 2020). Scannell and McPhaden (2018) analyse the ML heat budget from moored observations at 6°S, 8°E. They found that surface heat fluxes and vertical turbulent entrainment primarily control the changes in SST. Foltz et al. (2019) examined the residuum between the heat content change and the surface heat fluxes. They attribute horizontal heat advection and turbulent cooling as the main contributor to this residuum. Their results reveal a large residuum in tAUS of $\sim 60\ W\ m^{-2}$ increasing towards the coast. This suggests that in the near-coastal area different processes lead to the cooling of the ML compared to further offshore.

In the present study, we analyse the atmospheric and oceanic drivers of heat content variability in the tAUS. In contrast to previous studies, we evaluate the ML heat budget near the coast and further offshore separately. This allows us to investigate and discuss processes that lead to the observed stronger cooling close to the coast. Furthermore, utilizing shipboard measurements of ocean turbulence we present for the first time an estimate of the impact of turbulent heat loss at the base of the ML in the tAUS. The study is structured as follows: In Sections 2 and 3 data and methodology are described, respectively. In Section 4 we present the results of our study and in Section 5 we summarize and discuss the results.

2.3 Data

2.3.1 Shipboard measurements

In this study, we analyse data collected during 6 research cruises that have been conducted in Angolan waters between 2013 and 2022 on board of RV *Meteor*. During those cruises, ocean turbulence data were collected using a microstructure profiler manufactured by Sea & Sun Technology. The microstructure shear measured by the microstructure profiler can be used to estimate the dissipation rate of turbulent kinetic energy (TKE). The microstructure profiler was equipped with 2-3 airfoil shear sensors, an acceleration sensor, tilt sensors, a fast temperature sensor as well as standard CTD sensors. The microstructure profiles are measured by letting the loosely tethered probe fall free with a fall speed of $0.5\ -\ 0.6\ m\ s^{-1}$.

During the 6 cruises, a total of 701 microstructure profiles were measured. The schedule of the cruises as well as the number of microstructure profiles taken during the individual cruise are summarized in Table 2.1. A similar sampling strategy was chosen during the individual cruises that included a heavily sampled cross-shelf section at 11° S (Fig. 2.1b). However, the exact locations of microstructure measurements on the shelf differed amongst the cruises, which leads to an inhomogeneous distribution of microstructure profiles in different months. The distribution for each cruise is displayed in Fig. 2.3.

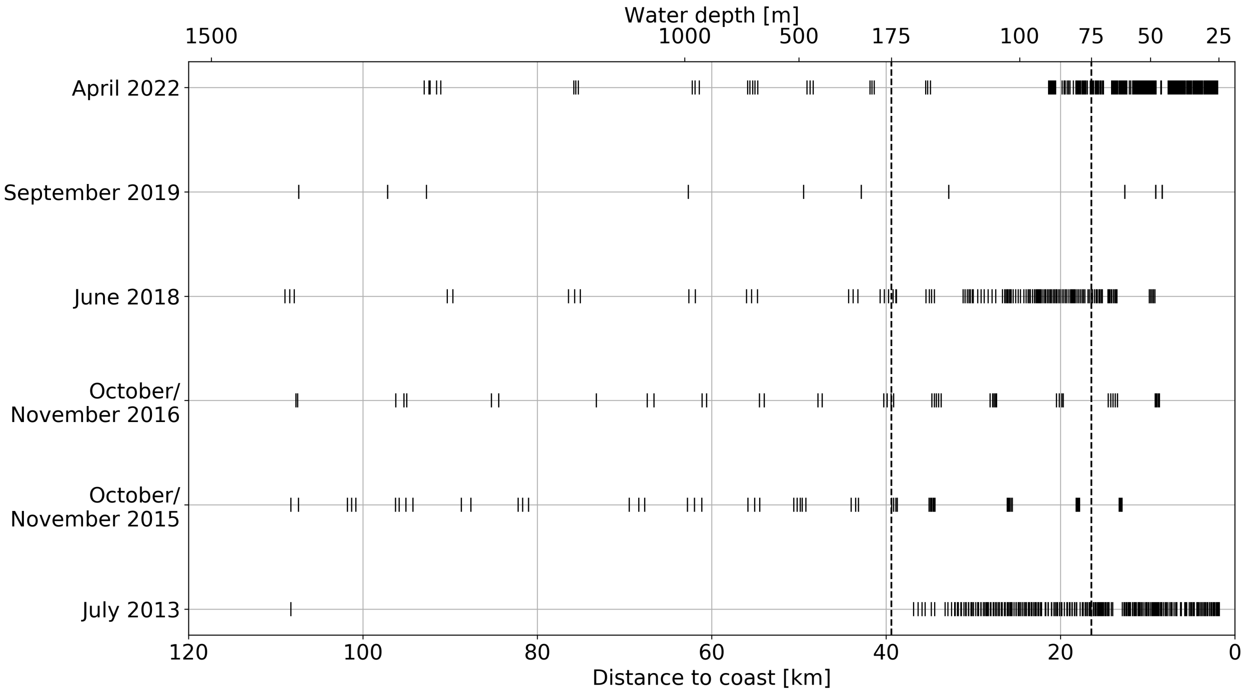

Figure 2.3: *Distribution of microstructure profiles at the 11○S section as a function of distance to the coast, cruise and water depth. Each tick marks a microstructure profile. The vertical dotted lines mark the three areas analysed in section 2.5.3: shallow water (water depth < 75 m), shelf break area (water depth > 75 m and < 175 m), and deep water (water depth > 175 m).*

Time	Cruise ID	Number of microstructure profiles
July 2013	M98	212
October/November 2015	M120	62
October/November 2015	M131	44
June 2018	M148	135
September 2019	M158	41
April 2022	M181	207

Table 2.1: *Overview of the time and number of microstructure profiles measured during the 6 research cruises analysed in this study.*

2.3.2 Mooring data

We compare satellite data products of SST, near surface horizontal velocities, and surface heat fluxes to data measured by a mooring at 6°S, 8°E (Fig. 2.1). The mooring is the Southeast Extension (SEE) of the Prediction and Research Moored Array in the Tropical Atlantic (PIRATA) program. The PIRATA-SEE mooring was deployed for one year between June 2006 and June 2007. In June 2013 it was redeployed until September 2018. In March 2019 it was redeployed again for 6 months.

2.3.3 Satellite and reanalysis data

Different satellite and reanalysis products are used to estimate terms of the seasonal ML heat budget equation. As the datasets are available for different periods of time, we restrict our analysis to the time period between 1993 and 2018 for which all products mentioned below are available.

2.3.3.1 Surface heat fluxes

The climatologic net surface heat fluxes are derived from satellite data. Short- and longwave radiations are taken from the TropFlux product (Kumar et al., 2012). The data are available on a 1°x1° grid from 1979 to the present at a daily and monthly resolution. However, at the time when this study was conducted, only data until December 2018 were made available.

Latent and sensible heat fluxes are taken from the MERRA2 product (Global Modeling and Assimilation Office (GMAO), 2008). The monthly mean fields are available on a 0.5° longitude × 2/3° latitude grid from 1979 onward.

We chose to use different data products for the individual terms of the surface heat fluxes after comparing different data products to the surface fluxes measured by the PIRATA-SEE mooring (Appendix A).

2.3.3.2 Sea surface temperature

SST analyses are based on the OSTIA product (Good et al., 2020). The OISTA product uses satellite data as well as in situ measurements to provide global, daily, gap-filled SST fields. The data are available on a 0.05°×0.05° grid from 1981 onward.

2.3.3.3 Surface velocities

Estimates of horizontal heat advection are based on near surface velocities of the OSCAR (Ocean Surface Current Analysis Real-time) product (ESR, 2009). The OSCAR dataset derives near surface ocean currents by using quasi-linear and steady flow momentum equations thus combining geostrophic, Ekman and Stommel shear dynamics. The basis is satellite and in situ measurements of sea surface height, surface vector wind and SST. The data are available on a 1/3°×1/3° grid with a temporal resolution of $5\,days$ from 21 October 1992 onward.

2.3.3.4 Mixed layer depth

Mixed Layer Depth (MLD) is derived from the global Mercator Ocean reanalysis (GLORYS) product (Lellouche et al., 2021). GLORYS is available daily from 1993-2019. It has a horizontal resolution of 1/12° and 50 vertical levels. We calculate the MLD using a temperature criterium, where we define the MLD as the depth where the temperature deviates by 0.2°C from the surface value. MLDs determined from GLORYS were compared to the MLDs determined from PIRATA-SEE data as well as to MLDs calculated from the hydrographic Nansen dataset (Tchipalanga et al., 2018b). The MLD calculated from the GLORYS dataset reproduces the observed MLD reasonably well (not shown).

2.4 Methods

2.4.1 Mixed layer heat budget

To assess the oceanic and atmospheric driver of heat content changes we calculate the ML heat budget by following the approach used by numerous previous observational studies (Stevenson and Niiler, 1983; Moisan and Niiler, 1998; Foltz et al., 2003, 2013; Hummels et al., 2014). The equation for the local heat balance in the ML can be expressed as:

$$h\,\rho\,c_p\,\frac{\partial T}{\partial t} = -\rho\,c_p\,h\,\vec{v}\cdot\vec{\nabla}T + q_{net}\ + r \tag{2.1}$$

where h is the MLD, c_p is specific heat capacity, T the mean ML temperature, $\vec{v}$ the mean horizontal velocities in the ML, q_net the net surface heat flux corrected for the shortwave radiation that penetrates through the ML, and r is the residual. Changes in the local heat content are balanced by the mean horizontal advection, the net surface heat flux, and the residual r. The residual contains errors of the terms of Eq. 2.1 and other processes. One of these processes, on which we will focus in the present study, is the heat loss due to turbulent mixing across the base of the ML, termed turbulent heat loss in the following. The influence of this term will be discussed based on estimates of mixing strength utilizing microstructure data collected during 6 cruises in the tAUS. However, the available data are not extensive enough to calculate a seasonal cycle of the turbulent heat loss. Other processes that are not evaluated here include the horizontal heat advection on temporal and spatial scales unresolved by the data used here (see section 2.6), vertical temperature velocity covariance and entrainment (Foltz et al., 2013; Stevenson and Niiler, 1983).

The evaluation of the terms of the ML heat budget is done using a box-averaging strategy. For that we consider two boxes (Fig. 2.1b). The coastal box includes the area from 8°S to 15°S within 1° off the coast. The offshore box has the same latitude range and extends from the coastal box to 10°E. All gridded terms are averaged spatially over the boxes. If a term of the ML budget consists of several variables with different spatial or temporal resolutions, we linearly interpolate the variable with the coarser resolution linearly onto the higher resolution grid. Furthermore, all gridded terms are averaged over the same time period (1993-2018).

2.4.1.1 Surface heat fluxes

The net surface heat flux consists of the sum of longwave and shortwave radiation as well as the latent and sensible heat fluxes. Shortwave radiation is corrected for the amount of radiation that penetrates through the ML while considering the absorption by phytoplankton. The vertical penetration of shortwave radiation can be estimated from climatological Chlorophyll-a concentrations. Morel and Antoine (1994) parameterize the irradiance at a certain depth by applying three exponentials. The first describes the absorption of the infrared parts of the sun spectrum depending on the angle of the incoming radiation. It decays on length scales between 0 to $0.267\,m$. The second and third exponentials express the absorption of the longer- and shorter-wavelength part of the visible part of the spectrum. We find that only the third exponential is of interest for our application as the decaying scales of the first two exponentials are much smaller than the MLD. Thus, the fraction of shortwave radiation penetrating through the ML is:

$$\frac{E(-h)}{E(0)} \approx (1-R)\,V_2\,exp(-\frac{h}{Z_2}) \tag{2.2}$$

where $R = 0.43$ is the infrared part of the solar spectrum and V_2 and Z_2 are polynomials of order 5 calculated with the monthly climatological Chlorophyll-a concentration and the constants given in (Morel and Antoine, 1994).

2.4.1.2 Mean horizontal heat advection

The mean horizontal heat advection is calculated using the OSCAR surface velocities and the horizontal gradient from the OISTA-SST product. Both the temporal and spatial resolution of the OSCAR surface velocities is coarser than that of the OSTIA SST. The OSCAR surface velocities are available with a 5-day resolution on a 1/3°x1/3° grid. However, also the OSTIA product has limited effective resolution in the region of the Angolan upwelling system. Due to persistent cloud cover in the area, high-resolution passive infrared SST data are rarely available and the SST retrieval largely has to rely on low-resolution $(50-60\,km)$ passive microwave data (Nielsen-Englyst et al., 2021). Thus, using these datasets we are not able to resolve horizontal heat advection on temporal scales shorter than $5\,days$ and spatial scales smaller than passive microwaves data resolution.

2.4.1.3 Turbulent heat loss at the base of the mixed layer

Turbulent heat fluxes are estimated from microstructure shear measurements. As the turbulent heat flux vanishes at the sea surface, its value across the ML base represents the turbulent heat flux divergence of the ML and thus the ML heat loss. The method used here to determine the turbulent heart flux is detailed in Hummels et al. (2014). A brief summary is provided below.

Data from airfoil shear sensors attached to microstructure probes are used to estimate dissipation rates of turbulent kinetic energy, ϵ, via the variance method while assuming isotropy. Through the integration of the shear wave number spectrum, $E_{du/dz}(k)$, is related to the dissipation rate of turbulent kinetic energy as

$$\epsilon = 7.5\,\nu \int_{k_{min}}^{k_{max}} E_{du/dz}(k)\,dk \tag{2.3}$$

where ν is the dynamic viscosity of seawater. The shear spectra are calculated from overlapping two-second ensembles which corresponds to ~ 1 m vertical resolution. Subsequently, the spectra are integrated between a lower ($k_{min} = 3cpm$) and higher wavenumber, k_{max}. The latter depends on the turbulence level and the noise level. To account for variance loss due to the limited resolution in wavenumber space, the spectra are fitted to the universal Nasmyth spectrum (Wolk et al., 2002).

The turbulent eddy diffusivity of mass is then calculated using

$$K_\rho = \Gamma\,\langle\epsilon\rangle\,N^{-2} \tag{2.4}$$

(Osborn, 1980) where Γ is the mixing efficiency (set to 0.2 following Gregg et al. (2018)) and N^2 is the buoyancy frequency squared, calculated from temperature, salinity, and pressure data recorded by the microstructure profiler. N^2 profiles were smoothed to vertical scales larger than the Ozmidov scale by using a least square fitting method to vertical property gradients. The window size is chosen depending on the distance to the ML with $3\,m$ directly below the ML increasing linearly to $30\,m$. Finally, the turbulent heat flux is estimated from $J_H = -\rho\,c_p\,K_\rho \partial T/\partial z$.

Turbulent heat fluxes are determined for each profile individually. For that, we change the vertical coordinate to $MLD + \delta z$ with a vertical resolution of $2\,m$. All measurements in the ML as well as $2\,m$ below it are disregarded because mixing efficiency Γ is unknown in low-stratified waters (Gregg et al., 2018) and to avoid using data impacted by ship turbulence. Note that we do not interpolate the dissipation rates of TKE onto this grid but average all measurements in the respective depth bins. The binned profiles of dissipation rates of TKE are then used to calculate the turbulent eddy diffusivity and finally the turbulent heat flux for each profile. To evaluate the ML heat loss, all estimates in the depth range between $2\,m$ and $15\,m$ below the ML are averaged. The use of this depth range is a trade-off between regions where we are able to estimate turbulent eddy diffusivities from microstructure data and statistical reliability of our results. Due to the lognormal distribution of the dissipation rates of TKE (e.g. Davis (1996)), it is desired to average many individual estimates of ϵ to increase statistical reliability.

2.4.2 Uncertainty estimation

The uncertainty of the monthly terms of the ML heat budget is calculated via: $err_{total} = \sqrt{err^2_{data} + err^2_{seasonal}}$. err_{data} is the uncertainty arising from the data collection. To estimate the uncertainty of the satellite/reanalysis products for this region, we calculate the RMS difference between the data and the data recorded by the PIRATA-SEE buoy. See Appendix A for the comparison of the individual variables used in the study. The seasonal error ($err_{seasonal}$) arises from the fact that we use a data record of finite length. It is the standard error of each month. The error of the terms of the ML heat budget calculated by combining different variables is calculated using standard error propagation.

To evaluate the uncertainty connected to the turbulent mixing we use the method of bootstrapping following the approach of Hummels et al. (2014). This method provides significance at the 95% confidence level.

2.5 Results

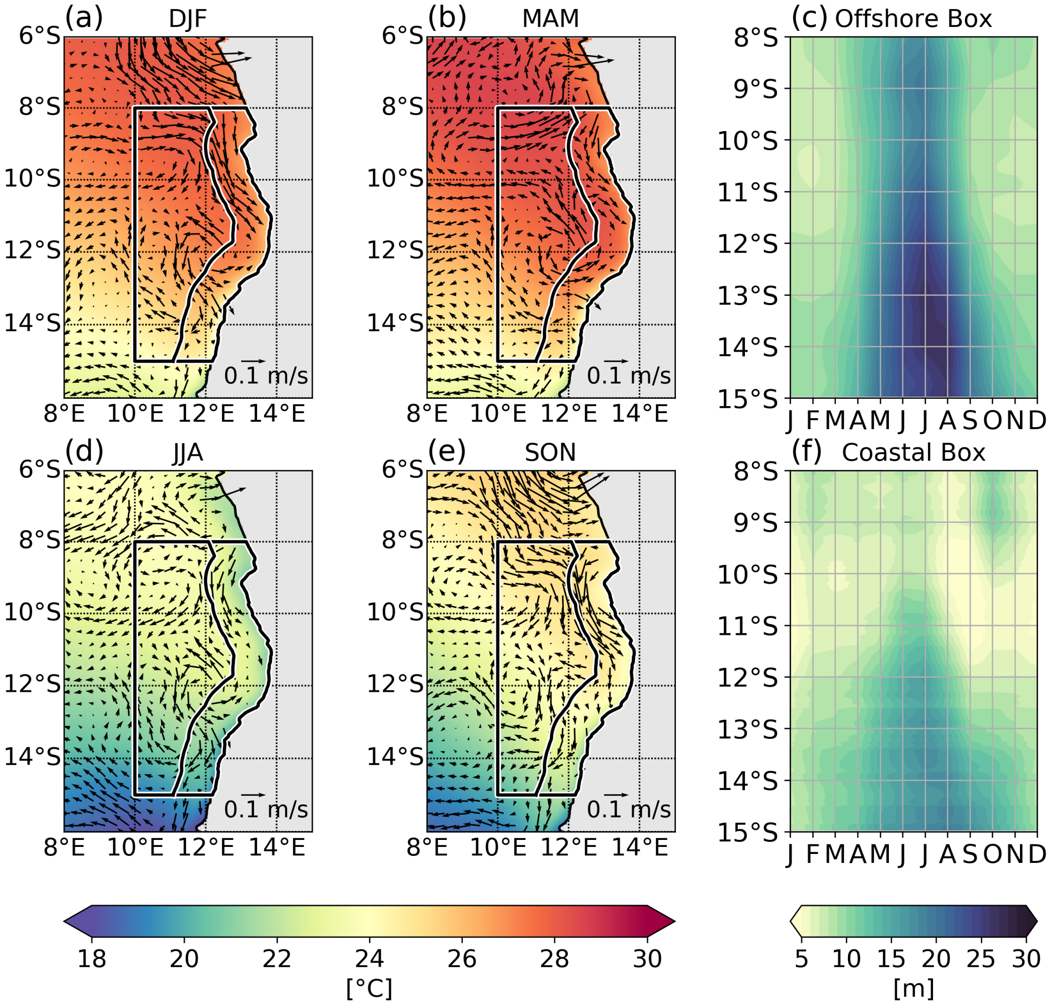

Figure 2.4: *(a), (b), (d), (e) Seasonal mean SST (colours) and surface velocities (arrows). The arrow length is referenced in the lower right corner of each subplot. Black boxes show the coastal and offshore boxes used for calculating the ML heat budget. (c) and (f) Hovmoeller plots of MLD as a function of latitude and month, zonally averaged over the (c) offshore and (f) coastal box.*

Although the tAUS region is situated in the tropics, SSTs undergo an elevated seasonal cycle (Fig. 2.4 a,b,d,e). The highest temperatures are found during austral autumn, reaching their maximum in March (Fig. 2.2, 28 °C in both boxes). The lowest temperatures are observed during austral winter in August (Fig. 2.2, 20.9 °C in the coastal and 21.5 °C in the offshore box). Accordingly, the ML cools between March and August and warms during the rest of the year. In the following sections, we analyse the atmospheric and oceanic processes impacting the described heat content changes followed by an analysis of the resulting ML budget.

Before turning to the individual processes, we look at the MLD and its changes throughout the year (Fig. 2.4 c, f). In general, the ML is shallower near the coast than further offshore. Additionally, the ML deepens with increasing latitude. In both boxes the deepest ML is found in July when the average MLD is $12.7\,m$ in the coastal and $22.9\,m$ in the offshore box. The shallowest ML in the coastal box is present in January when it averages $6.2\,m$ in the coastal box. In the offshore box, it reaches its minimum in February $(8.1\,m)$.

2.5.1 Surface heat fluxes

Surface heat fluxes show distinct seasonal cycles having similar characteristics in the offshore and the coastal box (Fig. 5). Differences between the boxes lie foremost in the amplitudes of the respective seasonal cycles. In both boxes, the incoming shortwave radiation peaks in January/February. The minimum in July is driven by the seasonal maximum in the solar zenith angle and the expansion of the low cloud cover (Scannell and McPhaden, 2018). The cloud cover is stronger further away from the coast (Zuidema et al., 2016) leading to higher incoming shortwave radiations over the coastal box. For the analyses of the ML heat budget, the amount of shortwave radiation that is absorbed within the ML is of interest. The fraction of shortwave radiation that is absorbed in the ML depends on the MLD and the chlorophyll concentration (see section 2.4.1.1). This fraction is largest in austral winter when the MLD and chlorophyll concentrations are at their seasonal maxima (Fig. 2.5). On average the shortwave radiation absorbed in the ML is higher in the coastal box. The largest differences between both boxes are observed in July when the ML in the coastal box receives $17\,W\,m^{-2}$ more shortwave radiation. The longwave radiation has its largest cooling effect in June. Between June and October, cooling by the longwave radiation is stronger in the coastal box compared to the offshore box. The latent heat flux has a similar seasonal cycle in both boxes. The smallest cooling effect is found between June and September when wind speeds are at their seasonal minimum. Latent heat flux cools the ML the strongest between February and May. Increased wind speed away from the coast (Fig. 2.1b) leads to an overall stronger cooling in the offshore box. The sensible heat flux is small in both boxes and constitutes a minor contribution to the net surface heat flux.

The resulting net surface heat flux has its minimum in June and its maximum in September in both boxes. The difference in the individual surface heat flux terms results in a stronger net surface heat flux in the coastal box compared to the offshore box. Thus, the net surface heat flux acts to dampen the observed SST differences between the coastal and the offshore area. Consequently, the surface fluxes are not able to explain the signal of cold water in the near coastal area of the tAUS. Note that the differences between the offshore and coastal box peaks between May and August when it is $\sim 30\,W\,m^{-2}$ stronger in the coastal box.

2.5.2 Mean horizontal advection

The seasonal cycle of the mean horizontal heat advection is determined by the seasonal cycle of the horizontal temperature gradient and the surface velocities (Eq. 2.1). Fig. 2.4 shows that within the

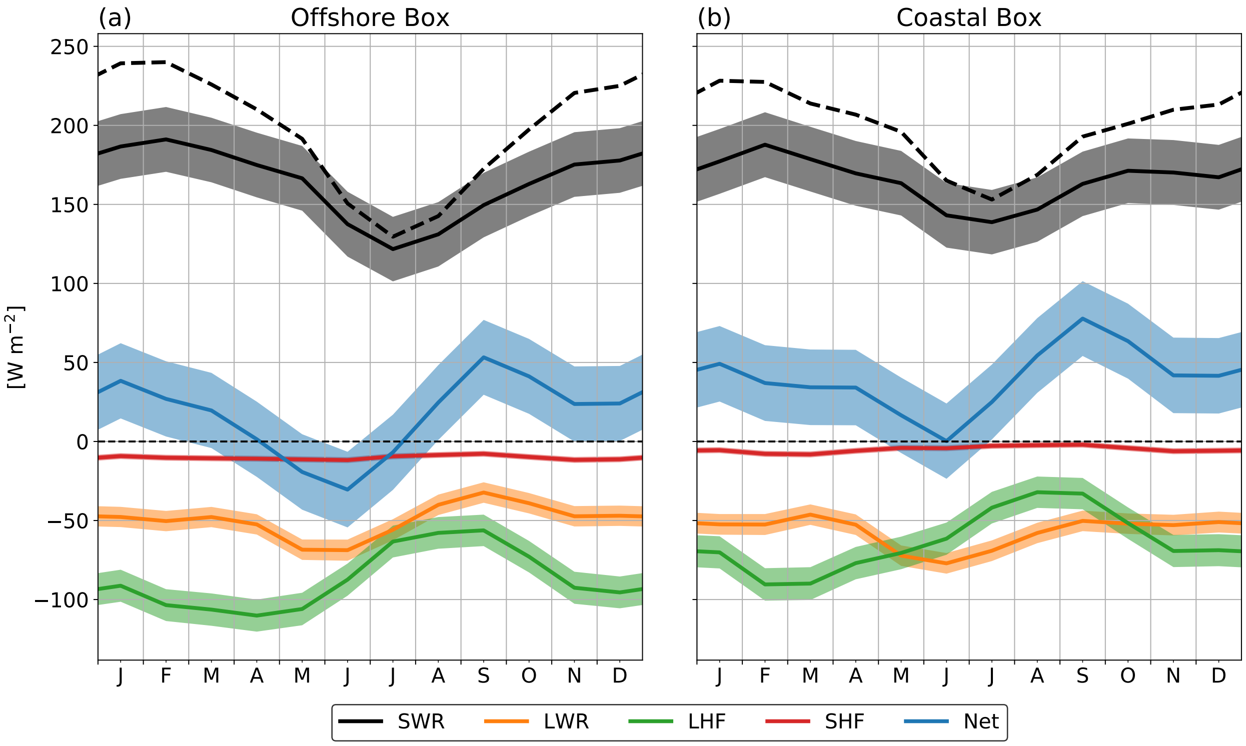

Figure 2.5: *Climatology of surface heat fluxes averaged over the (a) offshore and (b) coastal box. The black dashed line shows the climatology of the incoming shortwave radiation (SWR), the black solid line of the SWR absorbed in the mixed layer, the orange line of the longwave radiation (LWR), the green line of the latent heat flux (LHF), red line of the sensible heat flux (SHF), and blue line of the net surface heat flux. Shaded areas give the uncertainty estimate of the respective fluxes (see Sect. 2.4.2).*

coastal box the temperature decreases towards the coast throughout the year. This negative zonal temperature gradient is strongest between May and August ($\sim 12 \times 10^{-3}\,K km^{-1}$). A secondary maximum is found in January. In contrast, the meridional temperature gradient within the coastal box is always positive as SSTs increase towards the equator. On average its magnitude is $5 \times 10^{-3}\,K km^{-1}$ while its seasonal cycle is weak. The meridional temperature gradient averaged over the offshore box is of similar strength (on average $5 \times 10^{-3}\,K km^{-1}$) and also exhibits a weak seasonal cycle. The offshore zonal temperature gradient is always positive as well (on average $3 \times 10^{-3}\,K km^{-1}$).

The velocity field off the coast of Angola is generally weak (Fig. 2.4). Close to the coast, velocities along the coast dominate. Here, the velocities in the northern part of the tAUS are elevated compared to further south throughout the year. The southward velocity component peaks in October ($9\,cm\,s^{-1}$ averaged over the coastal box). Note that this maximum agrees well with the seasonal maximum of southward velocities of the Angola Current as shown from moored velocity observations in (Kopte et al., 2017). A secondary southward velocity maximum is found in February. The weakest meridional velocities are found in August when velocities are close to zero. In the offshore box, the velocity field is weaker and noisier than in the coastal box. One feature present throughout the year seems to be an anticyclonic rotation centred around 12°S, 12°E. Averaged over the offshore box the surface velocities do not exceed $3\,cm\,s^{-1}$. Furthermore, annually averaged velocities are smaller than $1\,cm\,s^{-1}$.

The resulting mean zonal and meridional heat advection are presented in Fig. 2.6. In both boxes, the total mean horizontal heat advection is dominated by the meridional component. Averaged over the year, the mean horizontal heat advection warms the ML in both regions, but its contribution is small compared to the net surface fluxes. The maximum in both boxes is reached in October when southward velocities are at the seasonal maximum. Then, horizontal heat advection amounts to $18 \pm 3\,W\,m^{-2}$ when averaged in the coastal box and $7 \pm 3\,W\,m^{-2}$ for the offshore box. Note that mean horizontal heat advection is calculated using five-day velocities available on a 1/3° grid. Heat advection on shorter time scales and smaller spatial scales cannot be determined from currently available datasets. This will be discussed in Sec. 2.6.

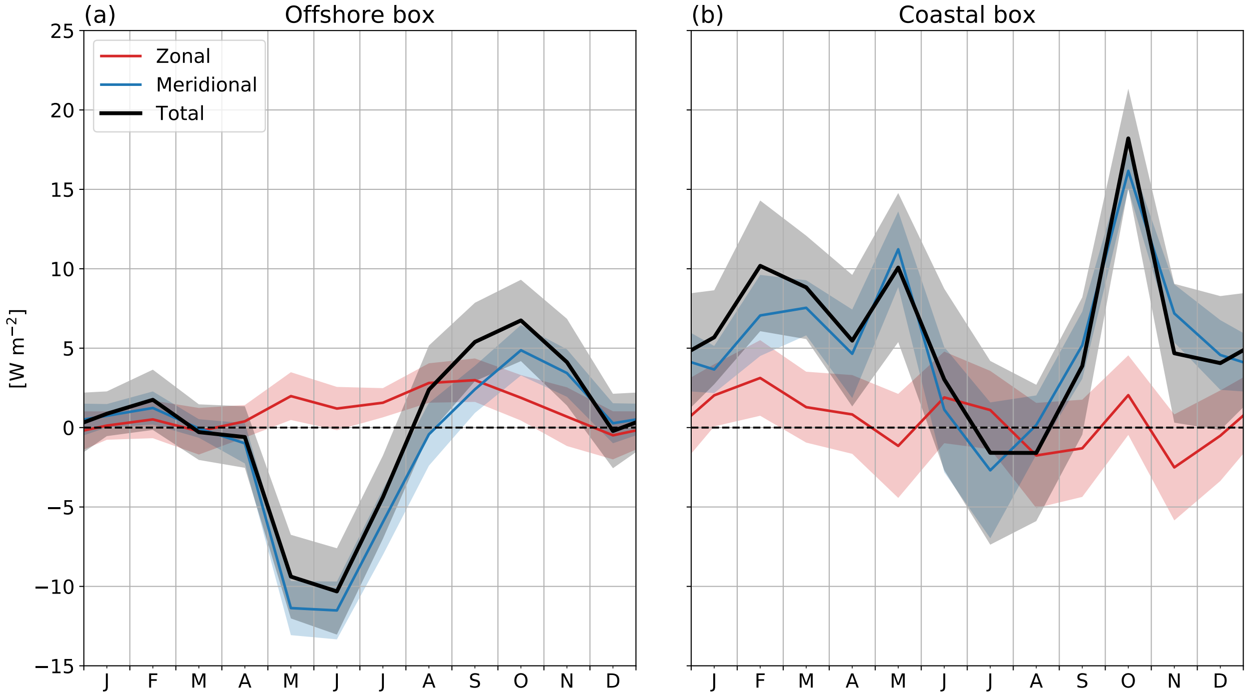

Figure 2.6: *Seasonal cycle of mean horizontal heat advection averaged over the coastal box (a) and the offshore box (b). Red lines present the mean zonal horizontal heat advection, blue lines the mean meridional horizontal heat advection, and the black lines the sum of both. Shaded areas give the estimated error (see Sect. 2.4.2).*

2.5.3 Turbulent heat loss at the base of the mixed layer

As has been reported from other upwelling regions (e.g., Perlin et al. (2005); Schafstall et al. (2010)), the microstructure profiles available in this study (section 2.3.1) indicate a strong dependence of the TKE dissipation rate on bathymetry. This is illustrated in Fig. 2.7 showing the mean distribution of TKE dissipation rates across the continental slope and shelf from 6 cruises at 11° S (see Fig.2.1b and Fig. 2.3 for details on data coverage).

Elevated dissipation rates of TKE close to the surface as well as in and above the bottom boundary layer are revealed. Furthermore, dissipation rates above $10^{-7}\,W\,kg^{-1}$ are found in the whole water column at the shelf break and in waters shallower than $75\,m$. In the depth range between $2\,m$ and $15\,m$ below the ML (Fig. 2.7a), which is used to determine the turbulent heat loss at the base of the ML, a TKE

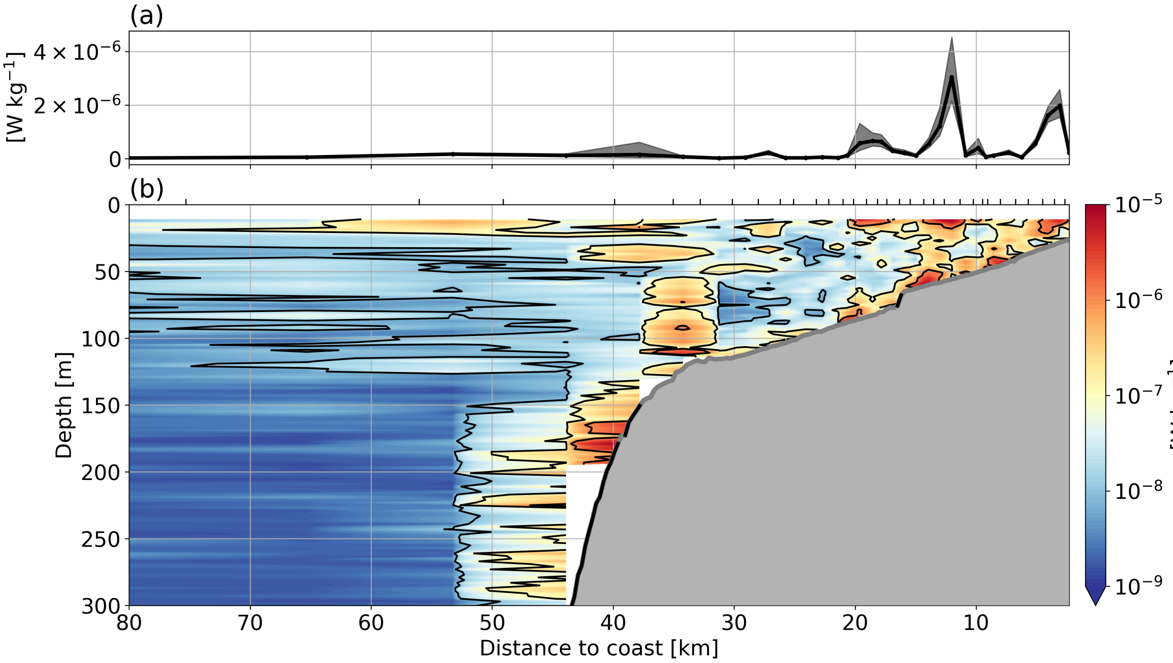

Figure 2.7: *Dissipation of TKE at the 11°S section (see Fig. 1b) as a function of distance to coast [km]. Microstructure data are binned together in groups of 20 profiles. (a) Mean dissipation of TKE averaged between 2 and 15 m below the ML. Grey shading shows 95% confidence interval calculated via bootstrapping. (b) Section of mean dissipation of TKE against depth and distance to the coast. Topography coloured in black marks supercritical slopes for the M2 tide calculated with the time averaged 11°S stratification from Kopte et al. (2017). Black ticks at the top of (b) mark the borders of the 20-profile groups.*

dissipation rate dependence on the water depth is also evident. Here, elvated dissipation rates of TKE that can exceed $1 \times 10^{-6}\, W\, kg^{-1}$ are particularly frequent in waters shallower than $75\, m$. Note that the microstructure shear data were taken during different seasons. However, we find similar dependences of dissipation rates of TKE on water depth when considering data from individual cruises separately (not shown). Thus, the cross-slope distribution of TKE dissipation rates likely does not exhibit elevated seasonal variability.

We conclude from the mean distribution of dissipation of TKE that turbulent heat flux at the Angolan shelf has to be analysed dependent on the water depth of the respective microstructure profile. The 701 microstructure profiles were thus allocated into three groups based on water depth: profiles measured in water depths larger than $175\, m$ (deep water), profiles measured in water depths between $75\, m$ and $175\, m$ (shelf break area), and profiles taken in water depths shallower than $75\, m$ (shallow water). Individual profiles were mapped as a function of vertical distance to the ML in $2\, m$ bins prior to averaging (Fig. 2.8).

The results in Fig. 2.8 clearly show differences between the three regions. The highest dissipation rates of TKE below the ML are found in shallow waters. These elevated dissipation rates of TKE ultimately lead to strongly elevated turbulent heat fluxes. Averaged between $2\, m$ and $15\, m$, the heat flux is $-188\, [-159, -222]\, W\, m^{-2}$ in shallow waters (Table 2.2). In the same depth range, the shelf break area exhibits $-49\, [-42, -58]\, W\, m^{-2}$. The heat loss in deep waters is even smaller ($-24\, [-21, -29]\, W\, m^{-2}$). These results show that turbulent heat loss at the base of the ML is an important cooling term of the ML heat

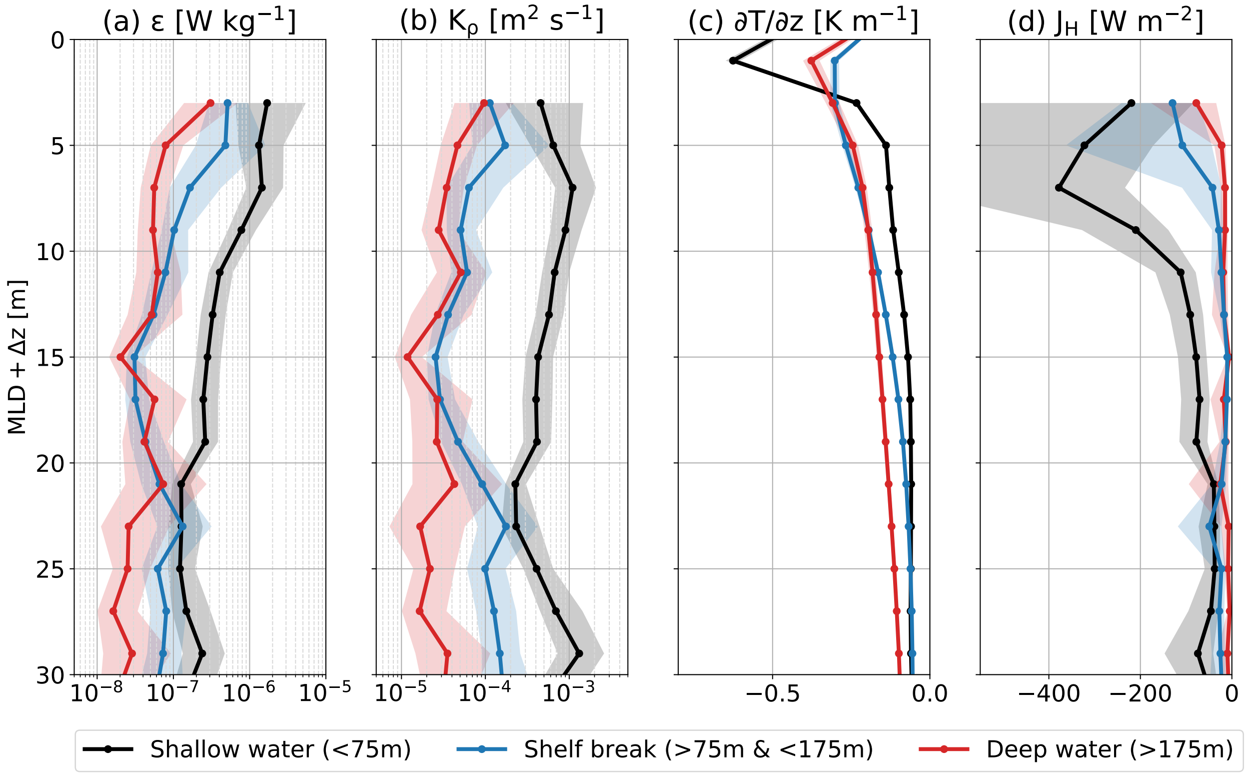

Figure 2.8: *Averaged profiles as a function of distance to the ML. Profiles taken during 6 different cruises are allocated into three groups according to the water depth where the profile was taken. Profiles taken in shallow water (water depth < 75 m, black), in the area of the shelf break (water depth > 75 m and < 175 m, blue), and in deep waters (water depth > 175 m, red) are grouped together. (a) shows the dissipation rate of TKE* $[W\,kg^{-1}]$*, (b) the eddy diffusivity* $[m^2\,s^{-1}]$*, (c) the vertical temperature gradient* $[K\,m^{-1}]$*, and (d) the turbulent heat flux* $[W\,m^{-2}]$*. The shaded areas give the 95% confidence intervals.*

budget. Here, especially the shallow waters play an important role as the heat loss is elevated by about a factor of 8 compared to deep waters.

Until now we only discussed the turbulent heat flux as a function of bathymetry. For the analyses of the heat content change throughout the year, the seasonality of the turbulent heat flux is also of interest. It is ambitious to discuss seasonal differences of turbulent heat flux based on the cruise data. The sampling strategy during the cruises was not the same, leading to a different distribution of measured profiles along the 11°S section during the different cruises (Fig. 2.3, Table 2.1). To discuss temporal variability, we present the averaged turbulent heat fluxes in the three different depth ranges between 2 m and 15 m (see section 2.4.1.3) during the different cruises (Table 2.2). The reported values clearly show large variability. In shallow waters, the fluxes range from $-3\,[-2, -3]\,W\,m^{-2}$ (October/November 2015) to $-390\,[-326, -470]\,W\,m^{-2}$ (April 2022). Similarly, in the area of the shelf break fluxes range from $-2\,[-1, -2]\,W\,m^{-2}$ (October/November 2015) to $-135\,[-116, -163]\,W\,m^{-2}$ (April 2022). In deep waters the minimum fluxes were measured during July 2013 ($-1\,[-0, -1]\,W\,m^{-2}$ and the highest were measured during September 2019 ($-46\,[-34, -64]\,W\,m^{-2}$). Note the variability between both cruises conducted in October/November: In October/November 2015 an averaged flux of $-3\,[-2, -3]\,W\,m^{-2}$ was measured in shallow waters whereas one year later the average flux is $-232\,[-188, -290]\,W\,m^{-2}$. Because of this large variability, we abstain from including seasonal estimates of turbulent heat flux at the base of the ML in the

Time	Cruise	Shallow waters ($< \mathbf{75\,m}$)		Shelf break area ($> \mathbf{75\,m} \,\&\, < \mathbf{175\,m}$)		Deep waters ($> \mathbf{175\,m}$)	
		$\mathbf{J_H}$ $[\mathbf{W\,m^{-2}}]$	N	$\mathbf{J_H}$ $[\mathbf{W\,m^{-2}}]$	N	$\mathbf{J_H}$ $[\mathbf{W\,m^{-2}}]$	N
July 2013	M98	-27 (-23,-32)	106	-15 (-13, -17)	105	-1 (0,-1)	1
October/ November 2015	M120	-3 (-2,-3)	5	-2 (-1, -2)	17	-7 (-6,-10)	40
October/ November 2016	M131	-232 (-188,-290)	10	-85 (-70, -105)	14	-21 (-17,-25)	20
June 2018	M148	-86 (-71,-107)	29	-60 (-50, -75)	84	-36 (-30,-45)	22
September 2019	M158	-47 (-35,-66)	16	-17 (-13, -25)	4	-46 (-34,-64)	21
April 2022	M181	-390 (-326,-470)	144	-135 (-116, -163)	38	-26 (-22,-31)	25
Mean		**-188** **(-159,-222)**	**310**	**-49** **(-42, -58)**	**262**	**-24** **(-21, -29)**	**129**

Table 2.2: *Turbulent heat flux (J_H) averaged between 2 and 15 m below the ML during the respective cruise for profiles taken in different depth ranges. 95% confidence interval is given in the brackets below. The number of profiles in each depth range is presented as well (N).*

budget. A possible seasonality in the turbulent heat flux term is discussed in Sec. 2.6. Furthermore, the calculated fluxes from the microstructure data can exhibit very high values. Especially the data recorded in April 2022 in shallow waters exhibit much higher heat losses than the amount of net surface heat fluxes that are put into the ML. In Sec. 2.6 we discuss a possible explanation for these high heat losses.

2.5.4 Mixed layer heat budget

Fig. 2.9 presents the individual terms of the ML heat budget analysed in this study as well as the resulting budget itself averaged over the coastal and the offshore box respectively. The net surface heat flux is an important term of the ML heat budget in both the offshore and the coastal box. In contrast, the mean horizontal heat advection term is small and of minor importance. Averaged over the year both terms have a warming effect on the ML in both boxes.

The sum of surface heat fluxes and mean horizontal heat advection show a similar seasonal cycle with different magnitudes in the coastal and the offshore box (Fig. 2.9 c, d). It is characterized by the seasonal cycle of the net surface heat fluxes and is only slightly modulated by the mean horizontal heat advection term. Consequently, the sum of both is positive throughout the year in the coastal box. Its maximum is found in September ($82 \pm 24\,W\,m^{-2}$) while its minimum is found in June ($3 \pm 24\,W\,m^{-2}$). In the offshore box, the sum of net surface heat flux and total horizontal heat advection is negative between May and June. Its maximum is found in September ($59 \pm 324\,W\,m^{-2}$) its minimum is detected in June ($41 \pm 24\,W\,m^{-2}$). The heat content change reveals that the ML cools from March to August in both

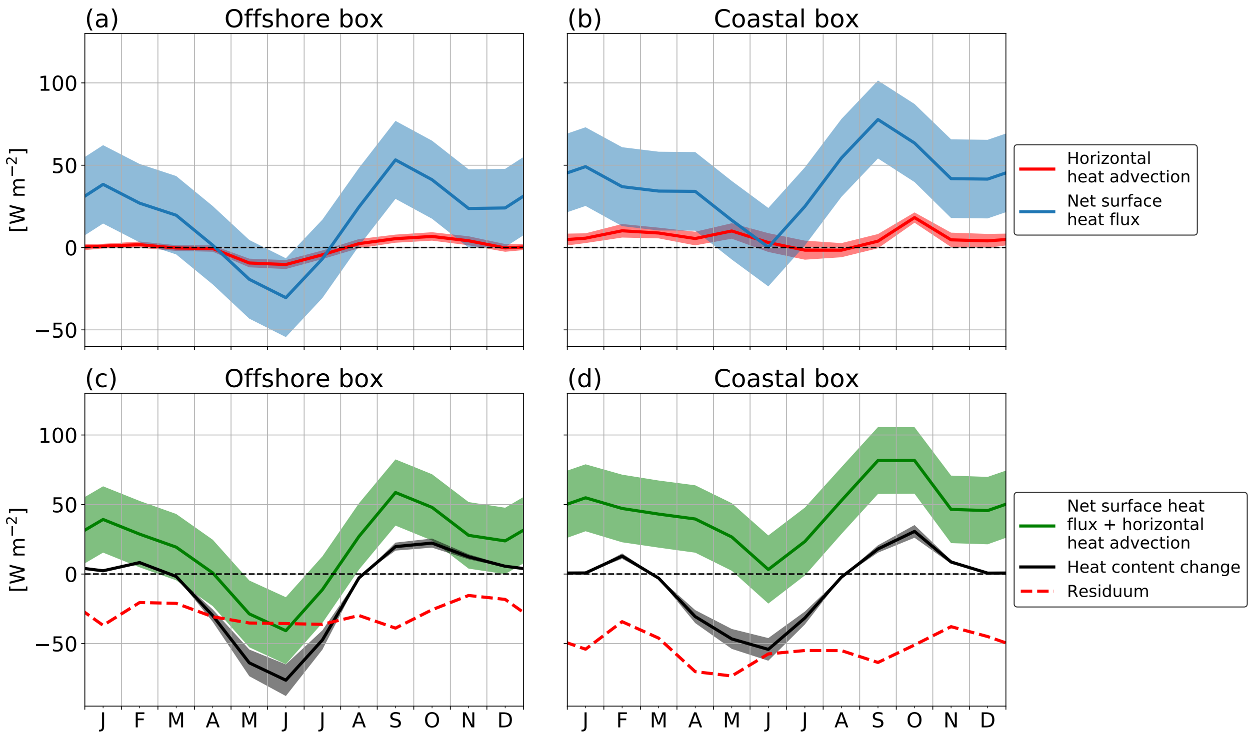

Figure 2.9: *(a) & (b) Individual contributions to the ML heat budget. Colours are explained in the legend. (c) & (d) Sum of net surface heat flux and horizontal heat advection (green lines), the observed heat content change (black lines), and the resulting residuum between both (red dashed line). (a) & (c) show budget terms averaged over the offshore box, (b) & (d) budget terms averaged over the coastal box.*

boxes. In austral winter, the heat content change is elevated in the offshore box compared to the coastal box. This may seem counterintuitive given the increased negative SST gradient during this period but is explained by the deeper ML in the offshore box compared to the coastal box (Figs. 2.4 c, f).

Comparing the heat storage term with the sum of mean horizontal heat advection and net surface heat fluxes reveals that a large residuum remains in the coastal box as well as in the offshore box (Fig. 2.9 c, d). In the coastal box, the residuum is considerably larger (on average $53\,W\,m^{-2}$). The average residuum in the offshore box is $29\,W\,m^{-2}$. The residuum undergoes a weak seasonal cycle which differs between the boxes. In the coastal box, the amount of the residuum has minima in February and November.

The residuum includes, amongst other things, contributions of the turbulent heat flux at the base of the ML. While we cannot calculate a seasonal cycle of this term for the coastal and the offshore box based on the microstructure data, an average contribution for the coastal box can be estimated. Analysis of the microstructure profiles revealed a dependence of the turbulence heat flux on bathymetry. Thus, we consider a weighted mean based on the area of the coastal box that falls into the respective depth ranges discussed in Sec. 2.5.3. In total, the water depth in 12% of the coastal box area is shallower than $75\,m$, water depth in 13% of the coastal box is between 75 and $175\,m$, and in 75% it is deeper than 175 m. The resulting weighted mean calculated over all microstructure profiles averaged between $2\,m$ and $15\,m$ below the ML yields a contribution of $-48\,[-43,-55]\,W\,m^{-2}$ to the ML heat budget. Comparing this to the average residuum of $53 \pm 320\,W\,m^{-2}$ in the coastal box underlines that turbulent heat loss at the base of the ML is an important process contributing to the cooling of the ML in the tAUS. The microstructure profiles further suggest that this process is particularly important in near coastal areas as the turbulent heat flux is much larger here than further offshore. The larger residuum in the coastal box compared to the offshore box supports these results.

The residuum also includes biases in the evaluated terms of the ML heat budget (see Sec. 2.4.1). To estimate possible sources of biases, we compared the satellite/ reanalyses data to in-situ data measured at the PIRATA-SEE mooring site at 6°S, 8°E (see Fig. 2.1 for location). The comparison detailed in Appendix A revealed large differences in monthly averaged surface heat flux components despite being estimated over the same time span. In particular, the monthly averages of shortwave radiation showed elevated differences between the TropFlux climatology and buoy shortwave radiation sensor data, suggesting that TropFlux shortwave radiation is biased high. The differences in the net surface heat flux range between $2\,W\,m^{-2}$ in May and $38\,W\,m^{-2}$ in January. This suggests that the satellite/reanalyses data may overestimate the amount of net surface heat fluxes and thus contribute to a positive residuum in the ML heat budget.

2.6 Summary and discussion

The tAUS is a highly productive ecosystem. In the tAUS surface temperatures are lower near the coast compared to further offshore. In austral winter, we find the lowest SSTs and the strongest cross-shore SST gradient in the tAUS. In this study, we calculate different terms of the ML heat budget based on satellite and reanalysis data to analyse atmospheric and oceanic drivers of heat content variability. The heat budget terms are averaged over two boxes: One located directly at the coast of the tAUS and one offshore of it. This allows us to analyse and discuss processes that might be of different importance in both regions. Additionally, we analyse the impact of turbulent heat flux at the base of the ML based on shipboard observations taken almost exclusively in the coastal box.

The surface heat fluxes are an important driver of ML heat content changes in the tAUS. The seasonal cycles of the surface heat flux terms are similar near the coast and further offshore. The strongest cooling term is the latent heat flux, which is larger in the offshore area of the tAUS due to decreasing wind speeds towards the coast. As the warming due to shortwave radiation is elevated in the coastal region as well, the resulting net surface heat flux is larger in the coastal box compared to the offshore area. Thus, net surface heat fluxes act to dampen the observed cross-shore temperature gradient. Note that the differences are particularly large during austral winter when the cross-shore temperature gradient is at its seasonal maximum (Fig. 2.10).

The mean horizontal heat advection contributes to the warming of the ML in the coastal region as well as offshore. However, the term is small. It is sustained by the southward advection of warm equatorial waters by the Angola Current, which peaks during October.

The turbulent heat flux at the base of the ML is estimated from shipboard microstructure measurements taken during 6 cruises. We find the amount of heat flux to vary with bathymetry. The highest TKE dissipation rates and consequently elevated turbulent heat fluxes are found in water depths shallower than $75\,m$, suggesting stronger cooling close to the coast compared to further offshore. This term thus acts to enhance a cross-shelf temperature gradient.

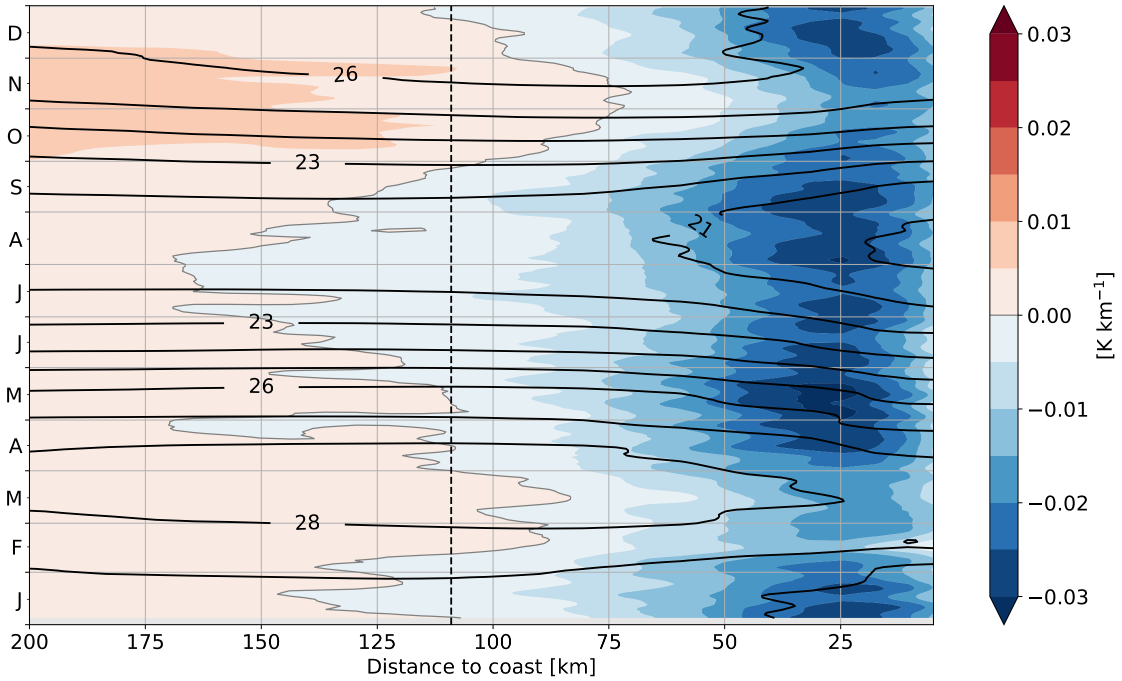

Figure 2.10: *Zonal temperature gradient (colours) and SST (contours) as a function of distance to coast averaged between 8°S and 15°S. Contour lines are every 1°C from 20°C to 28°C. Black dashed line gives the approximate extent of the coastal box. The data are treated with a 5-day running mean.*

The net surface heat fluxes and horizontal heat advection are not able to explain the observed heat content changes alone. Our analyses show that the turbulent heat flux at the base of the ML can explain a large proportion of the resulting residuum in the coastal box. The averaged residuum in the coastal box is nearly twice as large as in the offshore box, which supports the hypothesis that turbulent heat fluxes are more important near the coast compared to further offshore. Additionally, biases in the TropFlux surface heat fluxes may contribute to the residuum. As shown in the appendix, shortwave radiation from the climatology is larger than that measured by in-situ sensors on a PIRATA buoy situated in the proximity of the study site.

Our analysis of the ocean turbulence data reveal a connection between the amount of turbulent heat flux and bathymetry. Processes that lead to increased dissipation rates of TKE and ultimately increased turbulent heat fluxes in shallow waters on the Angolan shelf include internal waves and their interaction with the topography. Internal tides are assumed to be the largest contributor to the internal wave energy on the Angolan shelf (Zeng et al., 2021). They are generated by the interaction of the barotropic tide and the continental slope. In the tAUS, the topography is critical or supercritical with respect to the M2 tide at the continental slope mostly in the depth range between 200 and $500\,m$ (Fig. 2.8, Zeng et al. (2021)). Here, the largest portion of the internal tide energy is generated. While part of that energy was found to be dissipated locally or further offshore, a substantial part propagates onshore and was found to be dissipated in shallow waters near the coast (Zeng et al., 2021). Note that also smaller topographic features with critical slopes exist further onshore which can shape the local distribution of dissipation rates of TKE on the shelf as near-critical slopes are areas of enhanced velocity shear (Legg and Adcroft, 2003).

For the seasonal ML heat budget, the seasonality of turbulent heat flux at the base of the ML is of interest. The turbulent heat flux calculated from microstructure profiles exhibits a high variability but also suggests that turbulent heat loss is an important cooling term throughout the year. However, the data only provide snapshots of the dissipation at the Angolan shelf. A robust discussion of seasonal differences based on the data is thus ambitious. The model study of Zeng et al. (2021) showed that seasonal variations in the spatially averaged generation, onshore flux, and dissipation of internal tide energy are weak. However, due to the seasonal variation in stratification (passage of CTWs, seasonal cycle of SSS, SST differences through surface fluxes) the mixing due to internal tides is more effective during austral winter when stratification is weak. The seasonality of the residuum of the ML heat budget presented in this study seems to support this result. The amount of the residuum averaged over the coastal box is smallest in February and November (Fig. 2.9) when stratification in the tAUS is strongest (Kopte et al., 2017). Furthermore, the results of Zeng et al. (2021) fit well to describe the increased cross-shelf temperature gradient during austral winter. Fig. 2.10 shows the seasonal cycle of the zonal temperature gradient and SST as a function of distance to the coast. It reveals that the cooling and warming are not constant within $200\,km$ distance to the coast throughout the year. Particularly, the zonal maximum of SST (zero contour line of the zonal temperature gradient, Fig. 2.10) is in some months within the coastal box and in other months within the offshore box. Note that temperature differences averaged over both boxes (Fig. 2.2) are thus not a perfect proxy for the cross-shelf temperature gradient. The strongest negative zonal temperature gradient is found between April and September with a secondary maximum in December/January. This increased gradient cannot be explained by the net surface heat flux. The difference between net surface heat fluxes in the coastal and the offshore boxes experiences its seasonal maximum in austral winter. Thus, the net surface heat flux acts to dampen the observed zonal SST gradient. The difference between the horizontal heat advection in the coastal and the offshore boxes is small. Furthermore, the seasonal cycle of this difference does not correspond to the seasonal changes of the zonal temperature gradient. Hence, the mean horizontal advection likely plays no role for the increased zonal temperature gradient in austral winter.

Summarizing, stratification changes connected to the passage of CTWs, the seasonal cycle of SSS, and the changing net surface heat fluxes likely influence how effectively the ML close to the coast is cooled by the dissipation of the internal tide, introducing a semi-annual cycle to the strength of the cross-shore temperature gradient. Nevertheless, the microstructure measurements suggest that the turbulent heat flux is an important cooling term throughout the year setting up the negative cross-shore temperature gradient.

The analysis and the turbulent heat flux calculated from the microstructure measurements revealed a high variability between different cruises. The data collected in April 2022 shows especially high fluxes ($-390\,W\,m^{-2}$ in shallow waters). The influence of turbulent mixing on the temperature field can be seen in the transect measured on the shelf of Angola in water depths between $25\,m$ and $85\,m$ (Fig. 2.11). The MLD decreased from around $7\,m$ offshore to around $3\,m$ towards the coast. The recorded section reveals strong internal wave activity as isotherms show strong undulation indicative of onshore propagating internal waves (Fig. 2.11a). This activity is primarily restricted to water depths larger than $50\,m$. In shallower water, internal waves do not appear anymore suggesting the breaking of internal waves and dissipation of internal wave energy. It leads to high dissipation rates of TKE in this area with values mostly exceeding $10^{-7}\,W\,kg^{-1}$ here. The effect of the enhanced mixing due to breaking internal waves on the temperature field is pronounced. Temperatures are vertically much more homogenous near the coast than in deeper water. The high dissipation rates in this area are not directly connected to the ML as a local minimum at around $10\,m$ depth is detected. This suggests that the high mixing does not lead to a heat loss of the ML directly above. A very strong vertical temperature gradient of $\sim 1\,Km^{-1}$ below the ML supports the hypothesis that the mixing recorded here mostly affects the layer below the ML. Consequently, non-local effects have to play a role. Note in this context that the average heat loss in this area is estimated to be $390\,W\,m^{-2}$ (Table 2.2). This heat loss is higher than the heat input by the net surface heat flux and the mean horizontal heat advection. It implies that a one-dimensional view is not sufficient to understand the turbulent heat loss of the ML at the Angolan shelf. Horizontal advection on small spatial and temporal scales likely plays an important role in the redistribution of heat. Note that the model results of Zeng et al. (2021) reveal high spatial variability in dissipation at the Angolan shelf. This fits to our results and ultimately suggests that strong mixing and thus strong cooling of the ML in the tAUS locally occurs foremost in shallow areas and is redistributed by small scale horizontal advection. Processes that could be important in this context are the heat advection by nonlinear internal waves (Zhang et al., 2015) as well as the influence of lateral eddy fluxes (Thomsen et al., 2021). Further work has to be conducted to understand the redistribution of heat on small temporal and spatial scales in the tAUS.

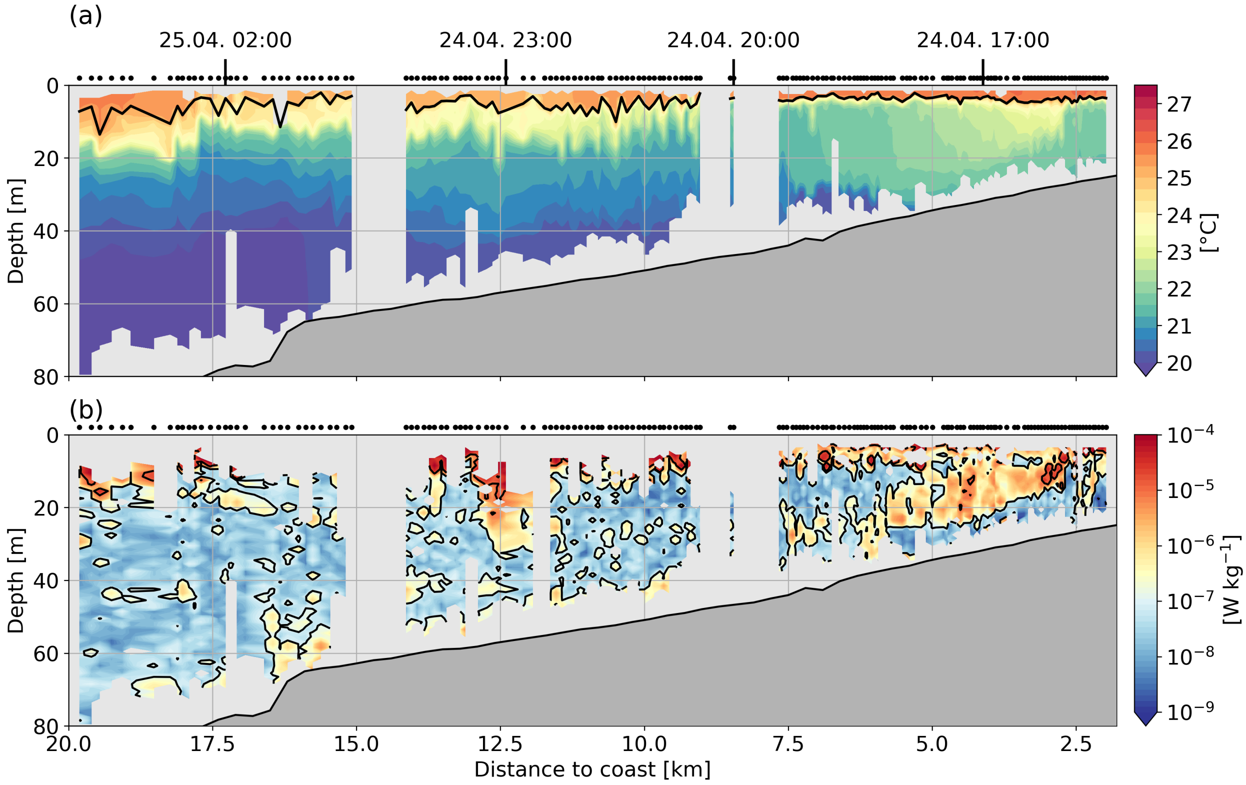

Figure 2.11: *Shipboard section taken at 11°S in April 2022. (a) shows temperature (colours) and MLD (black line). (b) displays the dissipation rate of TKE below the ML. Black points at the top of both panels mark the position of individual microstructure profiles.*

Seemingly contradicting our results, the study of Awo et al. (2022) showed that mean horizontal advection is an important term for the seasonal salinity budget. Their analysis shows that freshwater from the Congo River can reach 11°S by meridional advection in February/March and in October/November. Note that we also find a peak in southward surface velocities in February and October. The velocities are also stronger in the northern tAUS until ~11°S (Fig. 2.3). However, as the meridional temperature gradient is weak in that region, the mean horizontal advection is not important for the local ML heat budget. Thus, the results of our study do not oppose the results found by Awo et al. (2022).

The results of the present study show that the residuum of the ML heat budget is likely explained by the turbulent heat loss at the base of the ML and the uncertainties in the net surface heat flux primarily in the shortwave radiation. The uncertainties in the net surface heat flux represent a shortcoming of the study. This is especially important as the tAUS is a region with a large SST bias in state-of-the-art climate models (Richter, 2015; Kurian et al., 2021; Farneti et al., 2022). One discussed reason for the bias is excessive shortwave radiation due to a poor representation of shallow stratocumulus clouds (Huang et al., 2007). Our results show that the uncertainty in shortwave radiation is seasonally dependent and higher in months when low-level clouds dominate (Scannell and McPhaden, 2018). This indicates that the correct representation of clouds in both models and observations is still an issue. It has to be resolved, to get a better understanding of the tAUS and eastern boundary upwelling systems in general.

Summarizing, the study of the ML heat budget reveals that ML heat content changes in the tAUS are mostly determined by the surface heat fluxes and turbulent heat loss at the base of the ML. In contrast, the mean horizontal heat advection is of minor importance. The surface heat fluxes determine the seasonal cycle of heating and cooling of the ML and act to dampen the observed cross-shore temperature gradient. Turbulent heat loss at the base of the ML acts throughout the year in shallow waters of the tAUS. The microstructure data suggest that turbulent heat fluxes are capable of setting up the negative cross-shore temperature gradient. Stratification changes seem to control the amount of turbulent heat loss at the base of the ML, introducing a semi-annual cycle to the strength of the cross-shore temperature gradient.

2.7 Appendix A: Comparison of satellite and reanalysis data to moored observation

For the calculation of the ML heat budget, we rely on satellite/reanalysis data. To discuss uncertainties for the different datasets we compare them to in situ measurements at the PIRATA-SEE mooring (6°S, 8°E). In the following, we will discuss uncertainties based on the time series of the different variables (Fig. 2.12) as well as on the seasonal cycle (Fig. 2.13). Here, the seasonal cycle of the satellite/reanalysis data is always calculated for the time period when the PIRATA-SEE data are available for the individual variables and interpolated on the mooring location. Note that the incoming shortwave radiation in the TropFlux product is multiplied by the factor 0.945 to account for the part of the radiation that is reflected at the sea surface Kumar et al. (2012). To compare the different datasets, we multiplied the shortwave radiation measured by the PIRATA-SEE buoy and the MERRA2 data with the same factor.

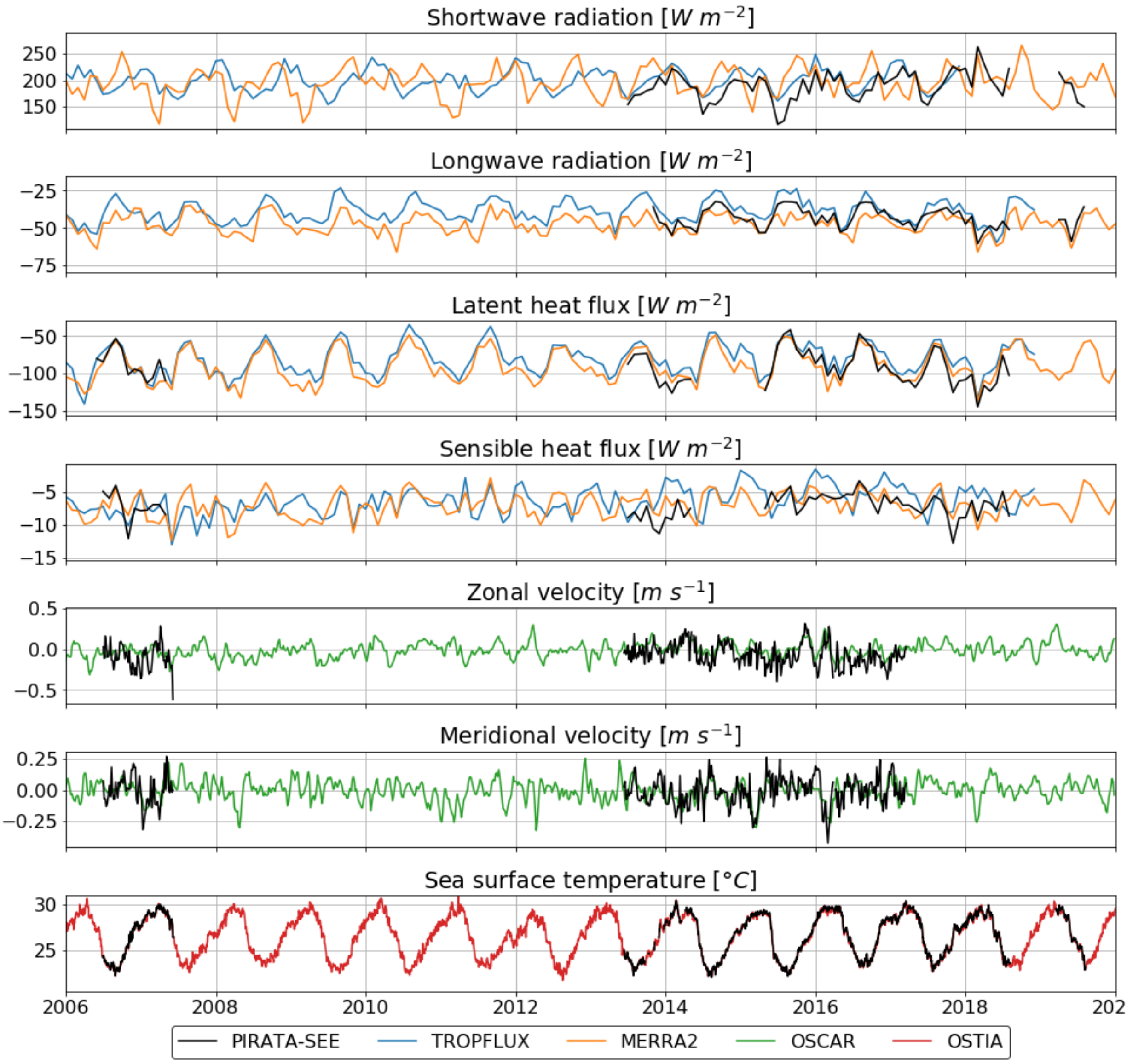

Figure 2.12: *Time series of variables (see titles of subplots) of the ML heat budget at 6°S, 8°E from in-situ data collected at the PIRATA-SEE mooring (black line) and from satellite/reanalysis data (colours, see legend). The daily PIRATA-SEE data are interpolated on the same time grid as the satellite/reanalysis data.*

2.7.1 Surface heat fluxes

The net surface heat flux is an important term of the ML heat budget in the tAUS as it is the largest warming term. From the time series differences between data from the in-situ fluxes measured by the PIRATA-SEE mooring and the surface fluxes from TropFlux and MERRA2 are recognizable (Fig. 2.12).

These differences are especially large for shortwave radiation. Here, the shortwave radiation of TropFlux data always show higher fluxes than the PIRATA-SEE data. In contrast, the shortwave radiation data from the MERRA2 product also exhibit lower heat fluxes than the in-situ data. These differences become even more evident looking at the seasonal cycles of shortwave radiation calculated from the different data products. The PIRATA-SEE data reveal a maximum in shortwave radiation in February and a minimum in August. The seasonal cycle of the TropFlux data also shows a minimum in August. However, the maximum is found in January. The seasonal cycle also reveals that the TropFlux data record higher shortwave radiation throughout the year. Seasonal dependence of the differences is visible as they are smaller between March and July than during the rest of the year. The seasonal cycle of the MERRA2 shortwave radiation differs much more from the PIRATA-SEE data. The maximum is found in October and the minimum in April. Between June and December, the shortwave radiation of MERRA2 is larger than the shortwave radiation of PIRATA-SEE and vice versa during the rest of the year.

The other terms of the surface heat fluxes show better agreement between the different datasets. The seasonal cycles of the longwave radiation calculated from TropFlux, MERRA2 and PIRATA-SEE data are similar. However, offsets between the different datasets exist. The seasonal cycle of longwave radiation calculated from the TropFlux (MERRA2) reveals less (more) radiation compared to the PIRATA-SEE data almost throughout the year. For the latent heat flux the differences between MERRA2 and PIRATA-SEE are small ($\sim 3\,W\,m^{-2}$. The differences between TropFlux and PIRATA-SEE are larger ($\sim 11\,W\,m^{-2}$) with TropFlux showing less latent heat flux throughout the year. The contribution of the sensible heat flux to the net surface heat flux is in general small. Nevertheless, the seasonal cycle of MERRA2 is in better agreement with the seasonal cycle of the PIRATA-SEE data than the TropFlux dataset.

After considering the results of the comparison between the satellite/reanalysis data and PIRATA-SEE data we decided to use the TropFlux dataset for shortwave and longwave radiation and MERRA2 for latent and sensible heat flux for the ML heat budget. We based this choice on the smallest root mean square (RMS) difference between the in-situ data and the different satellite/reanalysis products.

The comparison between the climatologies of the TropFlux/MERRA2 and the PIRATA-SEE data reveals a seasonal cycle in the differences between the different datasets. We want to investigate this bias by looking at the seasonal cycle of the mean differences between the time series (Fig. 2.14). The mean difference of shortwave radiation between the TropFlux product and the PIRATA-SEE measurements is higher than for the other heat flux terms and has a distinct seasonal cycle. Between July and February, the mean difference is higher ($\sim 15\,W\,m^{-2}$) than from March to June ($\sim 5\,W\,m^{-2}$). This seasonal cycle is most likely influenced by the seasonal prevalence of clouds of different types. Scannell and McPhaden (2018) show that at the PIRATA-SEE mooring site between January and April more high clouds than low clouds are present. This ratio is the other way around during the rest of the year. Note that the shortwave radiation measured by the PIRATA-SEE mooring is on average lower than what is measured by TropFlux suggesting that the satellite data overestimate the amount of shortwave radiation. In contrast to the shortwave radiation, the latent and sensible heat flux provided by MERRA2 compare reasonably well with the turbulent fluxes measured by the PIRATA-SEE buoy. Similarly, the mean difference of longwave radiation between TropFlux and PIRATA-SEE data ranges between $1 - 8\,W\,m^{-2}$ throughout the year. The bias of the net surface heat flux is dominated by the bias in shortwave radiation and ranges between $4\,W\,m^{-2}$in April and $38\,W\,m^{-2}$ in January.

Summarizing, comparisons of surface heat fluxes from different data sources show large uncertainties. The smallest differences are achieved using the TropFlux dataset for shortwave and longwave radiation and the MERRA2 dataset for latent and sensible heat flux.

To estimate the uncertainties of the sea surface heat fluxes for the ML heat budget we calculate the RMS differences between the PIRATA-SEE and the satellite/ reanalyses data from all available months. This RMS difference of the shortwave radiation is $20\,W\,m^{-2}$, for the longwave radiation $6\,W\,m^{-2}$, for the latent heat flux $10\,W\,m^{-2}$, and for the sensible heat flux $2\,W\,m^{-2}$.

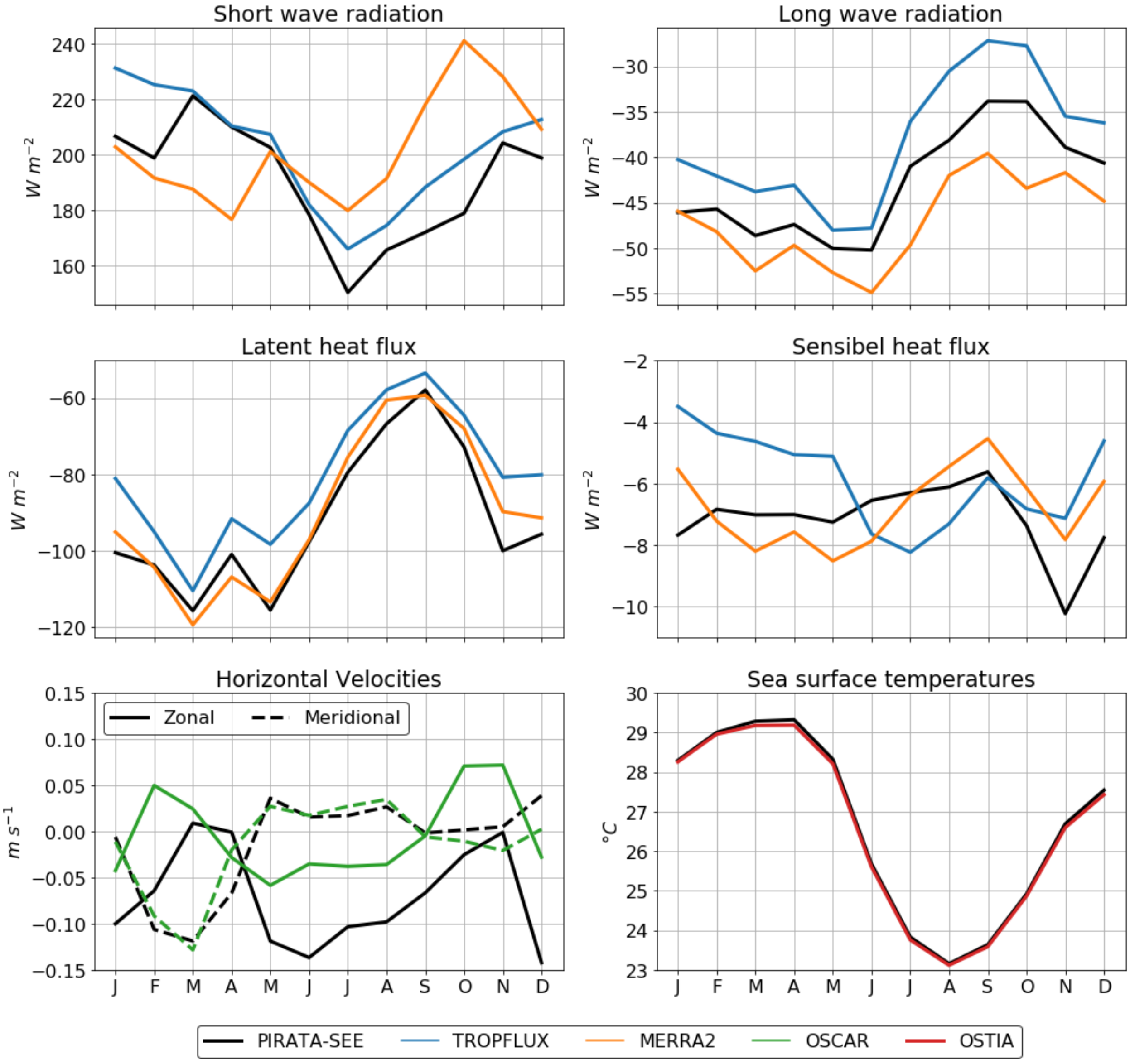

Figure 2.13: *Seasonal cycle of variables (see titles of subplots) used in the ML heat budget at 6°S, 8°E calculated from in-situ data collected at the PIRATA-SEE mooring (black line) and from satellite/reanalysis data (colours, see legend). The seasonal cycle from the satellite data is derived from the time period when PIRATA-SEE data are available.*

2.7.2 Horizontal velocities

We compare the horizontal velocities measured at the PIRATA-SEE mooring at 10 m depth with the OSCAR velocities. The seasonal cycle of meridional velocities is similar in both datasets. A minimum southward velocity is found in March. During the rest of the year, the velocities are small. The RMS difference based on monthly data is $7\,cm\,s^{-1}$. The seasonal cycle of the zonal velocities shows an offset of around $7\,cm\,s^{-1}$. The RMS difference based on monthly data is $10\,cm\,s^{-1}$. Note that the zonal velocities show anomalous southward velocities during the end of the first mooring period (2007) that are much stronger than all other recorded data. Comparing only the latter mooring period to the OSCAR data reveals a better agreement between both datasets (not shown).

2.7.3 Surface temperatures

The comparison between surface temperatures measured by the PIRATA-SEE mooring and the OSTIA SST product shows a very good agreement. The RMS difference between both products based on monthly data is 0.1°C.

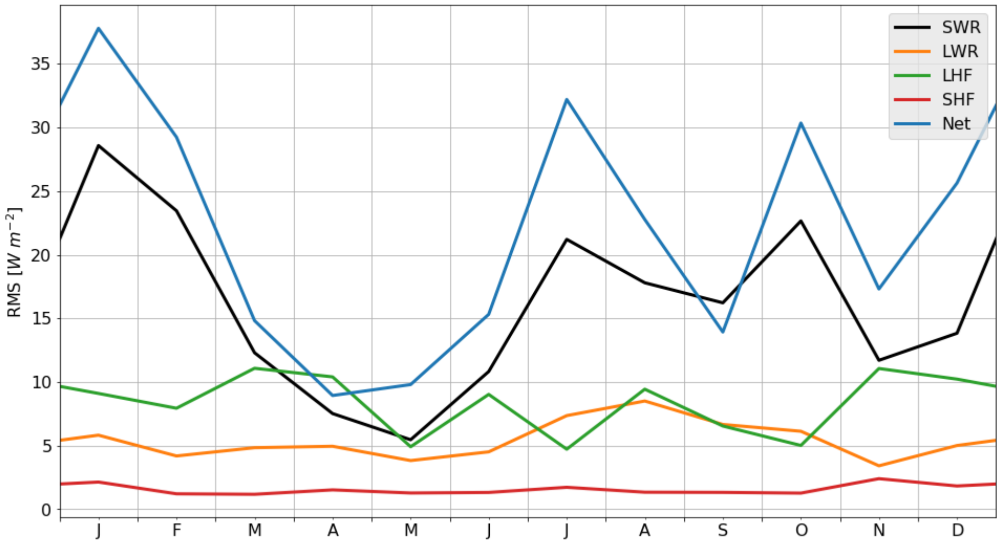

Figure 2.14: *Climatology of the mean difference between the satellite/reanalysis data and the in-situ measurements at the PIRATA-SEE mooring. For the shortwave (SWR) and longwave radiation (LWR) the TropFlux dataset is used, and for latent (LHF) and sensible heat flux (SHF) the MERRA2 dataset is used. The net surface heat flux (Net) is the mean difference of the sum of all fluxes between the satellite/reanalysis data and the in-situ measurements.*

Data availability

Publicly available datasets were used for this study. Data from TropFlux are from the Indian National Centre for Ocean Information Services and their website at https://incois.gov.in/tropflux/index.jsp (ESSO – Indian National Centre for Ocean Information Services, 2023). Data from MERRA2 can be downloaded from their website at https://doi.org/10.5067/LH0VEHYM7Y8Z (GMAO, 2008). The OSTIA-SST were accessed via the Coperni- cus Server (https://doi.org/10.48670/moi-00168, Good et al., 2020). Surface velocities are from the OSCAR dataset (https://doi.org/10.5067/OSCAR-03D01, ESR, 2009). Mixed layer depths were calculated using the GLORYS product (https://doi.org/10.48670/moi-00021, (Lellouche et al., 2021)). The data from the PIRATA Southeast Extension are available on the project website (https://www.pmel.noaa.gov/gtmba/, National Oceanic and Atmospheric Administration United States Department of Commerce, 2023). The net primary production dataset used in this study covers the period from 2002 to 2021 and is available online at http://orca.science. oregonstate.edu/1080.by.2160.8day.hdf.eppley.m.chl.m.sst.php (Ocean Productivity, 2023; downloaded in February 2022). ASCAT (https://www.remss.com/missions/ascat/, Ricciardulli and Wentz, 2016) and QSCAT (https://www.remss.com/missions/qscat/, Ricciardulli et al., 2011) are also publicly available. The ocean turbulence data used in this study are available under https://doi.org/10.1594/PANGAEA.953869 (Körner et al., 2023b).

Author contributions

MK performed the analysis and drafted the paper. PB and MD led the observational programme at sea. All co-authors reviewed the paper and contributed to the scientific interpretation and discussion.

Competing interests

The contact author has declared that none of the authors has any competing interests.

Disclaimer

Acknowledgments

We would like to thank Volker Mohrholz for contributing to the microstructure measurements during part of the cruises. We thank the captains, crews, scientists, and technicians involved in several research cruises in the tropical Atlantic who contributed to collecting data used in this study. The TropFlux data are produced under a collaboration between Laboratoire d'Océanographie: Expérimentation et Approches Numériques (LO- CEAN) from Institut Pierre Simon Laplace (IPSL, Paris, France) and the National Institute of Oceanography/CSIR (NIO, Goa, India), and they are supported by the Institut de Recherche pour le Développement (IRD, France). TropFlux relies on data provided by the ECMWF Re-Analysis Interim (ERA-Interim) and ISCCP projects. We are grateful to two anonymous reviewers for their helpful comments and suggestions, which helped improve the quality of this paper.

Financial support

The study was funded by EU H2020 under grant agreements 817578 (TRIATLAS project) and 101003470 (NextGEMS project). It was further supported by the German Federal Ministry of Education and Research as part of the SACUS (03G0837A), SACUS II (03F0751A), and BANINO (03F0795A) projects and by the German Science Foundation through several research cruises with *RV Meteor*.

Review statement

This paper was edited by Anne Marie Tréguier and reviewed by two anonymous referees.

3 Coastal trapped waves and tidal mixing control primary production in the tropical Angolan upwelling system

The tropical Angolan upwelling system (tAUS) is a highly productive ecosystem with distinct seasonal variability. Productivity peaks in a narrow stripe along the Angolan coast in late austral winter. The peak in productivity occurs about a month after the passage of an remotely forced upwelling coastal trapped wave (CTW). Previous studies have discussed that the peak in porductivity is controlled by the passage of the upwelling CTW (Ostrowski et al., 2009; Kopte et al., 2017; Tchipalanga et al., 2018a; Zeng et al., 2021; Brandt et al., 2023). However, the mechanism by which the CTW controls productivity in the tAUS is still not resolved (Brandt et al., 2023). The study presented in this chapter focuses on unraveling the mechanism behind the productivity peak in late austral winter in the tAUS. In this study, extensive observational datasets are utilized. Furthermore, the results are compared to the output of a regional ocean model.

The manuscript was published in *Science Advances* in January 2024.

Körner, M., Brandt, P., Illig, S., Dengler, M., Subramaniam, A., Bachèlery, M.-L., and Krahmann, G. (2024). Coastal trapped waves and tidal mixing control primary production in the tropical Angolan upwelling system, *Science Advances*, 10, eadj6686, https://doi.org/10.1126/sciadv.adj6686.

The candidate designed the study and carried out the analysis of all observational data products. The model ensemble means presented in Fig. 3.8 & 3.19 were provided by Serena Illig. The candidate produced all figures and authored the manuscript from the first draft to the final version.

3.1 Abstract

Eastern boundary upwelling systems are hotspots of marine life and primary production. The strength and seasonality of upwelling in these systems are usually related to local wind forcing. However, in some tropical upwelling systems, seasonal maxima of productivity occur when upwelling favorable winds are weak. Here, we show that in the tropical Angolan upwelling system (tAUS) the seasonal productivity maximum is due to the combined effect of coastal trapped waves (CTW) and elevated tidal mixing on the shelf. During austral winter, the passage of an upwelling CTW displaces the nitracline upward by more than $50\,m$. Thereby, nitrate-rich waters spread onto the shelf, where elevated vertical mixing causes a nitrate flux into the surface mixed layer. Interannual variability of the productivity maximum is strongly correlated to the amplitude of the upwelling CTW as seen in sea level data. Given that CTWs are connected to equatorial forcing, a predictability of the strength of the productivity maximum is suggested.

Teaser

Coastal trapped waves and near-coastal mixing explain the seasonal productivity in the Angolan upwelling system.

3.2 Introduction

The eastern boundary regions of the tropical Atlantic and Pacific oceans host highly productive ecosystems. These tropical upwelling systems represent a biodiverse marine environment and support one of the most productive marine food chains (Longhurst, 1993; Chavez et al., 2008; Sowman and Cardoso, 2010; Kirkman et al., 2016). They are of great importance for local and global fisheries and are affected by interannual climate variability and climate warming (Wang and McPhaden, 2000; Bakun and Weeks, 2008). It is therefore of great interest to understand the processes that drive these systems. In most tropical upwelling regions, wind stress maxima and productivity maxima are disjoint (Thomas et al., 2001, 2012) (Fig. 3.1 B-C). Thus, processes other than offshore Ekman transport must be the dominant drivers of productivity in these regions. Physical factors discussed in this context are the equatorial current system, surface heat fluxes, remote forcing along the equatorial waveguide and the mixed layer depth (Thomas et al., 2001; Tchipalanga et al., 2018a; Xue et al., 2022). Along with understanding the drivers of the tropical upwelling system, it is of great socio-economic interest to predict their variability. The coastal tropical upwelling system in the Pacific and Atlantic Ocean exhibits a pronounced seasonal cycle with important interannual variations superimposed (Echevin et al., 2008; Mao et al., 2020; Brandt et al., 2023). Note that state-of-the-art climate models have difficulties to realistically represent eastern boundary upwelling regions and their variability (Kurian et al., 2021; Farneti et al., 2022; Richter et al., 2022). Large warm biases in sea surface temperature (SST) are still present in the tropical eastern-boundary upwelling systems (Farneti et al., 2022), suggesting that the physical processes driving these systems are

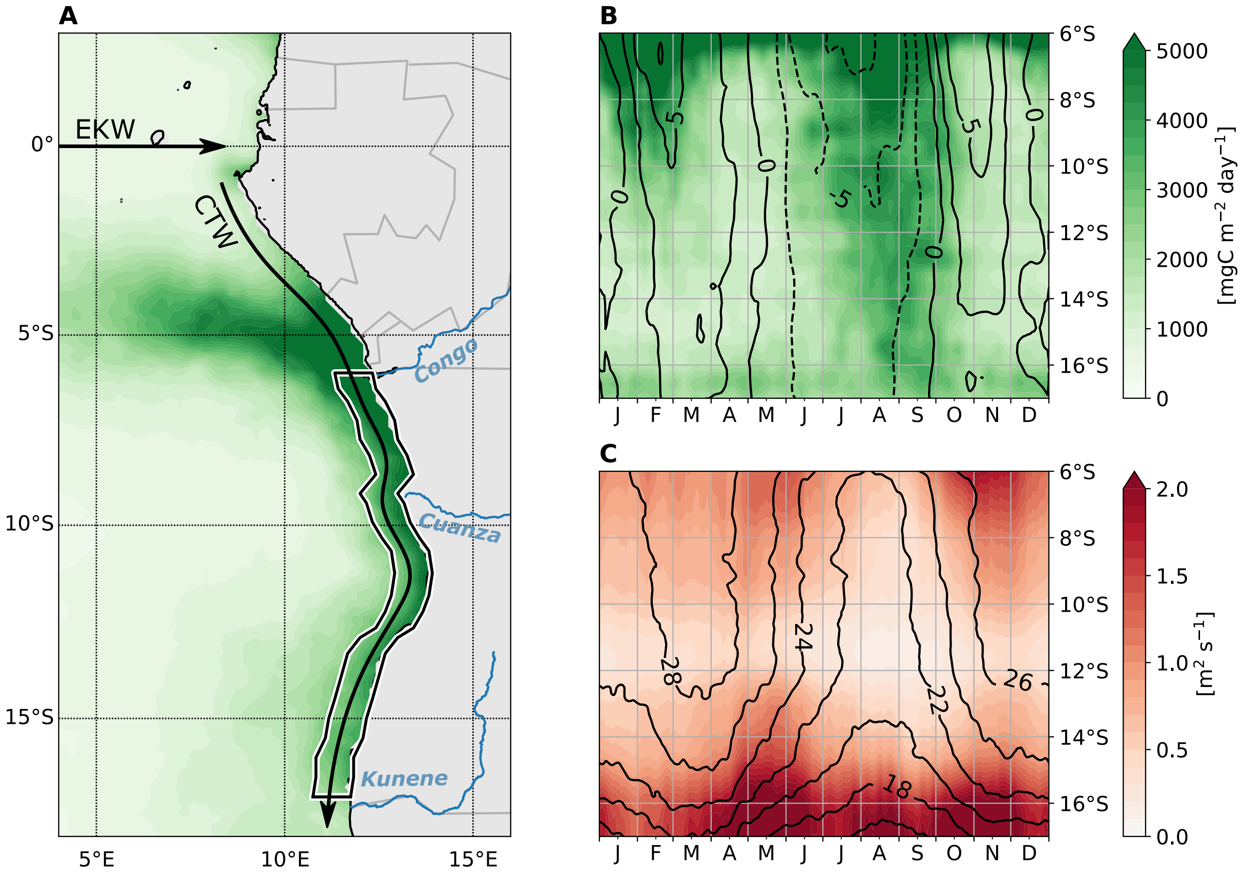

Figure 3.1: *Primary production and wind-driven upwelling in the tropical Angolan upwelling system.* ***A*** *Mean net primary production (NPP) in July – September. Black arrows mark the waveguide for equatorial Kelvin waves (EKW) and coastal trapped waves (CTW). The solid black box marks the tropical Angolan upwelling system (tAUS).* ***B*** *Hovmoeller plot showing the seasonal cycle of NPP (colors) and sea level anomaly (SLA) zonally averaged in the coastal box marked in A (black contour lines, solid lines positive and dashed lines negative SLA [cm]).* ***C*** *Colors show the seasonal cycle of the integrated wind-driven upwelling transport from the coast to one degree offshore representing the sum of Ekman and of wind-stress-curl-driven upwelling (see methods). Black contour lines show the seasonal cycle of the sea surface temperature [°C] zonally averaged in the coastal box marked in* ***A***

not fully captured in these models. It is crucial to advance process understanding and improve prediction skills to assess possible future changes within these systems e.g., due to anthropogenic influences.

In this study, we focus on the physical drivers of productivity in the tropical Angolan upwelling system (tAUS) in the Atlantic Ocean. Angolan waters are located between the Congo River outflow at 6°S and the Angola-Benguela frontal zone at 17°S (Fig. 3.1).

The tAUS is closely connected to equatorial dynamics. Zonal wind fluctuations at the equator excite equatorial Kelvin waves (EKWs), which propagate eastward, and upon encountering the eastern boundary, part of their energy is transformed into poleward propagating coastal trapped waves (CTWs) (Brink, 1982; Polo et al., 2008) (Fig. 3.1 A). CTWs exhibit signals in sea level anomaly (SLA) where upwelling (downwelling) CTWs are associated with a depression (elevation) in sea level. Poleward propagating CTWs not only modulate the near-coastal sea level, but depending on stratification and the local shelf and continental slope topography, they are also associated with specific spatial patterns of velocity and density anomalies. CTWs can be separated into different wave modes, with lower modes propagating faster and exhibiting larger cross-shelf and vertical scales of variability than higher modes (Clarke, 1977; Clarke and Brink, 1985; Brink, 1982, 1989; Illig et al., 2018b,a).

The seasonal cycle of SLA reveals that two equatorially forced downwelling and two equatorially forced upwelling CTWs propagate along the Angolan coast throughout the year (Polo et al., 2008; Rouault, 2012; Tchipalanga et al., 2018a) (Fig. 3.1 B). These waves differ in amplitude. The signal of the main downwelling CTW is visible in February, followed by the main upwelling CTW peaking in July. In October/November, the secondary downwelling CTW propagates along the coast, followed by a secondary upwelling CTW in December/January. The seasonal cycle of CTWs in the tAUS can thus be explained by a superposition of annual and semi-annual harmonics (Rouault, 2012; Tchipalanga et al., 2018a; Kopte et al., 2018). The dominance of the annual and semi-annual cycle is related to the dominant wind forcing in the equatorial Atlantic and to the basin resonance, relatively enhancing the semi-annual cycle(Philander and Pacanowski, 1981; Thierry et al., 2004; Brandt et al., 2016).

Productivity also shows variability on the semi-annual cycle (Fig. 3.1 B). The highest net primary production (NPP) is found in July–September during the main upwelling season. A secondary upwelling season is observed in February, which is weaker and restricted to the northern part of tAUS. Thus, productivity peaks about one month after the passage of the upwelling CTWs. Previous studies have discussed whether phytoplankton blooms are forced by CTWs, highlighting that productivity and the occurrence of upwelling CTWs are in phase (Ostrowski et al., 2009; Kopte et al., 2017; Tchipalanga et al., 2018a; Zeng et al., 2021; Brandt et al., 2023). However, the control on productivity by the upwelling CTWs is still not resolved (Brandt et al., 2023). Note that the wind-driven upwelling in the tAUS is in general weak and peaks in May and can thus not explain the seasonal cycle in NPP (Fig. 3.1 C). Further note that in the Peruvian upwelling system, where wind stress maxima and productivity maxima are also disjoint, the seasonal cycle of productivity is discussed to be related to the seasonality of the mixed layer depth with shallowest mixed layer depths during the maxima in productivity (Echevin et al., 2008; Xue et al., 2022). This mechanism that involve vertical dilution of phytoplankton and light limitation during periods of deep mixed layer cannot explain the productivity in the tAUS because in contrast to the Peruvian upwelling system the mixed layer depth is deepest during the main productivity season (Körner et al., 2023a).

In the Angolan and the Benguela upwelling systems extreme warm and cold events, the so-called Benguela Niños and Benguela Niñas, are the dominant mode of SST variability on interannual time scales (Shannon et al., 1986). This interannual variability peaks seasonally during the main downwelling season, between March and April (Imbol Koungue et al., 2017, 2019; Lübbecke et al., 2019; Illig et al., 2020) and thus plays a minor role in the productivity variability during the main upwelling season of the tAUS. While Benguela Niños and Benguela Niñas have been related to equatorially forced CTWs (Bachèlery et al., 2016b; Imbol Koungue et al., 2017; Bachèlery et al., 2020), local mechanisms can also modulate the strength of these extreme events (Richter et al., 2010; Lübbecke et al., 2019).

In general, CTWs can affect ecosystems productivity in multiple ways. One way is through their ability to vertically displace the nitracline. A modelling study conducted on the Peruvian upwelling system showed how equatorially forced intraseasonal CTWs of higher modes can induce phytoplankton blooms by vertically advecting the nitracline into the euphotic zone (Echevin et al., 2014). CTWs can also influence biogeochemical conditions through horizontal advection. Observations collected during an intraseasonal CTW event off the coast of Peru showed how nitrate-rich waters were transported along the coast by a low-mode downwelling CTW (Lüdke et al., 2020).

In the tAUS, the role of vertical mixing, as a mechanism for upward nitrate supply has been discussed on the basis of the investigated turbulent heat flux (Ostrowski et al., 2009; Brandt et al., 2023). The primary energy source for turbulence on the shelf of the tAUS is thought to be the dissipation of internal tidal energy (Zeng et al., 2021). The interaction of the barotropic tide with the continental slope leads to the generation of internal tides that partly propagate onto the continental shelf and dissipate in shallow water (Zeng et al., 2021). Elevated dissipation rates of turbulent kinetic energy are frequently observed in shallow waters on the Angolan shelf which are responsible for the near-shore cooling of surface waters (Zeng et al., 2021; Körner et al., 2023a). The regionally confined enhanced mixing on the shelf was associated with breaking internal waves resulting in the development of frontal structures that leads to the aggregation of small pelagic fish (Ostrowski and Bazika-Sangolay, 2016). However, the role of vertical mixing in the upward supply of nitrate in the tAUS has not been explicitly investigated so far.

In this study, we use hydrographic, oxygen, nitrate, ocean turbulence, and satellite data to analyze the physical drivers of seasonal and interannual variability of NPP in the tAUS. Additionally, we use a regional ocean model to corroborate the observational results. We find that CTWs and enhanced vertical mixing in the water column above the upper continental slope and shelf can explain productivity variability on both seasonal and interannual time scales.

3.3 Results

3.3.1 Seasonal changes in nitrate and density

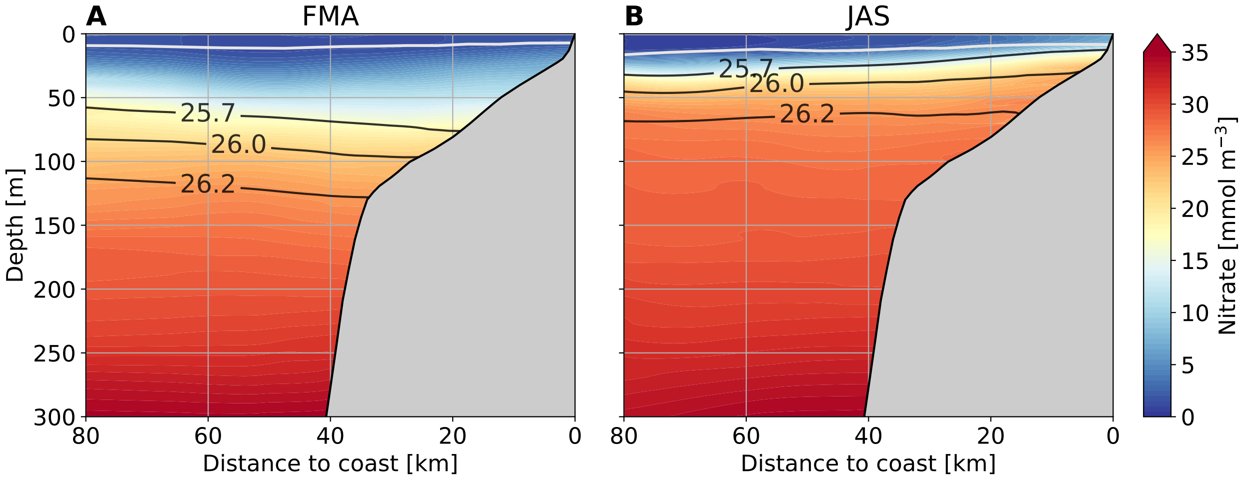

Figure 3.2: *Cross-shelf sections of nitrate during the downwelling and upwelling season. Cross-shelf sections of nitrate concentration inferred from oxygen data (see methods) as a function of distance to the coast. Data collected between 10°S and 12°S are projected onto the mean topography in this latitude band (see methods).* ***A*** *shows the mean section for February–April and* ***B*** *for July–September. Black lines show selected isolines of the mean potential density field. White lines show the mixed layer depth.*

In the tAUS, primary production undergoes a distinct seasonal cycle (Fig. 3.1 B). NPP is elevated during the main upwelling season in late austral winter (July – September) and low during the downwelling phases (February–April/October–December). NPP is limited by nitrate in this region (Moore et al., 2004; Browning et al., 2017). Therefore, to understand the seasonal differences in NPP, the seasonal distribution of nitrate is analyzed. We make use of an extensive dataset of conductivity-temperature-depth (CTD) and oxygen profiles collected between 1995 and 2022 (Tchipalanga et al., 2018a). From in-situ nitrate measurements in the tAUS, we derive a statistical relationship between the apparent oxygen consumption and nitrate (see methods). This allows us to use oxygen concentrations to estimate nitrate distributions and analyze their spatial and temporal variability. Most of the data were collected during either the main downwelling season (February–April) or during the main upwelling season (July–September).

The cross-shelf sections of inferred nitrate concentration calculated from data between 10°S and 12°S during these two seasons reveal distinct differences (Fig. 3.2). Nitrate concentrations in the upper ocean are much higher during the upwelling phase than during the downwelling phase. During the upwelling season, nitrate-rich water penetrates far onto the shelf, whereas during the downwelling season, the shelf is mostly covered by low-nitrate waters. Additionally, the upward displacement of nitrate-rich waters during the upwelling season results in a strengthening of the vertical nitrate gradient in the upper ocean.

The upward-displaced nitracline during the upwelling seasons is associated with concurrent upward-displaced isopycnal surfaces (Fig. 3.2). During both seasons, the position of the nitracline is located foremost between the $25.7\,kg\,m^{-3}$ and $26\,kg\,m^{-3}$ isopycnals. Both isopycnals experience elevated vertical displacements. From the downwelling to the upwelling season, the $25.7\,kg\,m^{-3}$ isopycnal is displaced by about $42\,m$, while the $26\,kg\,m^{-3}$ isopycnal is displaced by $62\,m$. Fig. 3.2 additionally shows the mixed layer depth during both seasons. On average it is $11.3\,m$ deep during the main upwelling season and thus slightly deeper than during the main downwelling season (on average $9.1\,m$).

The large vertical movement of the density surfaces and the nitracline raises the question of what causes this seasonal deformation of the nitrate and density fields. To answer this question, we examine the seasonal density fields closely. The most striking differences in the mean potential density fields are visible near the surface (Fig. 3.3 A-B). During the downwelling phase, low-density water occupies the upper $40\,m$ of the ocean, resulting in a strongly enhanced upper ocean stratification. In contrast, during the upwelling season, we find denser water near the surface, resulting in a weaker stratification below the mixed layer. These differences in the upper ocean can be explained by surface heat and freshwater fluxes, as well as river runoff, resulting in warmer and fresher surface waters during the downwelling season compared to the upwelling season (Tchipalanga et al., 2018a; Awo et al., 2022; Brandt et al., 2023; Körner et al., 2023a). Temperature differences are determined by the seasonal cycle of surface heat fluxes (Körner et al., 2023a), while changes in salinity are mainly influenced by the advection of freshwater from the Congo River by the southward flowing Angola Current (Awo et al., 2022). The strength of the Angola Current, and thus the strength of the freshwater advection, is modulated by the different phases of the semi-annual CTWs propagating southward along the Angolan coast. Peaks in southward freshwater advection are in phase with the downwelling CTWs in February/March and October/November. The low-salinity signal in the surface waters weakens southward due to vertical salt advection and mixing at the base of the mixed layer (Awo et al., 2022).

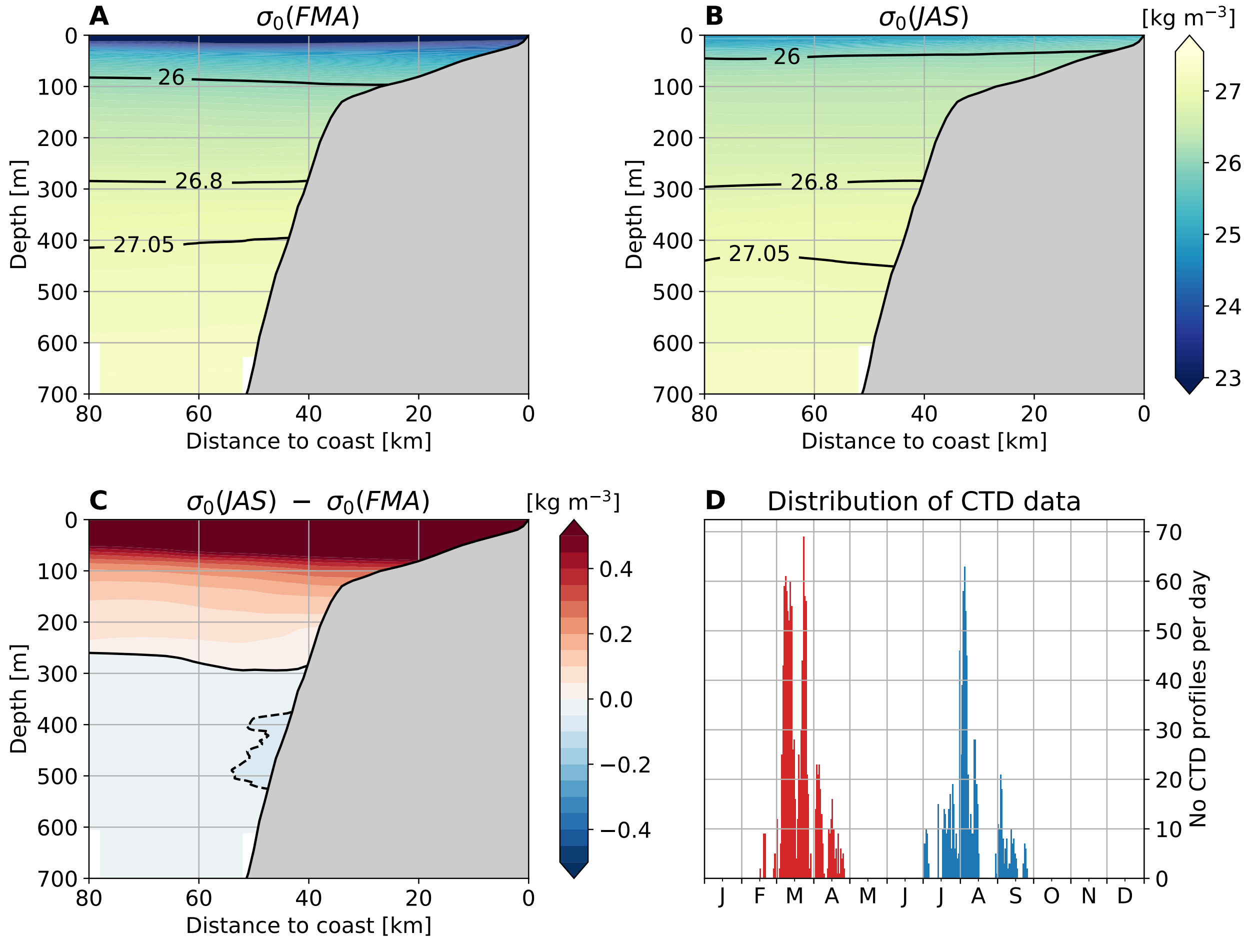

Figure 3.3: *Cross-shelf sections of potential density during the downwelling and upwelling season. Cross-shelf sections of potential density calculated from CTD data measured between 10°S and 12°S and projected onto the mean topography for* ***A*** *February–April and* ***B*** *July–September. Black lines show selected isolines of potential density to illustrate seasonal differences.* ***C*** *shows the difference between the density fields of both seasons. The solid black line marks the zero contour, the dashed black line marks the* $-0.05\,kg\,m^{-3}$ *contour.* ***D*** *shows the seasonal distribution of the CTD profiles used in* ***A*** *–* ***C****.*

Away from the surface, the density field also exhibits seasonal changes that cannot be explained by surface heat and freshwater fluxes. Fig. 3.3 A-B reveal that the $26\,kg\,m^{-3}$ isopycnal moves upward from the downwelling to the upwelling season, while the depth of the $26.8\,kg\,m^{-3}$ isopycnal is nearly constant and the $27.05\,kg\,m^{-3}$ isopycnal moves downward. Thus, the seasonal changes in the density field are depth dependent: Between the surface and about $300\,m$ depth, the potential density surfaces move upward or outcrop from the downwelling to the upwelling season, while between $300\,m$ and $700\,m$, the potential density surfaces move downward (Fig. 3.3 A-C). Note that both the upward and downward displacements are larger near the topography than further offshore at the same depth.

One possible mechanism that affects the depth of the density surfaces is wind-driven upwelling. However, the seasonality of the wind-driven upwelling does not match the seasonality of the vertical movements of density surface, i.e., wind-driven upwelling is found to be weakest during the upwelling season (Fig. 3.1 C) (Ostrowski et al., 2009). Another dynamic mechanism affecting the upward and downward movements of isopycnals is the passage of CTWs. CTWs originating at the equator are well observed by a SLA signal that propagates along the equatorial and coastal waveguides (Polo et al., 2008; Rouault, 2012). Variations in SLA associated with CTWs are the result of the steric height, which is caused by changes in water-column density. The seasonal maximum and minimum SLA in the tAUS are found at the beginning of the main downwelling and upwelling seasons, respectively (Fig. 1B). However, CTWs are associated with specific spatial (vertical and cross-shelf) structures that define different CTW modes which propagate with different phase velocities. Such CTW modes can be derived theoretically from the mean stratification and the cross-shelf topography (Brink, 1982)(Brink, 1989; Brink and Chapman, 1987; Illig et al., 2018b,a). Comparing the observed changes of the cross-shelf density field (Fig. 3.3 C) with the cross-shelf-depth structures of density anomaly of the theoretically derived CTW modes (Fig. 3.12) suggests that only high-mode CTWs are capable of explaining the observed seasonal differences. Particularly CTW modes 4 and 5 agree well with the observed density difference (Fig. 3.3 C) as the depth of the zero crossing (i.e., the depth at which density surfaces do not move) and the depth of maximum density change away from the surface is at comparable depth. This implies that in austral winter the passage of high-mode upwelling CTWs deforms the density field and leads to an upward advection of density surfaces near the shelf break. The nitrate field reflects these vertical motions. Thus, associated with the passage of high-mode upwelling CTWs, we observe enhanced nitrate levels within the euphotic zone and stronger vertical nitrate gradients near the surface.

Analyses of hydrographic, nutrient, and oxygen data suggest that high-mode CTWs play a crucial role in the upward advection of the nitracline. On seasonal time scales, the passage of CTWs is observable in SLA in the tAUS (Fig. 3.1 B)(Polo et al., 2008; Tchipalanga et al., 2018a). However, the gridded altimetric SLA data mostly capture low-mode CTWs. This is due to the decreasing cross-shelf scales of the SLA structure associated with CTWs for higher CTW modes (Fig. 3.12) suggesting that for a given horizontal resolution of gridded altimetric SLA data (i.e., $100\text{-}200\,km$ effective spatial resolution (Ballarotta et al., 2019)), low-mode CTWs are predominantly observed. Additionally, the number of zero crossings in the vertical density structure increases for higher CTW modes off the shelf leading to a cancellation effect when vertically integrating over positive and negative density anomalies to derive the steric height anomaly (Fig. 3.14). Thus, while high-mode CTWs are best represented by density changes in the depth range of the nitracline, low-mode CTWs are depicted in SLA data.

We analyze the relationship between the low-mode CTWs observable in SLA, the displacement of isopycnals observed in hydrographic data and the peak in NPP (Fig 3.4). The depths of the $26\,kg\,m^{-3}$ and $27.05\,kg\,m^{-3}$ isopycnals are highly variable both during individual cruises and between the cruises. Nevertheless, the data shows a synchronous heaving of the $26\,kg\,m^{-3}$ isopycnal and deepening of the $27.05\,kg\,m^{-3}$ isopycnal after the annual sea level minimum. Note that this movement of the isopycnals is not consistent with the vertical velocity structure of low-mode CTWs, but is consistent with those of higher modes (3.13). Furthermore, Fig. 4 shows that these density surfaces reach their seasonal minimum/maximum depth after the minimum in SLA. This suggests that low-mode CTWs observable in SLA are not the primary forcing of the vertical movements of the isopycnals in the upper ocean near the shelf break and ultimately do not control the position of the nitracline. The time delay between the low-mode CTWs observable in SLA and the high-mode CTWs deforming the density field is not clearly determinable from the hydrographic data. The timing of the NPP peak further supports the proposed relationship between low and high-mode CTWs and their effect on the nitracline, as NPP peaks approximately 40 days

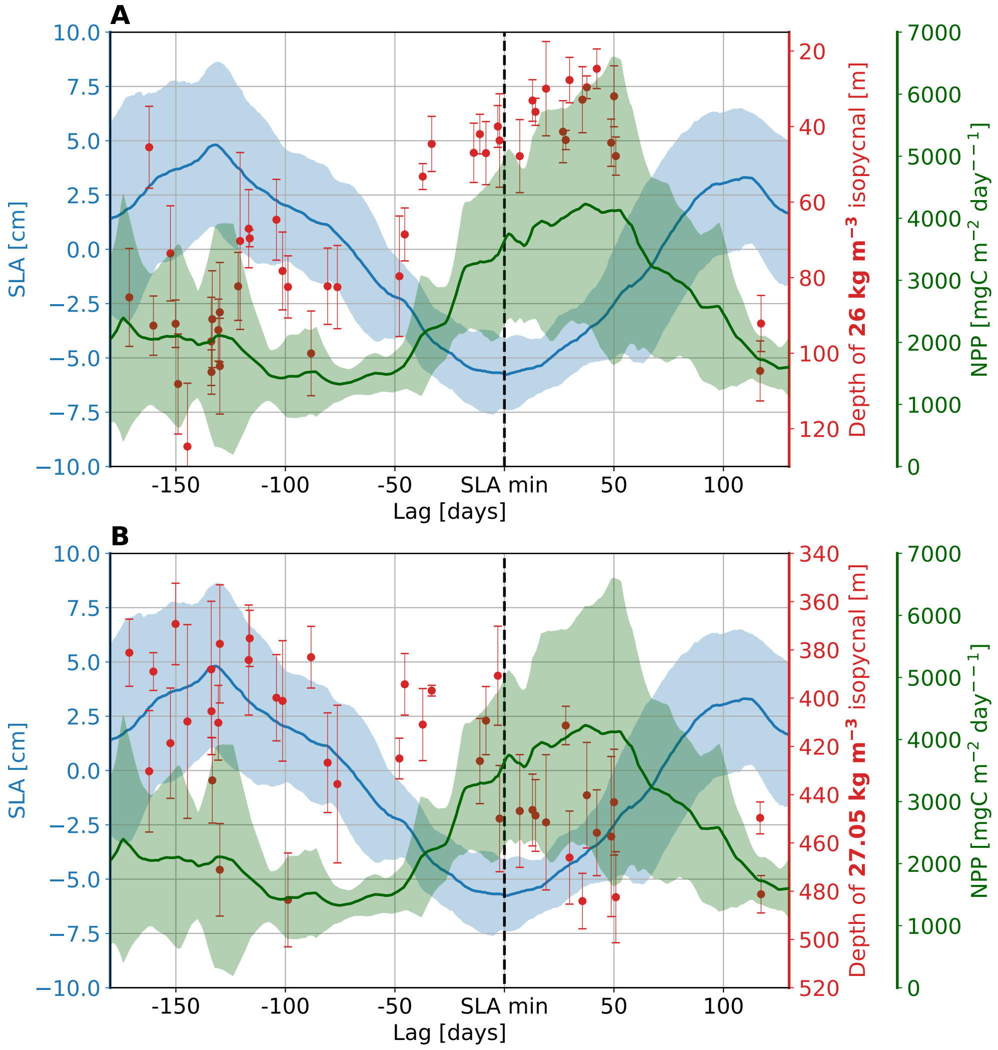

Figure 3.4: *Sea level anomaly (SLA), net primary production (NPP), and depth of isopycnals as a function of lag to the time of annual SLA minimum. SLA, NPP, and depth of* ***A*** $26\,kg\,m^{-3}$ *and* ***B*** $27.05\,kg\,m^{-3}$ *isopycnal as a function of time lag [days] with respect to the time of the annual minimum in SLA occurring during the main upwelling season. Blue lines show the mean SLA for 1995 – 2022. The timing of the annual SLA minimum is determined using the SLA time series treated with a low-pass filter (cut-off period of 135 days). Green lines show the mean NPP for 2002 – 2021. Shaded areas show the standard deviations. Red dots indicate the depth of the respective potential density surface averaged for each cruise considering all CTD profiles taken between* 250 *and* $1000\,m$ *water depth. Red bars indicate the standard deviation of the depth of the density surface. Data between 10°S and 12°S are used for all three variables. For both SLA and NPP, data within 1° off the coast are used.*

after the minimum in SLA. Analysis of velocity data of the upper 500 m observed at a mooring installed at the $1200\,m$ isobath supports the findings from the hydrographic data (Fig. 3.12). Note however that the position of the mooring is not ideal for separating different CTW mode contributions, as the velocity variability of the different modes is generally weak at this position. Nevertheless, the observed mean alongshore velocity component as a function of time-lag to the annual SLA minimum reveals a signal indicative of a high-mode upwelling CTW arriving about 25 days after the SLA minimum.

The cross-shelf sections of nitrate show that the nitracline not only moves upward between the downwelling and the upwelling seasons but that nitrate-rich water also penetrates far onto the shelf during the upwelling season (Fig. 3.2). To analyze the onshore transport of nitrate-rich waters, we look at the output of a regional ocean model (Fig. 3.18). In the model, the zonal velocities show onshore currents in the area of the shelf break associated with the passage of CTWs. The onshore flow is strongest at about mid-depth above the upper continental slope and shelf (Fig. 3.18 B). Furthermore, onshore velocities peak after the minimum in the SLA.

Overall, the observational data and the model output suggests that CTWs of different vertical structures propagate along the continental shelf in austral winter that are phase-locked to each other. At a given location in the tAUS, the low-mode CTW visible in SLA arrives first. Later (presumably about 25 days), the corresponding high-mode CTW arrives and impacts the depth of the nitracline as well as the onshore extent of nitrate-rich waters.

3.3.2 Upward nitrate supply by vertical mixing

Associated with the passage of high-mode CTWs during the upwelling season, nitrate-rich water is advected upward and onto the shelf toward the coast. Previous studies showed that the shelf region of the tAUS is a region of enhanced vertical mixing (Zeng et al., 2021; Brandt et al., 2023; Körner et al., 2023a). Since vertical mixing can influence the nitrate supply to the surface ocean (Cyr et al., 2015; Schafstall et al., 2010) we analyze its effect on the nitrate distribution in the tAUS.

Microstructure profiles collected during six research cruises conducted during different seasons allow us to analyze turbulence at a cross-shelf section at 11°S (Körner et al., 2023a). The mean distribution of dissipation rates of turbulent kinetic energy reveals a dependence on bathymetry (Fig. 3.5 A) (Körner et al., 2023a). Waters shallower than $75\,m$ mark a region of enhanced mixing where dissipation rates above $10^{-6} W kg - 1$ are frequently observed. Since vertical mixing on the shelf of the tAUS is mainly driven by internal tides and the tidal energy available for mixing on the shelf is nearly constant throughout the year (Zeng et al., 2021), the mean section of turbulence dissipation rate gives us an estimate of the distribution of mixing on the Angolan shelf at 11°S for the whole year.

To estimate diffusive nitrate fluxes due to vertical mixing in the tAUS, we combine all turbulence dissipation rates and derived eddy diffusivities from the microstructure dataset with the seasonally averaged nitrate gradients (see Methods). Since the dissipation rates show a dependence on bathymetry, we analyze the turbulent nitrate fluxes as a function of bathymetry by partitioning the data into three depth regions (following the approach of Körner et al. (2023a)). Vertical diffusive nitrate fluxes are calculated as a function of distance to the mixed layer, since we want to analyze the nitrate flux into the mixed layer from below.

The vertical nitrate gradient exhibits clear seasonal differences (Fig. 3.5 D). From February to April the vertical nitrate gradient below the mixed layer is nearly constant with values between $0.1\,mmol\,m^{-4}$ and $0.4\,mmol\,m^{-4}$ within $30\,m$ distance from the mixed layer. In contrast, the vertical nitrate gradient is strongly increased between July and September. There is a clear maximum within $10\,m$ below the mixed layer with values of up to $1\,mmol\,m^{-4}$. Furthermore, the vertical nitrate gradient is elevated in shallow waters compared to deeper waters.

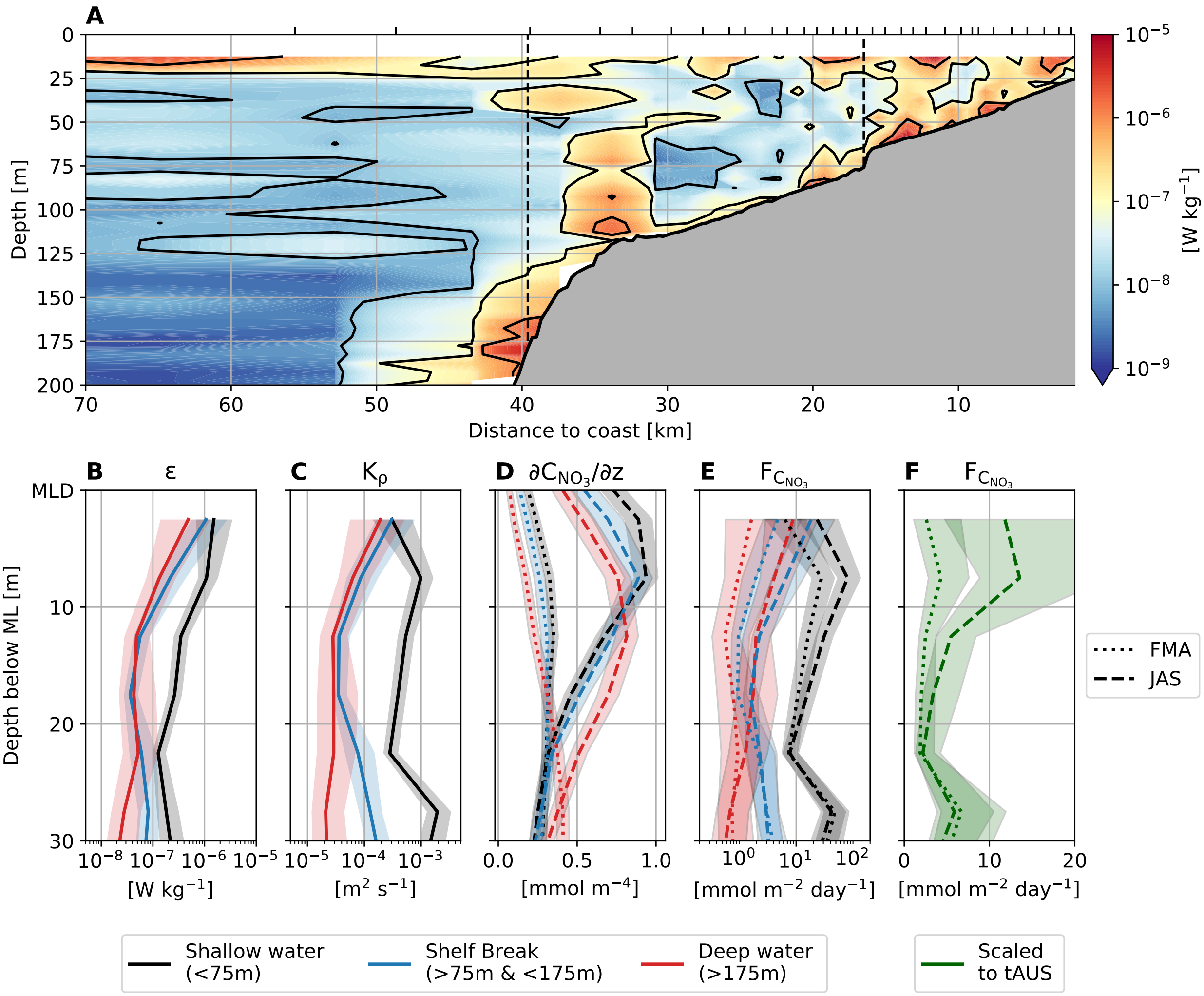

Figure 3.5: ***A*** *Mean section of dissipation rate of turbulent kinetic energy (TKE) at 11°S as a function of distance to coast from microstructure data. Microstructure data are binned together into groups of 20 profiles, the spatial extent of the groups is indicated by vertical ticks at the top of the plot. Measurements within the mixed layer and in the upper 10 m were discarded before averaging. Vertical dashed lines separate the three depth regions.* ***B*** *–* ***E*** *shows mean profiles taken in shallow water (water depth $< 75\,m$, black), in the area of the shelf break (water depth > 75 and $< 175\,m$, blue) and in deep waters (water depth $> 175\,m$, red) as a function of distance to the mixed layer depth.* ***B*** *shows the dissipation rate of TKE $[W\,kg^{-1}]$,* ***C*** *the eddy diffusivity $[m^2\,s^{-1}]$,* ***D*** *the vertical nitrate gradient [mmol m-4] inferred from oxygen data (see methods),* ***E*** *the turbulent nitrate flux $[mmol\,m^{-2}\,day^{-1}]$, and* ***F*** *the turbulent nitrate flux $[mmol\,m^{-2}\,day^{-1}]$ scaled to the whole tAUS.* ***D*** *-* ***F*** *show the results for February – April (dotted) and July – September (dashed), respectively. Shaded areas indicate 95% confidence intervals. Note the logarithmic scale in B, C and E.*

The resulting turbulent nitrate fluxes illustrate the temporal and spatial differences (Fig. 3.5 E). The turbulent nitrate flux into the mixed layer can be determined by averaging the profiles between $2\,m$ and $15\,m$ below the mixed layer. The highest turbulent nitrate fluxes are estimated during the upwelling season in shallow waters ($44.8\,[29.5,\,75.8]\,mmol\,m^{-2}\,day^{-1}$, values in brackets give the 95% confidence interval). The weakest turbulent nitrate fluxes are found during the downwelling season in deep waters ($1\,[0.5,\,2.5]\,mmol\,m^{-2}\,day^{-1}$).

These calculations clearly show that turbulent nitrate fluxes are strongly elevated in shallow waters during the upwelling season. However, only a small area within the tAUS has these shallow water depths. To estimate the turbulent nitrate flux over the whole tAUS (8°S-15°S, 1° distance to the coast), we scale the results found at the 11°S section to the whole tAUS. To do this, we compute a weighted mean based on the area of the tAUS that falls within the respective depth ranges (Fig. 3.5 F). The estimated mean turbulent nitrate flux for February – April is $3.1\,[1.9,\,5.9]\,mmol\,m^{-2}\,day^{-1}$ and $10.3\,[5.9,\,20.8]\,mmol\,m^{-2}\,day^{-1}$ for July – September. Assuming the validity of the Redfield ratio (C:N 6.6) (Schafstall et al., 2010) for phytoplankton this would support a carbon fixation of $307\,[188,\,578]\,mmol\,m^{-2}\,day^{-1}$ for February – April and $1007\,[574,\,1987]\,mmol\,m^{-2}\,day^{-1}$ for July–September. Thus, the new production due to turbulent nitrate flux supplies about 16 % [10 %, 30 %] during the downwelling phase and about 28 % [16 %, 55 %] during the upwelling phase to the NPP. Note that the net primary production is the result of new production due to nutrient input into the euphotic zone and regenerated production due to nutrient recycling in surface waters. The ratio of new and regenerated production is highly variable for each ecosystem (Eppley and Peterson, 1979; Messié and Chavez, 2015). Nevertheless, comparisons with potential new production rates in other eastern boundary upwelling regions suggests that turbulent nitrate fluxes play an important role for the NPP signal in the tAUS (Messié and Chavez, 2015).

The turbulent nitrate fluxes calculated here are elevated during the upwelling season compared to the downwelling season. Note that the fluxes presented here are calculated from two datasets that were measured non-simultaneously and independently of each other, which introduces additional uncertainties. The turbulence dataset was measured during cruises conducted in different seasons. We argue that the dataset can be averaged to provide a good estimation of the distribution of the turbulence dissipation rate at the Angolan shelf that is assumed to be constant throughout the year as Zeng et al. (2021) show that tidal energy available for mixing is nearly constant and seasonally independent. Furthermore, the results offer a convincing explanation for the seasonal difference in surface productivity observed in satellite data. The maximum vertical nitrate gradient is stronger during the upwelling season and is located in close proximity to the base of the mixed layer especially in shallow waters. Previous studies of the tAUS have shown that elevated vertical mixing occurs throughout the year and is an important mechanism for cooling the mixed layer near the coast (Zeng et al., 2021; Körner et al., 2023a). This further suggests that the mixing at the base of the mixed layer acting on different vertical nitrate gradients throughout the year, leads to a higher nitrate supply to the surface mixed layer and ultimately to higher NPP in the surface ocean during the austral winter.

3.3.3 Interannual variability of productivity in the tAUS

Satellite data show that the strength of the NPP signal in austral winter is subjected to interannual variability. We now investigate how this variability is related to the amplitude of CTWs arriving from the equatorial region into the tAUS. To estimate the interannual variability of the strength of CTWs and productivity, we rely on satellite data of SLA and NPP, as these datasets provide long time-series and are comparable on interannual time scales. For this analysis we focus on the area from 8°S to 15°S within 1° distance of the coast. We focus on this region to analyze the variability in the tAUS while excluding the direct influence of the Congo River and from the Angola-Benguela frontal zone (Fig. 3.1 B).

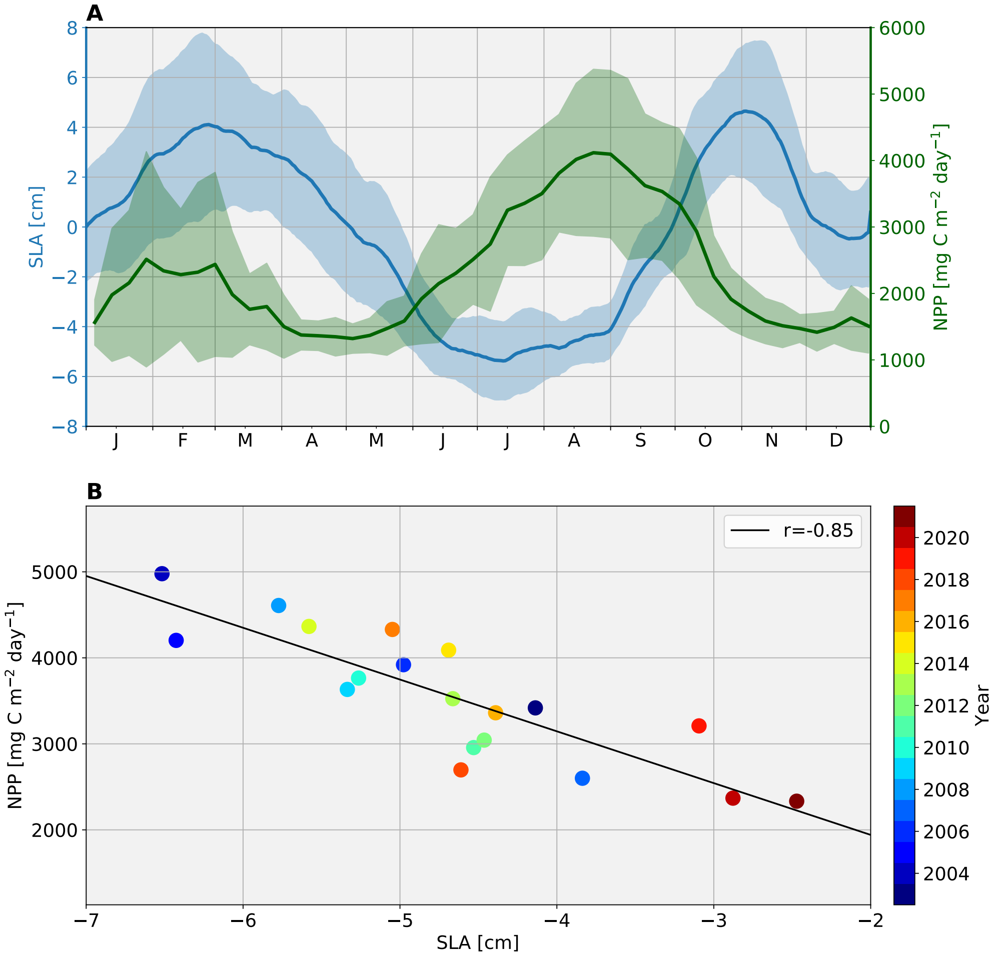

Figure 3.6: *Seasonal cycle and interannual variability of sea level anomaly (SLA) and net primary production (NPP).* ***A*** *Seasonal cycle of SLA (blue) and NPP (green) averaged between 8°S and 15°S within 1° off the coast. Shading indicates the standard deviation.* ***B*** *Scatter plot of three-month mean SLA centered around the annual SLA minimum versus three-month mean NPP lagged by 50 days. The annual minimum of SLA is determined using the SLA time series treated with a low-pass filter (cut-off period is $135\,days$). Colors indicate the respective year of the data point. Linear regression line and the Pearson's correlation coefficient, r, are also given. For both plots data from 2003 – 2021 was used.*

SLA data show that the timing of the upwelling CTW varies from year to year. Between 2003 and 2021, the SLA minimum was reached on average on July 21th with a standard deviation of $10\,days$. To evaluate the strength of the upwelling CTW, we calculate the three-month mean SLA centered around the annual SLA minimum for each year. We now want to correlate the strength of the SLA signal with the strength of the NPP signal. However, the seasonal cycle of SLA and NPP shows a lag between the two variables (Fig. 3.4, 3.6 A). Correlating the three-month mean SLA with the corresponding three-month mean NPP at different lags, reveals highest correlation with SLA leading NPP by 50 days (Fig. 3.19). The Pearson's correlation coefficient between three-month mean SLA and three-month mean NPP lagged by 50 days as shown in Fig. 3.6 B is -0.85, which is significant at the 99% confidence level. During the austral winter, 73% of the variance in the mean NPP signal can be attributed to the variability in the mean amplitude of the SLA. Note that NPP peaks on average on August 27th and thus $37\,days$ after the minimum in SLA. This discrepancy is most likely caused by noise in the NPP data. Note in this context that the NPP data product relies on temporal interpolation to fill gaps due to clouds which are persistent in austral winter in the tAUS (Modi et al., 2022). Thus, determining the exact lag between the minimum in SLA and the maximum in NPP is ambitious. Nevertheless, the correlation coefficient exceeds -0.8 for SLA leading NPP between 33 and $64\,days$ (Fig. 3.19). This suggests that the strong relationship between mean austral winter SLA and NPP signals presented in Fig. 3.6 is robust although the exact lag between the two peaks cannot be determined precisely.

The high correlation between the CTW signal observed in SLA and the corresponding NPP signal emphasizes the crucial role that CTWs play for biological productivity in the tAUS. Generally, years with a strong upwelling CTW signal in SLA in austral winter have higher NPP levels than years with weaker upwelling CTW signals. Between 2003 and 2021, the strongest upwelling CTW signal in SLA is found in 2004 (-6.5 cm), coinciding with the year of the highest NPP peak ($4978\,mgC\,m^{-2}day^{-1}$). In 2021, the weakest CTW signal (-2.4 cm) is associated with the lowest NPP peak ($2337\,mgC\,m^{-2}day^{-1}$). Note that the weakest upwelling CTW in 2021 was associated with the 2021 Benguela Niño, an extreme warm event observed by satellite SST in the tAUS (Brandt et al., 2023), which peaked anomalously late and significantly reduced the coastal productivity during austral winter (Illig and Bachèlery, 2023).

The analysis of satellite data reveals a high correlation between the magnitude of the SLA signal of the upwelling CTW in austral winter and the strength of the NPP peak delayed by about $40\,days$. Thus, years where the SLA signal of the CTW has higher amplitudes tend to have higher NPP. However, analyses of SLA, hydrographic and mooring data reveal that CTWs visible in SLA are not of the same wave mode as the one displacing the nitracline and thus, controlling the productivity. Finally, the high correlation between the amplitude of the low-mode CTWs and the strength of the productivity suggests that the generation mechanism of the high-mode CTWs must be linked to the presence of the low-mode CTWs.

3.4 Discussion

The analyses of hydrographic, biogeochemical, ocean turbulence, and satellite data highlight the crucial role of CTWs for the productivity in the tAUS. The main mechanism we propose to explain the seasonal productivity in the tAUS is based on the combined effect of upwelling CTWs and near-coastal mixing, as summarized in the schematic in Fig. 3.7. In austral winter, different upwelling CTWs are present in the tAUS (Fig. 3.7 A). The arrival of the faster low-mode CTW, which is visible in SLA data, is detected first. With some delay, the slower high-mode CTW, which primarily controls the depth of the nitracline, is observed in the tAUS. This high-mode CTW displaces the nitracline vertically by about $50\,m$ between the main downwelling season and the main upwelling season thus enhancing nitrate concentration within the euphotic zone. Associated with the passage of CTWs there is also a horizontal advection of nitrate-rich water towards the coast, ultimately reaching the area of high mixing in shallow waters of the Angolan shelf (Fig. 3.7 B). The presence of nitrate on the shelf, combined with high mixing rates, results in a higher turbulent nitrate flux into the surface mixed layer during the upwelling season compared to the downwelling season when nitrate concentrations on the shelf are low.

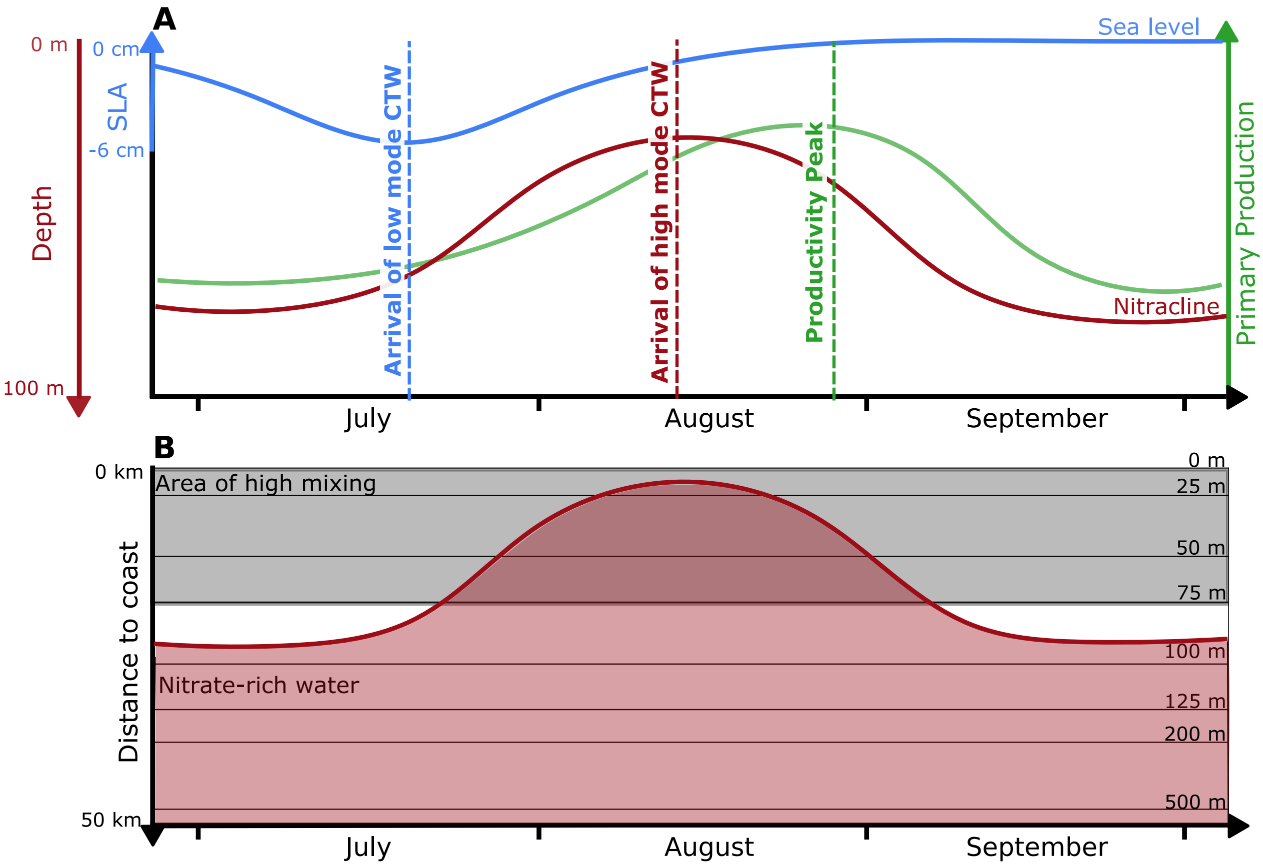

Figure 3.7: *Schematic view of how CTWs and mixing can explain the high productivity season in the tAUS.* ***A*** *Time evolution of sea level anomaly (blue), nitracline depth (red) and NPP (green) at a location in the tAUS near the shelf break.* ***B*** *Time evolution of the onshore extent of nitrate-rich water along a cross-shelf section in the tAUS. Grey area marks the area of high mixing. Black lines show the depth contours at $25\,m$ intervals ($0\,m$ – $125\,m$) and the $200\,m$ and $500\,m$ isobaths. Tick marks on the x-axes indicate the beginning of the respective month.*

Austral winter SLA and NPP correlate on interannual timescales, suggesting a linear relationship between the strength of the upwelling CTW signal, as observed in SLA and productivity. However, our results also suggest that the low-mode CTWs observed in SLA are not primarily responsible for the uplift of the nitracline. The question naturally arises as to how the low-mode and high-mode CTWs are related. The strong correlation between the SLA and NPP suggests that the low-mode and high-mode CTWs are phase-locked.

The velocity and potential density fields of a regional ocean model suggest, similar to the observations, that high-mode CTWs arrive at 11°S after the SLA minimum (Fig. 3.8 B). Isopycnals in the upper ocean reach their seasonal minimum depth after the minimum in SLA. The time-lag between the minimum depth of the $26\,kg\,m^{-3}$ isopycnal and the minimum in SLA is $30\,days$. Simultaneously, the depth of isopycnals at greater depths increases after the minimum in SLA. The velocity field shows upward propagating wave phases after the arrival of the SLA minimum, indicating downward energy propagation (Gill, 1982). We find the signals in the density and velocity field not only at 11°S but also at various latitudes (Fig. 3.8 A-C). Further south, at 21°S, the signal in the velocity field and the rise of the $26\,kg\,m^{-3}$ isopycnal is

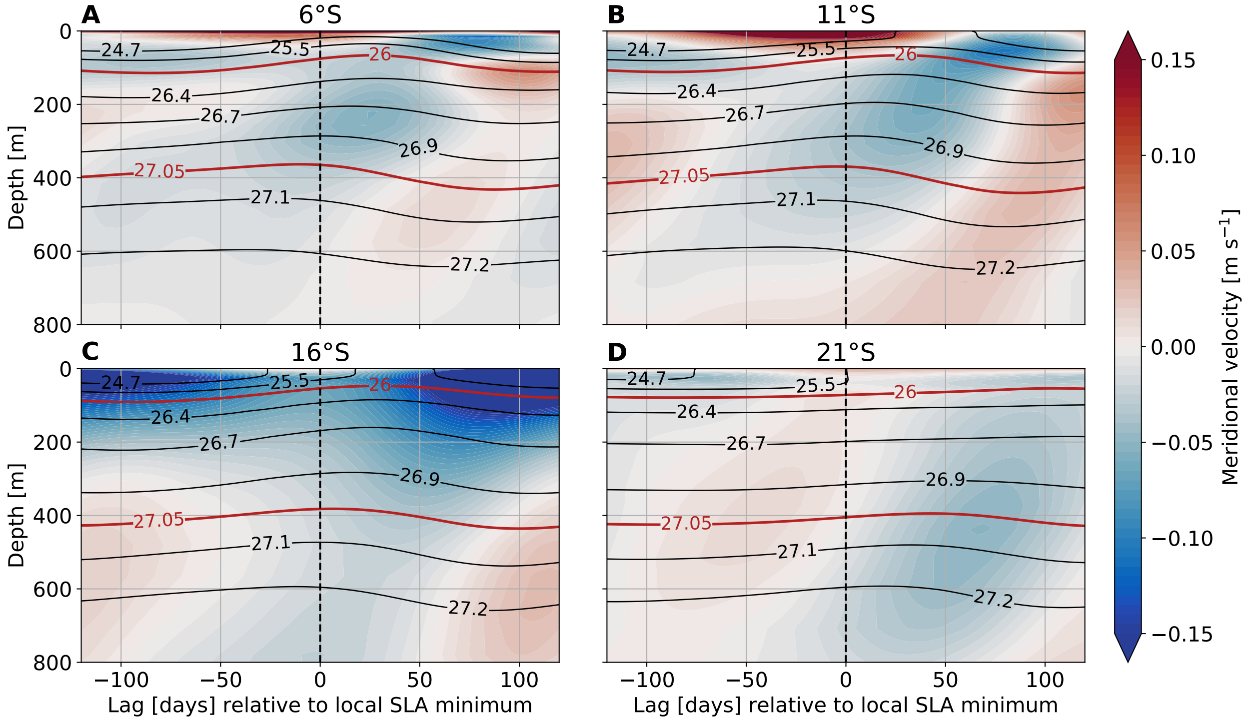

Figure 3.8: *Meridional velocity and potential density in a regional ocean model. Meridional velocity (colors) and potential density (lines) from the CROCO simulation. Fields are derived at the 800 m isobath for different latitudes as indicated in the titles of **A** – **D**. The fields are averaged as a function of the lag [days] to the local annual minimum in SLA and are a composite of 58 upwelling seasons. The mean flow is not subtracted; strongest near-surface southward flow is found at 16°S, consistent with the observed latitudinal variation in the strength of the Angola Current (Tchipalanga et al., 2018a).*

strongly reduced (Fig. 3.8 D). Note that the time-lag between low and high-mode CTW signals is of comparable length between 6°S and 16°S. Ultimately, this suggests that the low and high-mode CTWs are not waves propagating independently along the African continent as then the lag between the waves would increase southward along the coastal waveguide. Instead, these results suggest that high-mode CTWs are constantly generated with the arrival of low-mode CTWs. This mechanism is also supported by the strong correlation between SLA and NPP, suggesting a strong coupling between low and high-mode CTWs. The high-mode CTWs can be assumed to not propagate over long distances as they are likely to be highly dissipative (Illig et al., 2018b). Open questions remain regarding the origin and energetics of the high-mode CTWs displacing the nitracline and their coupling to the low-mode CTWs. How does energy transfer between low and high-mode CTWs work? One mechanism that could play a vital role in the forcing of high-mode CTWs is frictional effects. Romea and Allen (1984) investigates the effect of the bottom Ekman layer on CTWs under different slope conditions. They show that for slopes where the Rossby radius is large compared to the slope width, which is the case in the tAUS, the CTWs are strongly affected by the bottom stress and that the modal structures are altered. They further show that an onshore flow is induced. Thus, this mechanism could potentially explain the forcing of the high-mode CTWs as well as the onshore transport of nitrate-rich waters in the tAUS.

Results of this study show that there is a delay between the minimum in SLA and the rise of the nitracline of the order of $25\,days$, and that NPP peaks about $40\,days$ after the minimum in SLA. Consequently, this suggests that NPP peaks about $15\,days$ after the nitracline rise. Previous studies showed that the response of biological activity to nutrient supply is faster (Collos, 1986; Ferreira et al., 2020). In the tAUS the timing between the nitracline uplift and the peak in NPP is likely to be influenced by timescales of vertical mixing and horizontal exchange. The initial upwelling of the nitracline leads to an immediate increase in NPP (Fig. 3.4). Additionally, we find an enhanced turbulent nitrate flux into the surface ocean in the shallow waters of the tAUS. The nitrate-rich water is likely to be redistributed by small-scale horizontal advection as discussed in Körner et al. (2023a), leading to an increase in NPP further offshore as well. These processes could explain the delay between the uplift of the nitracline and the peak in NPP. However, further work must be done to understand the interplay between these processes. Note that the time-lag is of the same order of magnitude as the lag between nitracline upwelling by intraseasonal CTWs and phytoplankton blooms in the Peruvian upwelling system, as found in a modeling study (Echevin et al., 2014)).

The lag between the SLA signal and the NPP signal, together with the remote equatorial forcing of CTWs, provides a potential for predicting the strength of the austral winter NPP peak. A similar prediction system for SST was suggested for the interannual Benguela Niño and Niña events, which seasonally peak in austral fall (Imbol Koungue et al., 2017). To exploit the full potential of this mechanism, the cause of the interannual variability of the CTW signal in austral winter needs to be analyzed. Here, both local and remote mechanisms (interannual variability of equatorial winds) need to be considered.

This study focuses on the main productivity season in austral winter. However, a secondary peak in NPP is visible in January to February, which is weaker and restricted to the northern part of the tAUS (Fig. 3.1 B). Interannual variability of this secondary NPP peak is particularly elevated and the mean value is mostly controlled by strongly enhanced NPP in early 2016 (not shown). Further research has to be conducted to understand the dynamics and variability of the secondary peak of NPP in January to February.

The research presented here suggests that primary production in the tAUS is mainly controlled by CTWs. However, other mechanisms are able to modulate NPP as well. In austral winter, the wind driven upwelling transport is at its seasonal minimum (Fig. 3.1 C). The relaxation of alongshore winds lead to a reduced offshore Ekman transport. This can prolong the time upwelled nitrate-rich water spends near the surface before being subducted (Thomsen et al., 2021). This mechanism could further contribute to the enhancement to the nitrate concentration in the nearshore surface ocean. Note again that the mixed layer depth is deepest during the main upwelling season (Körner et al., 2023a). Thus, an effect of light limitation on the plankton growth due to changes in mixed layer depth as suggested for the Peruvian upwelling system (Xue et al., 2022) cannot explain the seasonality in net primary production in the tAUS.

This study suggests that CTWs play a crucial role in driving variability in productivity in the tAUS. Understanding how this mechanism behaves under a warming climate is of great socio-economic importance. Model projections indicate a future weakening of tropical upwelling in the Benguela and Canary upwelling regions, located equatorward of 20°, due to reduced alongshore winds (Wang et al., 2015; Sylla et al., 2019). However, as shown here, alongshore winds cannot explain either the seasonal upwelling in the tAUS nor its variability. It is therefore necessary to consider other factors in this context. Of particular interest is the possible change in the equatorial trade winds that triggers the remotely-forced CTWs.

This study focuses on explaining seasonal productivity in the tAUS. It is of high interest to determine whether similar mechanisms can be observed in other tropical upwelling systems, particularly in the Pacific and the Gulf of Guinea, where semi-annual variability associated with CTWs has been observed (Pizarro et al., 2002; Gómez-Valdivia et al., 2017; Brandt et al., 2023). Thus, this work may ignite further research aimed at identifying the role of CTWs and highlighting the importance of CTW modal contributions in other tropical upwelling systems. This, in turn, could ultimately lead to improved seasonal predictions of biological productivity in these highly relevant coastal systems.

3.5 Materials and Methods

3.5.1 Hydrographic, oxygen and nitrate data

In this study, we make use of extensive datasets of hydrographic, oxygen and nitrate data that has been collected in the tAUS (Fig. 3.9 and Table S1). Between 1995 and 2015, the EAF Nansen Programme of the Food and Agriculture Organization (FAO) of the United Nations conducted research cruises onboard of the R/V Dr. Fridtjof Nansen approximately twice a year (Tchipalanga et al., 2018a). In most years, the cruises were conducted once during the austral summer (February-April) and once during the austral winter (June–September). During these cruises conductivity-temperature-depth (CTD) and oxygen profiles were measured. In total more than 8000 CTD and oxygen profiles taken in Angolan waters were used. CTD measurements were mostly conducted in shallow waters and near the shelf break. For this study we use the data collected between 10°S and 11°S (Fig. 3.9).

In addition to the dataset from the Nansen program dataset, we use data from seven research cruises on board of *R/V Meteor* that were conducted in Angolan waters between 2013 and 2022. An overview table of the cruises and the data collected during the cruises used for this study can be found in the Supplements (Table S1). During all of these seven cruises, CTD and oxygen profiles were measured. Along with the CTD profiles, discrete water samples were taken for laboratory measurements of nitrate concentration. For the cruises from 2015 onward, continuous nitrate measurements were conducted along with the CTD/oxygen profiles.

3.5.2 Satellite data

Altimetric SLA data are used to analyze the surface signal from CTWs from 1993 – 2021. The SLA data used in this study are from Copernicus DUACS (https://doi.org/10.48670/moi-00148). The daily SLA fields are available with a horizontal resolution of $0.25° \times 0.25°$. Before conducting the analyzes, we removed the mean SLA and detrended the data.

We also use NPP data from Oregon State University to analyze biological activity in the tAUS (http://sites.science.oregonstate.edu/ocean.productivity/index.php). NPP is based on the Eppley Vertically

Generalized Production Model. It is based on chlorophyll concentration, SST, and photosynthetically available radiation from MODIS. The NPP fields are gap-free and have a horizontal resolution of 1/6°. We use the data between 2002 and 2021.

We calculate the integrated wind-driven upwelling using wind speed data from the Cross-Calibrated Multi-Platform (CCMP) product (https://www.remss.com). The six hourly data is available with a horizontal resolution of $0.25° \times 0.25°$ between 1993 – 2019. We subsample the data to daily data before calculating the integrated wind-driven upwelling.

The seasonal cycle of SST shown in Fig. 3.1 is from the Copernicus OSTIA product (Good et al., 2020) (https://doi.org/10.48670/moi-00168). The daily temperature fields are available with a horizontal resolution of $0.05° \times 0.05°$. We use the data from 1993 - 2021.

3.5.3 Mooring data

The CTW signal is analyzed in moored velocity data. The mooring is located at 13°00'E; 10°50'S (77 km offshore) at a water depth of about $1200\,m$ (Fig. S1). On the mooring, an upward-looking acoustic Doppler current profiler (ADCP) was installed at 500 m depth to measure the velocity up to $45\,m$ below the sea surface. In this study we use data collected between July 2013 and April 2022. For more details on the mooring data see Kopte et al. (2017); Imbol Koungue et al. (2021).

3.5.4 Calcualting nitrate concentration from oxygen

To understand primary productivity, the distribution of nitrate is of interest. In the tAUS, available nitrate data are restricted to data collected during R/V Meteor cruises. In contrast, oxygen data were collected during all CTD stations of *R/V Dr. Fridtjof Nansen* as well. For central water masses, Redfield (1934) showed that there is a tight relationship between nitrate concentration and oxygen consumption. For the tAUS, we use nitrate data measured from the discrete water samples of CTD profiles and dissolved oxygen concentrations to derive a similar relationship. The apparent oxygen utilization (AOU) is calculated as the difference between the oxygen saturation expected at equilibrium with air for a given temperature and salinity and the measured in-situ dissolved oxygen concentration. Oxygen saturation is determined using the Gibbs SeaWater Oceanographic Toolbox (McDougall and Barker, 2011). We use data collected between 8°S and 15°S between 10°E and the African coast in water shallower than $400\,m$. From these data points we calculate the relationship using linear regression. The results show the measured data points along with the linear fit, revealing a good correlation between the two variables (Fig. 3.10).

To evaluate the uncertainties of our approach, we compare nitrate concentrations measured by an optical nitrate sensor (SUNA) collected during a subset of the cruises (*R/V Meteor* cruises M131, M148, and M181) to the nitrate values derived from oxygen data. On average, the nitrate concentrations inferred from the oxygen data are $1.8\,\mu mol\,m^{-3}$ higher than those measured from the SUNA sensor. The root-mean-square differences between the two data sets in the upper $400\,m$ after removing the mean bias is

$2.4\,\mu mol\,m^{-3}$. Considering the accuracy of the SUNA measurements of about $0.65\,\mu mol\,m^{-3}$ Sakamoto et al. (2009) suggests that nitrate concentrations derived by using AOU here have small uncertainties.

3.5.5 Calculating mean sections from observations

In this study, we use CTD and nitrate profiles inferred from oxygen data to calculate mean cross-shelf sections of nitrate and density with data collected between 10°S and 12°S. The basis for the cross-shelf sections is the mean topography which we calculate based on the GEBCO topography (http://www.gebco.net). To compute the mean topography, we extract the topography along a line perpendicular to the coast for each latitude grid point of the GEBCO dataset between 10°S and 12°S. The orientation of the coast is calculated by considering the coastline 0.5° around the respective latitude. The topography is then averaged over the latitude. We now divide the mean topography into discrete bins with respect to the water depth and group the observed profiles into these bins. Since there is much more data available on the shelf than further offshore, the bin size increases with distance to the coast. Within $50\,km$ off the coast, the bin size is $5\,km$, and further offshore it is $15\,km$. After averaging the profiles grouped in each bin, we interpolate the data on a regular distance grid and smooth the section by applying a running mean (window size is $7\,km$).

3.5.6 Turbulent nitrate fluxes

We use ocean turbulence data to estimate turbulent nitrate fluxes in the tAUS (Fig. 3.9). Turbulence was measured using a loosely-tethered free-falling microstructure profiler manufactured by Sea& Sun Technology. The profiler was equipped with two to three airfoil shear sensors, an acceleration sensor, tilt sensors, a fast temperature sensor, and standard conductivity–temperature–depth (CTD) sensors. We estimate dissipation rates of turbulent kinetic energy (TKE),ϵ, from the data from the airfoil shear sensors (for detailed description see Hummels et al. (2014); Körner et al. (2023a)). For that we integrate the shear wave number spectrum of overlapping 2 seconds intervals while assuming isotropy. Loss of shear variance due to the limited resolution in wavenumber space was accounted for by fitting the spectra to the universal Nasmyth spectrum (Wolk et al., 2002) prior to integration.

To calculate the turbulent nitrate flux into the mixed layer we map the profiles as a function of depth below the mixed layer. We discard all measurements within the mixed layer and $2\,m$ from the mixed layer as the mixing efficiency is not well-defined in low stratified waters (Gregg et al., 2018). Additionally, we discarded all measurements in the upper $10\,m$ to exclude ship induced turbulence. To derive turbulent quantities, we bin the microstructure data in $5\,m$ depth bins with respect to the mixed layer depth. The mixed layer depth is defined as the depth at which the density deviates by $0.125\,kg\,m^{-3}$ from the surface value. The turbulent eddy diffusivity ($K_\rho = \Gamma\,\langle\epsilon\rangle\,N^{-2}$) is calculated by considering the stratification, defined by the squared Brunt-Väisäla frequency, N^2, within the same depth bins. The mixing efficiency Γ is set to 0.2 (Gregg et al., 2018). The vertical nitrate flux is then calculated as $F_{C_{NO_3}} = K_\rho\,\partial C_{NO_3}/\partial z$.

The turbulence data used in this study were collected during six research cruises aboard the R/V Meteor (see Supplements). These cruises were conducted at different times of the year, not primarily during the main upwelling and downwelling seasons. The primary energy source of vertical mixing in the tAUS is thought to be dissipation of internal tidal energy where energy available for mixing on the shelf is nearly constant throughout the year (Zeng et al., 2021). This is supported by observations as seasonal differences in the turbulence levels from the available data in the tAUS were not identified (Körner et al., 2023a). Therefore, we combine the ocean turbulence data collected during the six cruises on board of *R/V Meteor* with the seasonal gradients of nitrate from all available biogeochemical data. The 701 microstructure profiles provide an estimate of the mean distribution of mixing on the Angolan shelf at 11°S. Since the mean distribution of TKE dissipation rates shows a dependence on bathymetry (Fig. 5) (Körner et al., 2023a), we determine mean eddy diffusivities and turbulent nitrate fluxes as a function of bathymetry (following the approach of Körner et al. (2023a)). To do this, we divide the data into three depth regions: shallow waters (water depths $< 75\,m$), the shelf break area (water depths between $75\,m$ and $175\ m$), and deep waters (water depths $> 175\,m$). With mean vertical nitrate gradients calculated for the main downwelling and upwelling seasons, we are able to provide an estimate of the seasonally varying turbulent nitrate flux into the ocean mixed layer.

The uncertainties of the turbulent nitrate fluxes are described in terms of the 95% confidence limits ($CL95$) (following Hummels et al. (2014); Körner et al. (2023a)). $CL95$ for the turbulent dissipation rates of TKE are calculated via bootstrapping. $CL95$ for the Brunt-Väisäla frequency (N^2) and the vertical nitrate gradient ($\partial C_{NO_3}/\partial z$) are calculated by calculating the standard error (SE) and converting the SE to $CL95$ via $CL95 = \overline{x} \pm 1.96SE$. The uncertainties of the eddy diffusivity (K_ρ) and the turbulent nitrate flux ($F_{C_{NO_3}}$) is given via standard error propagation where the uncertainty of the mixing efficiency (Γ) is set to 0.004 (following (Laurent and Schmitt, 1999)).

3.5.7 Theoretical coastal trapped wave modes

CTWs are associated with specific spatial structures of the horizontal and vertical velocity components and density fields that can be described as a sum of modes (Brink, 1982; Clarke, 1977). Spatial structures, phase and group velocities of the respective CTW modes depend on stratification, cross-shore topography, latitude, and mean flow (Brink, 1982). Theoretical spatial structures for different CTW modes can be derived by considering a linear, inviscid, hydrostatic, free-surface ocean, for frequencies less than the inertial frequency, horizontally uniform stratification, and an alongshore non-varying bottom topography (Brink, 1982). To derive the CTW modal structures for the tAUS, we use the toolbox developed by Brink and Chapman with the mean flow set to zero (Brink and Chapman, 1987). We derive the spatial structures and phase speeds of CTW modes at 11°S within a distance of $400\,km$ from the coast using the mean cross shore topography (GEBCO) averaged between 10°S and 12°S. The mean stratification profile is calculated from hydrographic data used in this study (Fig. 3.11).

3.5.8 Regional Ocean model Configuration

The velocity field and the movement of the potential density surfaces relative to the SLA minimum are analyzed in a regional ocean model. We use the Coastal and Regional Ocean COmmunity (CROCO) model. The model configuration has previously been used to study the dynamics in the eastern-equatorial sector and along the coast of southwest Africa. Comparisons with observations as well as a detailed description of the model setup can be found in Illig et al. (2020), where the configuration used here is named CROCOLONG. The model spans the tropical Atlantic (30°S-10°N, 62.25°W-17.25°E) with a horizontal resolution of 1/12° and 37 terrain-following vertical levels. Model momentum, heat, and freshwater forcings are derived using bulk formulae based on daily surface fields from the DRAKKAR Forcing Set (DFS) v5.2 (Dussin et al., 2016). River runoff is not included in the simulation, instead the sea surface salinity is restored to CARS2009 climatological sea surface salinity Dunn (2009). After a 5-year spin-up, the model is run for 58 years (1958-2015), during which 3-day averages of the model output are stored.

3.5.9 Integrated wind-driven upwelling

To show the influence of the wind-driven upwelling on the tAUS variability, we calculate the seasonal cycle of the integrated wind-driven upwelling following Bordbar et al. (2021). It represents the sum of the coastal upwelling due to the coastal divergence of the Ekman transport driven by the meridional (along-shore) wind stress and the wind-stress-curl-driven upwelling within the coastal box. To do so, we first derive the wind stress from the $10\,m$ wind speed (u) using the bulk formula: $\tau = \rho_a\, c_d\, |u| u$, using a reference density $\rho_a = 1.22 kgm^{-3}$ and a drag coefficient $c_d = 0.0013$. The integrated wind-driven upwelling is then calculated via $W = -\tau^y_{x=-L}/\rho f$, with $\tau^y_{x=-L}$ being the meridional wind stress at one degree distance from the coast (extent of the coastal box),$\rho = 1025\, kg\, m^{-3}$ a reference density, and f the Coriolis parameter.

3.5.10 Different time periods of observation

In this study, many different observational datasets are used. These datasets cover different time periods which can introduce uncertainties. For most part of the study, we combine data from the same period to draw the respective conclusions. One exception is the relationship between the low-mode CTWs observable in SLA, the isopycnal displacement calculated from hydrographic data and NPP (Fig 3.12). A sensitivity test revealed that the results are similar even when cutting the data to the same time period (not shown). Note also that we remove the linear trend from all satellite observations before conducting our analyses to remove long-term changes.

Acknowledgments

We thank the captains, crews, scientists, and technicians involved in several research cruises in the tropical Atlantic who contributed to collecting data used in this study.

Funding

The study was funded by EU H2020 under grant agreements 817578 (TRIATLAS project). It was further supported by the German Federal Ministry of Education and Research as part of the SACUS (03G0837A), SACUS II (03F0751A), and BANINO (03F0795A) projects and by the German Science Foundation through several research cruises with *R/V Meteor*. Marie-Lou Bachèlery has received funding from the European Union's Horizon 2020 Research and Innovation Program for the project BENGUP under the Marie Skłodowska-Curie grant agreement ID 101025655. Ajit Subramaniam was supported by NASA grant 80NSSC21K0439, funding from the G. Unger Vetlesen Foundation and a fellowship from Columbia University's Center for Climate and Life. Model computations were performed on CALMIP computer at University Paul Sabatier (Toulouse, France, CALMIP, project 19002).

Authors contribution

Conceptualization: MK, PB, MD
Data Curation: MK, MD, GK, SI
Formal Analysis: MK
Methodology: MK, PB, SI, MD
Visualization: MK
Supervision: PB, MD
Writing—original draft: MK
Writing—review & editing: MK, PB, SI, MD, AS, MLB, GK

Competing interests

The authors declare no competing interests.

Data and materials availability

The sea level anomaly data used in this study can be accessed via the Copernicus Server (https://doi.org/10.48670/moi-00148). The net primary production dataset is available online at http://orca.science.oregonstate.edu/1080.by.2160.8day.hdf.eppley.m.chl.m.sst.php. CCMP Version-3.0 vector wind analyses are produced by Remote Sensing Systems. Data are available at www.remss.com. The OSTIA sea surface temperature dataset can be accessed via the Copernicus Server (https://doi.org/10.48670/moi-00168). The hydrographic and biogeochemical data collected on board of *R/V Dr. Fridtjof Nansen* used in this study are available at https://doi.org/10.1594/PANGAEA.886492. The hydrographic, oxygen and nitrate data collected on board of R/V Meteor used in this study are available https://doi.org/10.5281/zenodo.10062790. The microstructure data is available at https://doi.pangaea.de/10.1594/PANGAEA.953869.

The mooring data is available at https://doi.org/10.5281/zenodo.10062790. The model output is available at https://doi.org/10.5281/zenodo.10062790. All necessary code for the data analysis and the preparation of the figures are available at https://doi.org/10.5281/zenodo.10062790.

3.6 Supplementary Materials

Overview of observation

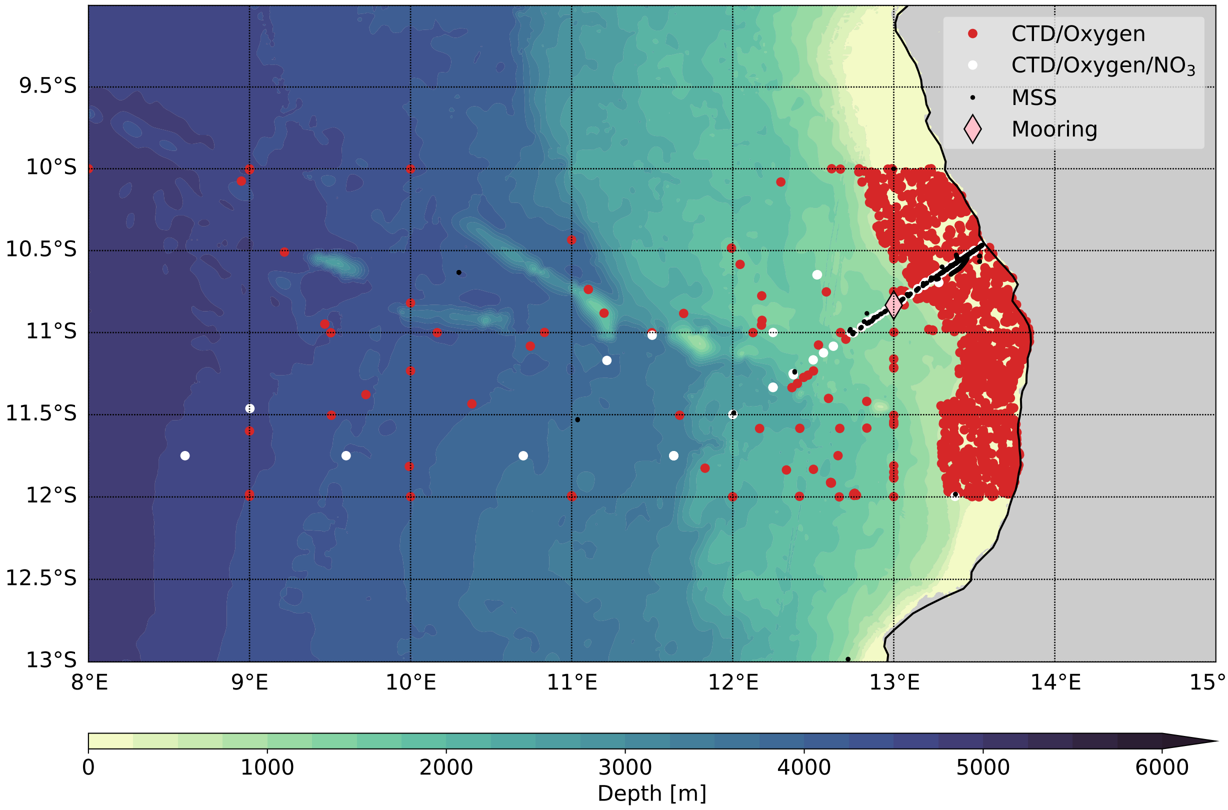

Figure 3.9: *Overview of observational data used in this study. Red points display conductivity-temperature-depth (CTD) and oxygen profiles. White points show CTD profiles where oxygen and nitrate were measured as well. Black points show the location of microstructure measurements. The pink diamond indicates the mooring position.*

Cruise	Time	CTD/Oxygen Profiles	Discrete NO_3 samples	Microstructure profiles
M89	June 2013	21	0	212
M120	Oct/Nov 2015	23	83	62
M121	Nov/Dec 2015	11	36	0
M131	Oct/Nov 2016	19	11	44
M148	July 2018	29	192	135
M158	Sep 2019	21	156	41
M181	Apr 2022	20	45	207

Table 3.1: *Overview of observational data collected during R/V Meteor cruises used in this study. The number of CTD/Oxygen profiles refers to the number of profiles taken between 8°S and 15°S east of 11°E. The number of discrete NO_3 samples refers to the number of samples used for the fit between NO3 and AOU (samples taken between 8°S and 15°S east of 11°E in the upper $400\,m$). The number of microstructure profiles refers to the number of profiles taken between 8°S and 15°S, east of 11°E.*

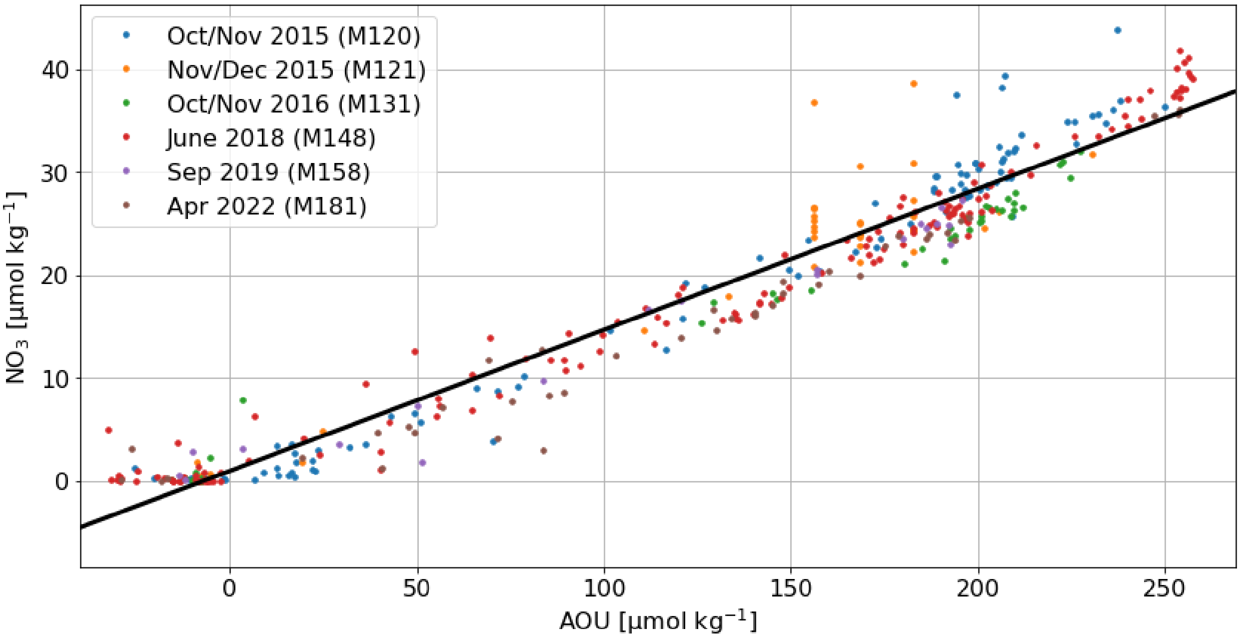

Figure 3.10: *Relationship between Apparent Oxygen Utilization (AOU) and Nitrate (NO_3). Dots show the bottle data of CTD casts taken in the upper $400\,m$. CTD casts were taken during different cruises (colors, see legend). The black line shows the linear fit of the sample data.*

Theoretically derived CTW modes

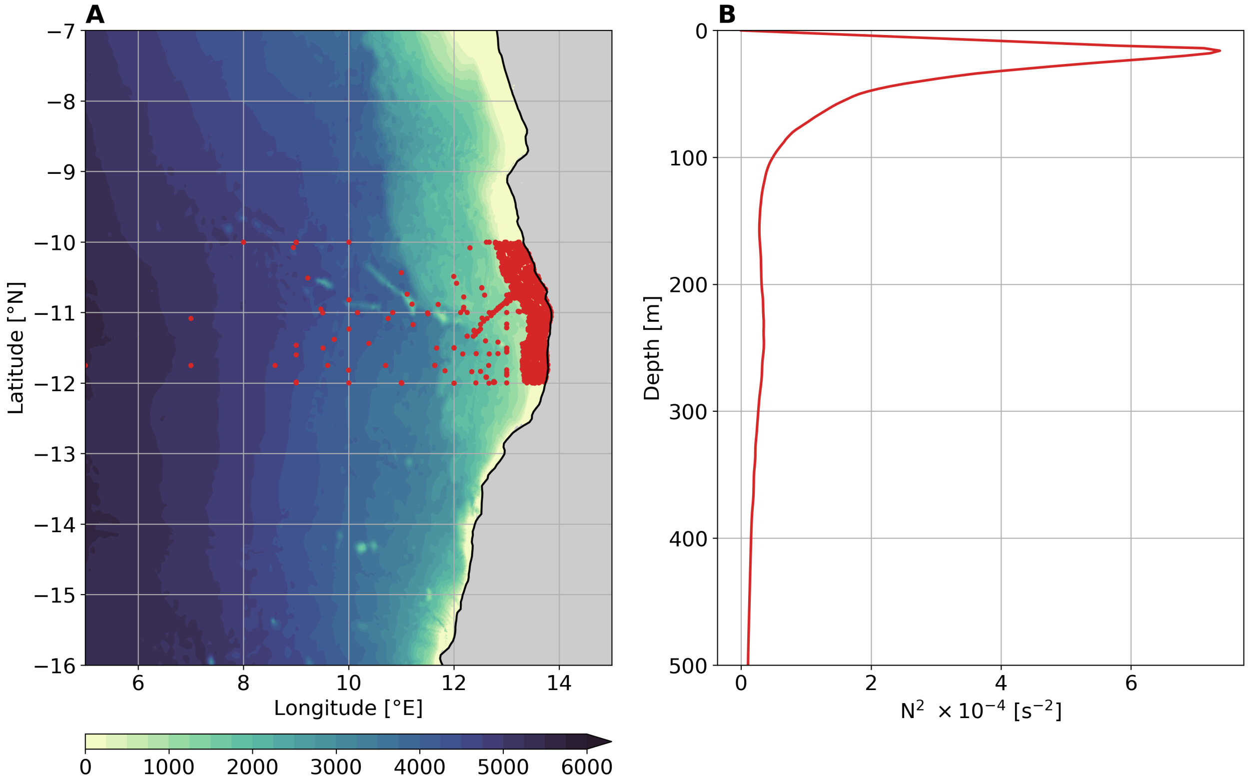

Figure 3.11: *Stratification used to calculate CTW modes. (a) shows the positions of the used CTD profiles (red dots) and the bathymetry (shading). (b) shows the mean profile of the squared Brunt-Väisäla frequency in the upper* $500\,m$.

CTW signal in moored velocity observation

We utilize moored velocity data to analyze the signal from CTWs on the Angolan shelf. The mooring is located at 10°50'S; 13°00'E at a water depth of approximately $1200\,m$ (Fig. 3.9). The mooring measures velocity in the upper $500\,m$ up to 45 m below the sea surface. We use geostrophic velocities from satellite observations to obtain information about the surface currents.

We analyze the alongshore velocities. Note that the mooring location is not ideal for separating the contribution of different CTW modes, as the velocity variability of the different modes is generally weak at this location (3.15).

To extract the signal of the seasonal CTWs in the moored velocity data, we first filter out the variability on intraseasonal time scales. We do this by applying a low-pass filter to the mooring time series with a cut-off period of $135\,days$ (3.16). We also subtract the mean velocity at each depth respectively to remove the influence of the Angola Current. We then average the velocity data with respect to the annual minimum in SLA (Fig. 3.17). The derived mean alongshore velocity component reveals a signal indicative of a high-mode upwelling CTW that arrives about $25\,days$ after the SLA minimum. In addition, the velocity field shows upward propagating wave phases after the arrival of the SLA minimum, indicating downward energy propagation.

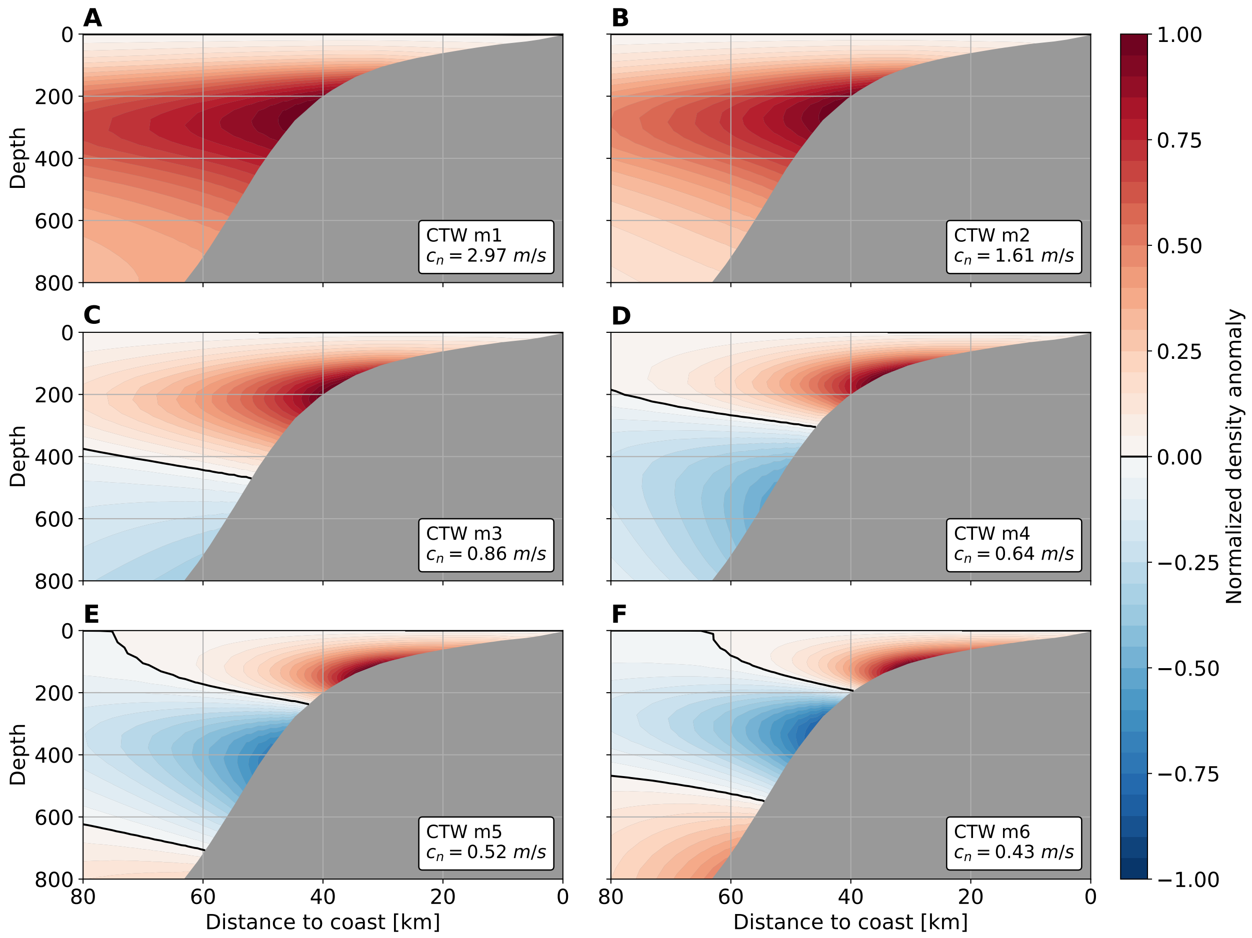

Figure 3.12: *Cross-shelf – depth structure of density anomaly of the first six theoretical CTW modes at 11°S based on stratification and cross-shelf topography. The black line marks the zero line. The distributions are normalized to the maximum density anomaly of each mode. The associated phase speed of each mode is given in the lower right corner.*

Note that Fig. 3.17 shows a mismatch between the geostrophic surface velocities and the moored velocities prior to the annual minimum in SLA. This mismatch could arise from low effective horizontal resolution of the gridded altimetric SLA data (i.e., 100-$200\,km$ effective spatial resolution).

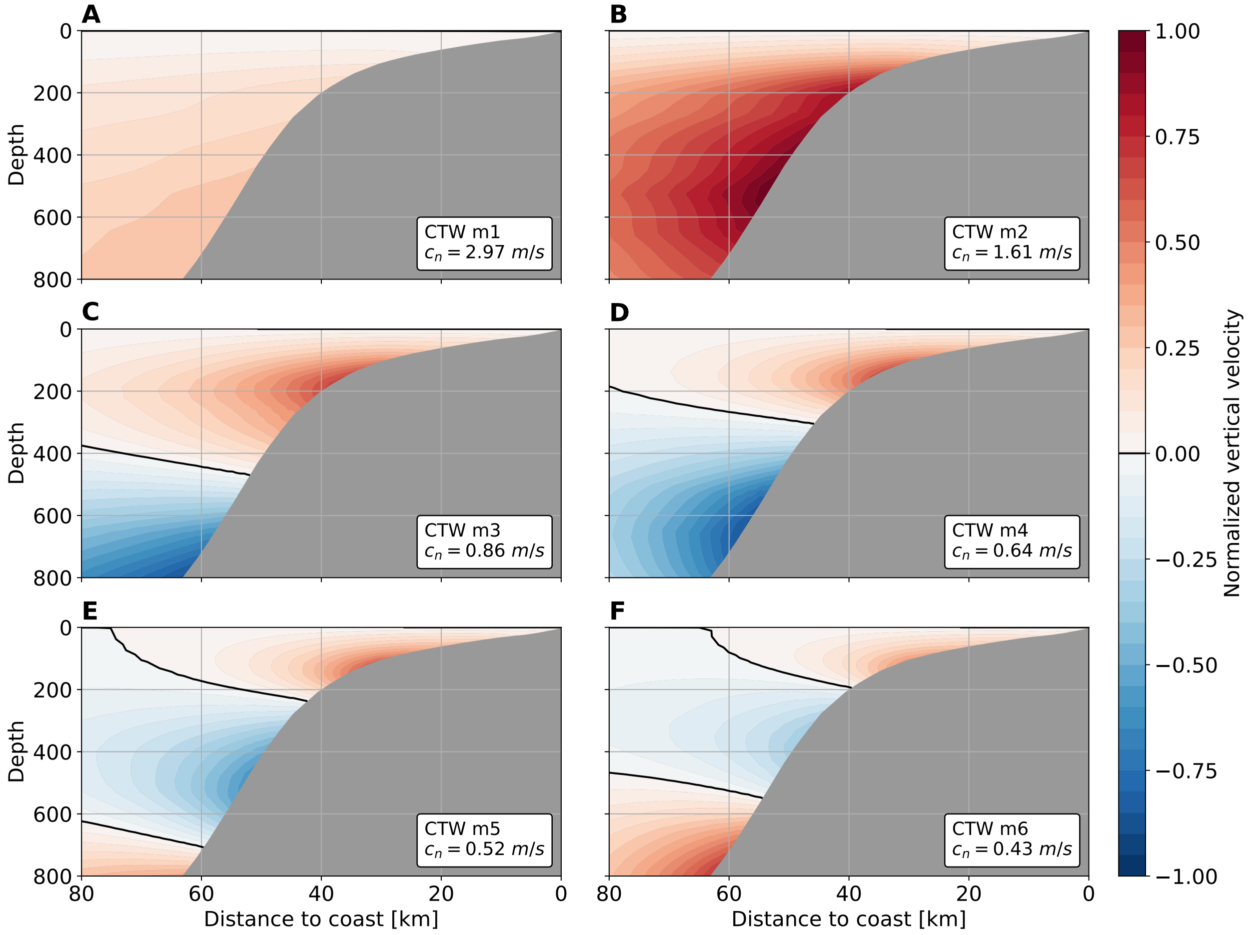

Figure 3.13: *Cross-shelf – depth structure of velocity structure functions of the first six theoretical CTW modes at 11°S based on stratification and cross-shelf topography. The black line marks the zero line. The fields are normalized to the maximum velocity of each mode. The associated phase speed of each mode is given in the lower right corner.*

Zonal velocity associated with the passage of CTWs in a regional ocean model

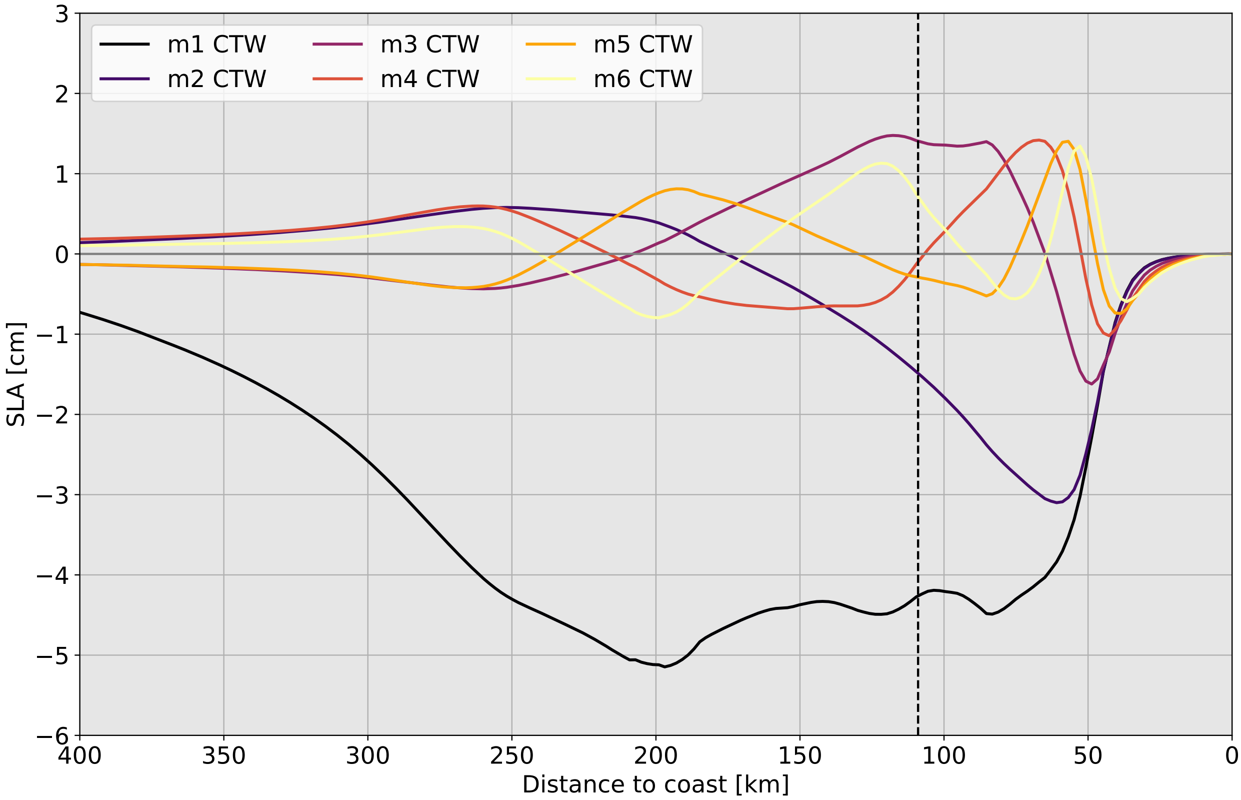

Figure 3.14: *SLA signal of the first six CTW modes as a function of the distance to the coast. The SLA is calculated by vertically integrating the normalized density structures and by multiplying by a typical density variation divided by the mean density* ($\delta\rho/\rho_0 = 1 \times 10^{-4}$)*. The dashed vertical line marks the distance of 1° in longitude.*

Lead lag correlation between SLA and NPP

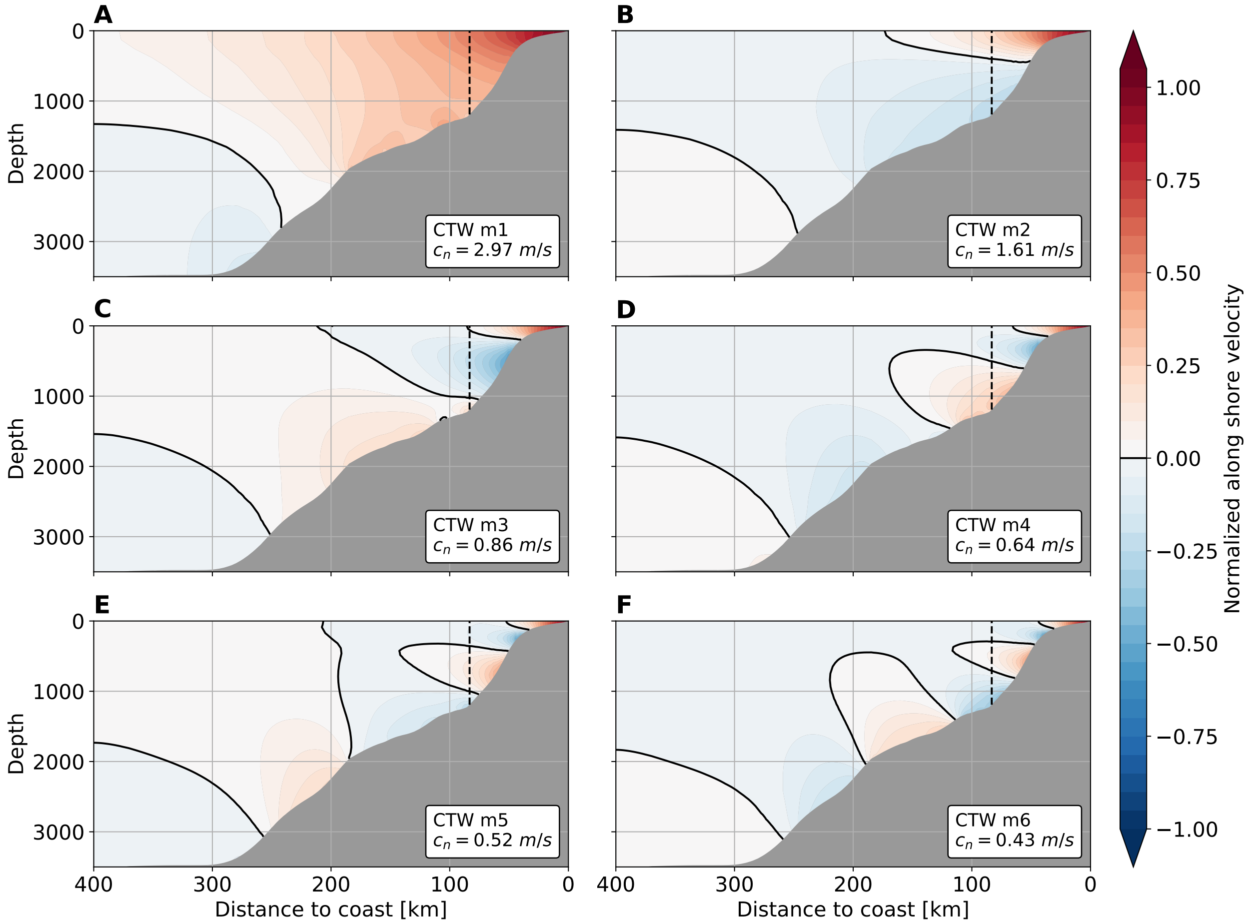

Figure 3.15: *Alongshore velocity structure functions of the first six theoretical CTW modes at 11°S. The fields are normalized to the maximum velocity of each mode. The structures correspond to upwelling CTWs. The associated phase speed of each mode is given in the lower right corner. The black line marks the zero line of the alongshore velocity. Black dashed lines give the position of the mooring.*

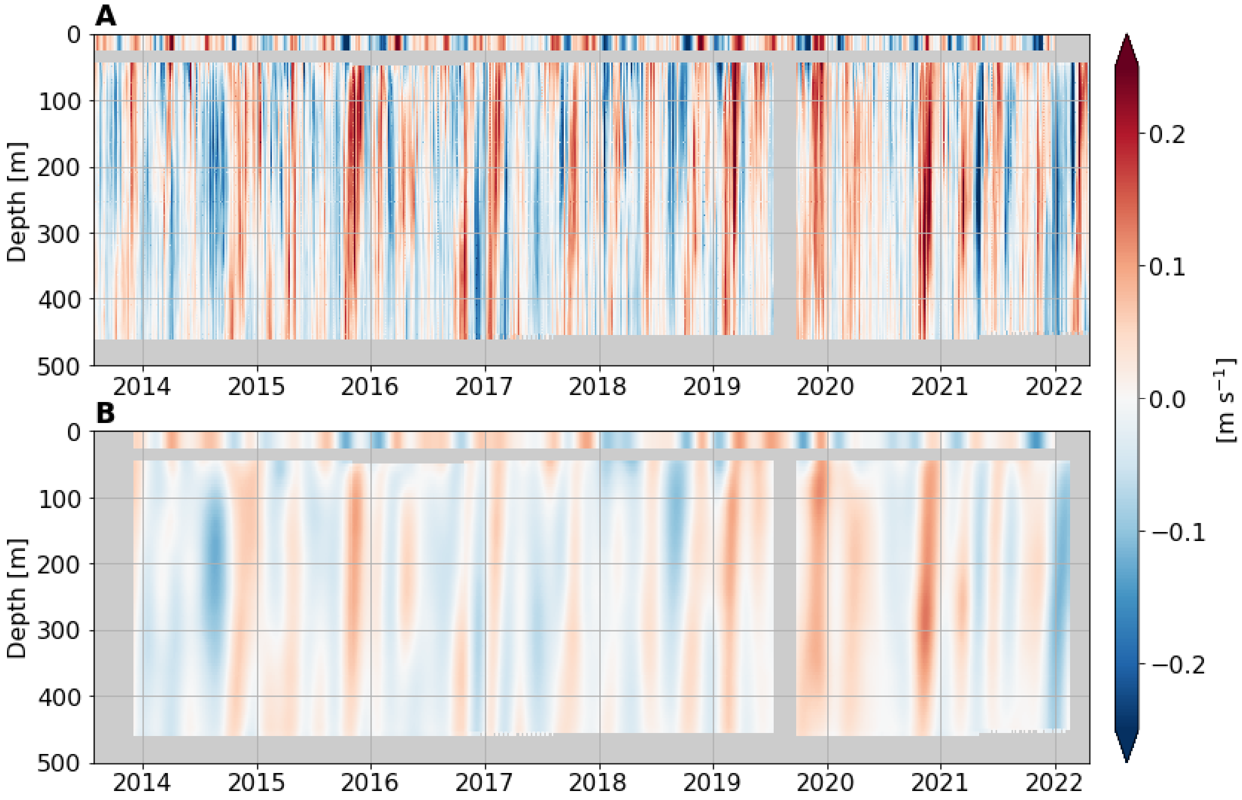

Figure 3.16: *(a) Observed alongshore velocity (rotated by -34°) of a mooring installed at* $13°00'E$; $10°50'S$ *(1200 m depth). Positive values represent northward flow and negative velocities southward flow. (b) shows the same as (a), but intraseasonal variability is removed by applying a low-pass filter (cutoff period = 130 days). At the surface, the corresponding geostrophic alongshore velocities from SLA are plotted. The mean velocity profile has been subtracted. The geostrophic velocities are taken from the SLA DUCAS satellite data product (https://doi.org/10.48670/moi-00148).*

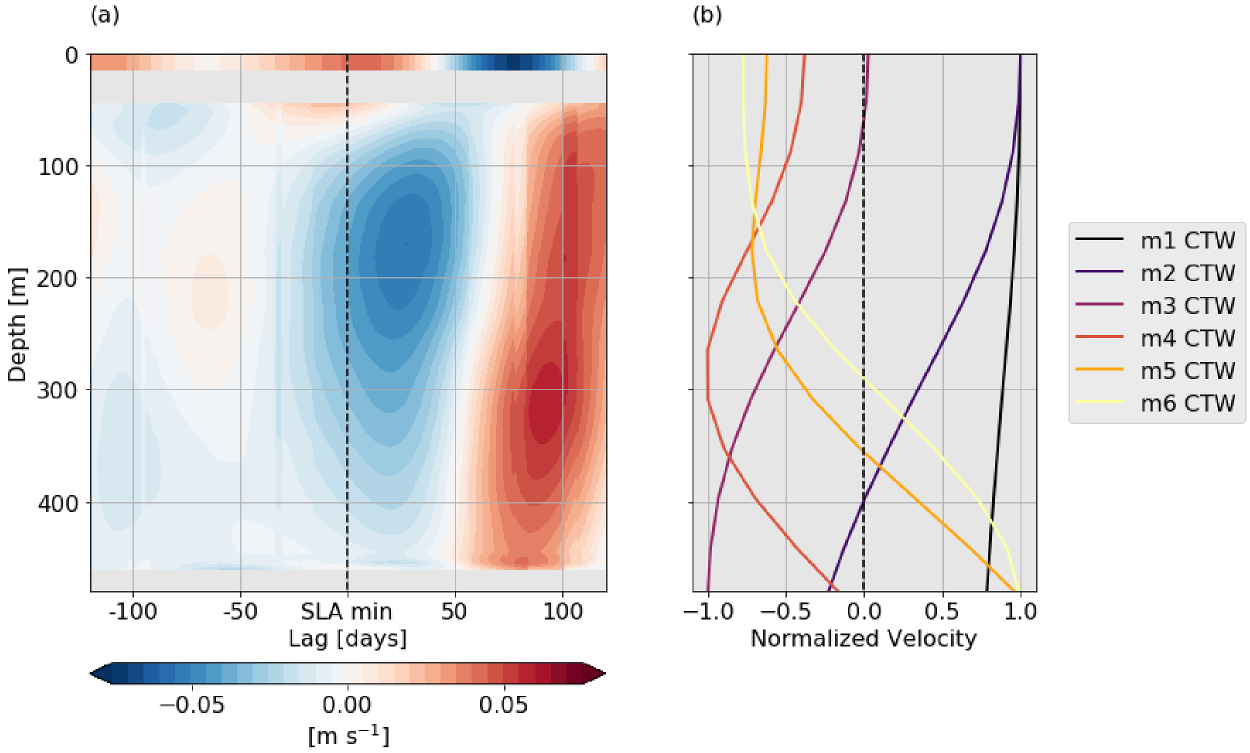

Figure 3.17: *(a) Mean alongshore velocities averaged with respect to the annual SLA minimum. The mean velocity profile has been subtracted. (b) Vertical structures of alongshore velocity of the first six CTW modes at the mooring locations (see Fig. 3.14). The velocity structures are normalized with respect to the maximum in the profiles shown here.*

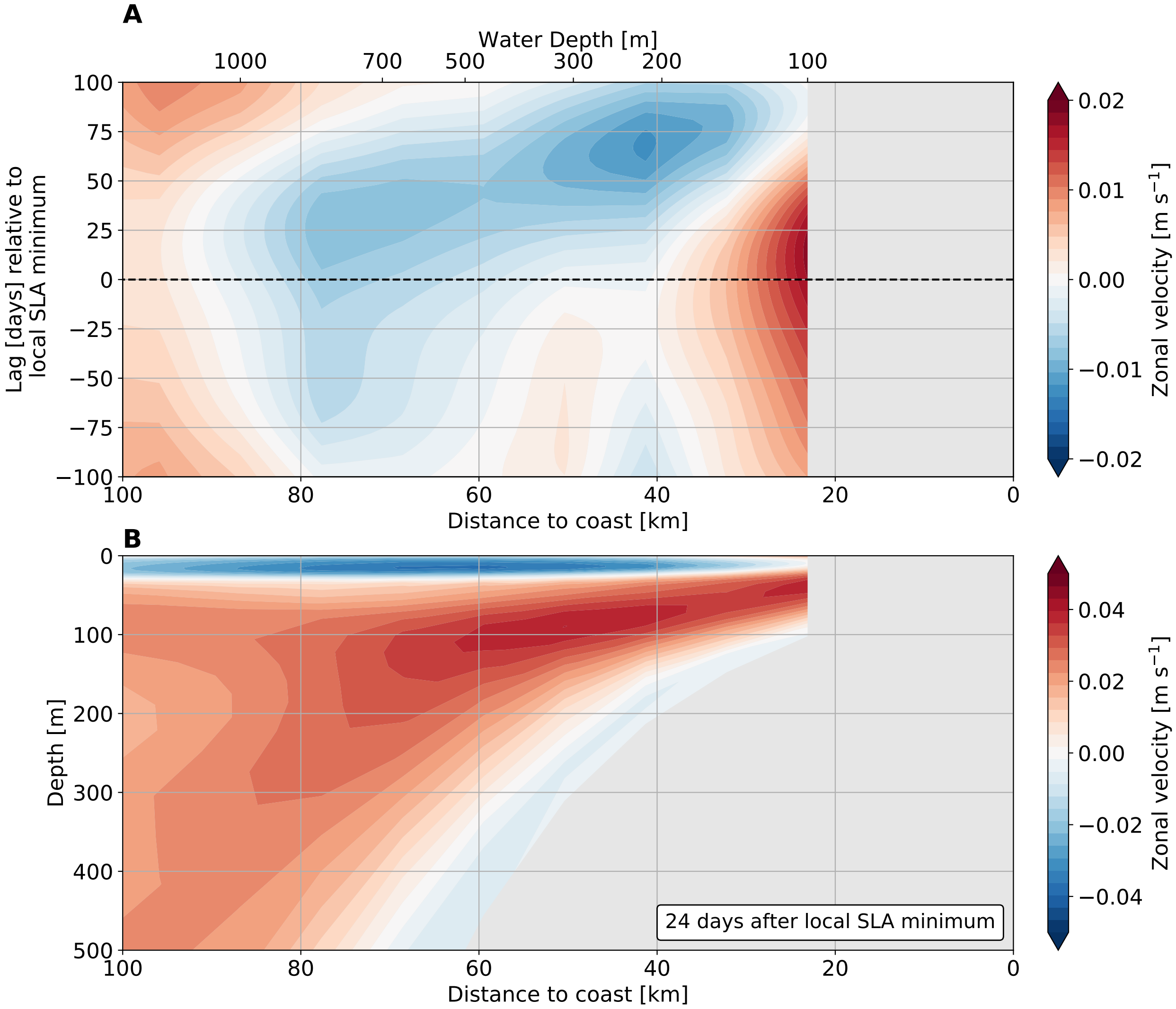

Figure 3.18: *Zonal velocity at 11°S in a regional ocean model. (a) Zonal velocity from the CROCO simulation averaged within 10 – 50 m above the topography as a function of distance to the coast and lag [days] relative to the local SLA minimum. (b) Cross-shelf section of CROCO zonal velocity 24 days after the local SLA minimum. Fields presented here are composite of 58 upwelling seasons.*

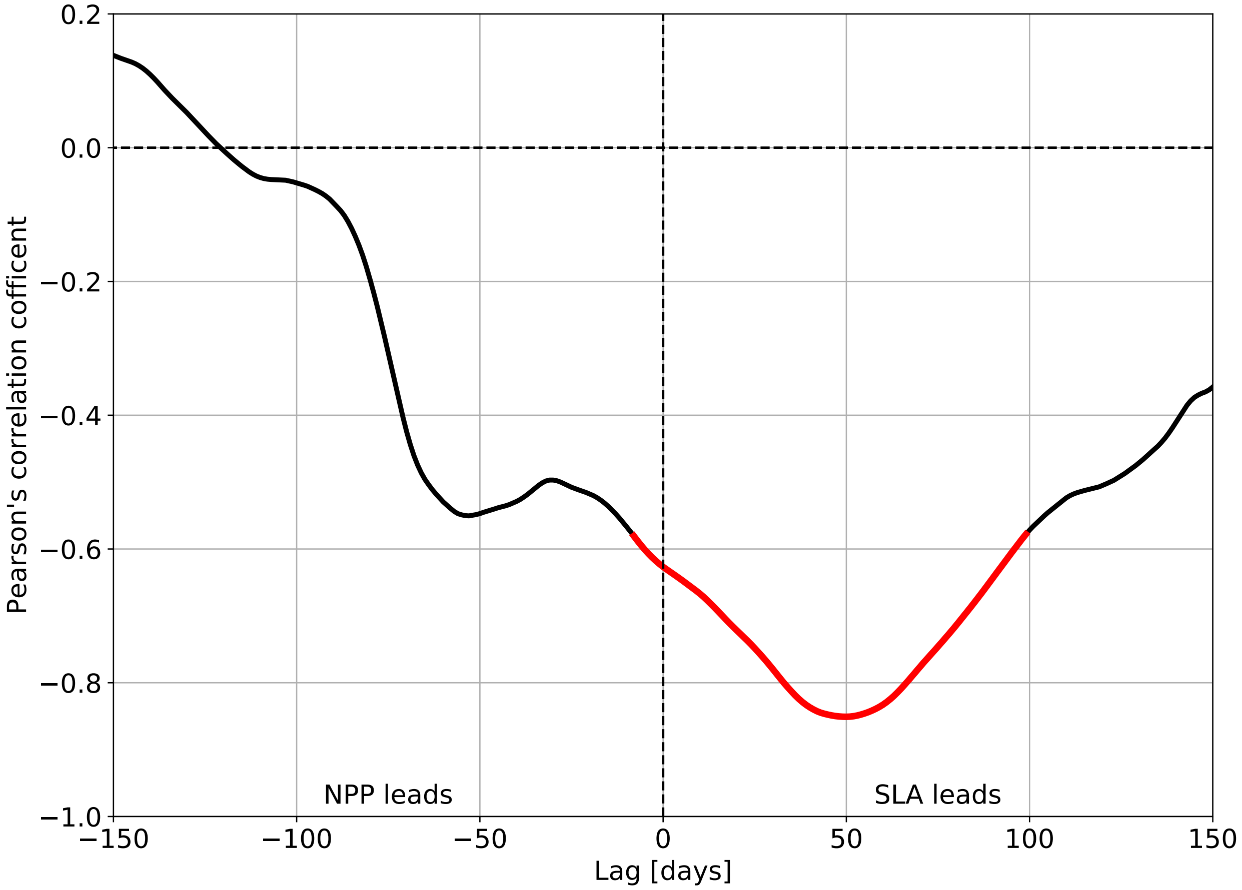

Figure 3.19: *Pearson's correlation coefficient derived by correlating the interannual time series of the three-month mean SLA around the annual SLA minimum in the austral winter with the corresponding three-month mean NPP time series at different lags. The timing of the annual minimum SLA is determined using the SLA time series treated with a low-pass filter (cut-off period of 130 days). Red line shows significant correlation at the 99% confidence level. Both NPP and SLA data is averaged between 8°S and 15°S within 1° distance to the coast. Data from 2003 – 2021 was used.*

4 Strength and timing of remotely forced Angolan coastal upwelling in austral winter

The results of chapter 3 show that coastal trapped waves (CTWs) play an important part in controlling the productivity in the tropical Angolan upwelling system (tAUS) during the main productivity season in late austral winter. One promising result of chapter 3 is the high correlation between the strength of the CTW and the strength of the productivity peak. This suggests a general predictability of productivity in the tAUS, as the CTW is remotely forced. This chapter now explores the dynamics behind the year-to-year variability of the main upwelling CTW in the tAUS. For that, regression maps with different time lags of sea surface temperature, sea level anomaly, and wind onto the timing and the strength of the annual upwelling CTW are calculated. This allows for an analyses of how variability in the tropical and subtropical Atlantic Ocean influences the characteristics of the upwelling CTW in the tAUS.

The manuscript is in preparation for submission to *Scientific Reports*.

Körner, M., Brandt, P., Dengler, M., Strength and timing of remotely forced Angolan coastal upwelling in austral winter, *in preparation*.

The candidate designed the study and carried out the analysis, produced all figures, and authored the manuscript from the first draft to the version presented here.

4.1 Abstract

The tropical Angolan upwelling system (tAUS) is a highly productive ecosystem of great socio-economic importance. Productivity peaks in austral winter and is connected to the passage of a remotely forced upwelling coastal trapped wave (CTW), where the strength of the productivity peak is connected to the amplitude of the upwelling CTW. Here, we analyze the year-to-year variability of timing and amplitude of the austral winter upwelling CTW. We examine sea surface temperature (SST), SLA, and wind fields. Our results show that the timing and amplitude of the austral winter upwelling CTW in tAUS are influenced by variability in different regions. The timing of the CTW is mostly influenced by variability in the equatorial region and along the southern African coast. Here, weaker equatorial easterlies from April to July likely induces changes in the generation of Kelvin waves leading to a late arrival of the upwelling CTW. The amplitude of the CTW is influenced by variability in the eastern equatorial Atlantic and in the central South Atlantic. A cooling in the eastern equatorial Atlantic four to three months before the arrival of the CTW causes stronger zonal winds, ultimately leading to a stronger austral winter upwelling CTW. We further find that the amplitude of the CTW is less influenced by equatorial dynamics after the year 2007. Our results suggest that the timing and amplitude of the upwelling CTW in the tAUS during austral winter are predictable on seasonal time scales.

4.2 Introduction

Angolan waters host a highly productive ecosystem of high socio-economic importance: the tropical Angolan upwelling system (tAUS) (Sowman and Cardoso, 2010; Kirkman et al., 2016; Tchipalanga et al., 2018a; Brandt et al., 2023). Productivity in the tAUS undergoes a distinct seasonal cycle as productivity peaks in austral winter in a narrow stripe along the Angolan coast(Ostrowski et al., 2009; Brandt et al., 2023; Körner et al., 2024). The peak in productivity is connected to the passage of coastal trapped waves (CTWs) propagating along the African continent (Körner et al., 2024).

CTWs can be remotely forced at the equator. Wind fluctuations at the equator excite equatorial Kelvin waves, which propagates eastward. Upon reaching the eastern boundary, part of their energy is transformed into westward-propagating Rossby waves and part of it is transformed into poleward-propagating CTWs (Moore et al., 1978; Picaut, 1983; Polo et al., 2008) (Fig. 4.1 a). CTWs exhibit signals in sea level anomaly (SLA) data where upwelling (downwelling) CTWs are associated with a depression (elevation) in sea level. SLA data reveal the passage of two upwelling and two downwelling CTWs throughout the year (Rouault, 2012; Tchipalanga et al., 2018a; Brandt et al., 2023; Körner et al., 2024). Körner et al. (2024) recently showed that the combined effect of the passage of upwelling CTWs and near-coastal mixing can explain the seasonal productivity maximum in the tAUS. They further show that the strength of the CTW is correlated with the strength in primary production, peaking about 40 days later. This suggests a general predictability of the strength of productivity in the tAUS as the CTWs are remotely forced.

On interannual time scales, the strongest modes of variability in the tAUS are extreme warm and cold events, so-called Benguela Niños and Niñas (Shannon et al., 1986; Imbol Koungue et al., 2019). The

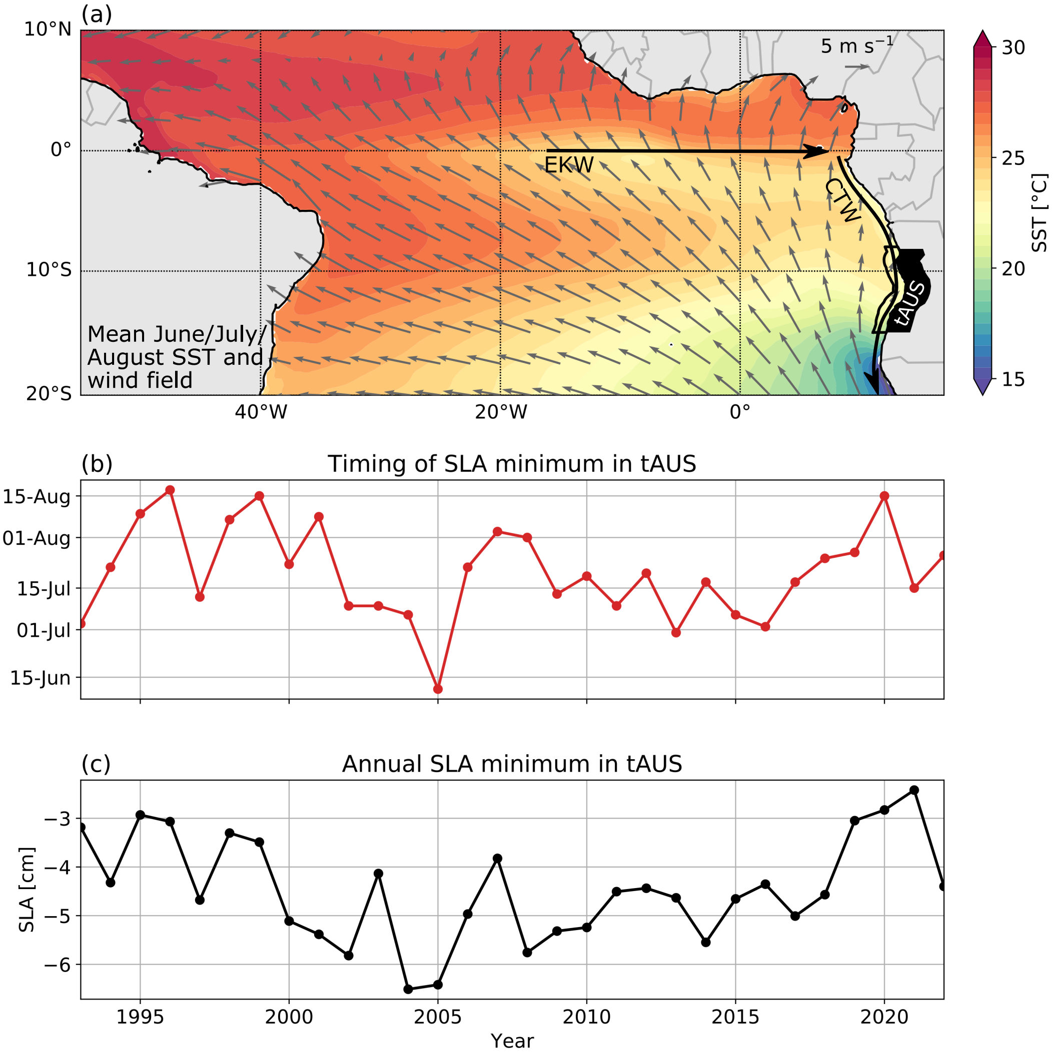

Figure 4.1: ***(a)*** *Mean June – August sea surface temperature (SST) and wind fields. Black box marks the tropical Angolan upwelling system (tAUS, 8°S – 15°S, 1° distance to the coast). Black lines indicate the propagation path of equatorial Kelvin waves (EKW) and coastal trapped waves (CTW).* ***(b)*** *Timing and* ***(c)*** *amplitude of sea level anomaly (SLA) minimum in tAUS. SLA data treated with lowpass filter to find the timing of the annual minimum (cut off period is $1/135\ days^{-1}$). The amplitude of the SLA minimum is the three-month mean SLA centered around its annual minimum.*

forcing of Benguela Niños and Niñas has been related to equatorially forced CTWs (Bachèlery et al., 2016b; Imbol Koungue et al., 2017) although local mechanisms can also modulate their strength (Lübbecke et al., 2019). Benguela Niños and Niñas peak seasonally during the main downwelling season, between March and April (Lübbecke et al., 2010; Imbol Koungue et al., 2019; Illig et al., 2020). Thus, their influence on the productivity season in the tAUS is small. The 2021 Benguela Niño is an important exception as it peaked anomalously late and significantly reduced coastal productivity during austral winter (Illig and Bachèlery, 2023).

The tAUS is closely connected to equatorial dynamics. Both the equatorial Atlantic, the tAUS, and the connection between both systems are subject to climate variability (Tokinaga and Xie, 2011; Servain et al., 2014; Prigent et al., 2020b,a, 2023). The sea surface temperature (SST) in the equatorial Atlantic warmed over the recent decades, while at the same time the variability of SST reduced (Tokinaga and Xie, 2011; Prigent et al., 2020b). Prigent et al. (2020b) find a shift in SST variability at the equator after the year 2000 associated with a weakening in the Bjerknes feedback and stronger net heat flux damping. SST in the Angola Benguela area (ABA) warmed over the recent decades as well. Additionally, changes in temperature and salinity have led to an intensification of stratification since 2006 in this region (Roch et al., 2021). Furthermore, the reduced variability in SST in the ABA is associated with less influence of the equatorial remote forcing on the region and a strengthening of the influence of local atmospheric forcing (Prigent et al., 2020a). Model projections show a reduction of SST variability during the peak season of interannual variability in response to increasing greenhouse gas concentrations (Prigent et al., 2023).

In this study, we investigate the remote and local influences of tropical Atlantic variability on the timing and strength of the upwelling CTW in the tAUS in austral winter. The motivation of this study is the connection between the strength of the upwelling CTW and the strength of the productivity peak in the tAUS. Understanding the dynamical factors controlling the timing and amplitude of the upwelling CTW could give valuable insights into the variability of the productivity of the tAUS.

4.3 Results

4.3.1 Interannual variability of the austral winter SLA minimum in the tAUS

In austral winter, an upwelling CTW propagates along the Angolan coast, which can be seen in SLA data (Rouault, 2012; Tchipalanga et al., 2018a; Brandt et al., 2023; Körner et al., 2024). In this study, we analyze the characteristics of the upwelling CTW in terms of its signal in SLA. We analyze the timing and amplitude of the SLA minimum that is associated with the upwelling CTW. Here, the amplitude of the SLA minimum describes the absolute peak of the annual SLA minimum, where higher amplitudes describe larger negative values of the SLA. Fig. 4.1 b-c shows that both the timing and amplitude of the annual SLA minimum undergo year-to-year variability.

Within the measurement period (1993-2022) the timing of the annual SLA minimum ranges between the 11^{th} of June measured in 2005 and the 17^{th} of August measured in 1996. On average, the SLA minimum is reached on the July 20^{th} with a standard deviation of 15 days.

The amplitude of the SLA minimum is on average $4.5\,cm$ with a standard deviation of $1.1\,cm$. The highest amplitude of the SLA minimum was recorded in 2004 (6.5 cm) and the lowest was recorded in 2021 ($2.4\,cm$). The amplitude of the SLA minimum undergoes multidecadal variability (Fig. 4.1 c). Possible explanations for the multidecadal variability are considered in the discussion.

The timing and amplitude of the austral winter SLA minimum are moderately correlated (Pearson correlation coefficient of 0.5). That means if the SLA minimum is occurring earlier in the year, the amplitude of the minimum tends to be higher. In the following we investigate the connection of SLA, SST, and wind field on both the timing and strength of the CTW.

4.3.2 Timing of the SLA minimum

We conducted regressions of monthly anomalies of wind, SLA, and SST onto the timing of the SLA minimum to understand the factors driving the variability in the arrival of upwelling CTW during austral winter. The monthly regression maps for the period February to September of SLA and wind are presented in Fig. 4.2, with results for SST presented in Fig. 4.6. The pattern of the regression maps corresponds to an SLA minimum later in the year, indicating a delayed arrival of the upwelling CTW.

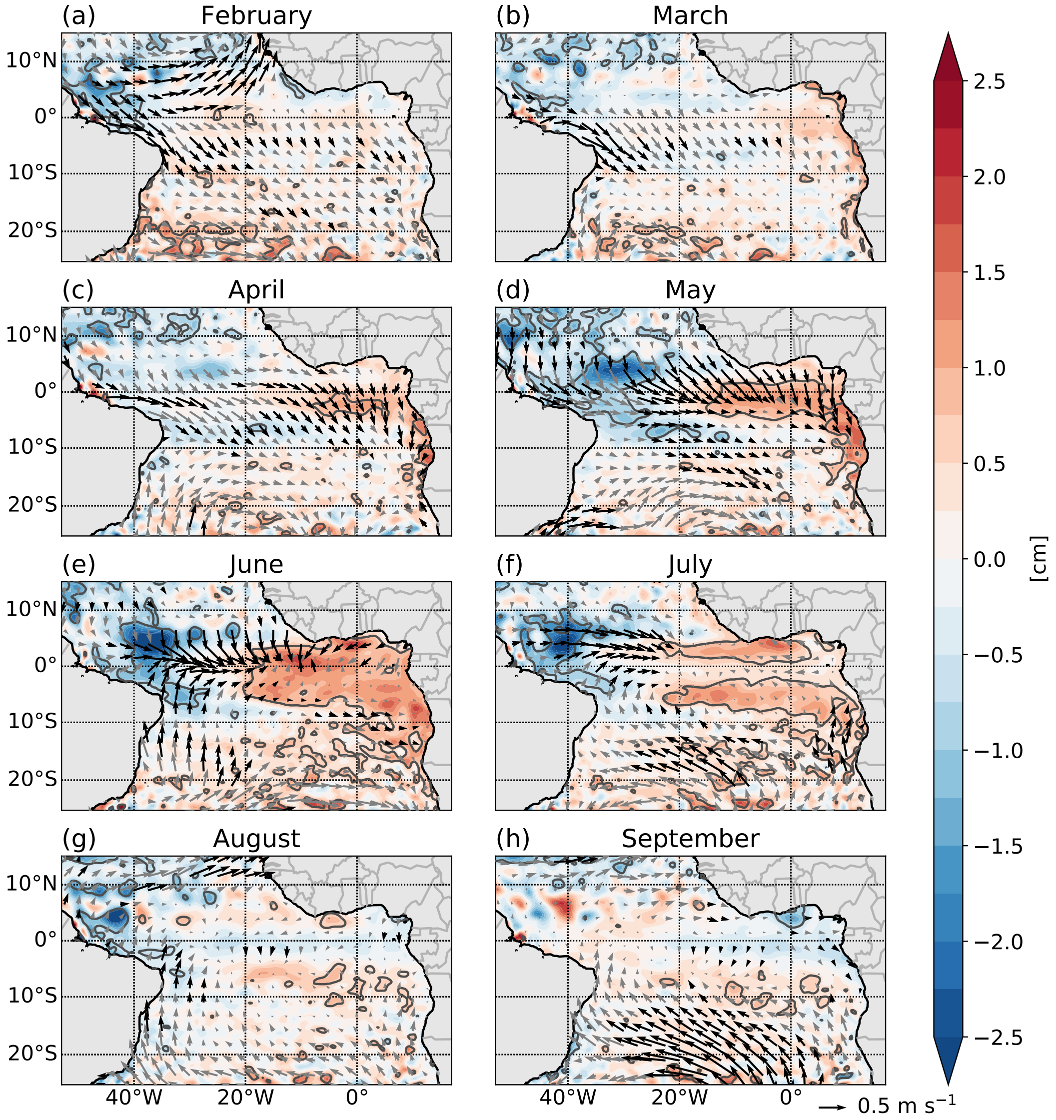

Figure 4.2: *Regression maps of SLA (colors) and winds (arrows) on the timing of the SLA minimum in the tAUS presented in Fig. 4.1 b. Regressions are calculated separately for the different months from February to September. Significant correlation (95% confidence level) between timing and SLA as well as timing and winds are marked by grey contour lines and black arrows, respectively.*

In February, north of the equator, northwesterly wind anomalies, indicative of weaker trade winds, are associated with a late arrival of the upwelling CTW (Fig. 4.2 a). Note that wind anomalies in this region can excite Rossby waves, which propagate westward and can reflect into equatorial Kelvin waves (Foltz and McPhaden, 2010; Richter et al., 2022; Lee et al., 2023). These Kelvin waves could potentially influence the arrival time of the CTW in the tAUS, offering a dynamical explanation for the observed correlation with trade winds north of the equator. Interestingly, and contrary to expectations, the Rossby wave signals are not visible in the SLA regression (Fig. 4.2 a-c). However, the regression maps of SST show significant regressions that show higher SST in the western equatorial Atlantic in the region of the wind anomalies (Fig. 4.6 a-c).

The regression maps from April to July show a significant regression of the timing of the SLA minimum onto the equatorial wind and SLA field (Fig. 4.2 c-f). At the equator, westerly wind anomalies, indicating weaker winds, are associated with the delayed arrival of the CTW. The spatial distribution of these anomalies evolves from the eastern equatorial Atlantic in April to the central and finally to the western equatorial Atlantic in July. Simultaneously, positive SLA anomalies in the eastern equatorial Atlantic in April transition into a dipole pattern with positive anomalies in the east and negative anomalies in the western equatorial Atlantic during May and June. In July, positive SLA north and south of the equator are linked to the late arrival of the CTW, while directly at the equator, no significant regression is visible. In addition to the remote forcing of the timing of the upwelling CTW, the regression analysis also indicates local influences in July. Northward wind anomalies along the African coast, indicating stronger alongshore winds, contribute to a postponed CTW arrival, possibly by generating a late local upwelling signal (Fig. 4.2 f).

In August and September, the regression maps show nearly no significant regression of the timing of the SLA minimum onto the wind and SLA field (Fig. 4.2 g-h). One exception is the wind field at around 20°S in September, suggesting that a late arrival is connected to a stronger South Atlantic Cyclone (SAA) in the following September.

These patterns of regression of the timing of the SLA minimum in the tAUS onto the wind and SLA fields show how weaker winds in different regions of the equatorial Atlantic during April to July lead to changes in the excitement of the equatorial Kelvin waves visible in the SLA pattern and ultimately to changes in the arrival of the upwelling CTW in the tAUS. Noteworthy is the SLA pattern visible north and south of the equator in July. This pattern fits the signal of westward propagating Rossby waves, which are forced together with the CTWs by the reflection of an equatorial Kelvin wave at the eastern boundary.

Similar to the SLA fields, between April and July, the regression maps of SST onto the timing of the SLA show significant regression in the equatorial region as well (Fig. 4.6). Positive SST anomalies in April in the eastern equatorial Atlantic indicate a late arrival of the annual upwelling CTW. This area of significant regressions spread in May and June, covering nearly the whole equatorial Atlantic as well as the south-eastern tropical Atlantic Ocean and the Gulf of Guinea. In July, the regression pattern indicates a Rossby wave signal as significant regression with positive SST anomalies north and south of the equator is visible. This signal is longer persistent, as it is still visible in August (Fig. 4.6 g). In comparison to the SLA regression maps, the regression maps of SST show larger areas of significant regression, especially along the African coast.

Overall, the regression maps suggest that weakened equatorial winds from April to July influence the generation of equatorial Kelvin waves, shaping SLA and SST patterns and resulting in a late arrival of the upwelling CTW in the tAUS. Furthermore, we find weakened trade winds north of the equator in February connected to the late arrival of SLA. A potential explanation for this signal is the excitement of Rossby waves leading to a warming of the western equatorial Atlantic.

4.3.3 Amplitude of the SLA minimum

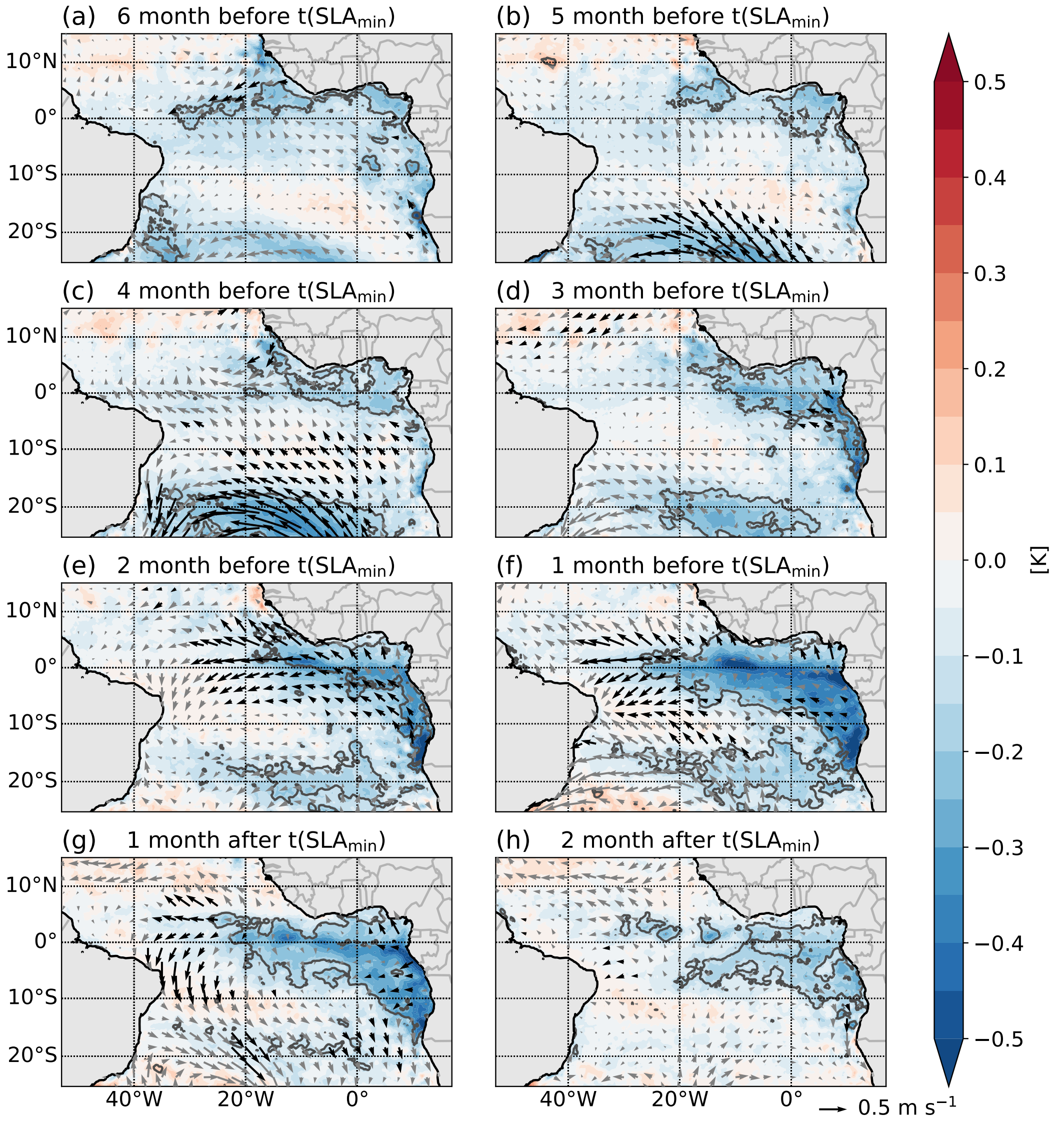

Figure 4.3: *Regression maps of SST (colors) and winds (arrows) on the amplitude of the SLA minimum in the tAUS presented in Fig. 4.1 c. Regressions are calculated for time periods relative to the timing of the annual SLA minimum (t(SLAmin)) given in the titles (see methods). Significant correlation (95% confidence level) between the amplitude and SST and the amplitude and winds are marked by grey lines and black arrows.*

We calculated regressions of anomalies of wind, SLA, and SST onto the amplitude of the SLA minimum to understand the factors driving the variability in the strength of the upwelling CTW during austral winter. The regressions are calculated for the anomalies relative to the timing of the annual SLA minimum. The monthly regression maps, spanning from six months before to two months after the SLA minimum, for SST and wind are presented in Fig. 4.3, with results for SLA presented in Fig. 4.7. The pattern of the regression maps corresponds to a higher amplitude of the SLA minimum, indicating a stronger upwelling CTW.

Five to four months before the SLA minimum, significant regressions of the wind field in the South Atlantic onto the amplitude of the SLA minimum are visible (Fig. 4.3 b-c). The maps suggest that a stronger SAA is linked to a higher amplitude of the SLA minimum and thus a stronger upwelling CTW. This signal is mirrored in SST, showing a significant regression with negative SST anomalies in the area of enhanced wind anomalies. Similar patterns are observed in SLA, with a patchier signal of negative SLA in the same region (Fig. 4.7 a-b). The fact that the same region shows up in all three variables suggests that there is indeed a connection between the SAA strength and the amplitude of the upwelling CTW five to four months later. Additionally, negative SST anomalies in the Gulf of Guinea and the eastern equatorial Atlantic exhibit a significant regression with a higher amplitude of the SLA minimum, with no corresponding signal in wind and SLA in this region. This raises the question of the origin of the cooling in the eastern equatorial Atlantic. One possible explanation is that the cooling in this area is connected to the stronger SAA. A stronger SAA could influence the distribution of clouds over the tropical Atlantic Ocean, inducing the cooling. To check this hypothesis, we conducted regression analyses of the total cloud cover onto the amplitude of the SLA minimum (Fig. 4.8). The results indicate that four to three months before the SLA minimum higher cloud cover over the eastern equatorial Atlantic is connected to a higher amplitude of the SLA minimum. Note that only a small area of this pattern shows a significant correlation questioning the robustness of this result. Nevertheless, this theory offers a dynamical explanation of the connection between the SAA strength, the cooling of the eastern tropical Atlantic, and the amplitude of the SLA minimum five to four months later.

Three months before the SLA minimum, the significant regression with the wind field of SAA vanishes (Fig. 4.3 d). However, the signals in SST and SLA in the region are still persistent (Fig. 4.3 d & 4.7 d). Additionally, the signal in SST in the eastern equatorial Atlantic remains persistent as well.

A connection between the amplitude of the SLA minimum and the equatorial wind field is visible 2 months before the SLA minimum (Fig. 4.3 e). Easterly wind anomalies in the eastern and central equatorial Atlantic, indicating a stronger equatorial easterlies, are connected with a higher amplitude of the SLA minimum. These easterly wind anomalies are likely a reaction of the wind field to the lower SST visible before (Fig. 4.3 d). The lower SST anomaly signals are also visible 2 months before the SLA minimum (Fig. 4.3 e). The signal in SST becomes stronger and the area of this signal expands covering the eastern equatorial Atlantic, Gulf of Guinea, and along the southern African coast up until the ABFZ. One month before the SLA minimum, the area of significant regression of the wind field shifts westward (Fig. 4.3 f). At the same time, the area of significant regression of negative SST anomalies expands, now covering the equatorial region east of 25°W. Similar signals as the ones in SST are observable in SLA (Fig. 4.7 e-f).

One month after the SLA minimum, the regression maps still indicate colder-than-usual SSTs in the equatorial region and along the Angolan coast connected to a stronger upwelling CTW, although the signal is weaker (Fig. 4.3 g). Meanwhile, significant regressions of stronger winds in the western equatorial Atlantic are visible. Two months after the SLA minimum, no significant regression is observed in the wind field, however the eastern equatorial Atlantic remains colder.

The regression maps of SST, SLA, and wind onto the amplitude of the SLA minimum reveal distinct regions influencing the strength of the upwelling CTW. An influence of the strength of the SAA is evident five months before the SLA minimum. The strengthening of the SAA likely leads to a shift in cloud cover, leading to a cooling in the eastern equatorial Atlantic. Two months before the SLA minimum, the equatorial wind field reacts to the low SST anomalies in the eastern equatorial Atlantic, with the maps illustrating that a stronger wind field in the eastern and central equatorial Atlantic leads to stronger SST anomalies, negative SLA, and subsequently a stronger upwelling CTW. This regression analysis reveals the remote influences of both the SAA strength and equatorial wave dynamics on the strength of the upwelling CTW.

4.3.4 Temporal evolution of the equatorial connection

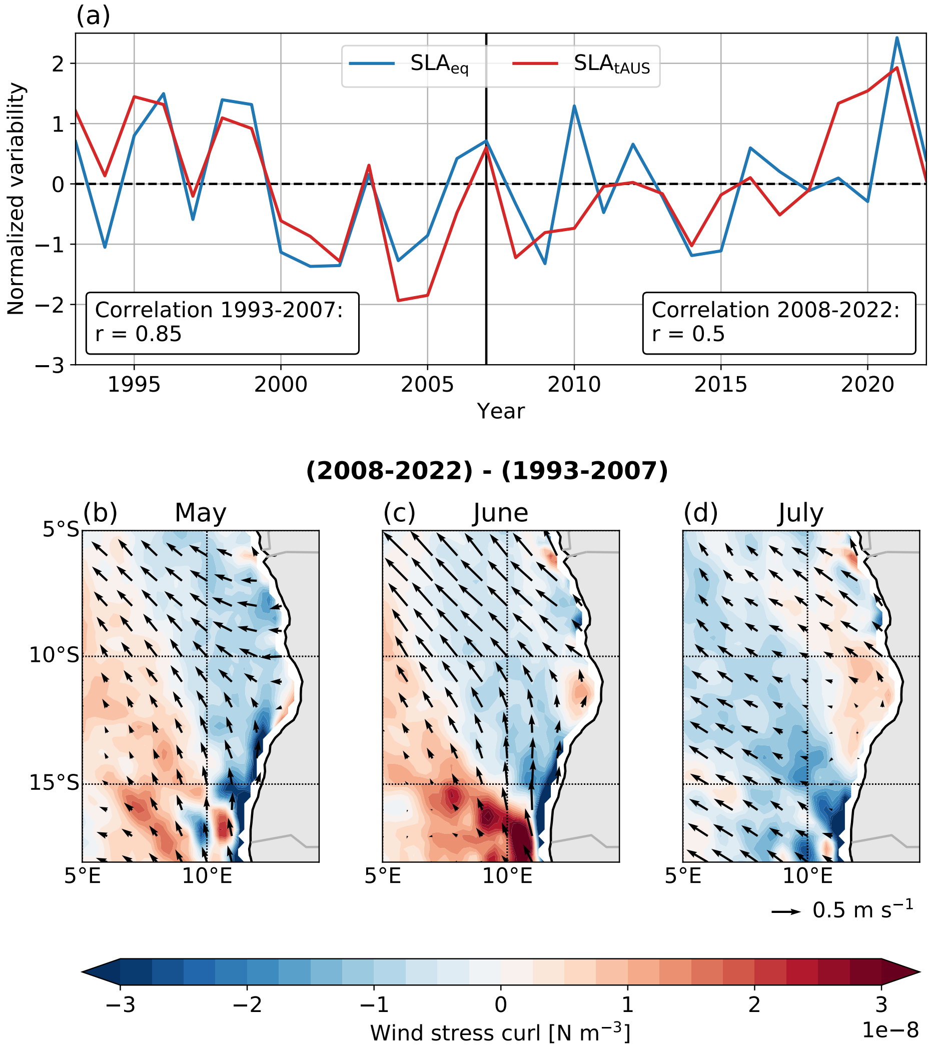

Figure 4.4: ***(a)*** *Amplitude of SLA minimum in austral winter in the tAUS (red; 8°S – 15°S, 1° distance to the coast) and at the equator (blue; 20°W – 0°, 1°S – 1°N). Both time series are normalized by their respective standard deviations. The Pearson correlation coefficient between both time series is given for the two different time periods.* ***(b)*** *–* ***(d)*** *Difference of the wind field (arrows) and the windstress curl (colors) between 2008 – 2022 and 1993 – 2007 for the month May, June and July.*

A previous study showed that the respective role of remote equatorial to local forcing of SST anomalies in the ABA changes over time (Prigent et al., 2020a). We now discuss the amplitude of the SLA minimum at the equator and in the tAUS to assess changes in the relationship between both regions. A high co-variation is expected if the strength of the SLA minimum in the tAUS is strongly related to equatorial dynamics.

Fig. 4.4 a shows the time series of the amplitude of the austral winter SLA minimum at the equator (20°W – 0°E; 1°N – 1°S) and in the tAUS (8°S – 15°S, 1° distance to the coast). It becomes evident that the SLA minimum at each location undergoes multidecadal variability. Moreover, a distinct shift in the relationship between the SLA minimum in these regions becomes apparent during the period 1993 – 2022. From 1993 to 2007, the amplitude of the SLA minimum at the equator and in the tAUS exhibits a close connection, evident through a Pearson correlation coefficient of 0.85 (significant at a 95% confidence level). After 2007 the correlation is much weaker (Pearson correlation coefficient of 0.5, not significant at 95% confidence level) indicating a diminished connection between the two regions. Concurrently, there is a reduction in the variability of the amplitude of the SLA minimum in both areas. In the tAUS, the standard deviation decreases by 18%, declining from $1.16\,cm$ (1993-2007) to $0.95\,cm$ (2008-2022). At the equator, the reduction is somewhat weaker as the standard deviation decreases by 10%, shifting from $1.54\,cm$ (1993-2007) to $1.38\,cm$ (2008-2022). Thus, over the measurement period, the variability in each region decreases, accompanied by a decline in the correlation between the two areas. It is worth mentioning that the last two years of the time series exhibit strong co-variability again.

We want to analyze the possible reasons for this changing behavior. Note that we abstain from calculating regressions for both time periods separately, as this would mean regression on very short time series. Especially in the second period, little variability in the time series would make the analysis less robust. Instead, we focus on examining mean state changes in the wind fields between the two time periods. Fig. 4.4 b-d shows that between 2008 and 2022 the local wind fields showed stronger alongshore wind in May – July. Especially in May and June, differences are visible. The changes in wind are associated with negative wind stress curl anomalies (i.e., upwelling-favoring anomalies) along the coast during these months. These results suggest an increase of local forcing in the second period, potentially weakening the connection to the equator. In the next section, we will discuss this in greater detail.

4.4 Discussion

In this study, we investigate the interannual variability of the timing and amplitude of the austral winter upwelling CTW in the tAUS and their potential controlling mechanisms. The timing and amplitude of the SLA minimum (used as a proxy for the CTW) in tAUS exhibit a weak correlation between the two variables. This suggests that there must be differences in the forcing of these characteristics of the CTW.

The timing of the SLA minimum (i.e., timing of the CTW) seems to be mainly influenced by equatorial variability from April to July. In these months, weaker winds, warmer SSTs, and a dipole structure in SLA with negative anomalies in the east are connected with a late SLA minimum. The pattern fit well with

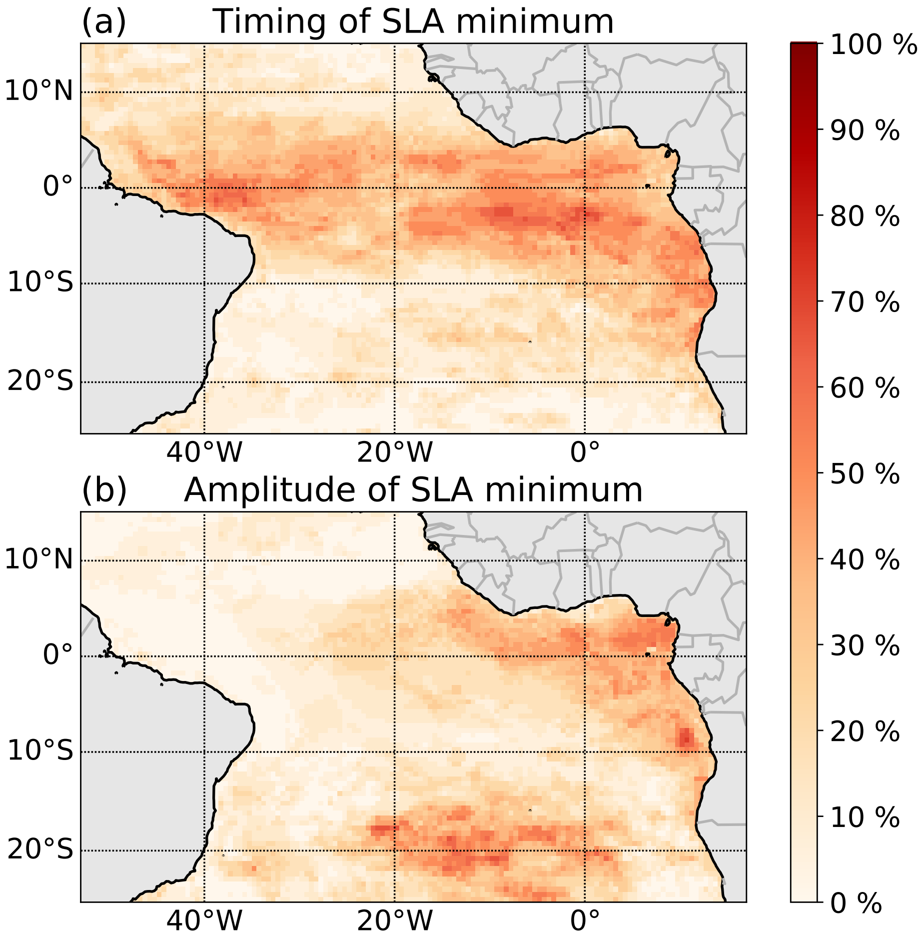

Figure 4.5: *Heat map of the significant correlation (95% confidence level) of the SST, SLA and wind field onto* ***(a)*** *the timing of the SLA minimum and* ***(b)*** *the amplitude of the SLA minimum. Pixel showing 100% corresponds to location with significant correlation in all three variables for the whole time period. The heat map is calculated for the time period of* ***(a)*** *February – July and* ***(b)*** *six – one month before the SLA minimum.*

how wind anomalies in the equatorial region alter the excitement of equatorial Kelvin waves, shaping the SST and SLA pattern and affecting the arrival of the upwelling CTW in the tAUS. Furthermore, there is an indication that the strength of trade winds north of the equator in February plays a role for the timing of the SLA minimum. This signal in the wind field is connected to a warming of the western equatorial Atlantic, likely by the excitement of westward propagating Rossby waves.

The amplitude of the SLA minimum (i.e., the strength of the upwelling CTW) appears to be linked to the strength of the SAA five to four months before the SLA minimum, with a stronger SAA connected to a higher amplitude of the SLA minimum. The strengthening of the SAA might influence the cloud cover over the eastern equatorial Atlantic, leading to cooling in this region. Note that the connection between the strength of the SAA and the cooling of the eastern equatorial Atlantic is not robust. More work has to be done to understand if and how both signals are connected. The equatorial wind field reacts to the cooling in the eastern equatorial Atlantic two to one month before the SLA minimum with eastward anomalies. These eastward wind anomalies in turn likely influence the strength of the equatorial Kelvin wave, leading to negative SLA and enhancing the SST anomalies at the equator.

These regression analyses suggest that the timing and amplitude of the austral winter upwelling CTW in tAUS are influenced by variability in different regions. We calculate heat maps to identify regions with significant correlations of SST, SLA, and wind with the timing and amplitude of the SLA minimum, respectively (Fig. 4.5). Fig. 4.5 a clearly shows that the timing of the SLA minimum is mostly influenced by variability in the equatorial region and along the southern African coast north of the ABFZ. The amplitude of the SLA minimum is influenced by variability in the eastern equatorial Atlantic and in the central South Atlantic, a region characterizing the strength of the SAA (Fig. 4.5 b).

Our results further show that the connection between the variability of the amplitude of the SLA minimum at the equator and in the tAUS underwent changes. Between 1993 and 2007 the amplitude of the SLA minimum in the tAUS and at the equator exhibited a high correlation, while between 2007 and 2022 the correlation weakened and the variability in both regions declined. Prigent et al. (2020a) investigated the connection between equatorial SST variability and SST variability in the ABA, focusing on the peak season of interannual variability (March – May). They found that after the year 2000 the influence of equatorial forcing on SST variability in the ABA weakened while local atmospheric influences became more important.

The question arises on the origin of the changes in the co-variability between the two regions. Historic CMIP6 model runs show a decline in tropical Atlantic SST variability since the 1970s (Sobral Verona et al., 2023). Furthermore, model projections suggest a reduction of SST variability in the ABA in response to increasing greenhouse gas concentrations (Prigent et al., 2023). Climate projections further suggest a weakening of Atlantic Niño variability, attributed to a decoupling of subsurface and surface processes (Crespo et al., 2022; Deppenmeier, 2022). However, the results of Sobral Verona et al. (2023) also highlight high multidecadal variability in the tropical Atlantic variability, potentially linked to Atlantic Meridional Oscillation, which exhibits increased equatorial variability in negative phases (Martín-Rey et al., 2018). Additionally, El Niño/Southern Oscillation (ENSO) experiences a reduction in variability in recent decades as well (Lübbecke and Mcphaden, 2014; Li et al., 2019; Hu et al., 2020) which is of interest for the Atlantic Ocean as ENSO influences tropical Atlantic variability (Chang et al., 2006; Latif and Grötzner, 2000). Thus, the existing studies show a complex picture of multidecadal variability and response to global warming, with an overall expectation of reduced variability in the future (Prigent et al., 2023). Note that in the last few years, variability at the equator and in the ABA picked up again, with major warm events recorded in 2019 and 2021 (Richter et al., 2022; Lee et al., 2023; Illig and Bachèlery, 2023). This underlines that further work is needed to understand the future of tropical Atlantic variability. Our study underlines that this is important not only in the context of SST variability and extreme events but also for the year-to-year variability of the upwelling season in the tAUS.

The amplitude of the SLA minimum undergoes multidecadal variability (Fig. 4.1 c). Note that in this study, we removed the linear trend in SLA. The linear trend of the amplitude of the SLA minimum over the period of 1993 - 2022 is $3.6\,mm\,year^{-1}$, the acceleration is $0.2\,mm\,year^{-2}$ (determined via a second order polynomial fit). Globally, sea levels rise as a response to climate warming, which is accelerating since the 1960s (Dangendorf et al., 2019). The global estimates over the satellite area shows a linear sea level rise of $3\,mm\,year^{-1}$ and an acceleration of $0.1\,mm\,year^{-2}$ (Nerem et al., 2018; Cazenave et al., 2019; Dangendorf et al., 2019). This suggests that part of the multidecadal variability in the amplitude of the

SLA minimum can potentially be attributed to global warming. Especially as Dangendorf et al. (2019) showed that the acceleration of sea level rise in the South Atlantic is higher than the global average. However, climate variability might also contribute to the multidecadal variability. Here, the changes in the SAA and its influence on the tAUS could play a role. Averaging wind speed anomalies between 20°W-0°E and 30°S-20°S 5 months before the SLA minimum show similar multidecadal variability as well (not shown). This underlines the influence of the SAA on the variability of the amplitude of the SLA minimum.

The present study gives valuable insights into how variability in different areas of the tropical and South Atlantic influences the timing and strength of the austral winter upwelling CTW in tAUS. This study thus lays the groundwork for future attempts to predict the timing and strength of the CTW. This prediction would be of high interest as the strength of the productivity peak in the tAUS in austral winter is related to the strength of the CTW (Körner et al., 2024).

4.5 Methods

4.5.1 Satellite/Reanalysis data

To investigate the amplitude and timing of the austral winter upwelling CTW, we make use of different satellite data products.

The SLA data used in this study are from Copernicus (https://doi.org/10.48670/moi-00148). The daily SLA fields are available with a horizontal resolution of a 0.25° x 0.25° grid since 1993.

The SST fields used in this study are from the OSTIA product (Good et al., 2020). The OISTA product uses satellite data as well as in situ measurements to provide global, daily, gap-filled SST fields. The data are available on a $0.05^\circ \times 0.05^\circ$ grid from 1981 onward.

The wind speed and cloud cover data used in this study are from the ERA5 reanalysis product (Hersbach et al., 2020). The zonal and meridional components of wind speed 10 m above the earth's surface and the cloud cover are available on a horizontal grid with a resolution of 0.25° x 0.25°. The hourly data are available from 1940 onward. We calculate daily averages before using the data.

For the study, we use data from January 1993 – December 2022 as data from all products are available in this time period.

4.5.2 Determining timing and amplitude of SLA minimum

The timing and amplitude of the annual minimum in SLA are calculated considering the time series of SLA averaged in the tAUS. To derive the time series of SLA in the tAUS, we first remove the linear trend in SLA data at each grid point. Afterwards we average SLA over the area of the tAUS considered in this study (8°S-15°S, 1° distance to the coast). We then filter out high-frequency variability by applying Cosine-Lanczos filter as formulated by Thomson and Emery (2014). We choose a cutoff frequency of

$1/135\,days^{-1}$ to filter out the effect of intraseasonal CTWs that are commonly observed in the tAUS with periods of 90 and 120 days (Imbol Koungue and Brandt, 2021). To determine the amplitude of the SLA minimum, we average 90 days of the unfiltered SLA time series centered around its annual minimum.

4.5.3 Regression analysis

We conduct regression analysis of various fields on the timing and amplitude of the annual SLA minimum in the tAUS. Prior to calculating the regressions, we remove the mean and the linear trend of the time series of the timing and the amplitude of the annual SLA minimum. Additionally, we normalize the time series by their respective standard deviations. Both timeseries are thus unitless and the regression fields have the unit of the field variable.

For the regression analysis on the timing of the SLA minimum, we consider monthly SLA, SST, and wind fields and calculate the regression at each grid point of these fields individually. Before calculating the regressions, we remove the mean and the linear trend at each grid point. The mean and the trend are calculated for the time series at this grid point of the respective month. Thus, the trend of the respective month is removed, not the trend over the complete time series.

The regression analysis on the amplitude of the annual SLA minimum is calculated for SLA, SST, and wind fields. The regressions are calculated for the anomalies relative to the timing of the annual SLA minimum. For that, the daily anomalies of the SLA, SST, and wind fields are calculated by removing the daily climatology. We then map the anomalies as a function of lag in days relative to the annual SLA minimum as presented in Fig. 4.1 b. The anomalies are then averaged in bins with a bin size of 30 days. Thus, the resulting fields depict the SLA, SST, and wind anomalies relative to the timing of the annual SLA minimum. Before calculating the regression, the mean and the linear trend at each grid point are removed. The mean and the trend are calculated for the time series at this grid point over the respective time period.

Acknowledgments

The study was funded by EU H2020 under grant agreement 817578 (TRIATLAS project).

Author contributions

MK performed the analysis and drafted the paper. All co-authors reviewed the paper and contributed to the scientific interpretation and discussion.

Data availability

Publicly available datasets were used for this study. The sea level anomaly data can be accessed via the Copernicus server (https://doi.org/10.48670/moi-00148). The sea surface temperature data are from the OISTA product (https://doi.org/10.48670/moi-00169). The wind and cloud cover data are from ERA5 (https://doi.org/10.24381/cds.adbb2d47).

4.6 Supplementary Materials

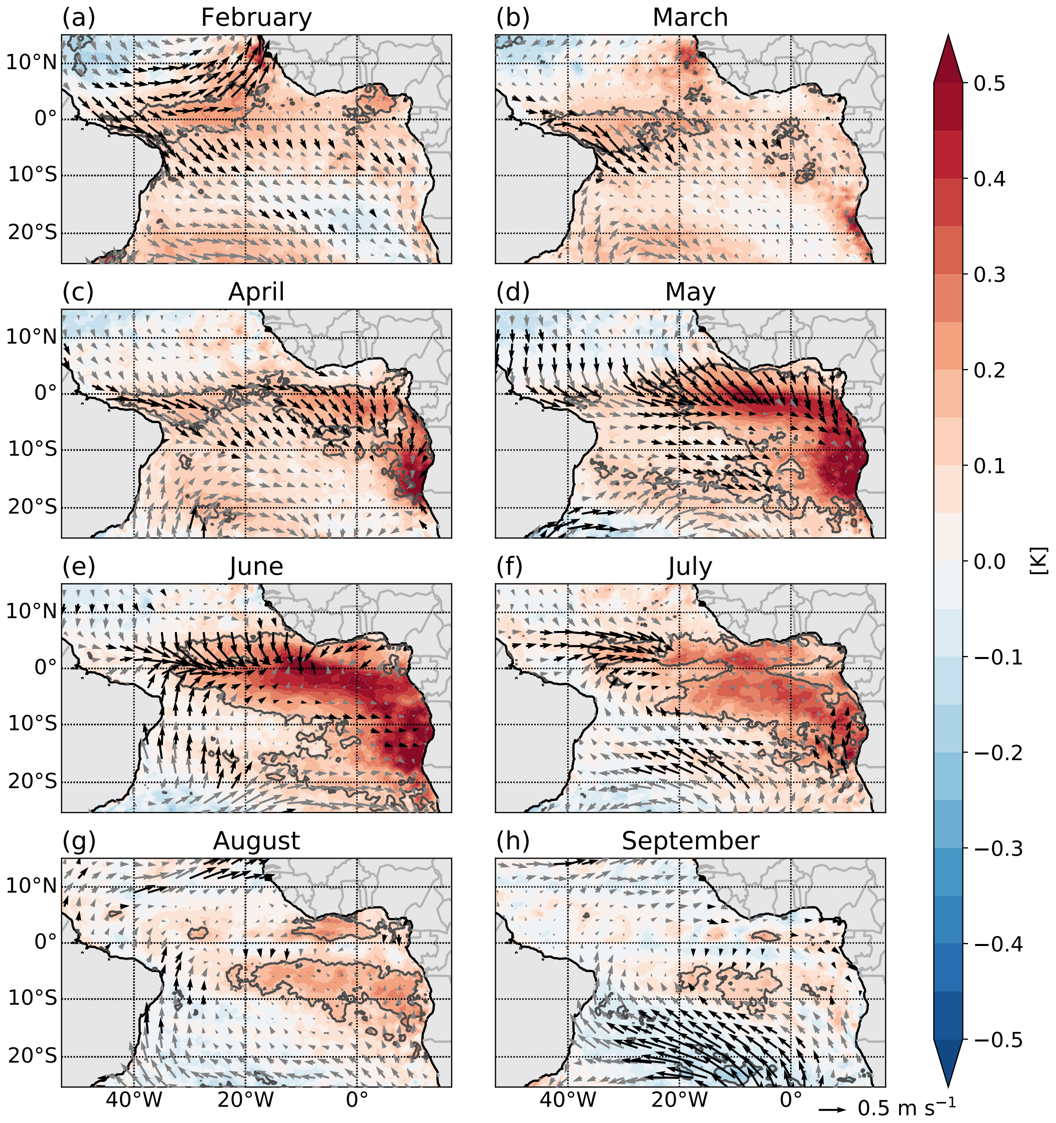

Figure 4.6: *Regression maps of SST (colors) and winds (arrows) on the timing of the SLA minimum in the tAUS presented in Fig. 4.1 b. Regressions are calculated separately for the different months from February to September. Significant correlation (95% confidence level) between timing and SLA as well as timing and winds are marked by grey contour lines and black arrows, respectively.*

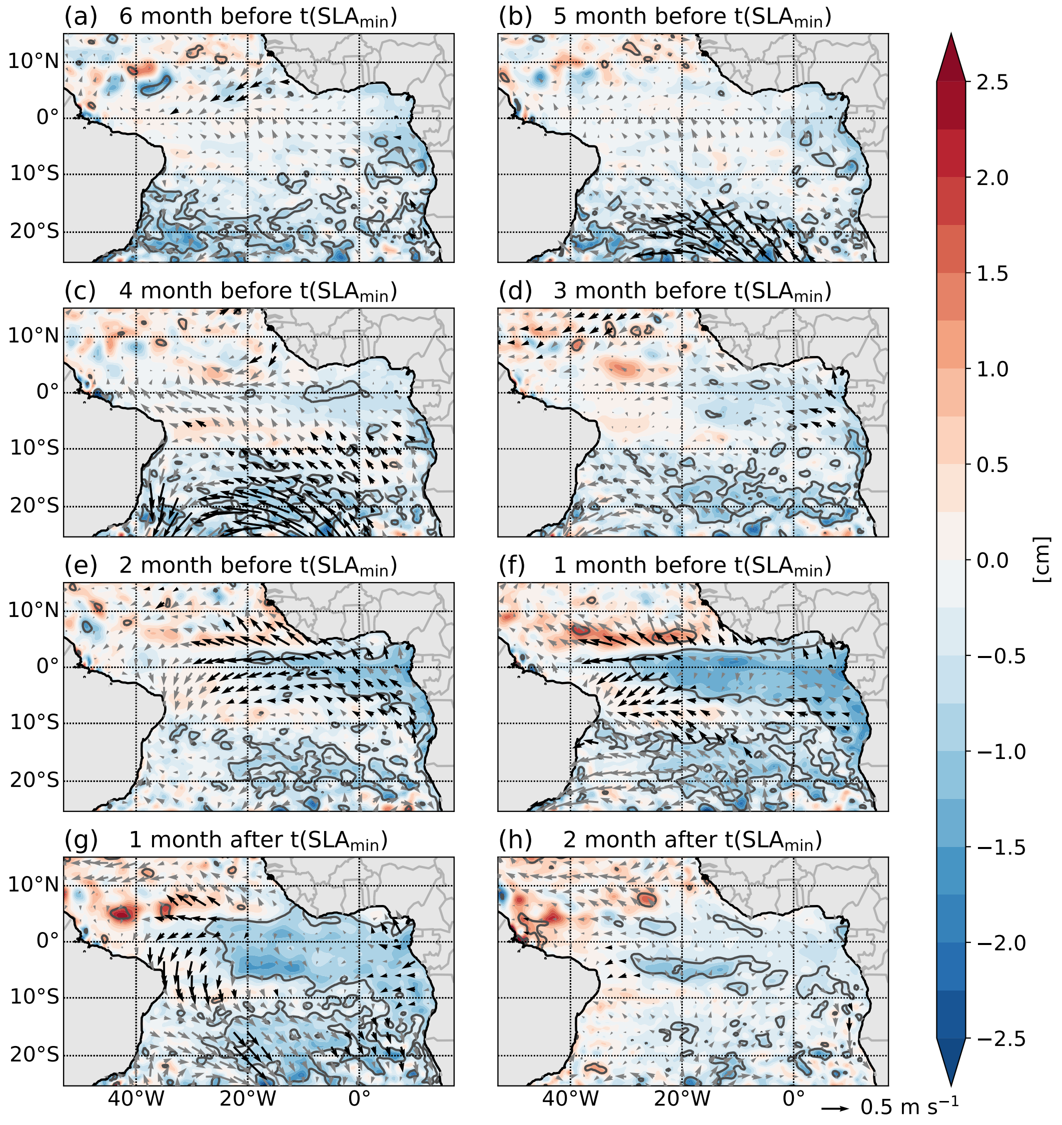

Figure 4.7: *Regression maps of SLA (colors) and winds (arrows) on the amplitude of the SLA minimum in the tAUS presented in Fig. 4.1 c. Regressions are calculated for time periods relativ to the timing of the annual SLA minimum (t(SLAmin)) given in the titles (see methods). Significant correlation (95% confidence level) between the amplitude and SST and the amplitude and winds are marked by grey lines and black arrows.*

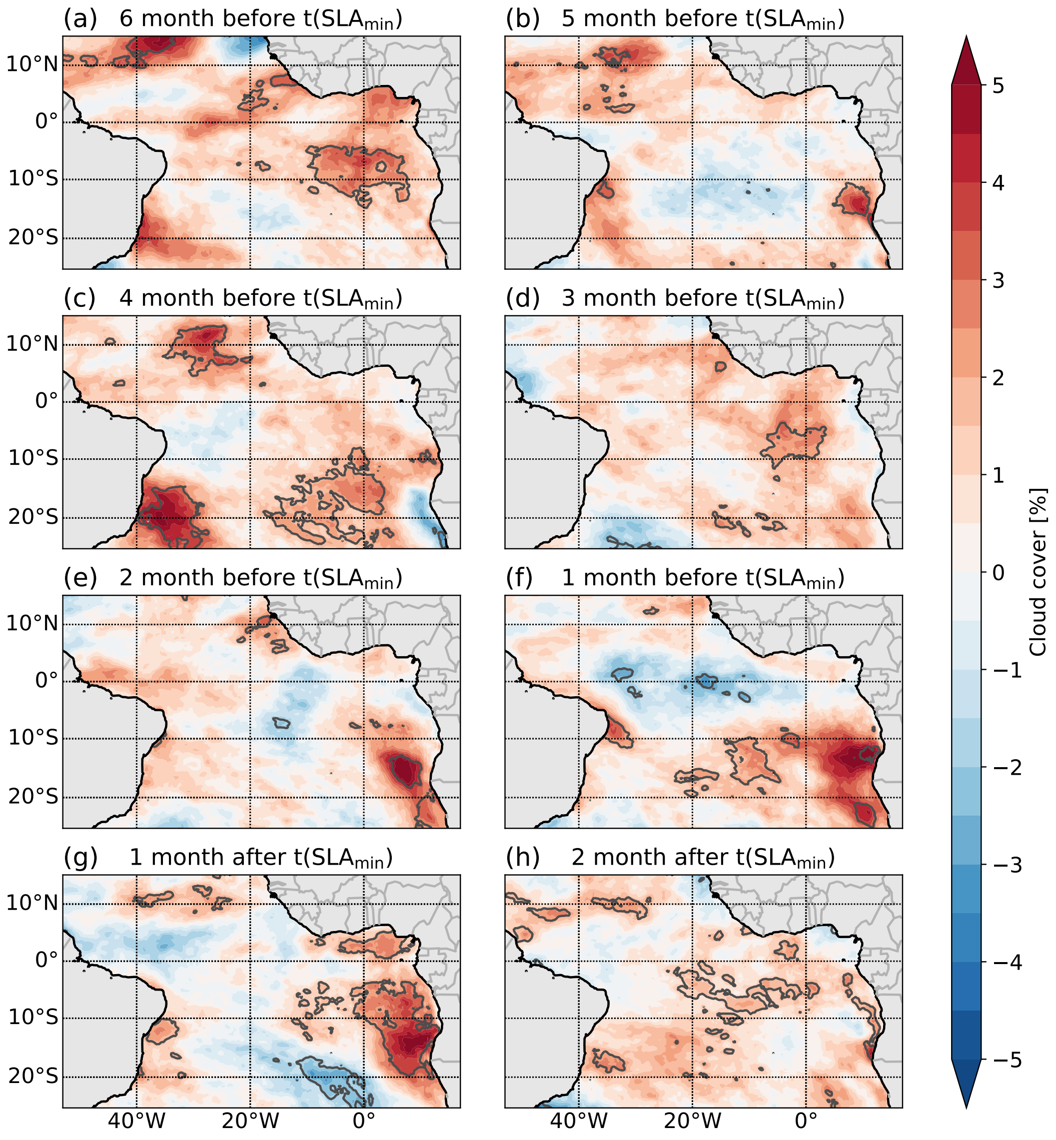

Figure 4.8: *Regression maps of total cloud cover (colors) on the amplitude of the SLA minimum in the tAUS presented in Fig. 4.1 c. Regressions are calculated for time periods relative to the timing of the annual SLA minimum given in the titles (see methods). Significant correlation (95%) between the amplitude of the SLA minimum and the total cloud cover are marked by grey lines.*

5 Summary, Discussion & Outlook

5.1 Summary & Discussion

The tropical Angolan upwelling system (tAUS) is a highly productive ecosystem of great socio-economic importance (Hutchings et al., 2009; Sowman and Cardoso, 2010; FAO, 2022). Characteristics of the tAUS are shaped both by local as well as remote factors, where equatorial dynamics play an important role. Conditions in the tAUS display pronounced seasonal variability, with numerous characteristics exhibiting enhanced variations on both annual and semi-annual time scales. The work presented in this thesis takes a closer look at the physical drivers of this seasonal variability. In this chapter, the scientific questions raised in chapter 1 are revisited and discussed. The results of this thesis are thereby summarized and integrated into the current level of knowledge and the scientific progress is pointed out.

What physical drivers shape the seasonal variability in the tAUS?

This thesis examines the dynamics of seasonal variability in the tAUS. The studies presented in chapter 2 & 3 focus on explaining the mechanism behind the seasonal cycle in sea surface temperature (SST) and productivity, highlighting the role of CTWs, surface heat fluxes, and near-coastal mixing in shaping conditions in the tAUS. In the following, I will summarize the most important findings of this thesis concerning the mechanisms controlling the seasonal variability of SST and productivity. Afterwards, I will discuss the individual processes in greater detail.

In the tAUS, the SST directly at the coast is colder than further offshore throughout the year. Both the SST and the strength of the cross-shore SST gradient exhibit seasonal variability. In chapter 2, a mixed layer heat budget is presented, analyzing the atmospheric and oceanic drivers of SST variability. The analyses are conducted for the coastal and offshore region separately to analyze differences between the regions. The results suggest that the seasonal cycle of SST is mainly driven by surface heat fluxes and turbulent heat loss at the base of the mixed layer. The turbulent heat loss at the base of the mixed layer is much stronger in shallow waters at the shelf. The strong near-coastal mixing is likely responsible for setting up the negative cross-shore SST gradient. The surface heat fluxes, in contrast, act to dampen the temperature differences between the coastal and offshore regions. While the seasonal cycle of SST is dominated by annual variability, the cross-shore SST gradient shows dominant variability on semi-annual time scales. The results of chapter 2 suggest that this semi-annual cycle of the cross-shore SST gradient is driven by tidal mixing acting on seasonal different background stratification. The near-coastal cooling is more effective under weakly stratified conditions. Stratification is controlled by the passage of coastal trapped waves (CTWs), changes in sea surface salinity (SSS) and SST and exhibits a semi-annual cycle. Phases of weak stratification coincide with enhanced cross-shore SST gradients.

Primary productivity in the tAUS undergoes a semi-annual cycle, with the main productivity peak in late austral winter. Chapter 3 takes a closer look at the mechanism that drives productivity in the tAUS during the main upwelling season. In the study, observational datasets consisting of extensive shipboard observations and satellite data, as well as the output of a numerical model are utilized. Chapter 3 shows that CTWs and near-coastal mixing play a crucial role in driving the seasonal cycle of productivity in the tAUS. The proposed mechanism relies on the interplay between CTWs of different vertical structures and near-coastal mixing. Faster low-mode CTWs, evident in sea level anomaly (SLA) data, arrive in austral winter in the tAUS first. Subsequently, slower high-mode CTWs, primarily influencing the depth of the nitracline, are detectable. These high-mode CTWs induce a vertical displacement of the nitracline by approximately 50 meters between the main downwelling season and the main upwelling season. Concomitant with the passage of the CTWs, nitrate-rich water is advected toward the coast, ultimately reaching the shallow waters of the Angolan shelf, a region characterized by high mixing rates. The presence of nitrate-rich waters on the shelf results in an enhanced turbulent nitrate flux into the surface mixed layer during the upwelling season. This contrasts with the downwelling season, when nitrate concentrations on the shelf are low.

Summarizing, the results of this thesis show that CTWs, near-coastal mixing, and surface heat fluxes are essential processes to explain the seasonal variability of SST and productivity in the tAUS. The seasonal cycle of SST is mainly driven by surface heat fluxes and near-coastal mixing. The semi-annual cycle of the cross-shore SST gradient can be explained by near-coastal mixing acting on seasonal different background stratification, which is partly driven by the passage of CTWs. The combined effect of CTWs and near-coastal mixing can explain the productivity peak during austral winter.

The results of chapters 2 & 3 show that CTWs play an important role in shaping characteristics in the tAUS on seasonal time scales. The importance of CTWs and thus equatorial dynamics for the tAUS was pointed out by many previous studies before (e.g. Picaut (1983); Rouault (2012); Tchipalanga et al. (2018a)). This thesis now advances our understanding of how CTWs shape the seasonal variability of primary productivity and cross-shore SST differences in the tAUS. Previous studies suggested that CTWs play a role in productivity, highlighting the timing between the passage of the upwelling CTW and the peak in productivity about a month later (Ostrowski et al., 2009; Tchipalanga et al., 2018a; Brandt et al., 2023). The results in this thesis now propose a mechanism for how CTWs control productivity in the tAUS and thus contribute to a better process understanding. Here especially, the presence of high-mode CTWs and their effect on the depth of the nitracline is a new insight into the dynamics of the tAUS. The high-mode CTWs are phase-locked to the low-mode CTWs and are constantly generated with the arrival of low-mode CTWs. The high-mode CTWs do not only affect the depth of the nitracline but also strongly deform the local density field. Previous studies showed a strong semi-annual cycle in the vertical isopycnal movement (Ostrowski, 2007; Rouault, 2012; Kopte et al., 2017) which can now be better understood in the context of the passage of CTWs of different vertical and cross-shelf structures. Furthermore, chapter 3 shows an onshore transport of nitrate-rich water connected to the passage of CTWs. The presence of nitrate-rich South Atlantic central water (SACW) on the Angolan shelf during upwelling phases was described before (Ostrowski, 2007; Ostrowski et al., 2009). The results of this thesis now advance our understanding of how upwelling source water is transported onshore. Additionally, Kopte et al. (2018) analyzed the annual and semi-annual cycle of alongshore velocity at 11°S off Angola.

They found that in their single-baroclinic-mode simulations with a reduced-gravity model, the simulated semi-annual cycle of alongshore velocity lacks amplitude at mid-depth in comparison to observations. This points toward a missing mechanism in the simulations, allowing energy to transfer between different modes. The high-mode CTWs could explain the velocity at mid-depth and thus explain the mismatch between the model and the observation, as by design, high-modal structures are not present in their model set-up. Summarizing, the results of this thesis contribute to a better process understanding on how CTWs affect characteristics in the tAUS. Note that open questions remain, especially concerning the energy transfer between low-mode CTWs and high-mode CTWs. This will be addressed in more detail in the outlook below.

The results of chapters 2 & 3 show the importance of turbulent fluxes for both near-coastal cooling and upward nitrate flux. Thereby, for the first time, estimates of turbulent heat loss at the base of the mixed layer and turbulent upward nitrate flux in the tAUS are presented. Thus, the results of this thesis contribute towards a better understanding of the impact of turbulent mixing and how it can shape the hydrographic and biogeochemical characteristics of an ecosystem. The results show that turbulence is important for providing nitrate to the upper water column, which has also been observed in other productive ecosystems (e.g. Hales et al. (2005); Schafstall et al. (2010); Li et al. (2012); Kaneko et al. (2013); Cyr et al. (2015)). The analysis of turbulent fluxes conducted in this thesis is based on an extensive microstructure dataset. These analyses shed light on the distribution of turbulence in the tAUS, as they show that very high mixing rates are frequently observed in very shallow waters on the Angolan shelf. This mean distribution agrees well with the results of an idealized model simulation investigating internal tides at the Angolan continental slope and shelf (Zeng et al., 2021). Furthermore, the distribution also fits the observation of ISW and their breaking location on the shelf (Ostrowski, 2007; Ostrowski and Bazika-Sangolay, 2016). The results of this thesis underline that understanding variability in the background conditions is important for understanding the effect of turbulent fluxes. Mixing acting on different vertical nitrate gradients leads to a more tubulent nitrate flux during main upwelling season. Stronger cross-shore SST gradients during phases of weak stratification suggests more effective mixing. Nevertheless, the microstructure dataset shows high temporal and spatial variability, and open questions remain concerning the small-scale processes in the tAUS. This will be addressed in more detail in the outlook below.

The results of the mixed layer heat budget analysis in chapter 2 show that the seasonal cycle in SST is mainly driven by surface heat fluxes and turbulent heat loss at the base of the mixed layer. The importance of the surface heat fluxes for the seasonal cycle of SST was pointed out by other studies conducted in this region as well (Scannell and McPhaden, 2018; Foltz et al., 2019; Deppenmeier et al., 2020). Note that the southeastern tropical Atlantic is subject to a warm bias in SST in state-of-the-art climate models (Richter, 2015; Richter and Tokinaga, 2020; Kurian et al., 2021; Farneti et al., 2022). The reason for this warm bias is discussed to be connected to the representation of the atmosphere in these models (Huang et al., 2007; Hourdin et al., 2015; Voldoire et al., 2019; Richter and Tokinaga, 2020). Note here that the results of chapter 2 show that the satellite and reanalysis products are also subject to large uncertainties compared to ground-based observations. These results underline the gap in our knowledge concerning the surface heat fluxes in this region. The results of chapter 2 further show that turbulent heat loss at the base of the mixed layer is an important cooling term in the mixed layer heat budget, likely setting up the negative cross-shore SST gradient. Note in this context that warm bias in SST in state-of-the-art climate models is stronger at the coast than further offshore. Furthermore, it is stronger in austral winter than in austral summer (Richter and Tokinaga, 2020). This suggests that near-coastal mixing is not correctly represented in these climate models.

What controls the year-to-year variability of the main upwelling season in the tAUS?

The results of this thesis show how CTWs control the primary productivity in the tAUS during the main upwelling season in austral winter. Both the amplitude of the annual main upwelling CTW in austral winter and the peak in primary productivity undergo year-to-year variability. The strength of the CTW is strongly correlated with the peak in net primary production (NPP) occurring about 40 days later. This underlines the crucial role CTWs play in controlling primary productivity. It furthermore suggests a general predictability of the strength of productivity. Therefore, analyzing the remote and local influences of tropical Atlantic variability on the characteristics of the upwelling CTW gives insights into the controlling factors of the year-to-year variability of the main upwelling season in the tAUS.

In chapter 4, the dynamical factors controlling the timing and amplitude of the upwelling CTW are analyzed. The analysis shows that the timing and the amplitude of the main upwelling CTW in the tAUS are moderately correlated, such that if the CTW arrives earlier in the year, it tends to be stronger. Regression analyses further show that both the amplitude and timing of the upwelling CTW are connected to the variability of SST, wind, and SLA in the tropical and subtropical Atlantic. The timing of the upwelling CTW has been observed to occur between mid-June and mid-August. Regression maps suggest that weakened equatorial winds from April to July influence the generation of equatorial Kelvin waves, leading to a later arrival of the upwelling CTW in austral winter. The amplitude of the upwelling CTW is connected to the strength of the South Atlantic Anticyclone (SAA) four to five months before the SLA minimum. At the same time a cooling in the eastern equatorial Atlantic is connected to a stronger upwelling CTW. The strengthening of the SAA and the cooling in the eastern equatorial Atlantic might be connected through a change in cloud cover. However, the relationship is not robust and open questions remain. The equatorial wind field reacts to the cooling in the eastern equatorial Atlantic, leading to stronger winds two to one months before the SLA minimum. These eastward wind anomalies in turn likely influence the strength of the equatorial Kelvin wave leading to negative SLA and enhancing the SST anomalies at the equator. These results show that the variability of the timing and amplitude of the upwelling CTW are influenced by different regions in the tropical and subtropical Atlantic.

The findings of this thesis suggest that the timing and amplitude of the upwelling CTW in the tAUS during austral winter are predictable on seasonal time scales. This promising result implies that NPP is also potentially predictable on seasonal time scales. Such predictions are of great interest for local communities, as the tAUS is an ecosystem of high socio-economic interest (Hutchings et al., 2009; Sowman and Cardoso, 2010; FAO, 2022). This thesis lays the groundwork for further work on the prediction by analyzing dynamical factors influencing CTW characteristics. Similar predictive systems are also suggested for predicting Benguela Niño/Niña events (Imbol Koungue et al., 2017). However, recent studies reveal current challenges in predicting extreme events in SST in the tropical Atlantic on time scales longer than one month (Oettli et al., 2021; Li et al., 2023). A more detailed discussion on this and a possible route towards a predictive system for the strength of the productivity peak in the tAUS is presented in the outlook below.

The results in chapter 4 show that the remote influence of equatorial dynamics on the characteristics of the upwelling CTW is not constant over time. Between 1993 and 2007 a strong connection between variability at the equator and variability in the tAUS was observed, while between 2007 and 2022 the correlation weakened and the variability in both regions declined. Furthermore, there are indications that after the year 2007 local effects have a stronger influence on the CTW dynamics in the tAUS. Similar changes in variability have been shown for the variability of SST in both the equatorial Atlantic as well as in the Angola-Benguela Area (e.g. Tokinaga and Xie (2011); Servain et al. (2014); Prigent et al. (2020b,a); Crespo et al. (2022); Sobral Verona et al. (2023)). Many of these studies focus on SST variability in the context of extreme events, i.e. Atlantic and Benguela Niños/Niñas and show a general reduction in variability in recent decades. Analyzing the drivers of this change in variability is complex, as high multidecadal variability in the tropical Atlantic variability makes it hard to disentangle a response to climate warming from natural variability (Sobral Verona et al., 2023). Nevertheless, model projections suggest reduced variability in response to enhanced greenhouse gas forcing (Crespo et al., 2022; Prigent et al., 2023). In contrast to the studies discussed here, chapter 4 analyzes the year-to-year variability of CTWs during the main upwelling season. Nevertheless, similar results are found, showing a reduction in variability and weakened co-variability between the equator and the tAUS. Thus, the results of this thesis underline the need for a better understanding of tropical Atlantic variability. This understanding is crucial not only for comprehending extreme events but also for the variability of the upwelling season in the tAUS.

5.2 Outlook

The results of this thesis have advanced our understanding of the dynamics in the tAUS, providing new insights into how CTWs and near-coastal mixing can shape the characteristics of an ecosystem. Naturally, unresolved issues and open questions remain, which potentially could inspire further work. Some potential future projects are summarized in the following.

Predicting productivity in the tAUS

One promising outcome of this thesis is the implication that the peak in productivity in the tAUS is predictable on seasonal time scales. The results of this thesis lay the groundwork for further work on this subject. Given that productivity is tied to the dynamics of the upwelling CTW, predicting the strength of the upwelling CTW in austral winter is a crucial initial step.

One potential way to achieve predictions involves the use of dynamical forecasting systems. Similar systems have been suggested for predicting SST concerning extreme events (Imbol Koungue et al., 2017).

Despite advancements in improving model skills, recent studies have shown limited success in predicting SST anomalies in the tropical Atlantic, especially concerning extreme events (Counillon et al., 2021; Li et al., 2023). This challenge has been associated with a warm bias in state-of-the-art climate models, affecting the signal-to-noise ratio (Hu et al., 2013; Counillon et al., 2021; Li et al., 2023). Additionally, the complex nature of the forcing mechanisms, involving both local and remote oceanic and atmospheric influences (Lübbecke et al., 2019; Illig et al., 2020; Imbol Koungue et al., 2021), further complicates the prediction of extreme events in SST (Li et al., 2023). For predicting the strength and timing of the upwelling CTWs in austral winter in the tAUS, the warm bias in SST models is of secondary importance. Hence, predictions based on a dynamical forecasting system still hold promise. However, the results from chapter 4 suggest complex influences of tropical and subtropical variability on the strength and timing of the upwelling CTW in austral winter. It is theredore crucial to answer open questions and to ensure that the dynamical connections are accurately represented in the models for more reliable predictions.

Predicting the timing and strength of the upwelling CTW in austral winter in the tAUS can also be achieved via a statistical approach. Here, studies about using statistical models to predict El Niño Southern Oscilation (ENSO) in the Pacific Ocean can act as an inspiration for further work (e.g. Penland (1996); Mason and Mimmack (2002); Clarke and Van Gorder (2003); Petrova et al. (2017)). Such statistical models can be based on multivariate linear regression (Mason and Mimmack, 2002; Tseng et al., 2017) which could also be used for the prediction of the timing and strength of the upwelling CTW based on the results of chapter 4.

Another form of statistical model uses machine learning methods (Tang et al., 2018). Recent studies have made great progress predicting ENSO by applying deep learning methods such as convolutional neural network (CNN) models (Ham et al., 2019, 2021) and Taylor-ResNet model (Chen et al., 2023). These studies could act as a basis for the prediction of the timing and strength of the upwelling CTW in the tAUS. Note that one issue with using machine learning methods is the relatively short observational time period available to train the models. To resolve this problem, Ham et al. (2019, 2021) applied transfer learning using the output of climate models to train their CNN model. However, this is only successful if the model realistically simulates ENSO to some extent (Ham et al., 2019). Thus, models used to train a similar predictive model for the CTW dynamics of the tAUS have to be carefully selected.

A deeper understating of coastal trapped wave dynamics

One central result of this thesis is the presence of high-mode CTWs on the Angolan shelf in austral winter and their role in controlling the depth of the nitracline (chapter 3). The model results suggest that high-mode CTWs are phase-locked to the low-mode CTWs, where high-mode CTWs are constantly generated behind the low-mode CTWs. The good correlation between the observed SLA minimum (i.e. signal of the low-mode CTWs) and peak in NPP underlines the tight link between low- and high-mode CTWs. Thus, both observations and model output suggest similar results. Nevertheless, there are still many open questions about the dynamics of the high-mode CTWs and how they are connected to the low-mode CTWs: How is the energy scattered from low to high-mode CTWs? What role do friction, stratification, and topography changes along the wave path play in the energy scattering? What is the timing between the arrival of the low-mode and high-mode CTWs? Answering these questions is fundamental for a better understanding of CTW dynamics.

Tackling these open questions poses a challenge because of the complex dynamics behind CTWs. One possible route to answering some of these questions is to utilize models. Here, sensitivity experiments using an idealized numerical model could help to investigate the dynamics behind the high-mode CTWs. One such sensitivity experiment could involve running the model with reduced friction on the shelf/at the continental slope. These experiments could help to analyze how friction in this region alters CTW modal structures. The results could be interpreted in the context of previous work concerning frictional effects on CTWs (Brink, 1991; Romea and Allen, 1984; Brink, 2006). Another sensitivity experiment could involve running the model with horizontally uniform stratification. Along the wave guide, the CTWs are subject to stratification changes both in the cross-shelf direction as well as in the along-shelf direction. These stratification changes could impact modal structures. Further sensitivity experiments could involve using constant topography along the continental wave guide to analyze the influence of topography changes along the wave path on the modal structures.

A greater insight into CTW dynamics in the tAUS could also be provided by a more in-depth analysis of the surface signal of CTWs. The surface signal of CTWs is dominated by low-mode CTWs. This is due to the decreasing cross-shelf scales of the SLA structure associated with CTWs and the low effective resolution of SLA data of about $100\text{-}200\,km$ (Ballarotta et al., 2019). Nevertheless, the high-mode CTWs have a signal in SLA (Fig. 3.12). Here, data from the SWOT satellite mission (https://swot.jpl.nasa.gov) could give new insights into the CTW dynamics, as the data from the SWOT mission will have a much higher horizontal resolution. The data from the SWOT mission is not available yet and is thus subject to future studies.

A greater insight into turbulent processes

The results of this thesis show that turbulent fluxes play a central role in shaping characteristics in the tAUS. To analyze turbulent fluxes, an extensive microstructure dataset was used. The fluxes were analyzed quantitatively by averaging profiles taken in different depth ranges. This method is based on the assumption that the microstructure dataset is a good representation of the mean distribution of turbulence. However, the microstructure dataset showed high spatial and temporal variability. For instance, in April 2022, very high dissipation rates of turbulent kinetic energy were observed, likely attributed to the breaking of internal waves. Remarkably, the turbulent heat fluxes associated with this event were higher than the incoming net surface heat fluxes, highlighting the substantial impact of individual mixing events. This observation also emphasizes the challenges in measuring dissipation rates in such small-scale event-driven mixing regimes as spatial and temporal variability are high. Because of the high number of microstructure profiles available for this thesis, the turbulent fluxes presented here are likely still a good estimate. Nevertheless, a deeper understanding of the internal wave field and its dissipation could lead to a better understanding of turbulent fluxes. Further understanding of the characteristics of the internal wave field is also important to understand the distribution of small pelagic fish. Ostrowski and Bazika-Sangolay

(2016) showed how pelagic fish aggregations can be located inshore of a shallow front induced by internal wave breaking.

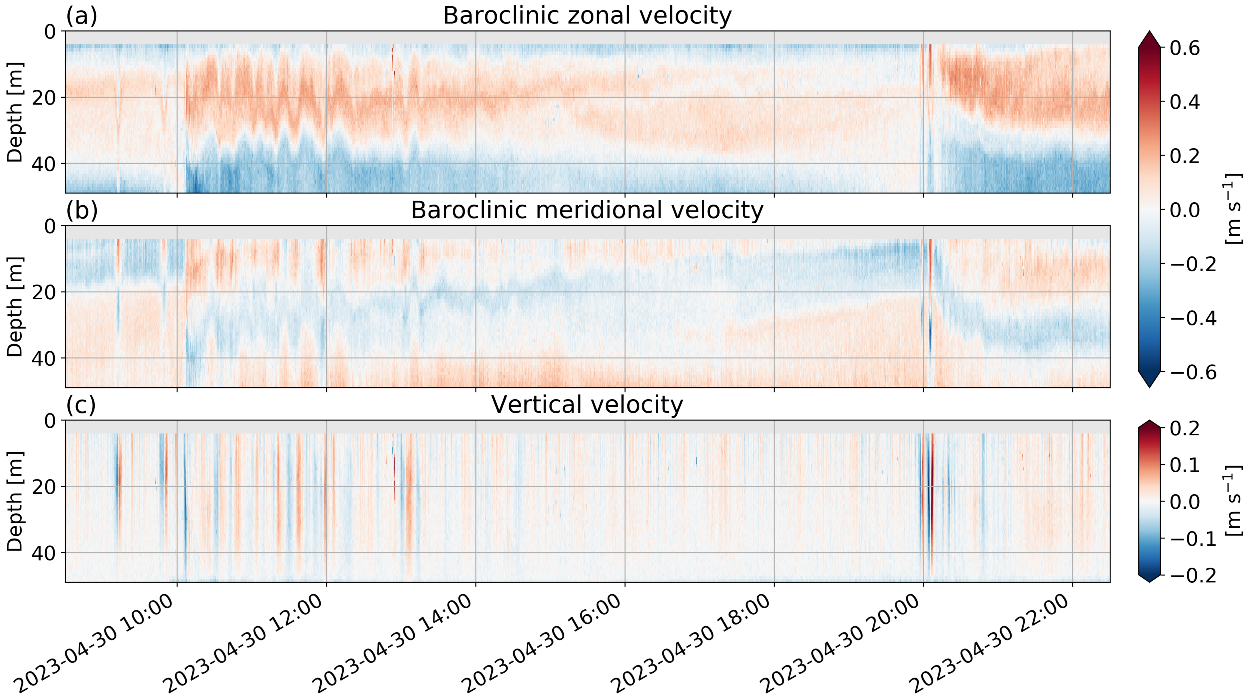

Figure 5.1: *Velocity time series from short-term mooring installed at the Angolan shelf at* $10°33'S$; $13°30'E$ *in 50 m depth. The mooring has been installed there between the 2023-04-29 and the 2023-05-07. This figure shows the velocity from 2023-04-30 08:30 UTC until 2023-04-30 22:30 UTC. (a) displays the baroclinic zonal, (b) the baroclinic meridional, and (c) the vertical velocity. Note the different colorscale used for the horizontal (a) & (b) and the vertical velocity (c).*

One possible route to gain a deeper understanding of the small-scale processes is by characterizing singular wave driven mixing events. One presumably important form of wave-driven mixing events in the tAUS is connected to the breaking of internal solitary waves (ISWs). Energetic ISWs have been frequently observed on the Angolan shelf (Ostrowski et al., 2009; Ostrowski and Bazika-Sangolay, 2016). Characterizing ISWs and their energetics poses a challenge as they exhibit high spatial and temporal variability. Two research cruises on *R/V Meteor* in June 2018 and April/May 2023 were conducted, collecting high-resolution data that could be used for process studies on ISWs. The available datasets include velocity data from short-term moorings installed at various depths. Exemplary measurements of ISW packages in the mooring data are presented in Fig. 5.1. In the course of about 12 hours, two ISW packages arrive at the mooring site. Zones of convergence and divergence associated with these waves induce high vertical velocities. Furthermore, they are accompanied by high vertical shear of the horizontal velocities. This short record of velocity measurement on the Angolan shelf also shows high variability of the characteristics between the wave events. In addition to the mooring data, during the cruise in April/May 2023 surface drifters were deployed with the aim to measure the lateral mass transport of ISW induced by the Stokes drift. These datasets could help to characterize ISWs on the Angolan shelf, giving further insights into their role in vertical mixing and lateral exchange. Studies of ISW on the Angolan shelf could follow the example of studies on ISW conducted in other shelf systems. Examples are the observational studies conducted at the New Jersey shelf (Shroyer et al., 2010a,b; Nash et al., 2012), the Oregon coast (D'Asaro et al., 2007; Moum et al., 2007a,b), the Washington shelf (Zhang et al., 2015), or the South China Sea (Lien et al., 2013). Insights gained in these process studies could be scaled up via satellite data, as ISW have a signal in synthetic aperture radar (SAR) images (Brandt, 1996; Zhang et al., 2015; Zeng et al., 2021). The challenges of such studies include the unpredictability of internal tides, as internal tides in coastal regions usually come from multiple locations, possibly including remote and local sources (Nash et al., 2012; Alford et al., 2012).

The secondary productivity peak in the tAUS

In the tAUS, NPP not only peaks in late austral winter but also exhibits a secondary peak in January/February. The secondary peak is notably weaker and primarily confined to the northern tAUS (Fig. 1.2). The timing of the secondary NPP peak aligns with the passage of the secondary upwelling CTW, which occurs about a month earlier. This suggests that similar mechanisms are at play to force this secondary NPP peak as for the main productivity season presented in this thesis. However, a more detailed examination of the secondary productivity is essential to confirm this hypothesis.

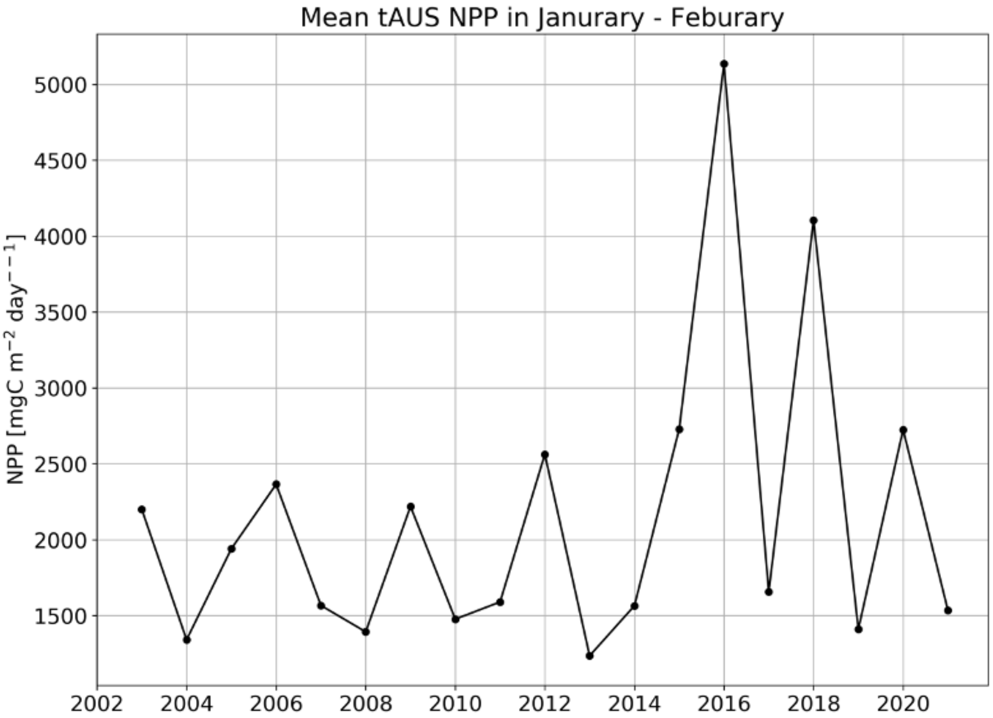

Figure 5.2: *Time series of mean January – February net primary production (NPP) averaged over the tAUS (8°S - 15°S, 1° distance to the coast). NPP data from 2003-2021 is used from the ocean productivity site (http://orca.science.oregonstate.edu/1080.by.2160.8day.hdf.eppley.m.chl.m.sst.php).*

Satellite data of NPP during January-February reveals high interannual variability of the secondary NPP peak in the tAUS (Fig. 5.2). Notably, the mean NPP during these months is largely influenced by a singular event in 2016. In 2016 a Benguela Niño occurred off the coast of Angola (Lübbecke et al., 2019). During this event, freshwater from the Congo River was advected anomalously far south. Another strong NPP peak in January/February occurred in 2018, coinciding with an anomalous southward advection of the Congo River plume as well (Martins and Stammer, 2022). Note that satellite data could overestimate NPP because of colored dissolved organic matter from the Congo River (Del Vecchio and Subramaniam, 2004). This raises the possibility that the observed signal may stem from the intrusion of freshwater into the tAUS. The possible influence of freshwater on the NPP signal in the tAUS poses a challenge in interpreting the secondary NPP data. A comparison between SSS and NPP data might help to disentangle the signals. The results of this thesis underline the importance of the vertical movement of the nitracline as well as the onshore advection of nitrate-rich water for the main NPP peak. Further analysis of the secondary NPP peak could thus include the analysis of the isopycnal movement in the range of nitracline associated with the passage of the secondary CTW. Unfortunately, the availability of hydrographic data during January/February is limited (Kopte et al., 2017). A potential solution to this challenge could involve analyzing the output of reanalysis products like GLORYS12 (Lellouche et al., 2021), which compared well to observations in this region (see chapter 2).

What drives seaonality in productivity in other tropical upwelling systems?

The thesis focuses on the drivers of seasonal variability in the tAUS. The tAUS is not the only tropical upwelling system in the world. Located at the eastern boundary of the Atlantic and Pacific Oceans exist other highly productive upwelling systems. They are also of great importance for local fisheries and are key regions in biogeochemical cycles (Kämpf and Chapman, 2016). Similarly to the tAUS, in other tropical upwelling systems, maxima in local wind-driven upwelling and productivity maxima are also disjoint (Thomas et al., 2001, 2012). This suggests that other processes drive productivity in these regions. Based on the results of this thesis, it is of high interest to analyze whether similar mechanisms as in the tAUS might exist in other tropical upwelling systems. It is especially of interest if the presence of high-mode CTWs and their role in controlling the depth of the nitracline is unique for the tAUS. Such investigations might contribute to a better understanding of the factors influencing seasonal variations in biological productivity in these important coastal systems.

In the northern hemisphere of the tropical Atlantic, the Gulf of Guinea Upwelling System (GGUS) stands out as a highly productive ecosystem, influenced by both local and remote forcing. For a review of the physical processes in the GGUS, the reader is referred to Brandt et al. (2023). Current research emphasizes the role of the eastward-flowing Guinea current for the upwelling in the GGUS, highlighting the role of nonlinear effects and the shape of the coastline (Djakouré et al., 2014, 2017). Furthermore, for the eastern GGUS, the role of local wind-driven upwelling is highlighted (Brandt et al., 2023). The GGUS is influenced by equatorial dynamics via the propagation of Kelvin waves and CTWs (Picaut, 1983; Polo et al., 2008). The equatorial forcing is similar to the equatorial forcing in the tAUS, as both north and southward CTWs are forced at the eastern boundary (Brandt et al., 2023). Thus, it would be interesting to revisit the role of CTWs in the GGUS in the context of the results found in this thesis. Especially the modal structures of CTWs and their influence on the conditions in the GGUS would be of interest.

In the southern hemisphere of the Pacific Ocean, the Peruvian upwelling system (PUS) is a highly productive ecosystem (Chavez et al., 2008). In contrast to tAUS alongshore upwelling favorable winds are stronger. However, the peak in productivity is also disjoint from the peak in local wind-driven upwelling

(Chavez and Messié, 2009; Thomas et al., 2001, 2012; Xue et al., 2022). The seasonal cycle in productivity in the PUS has been linked to changes in mixed layer depth, as a deep mixed layer reduces growth due to limited light (Echevin et al., 2008; Xue et al., 2022). Conditions in the PUS are influenced by CTWs on different time scales (Gutiérrez et al., 2008; Pizarro et al., 2002; Illig et al., 2018b,a). Echevin et al. (2014) found that intraseasonal CTWs can induce phytoplankton blooms in the PUS. Interestingly, they find the presence of high-mode intraseasonal CTWs in their model simulation, which control the depth of the nitracline. Thus, with the results of this thesis, the role of CTWs for productivity in the PUS could be revisited. In contrast to the Atlantic, the Pacific does not exhibit a strong annual and semi-annual cycle. Thus, the effect of CTWs might be harder to point out. Nevertheless, they could play an important role for the productivity in the PUS, maybe also for the seasonal peak in productivity.

References

Alford, M. H., Mickett, J. B., Zhang, S., MacCready, P., Zhao, Z., and Newton, J. (2012). Internal waves on the Washington continental shelf. *Oceanography*, 25(2):66–79, ISSN: 10428275, DOI: 10.5670/oceanog.2012.43.

Apel, J. R. (2002). Oceanic internal waves and solitons. *An atlas of oceanic internal solitary waves*, 1:1–40, http://www.internalwaveatlas.com/Atlas2_PDF/IWAtlas_Pg001_Background&Theory.pdf.

Awo, F. M., Rouault, M., Ostrowski, M., Tomety, F. S., Da-Allada, C. Y., and Jouanno, J. (2022). Seasonal cycle of sea surface salinity in the Angola Upwelling System. *Journal of Geophysical Research: Oceans*, 127(7):e2022JC018518, DOI: 10.1029/2022JC018518.

Bachèlery, M. L., Illig, S., and Dadou, I. (2016a). Forcings of nutrient, oxygen, and primary production interannual variability in the southeast Atlantic Ocean. *Geophysical Research Letters*, 43(16):8617–8625, ISSN: 19448007, DOI: 10.1002/2016GL070288.

Bachèlery, M.-L., Illig, S., and Dadou, I. (2016b). Interannual variability in the South-East Atlantic Ocean, focusing on the Benguela Upwelling System: Remote versus local forcing. *Journal of Geophysical Research: Oceans*, 121(1):284–310, ISSN: 21699291, DOI: 10.1002/2015JC011168.

Bachèlery, M.-L., Illig, S., and Rouault, M. (2020). Interannual Coastal Trapped Waves in the Angola-Benguela Upwelling System and Benguela Niño and Niña events. *Journal of Marine Systems*, 203:103262, ISSN: 09247963, DOI: 10.1016/j.jmarsys.2019.103262.

Baines, P. G. (1982). On internal tide generation models. *Deep Sea Research Part A, Oceanographic Research Papers*, 29(3):307–338, ISSN: 01980149, DOI: 10.1016/0198-0149(82)90098-X.

Bakun, A. and Weeks, S. J. (2008). The marine ecosystem off Peru: What are the secrets of its fishery productivity and what might its future hold? *Progress in Oceanography*, 79(2-4):290–299, ISSN: 00796611, DOI: 10.1016/j.pocean.2008.10.027.

Ballarotta, M., Ubelmann, C., Pujol, M.-I., Taburet, G., Fournier, F., Legeais, J.-F., Faugère, Y., Delepoulle, A., Chelton, D., Dibarboure, G., and Picot, N. (2019). On the resolutions of ocean altimetry maps. *Ocean Science*, 15(4):1091–1109, DOI: 10.5194/os-15-1091-2019.

Berrit, G. R. (1976). Les eaux froides cotieres du Gabon a L'Angola sont-elles dues a un upwelling d'Ekman. *Cahier ORSTOM Séries Océanographie*, 14:273–278, https://horizon.documentation.ird.fr/exl-doc/pleins_textes/cahiers/oceanographie/19727.pdf.

Blamey, L. K., Shannon, L. J., Bolton, J. J., Crawford, R. J., Dufois, F., Evers-King, H., Griffiths, C. L., Hutchings, L., Jarre, A., Rouault, M., Watermeyer, K. E., and Winker, H. (2015). Ecosystem change in the southern Benguela and the underlying processes. *Journal of Marine Systems*, 144:9–29, ISSN: 09247963, DOI: 10.1016/j.jmarsys.2014.11.006.

Boely, T. and Fréon, P. (1980). Coastal pelagic resources. *The fish resources of the Eastern Central Atlantic*.

Bordbar, M. H., Mohrholz, V., and Schmidt, M. (2021). The Relation of Wind-Driven Coastal and Offshore Upwelling in the Benguela Upwelling System. *Journal of Physical Oceanography*, 51(10):3117–3133, ISSN: 15200485, DOI: 10.1175/JPO-D-20-0297.1.

Boyer, D. C., Boyer, H. J., Fossen, I., and Kreiner, A. (2001). Changes in abundance of the northern Benguela sardine stock during the decade 1990-2000, with comments on the relative importance of fishing and the environment. *African Journal of Marine Science*, 23:67–84, https://www.ajol.info/index.php/ajms/article/view/33342.

Brandt, P. (1996). *Interne Wellen in den Straßen von Gibraltar und Messina*. Doctoral dissertation, Universität Hamburg.

Brandt, P., Alory, G., Awo, F. M., Dengler, M., Djakouré, S., Imbol Koungue, R. A., Jouanno, J., Körner, M., Roch, M., and Rouault, M. (2023). Physical processes and biological productivity in the upwelling regions of the tropical Atlantic. *Ocean Science*, 19(3):581–601, DOI: 10.5194/os-19-581-2023.

Brandt, P., Bordbar, M. H., Coelho, P., Koungue, R. A. I., Körner, M., Lamont, T., Lübbecke, J. F., Mohrholz, V., Prigent, A., Roch, M., Schmidt, M., van der Plas, A. K., and Veitch, J. (2024). *Physical Drivers of Southwest African Coastal Upwelling and Its Response to Climate Variability and Change*, pages 221–257. Springer International Publishing, Cham, ISBN: 978-3-031-10948-5, DOI: 10.1007/978-3-031-10948-5_9.

Brandt, P., Claus, M., Greatbatch, R. J., Kopte, R., Toole, J. M., Johns, W. E., and Böning, C. W. (2016). Annual and Semiannual Cycle of Equatorial Atlantic Circulation Associated with Basin-Mode Resonance. *Journal of Physical Oceanography*, 46(10):3011–3029, ISBN: 978-0-203-08066-5, ISSN: 0022-3670, DOI: 10.1175/JPO-D-15-0248.1.

Brink, K. (1982). A comparison of Long Coastal Trapped Wave Theory with Observation off Peru. *Journal of Physical Oceanography*, 12:987–913, https://doi.org/10.1175/1520-0485(1982)012%3C0897:ACOLCT%3E2.0.CO;2.

Brink, K. and Chapman, D. C. (1987). Programs for computing properties of coastal-trapped waves and wind-driven motions over the continental shelf and slope. DOI: 10.1575/1912/5363.

Brink, K. H. (1983). The near-surface dynamics of coastal upwelling. *Progress in Oceanography*, 12(3):223–257, ISSN: 00796611, DOI: 10.1016/0079-6611(83)90009-5.

Brink, K. H. (1989). Energy conservation in coastal-trapped wave calculations. *Journal of physical oceanography*, 19(7):1011–1016, https://doi.org/10.1175/1520-0485(1989)019%3C1011:ECICTW%3E2.0.CO;2.

Brink, K. H. (1991). Coastal-Trapped Waves Continental Shelf. *Annual Review of Fluid Mechanics*, 23:389–412, DOI: 10.1146/annurev.fl.23.010191.002133.

Brink, K. H. (2006). Coastal-trapped waves with finite bottom friction. *Dynamics of Atmospheres and Oceans*, 41(3-4):172–190, ISSN: 03770265, DOI: 10.1016/j.dynatmoce.2006.05.001.

Browning, T. J., Achterberg, E. P., Rapp, I., Engel, A., Bertrand, E. M., Tagliabue, A., and Moore, C. M. (2017). Nutrient co-limitation at the boundary of an oceanic gyre. *Nature*, 551(7679):242–246, ISSN: 14764687, DOI: 10.1038/nature24063.

Cane, M. A. and Moore, D. W. (1981). A Note on Low-Frequency Equatorial Basin Modes. *Journal of Physical Oceanography*, 11:1578–1584, DOI: 10.7916/D84J0QQW.

Cazenave, A., Hamlington, B., Horwath, M., Barletta, V. R., Benveniste, J., Chambers, D., Döll, P., Hogg, A. E., Legeais, J. F., Merrifield, M., Meyssignac, B., Mitchum, G., Nerem, S., Pail, R., Palanisamy, H., Paul, F., von Schuckmann, K., and Thompson, P. (2019). Observational requirements for long-term monitoring of the global mean sea level and its components over the altimetry era. *Frontiers in Marine Science*, 6(SEP):1–14, ISSN: 22967745, DOI: 10.3389/fmars.2019.00582.

Chang, P., Fang, Y., Saravanan, R., Ji, L., and Seidel, H. (2006). The cause of the fragile relationship between the Pacific El Niño and the Atlantic Niño. *Nature*, 443(7109):324–328, ISSN: 14764687, DOI: 10.1038/nature05053.

Chapman, D. C. (1987). Application of wind-forced, long, coastal-trapped wave theory along the California coast. *Journal of Geophysical Research: Oceans*, 92(C2):1798–1816, ISSN: 21699291, DOI: 10.1029/JC092iC02p01798.

Chavez, F. P., Bertrand, A., Guevara-Carrasco, R., Soler, P., and Csirke, J. (2008). The northern Humboldt Current System: Brief history, present status and a view towards the future. *Progress in Oceanography*, 79(2-4):95–105, ISSN: 00796611, DOI: 10.1016/j.pocean.2008.10.012.

Chavez, F. P. and Messié, M. (2009). A comparison of Eastern Boundary Upwelling Ecosystems. *Progress in Oceanography*, 83(1-4):80–96, ISSN: 00796611, DOI: 10.1016/j.pocean.2009.07.032.

Chen, Y., Huang, X., Luo, J. J., Lin, Y., Wright, J. S., Lu, Y., Chen, X., Jiang, H., and Lin, P. (2023). Prediction of ENSO using multivariable deep learning. *Atmospheric and Oceanic Science Letters*, 16(4), ISSN: 23766123, DOI: 10.1016/j.aosl.2023.100350.

Clarke, A. J. (1977). Observational and Numerical Evidence for Wind-Forced Coastal Trapped Long Waves. *Journal of Physical Oceanography*, 7(2):231–247, ISSN: 0029-5582, DOI: 10.1175/1520-0485(1977)007<0231:OANEFW>2.0.CO;2.

Clarke, A. J. and Brink, K. H. (1985). The response of stratified, frictional flow of shelf and slope waters to fluctuating large-scale, low-frequency wind forcing. *Journal of Physical Oceanography*, 15(4):439–453, https://doi.org/10.1175/1520-0485(1985)015%3C0439:TROSFF%3E2.0.CO;2.

Clarke, A. J. and Van Gorder, S. (2003). Improving El Niño prediction using a space-time integration of Indo-Pacific winds and equatorial Pacific upper ocean heat content. *Geophysical Research Letters*, 30(7):2–5, ISSN: 00948276, DOI: 10.1029/2002GL016673.

Collos, Y. (1986). Time-lag algal growth dynamics: biological constraints on primary production in aquatic environments. *Marine Ecology Progress Series*, 33:193–206, ISSN: 0171-8630, DOI: 10.3354/meps033193.

Counillon, F., Keenlyside, N., Toniazzo, T., Koseki, S., Demissie, T., Bethke, I., and Wang, Y. (2021). Relating model bias and prediction skill in the equatorial Atlantic. *Climate Dynamics*, 56(7-8):2617–2630, ISBN: 0123456789, ISSN: 14320894, DOI: 10.1007/s00382-020-05605-8.

Crespo, L. R., Prigent, A., Keenlyside, N., Koseki, S., Svendsen, L., Richter, I., and Sánchez-Gómez, E. (2022). Weakening of the Atlantic Niño variability under global warming. *Nature Climate Change*, 12(9):822–827, ISBN: 4155802201, ISSN: 17586798, DOI: 10.1038/s41558-022-01453-y.

Cyr, F., Bourgault, D., Galbraith, P. S., and Gosselin, M. (2015). Turbulent nitrate fluxes in the Lower St. Lawrence Estuary, Canada. *Journal of Geophysical Research C: Oceans*, 120(3):2308–2330, ISSN: 21699291, DOI: 10.1002/2014JC010272.

Dangendorf, S., Hay, C., Calafat, F. M., Marcos, M., Piecuch, C. G., Berk, K., and Jensen, J. (2019). Persistent acceleration in global sea-level rise since the 1960s. *Nature Climate Change*, 9(9):705–710, ISSN: 17586798, DOI: 10.1038/s41558-019-0531-8.

D'Asaro, E. A., Lien, R. C., and Henyey, F. (2007). High-frequency internal waves on the Oregon continental shelf. *Journal of Physical Oceanography*, 37(7):1956–1967, ISSN: 00223670, DOI: 10.1175/JPO3096.1.

Dauxois, T., Didier, A., and Falcon, E. (2004). Observation of near-critical reflection of internal waves in a stably stratified fluid. *Physics of Fluids*, 16(6):1936–1941, ISSN: 10706631, DOI: 10.1063/1.1711814.

Davis, R. E. (1996). Sampling turbulent dissipation. *Journal of Physical Oceanography*, 26(3):341–358, https://doi.org/10.1175/1520-0485(1996)026%3C0341:STD%3E2.0.CO;2.

Del Vecchio, R. and Subramaniam, A. (2004). Influence of the Amazon River on the surface optical properties of the western tropical North Atlantic Ocean. *Journal of Geophysical Research: Oceans*, 109(11):1–13, ISSN: 21699291, DOI: 10.1029/2004JC002503.

Deppenmeier, A.-L. (2022). The Atlantic Niño weakens. *Nature Climate Change*, 12(9):780–781, ISSN: 1758-6798, DOI: 10.1038/s41558-022-01460-z.

Deppenmeier, A. L., Haarsma, R. J., van Heerwaarden, C., and Hazeleger, W. (2020). The southeastern tropical atlantic sst bias investigated with a coupled atmosphere-ocean single-column model at a pirata mooring site. *Journal of Climate*, 33(14):6255–6271, ISSN: 08948755, DOI: 10.1175/JCLI-D-19-0608.1.

Ding, H., Keenlyside, N. S., and Latif, M. (2009). Seasonal cycle in the upper equatorial Atlantic Ocean. *Journal of Geophysical Research: Oceans*, 114(9):1–16, ISSN: 21699291, DOI: 10.1029/2009JC005418.

Djakouré, S., Penven, P., Bourlès, B., Koné, V., and Veitch, J. (2017). Respective roles of the Guinea current and local winds on the coastal upwelling in the northern Gulf of Guinea. *Journal of Physical Oceanography*, 47(6):1367–1387, ISSN: 15200485, DOI: 10.1175/JPO-D-16-0126.1.

Djakouré, S., Penven, P., Bourlès, B., Veitch, J., and Koné, V. (2014). Coastally trapped eddies in the north of the Gulf of Guinea. *Journal of Geophysical Research: Oceans*, 119(10):6805–6819, DOI: 10.1002/2014JC010243.

Dunn, J. (2009). CARS 2009: CSIRO atlas of regional seas.

Dussin, R., Barnier, B., Brodeau, L., and Molines, J. M. (2016). The making of Drakkar forcing set DFS5. *DRAKKAR/MyOcean Report 01-04-16, LGGE, Grenoble, France*, (April), https://www.drakkar-ocean.eu/publications/reports/report_DFS5v3_April2016.pdf.

Echevin, V., Albert, A., Lévy, M., Graco, M., Aumont, O., Piétri, A., and Garric, G. (2014). Intraseasonal variability of nearshore productivity in the Northern Humboldt Current System: The role of coastal trapped waves. *Continental Shelf Research*, 73:14–30, ISSN: 02784343, DOI: 10.1016/j.csr.2013.11.015.

Echevin, V., Aumont, O., Ledesma, J., and Flores, G. (2008). The seasonal cycle of surface chlorophyll in the Peruvian upwelling system: A modelling study. *Progress in Oceanography*, 79(2-4):167–176, ISSN: 00796611, DOI: 10.1016/j.pocean.2008.10.026.

Einstein, A. (1905). Über die von der molekularkinetischen Theorie der Wärme geforderte Bewegung von in ruhenden Flüssigkeiten suspendierten Teilchen. *Annalen der physik*, 4, DOI: 10.1002/andp.19053220806.

Eppley, R. W. and Peterson, B. J. (1979). Particulate organic matter flux and planktonic new production in the deep ocean. *Nature*, 282(5740):677–680, DOI: 10.1038/282677a0.

ESR (2009). OSCAR third deg. Ver. 1. PO.DAAC, CA, USA, Dataset accessed [2021]. https://doi.org/10.5067/OSCAR-10D01.

FAO (2022). Fishery and aquaculture country profiles: Republic of Angola. https://www.fao.org/fishery/en/facp/ago?lang=en.

Farneti, R., Stiz, A., and Ssebandeke, J. B. (2022). Improvements and persistent biases in the southeast tropical Atlantic in CMIP models. *npj Climate and Atmospheric Science*, 5(1):42, ISBN: 4161202200264, DOI: 10.1038/s41612-022-00264-4.

Ferrari, R. and Wunsch, C. (2009). Ocean circulation kinetic energy: Reservoirs, sources, and sinks. *Annual Review of Fluid Mechanics*, 41:253–282, ISSN: 00664189, DOI: 10.1146/annurev.fluid.40.111406.102139.

Ferreira, A., Sá, C., Silva, N., Beltrán, C., Dias, A. M., and Brito, A. C. (2020). Phytoplankton response to nutrient pulses in an upwelling system assessed through a microcosm experiment (Algarrobo Bay, Chile). *Ocean and Coastal Management*, 190(March), ISSN: 09645691, DOI: 10.1016/j.ocecoaman.2020.105167.

Fick, A. (1855). V. On liquid diffusion. *The London, Edinburgh, and Dublin Philosophical Magazine and Journal of Science*, 10(63):30–39, DOI: 10.1080/14786445508641925.

Florenchie, P., Lutjeharms, J. R., Reason, C. J., Masson, S., and Rouault, M. (2003). The source of Benguela Niños in the South Atlantic Ocean. *Geophysical Research Letters*, 30(10):10–13, ISSN: 00948276, DOI: 10.1029/2003gl017172.

Foltz, G. R., Brandt, P., Richter, I., Rodriguez-fonseca, B., Hernandez, F., Dengler, M., Rodrigues, R. R., Schmidt, J. O., Yu, L., Lefevre, N., Da Cunha, L. C., McPhaden, M. J., Araujo Filho, M. C., Karstensen, J., Hahn, J., Martín-Rey, M., Patricola, C. M., Poli, P., Zuidema, P., Hummels, R., Perez, R. C., Hatje, V., Luebbecke, J., Polo, I., Lumpkin, R., Bourlès, B., Asuquo, F. E., Lehodey, P., Conchon, A., Chang, P., Dandin, P., Schmid, C., Sutton, A. J., Giordani, H., Xue, Y., Illig, S., Losada, T., Grodsky, S., Gasparin, F., Lee, T., Mohino, E., Nobre, P., Wanninkhof, R., Keenlyside, N. S., Garcon, V., Sanchez-Gomez, E., Nnamchi, H. C., Drevillon, M., Storto, A., Remy, E., Lazar, A., Speich, S., Goes, M. P., Dorrington, T., Johns, W. E., Moum, J. N., Robinson, C., Perruche, C., Souza, R. B., Gaye, A., Lopez-Parages, J., Monerie, P. A., Castellanos, P., Benson, N. U., Hounkonnou, M. N., and Duha, J. T. (2019). The tropical atlantic observing system. *Frontiers in Marine Science*, 6(APR):1–36, ISSN: 22967745, DOI: 10.3389/fmars.2019.00206.

Foltz, G. R., Grodsky, S. A., Carton, J. A., and McPhaden, M. J. (2003). Seasonal mixed layer heat budget of the tropical Atlantic Ocean. *Journal of Geophysical Research*, 108(C5):1–13, ISSN: 0148-0227, DOI: 10.1029/2002jc001584.

Foltz, G. R. and McPhaden, M. J. (2010). Interaction between the Atlantic meridional and Niño modes. *Geophysical Research Letters*, 37(18):1–5, ISSN: 00948276, DOI: 10.1029/2010GL044001.

Foltz, G. R., Schmid, C., and Lumpkin, R. (2013). Seasonal cycle of the mixed layer heat budget in the northeastern tropical atlantic ocean. *Journal of Climate*, 26(20):8169–8188, ISSN: 08948755, DOI: 10.1175/JCLI-D-13-00037.1.

Gammelsrød, T., Bartholomae, C. H., Boyer, D. C., Filipe, V. L., and O'Toole, M. J. (1998). Intrusion of warm surface water along the Angolan-Namibian coast in February-March 1995: The 1995 Benguela Nino. *South African Journal of Marine Science*, (19):41–56, ISSN: 02577615, DOI: 10.2989/025776198784126719.

Garett, C. and Kunze, E. (2007). Internal tide generation in the deep ocean. *Annual Review of Fluid Mechanics*, 39:57–87, ISBN: 0824307399, ISSN: 00664189, DOI: 10.1146/annurev.fluid.39.050905.110227.

Gill, A. (1982). *Atmosphere-ocean Dynamics*. ISBN: 0122835204.

Gill, A. E. and Clarke, A. J. (1974). Wind-induced upwelling, coastal currents and sea-level changes. *Deep-Sea Research and Oceanographic Abstracts*, 21(5):325–345, ISSN: 00117471, DOI: 10.1016/0011-7471(74)90038-2.

Global Modeling and Assimilation Office (GMAO) (2008). tavgM_2d_ocn_Nx: MERRA 2D IAU Ocean Surface Diagnostic, Monthly Mean V5.2.0, Greenbelt, MD, USA, Goddard Earth Sciences Data and Information Services Center (GES DISC), Accessed: [2021],. DOI: 10.5067/LH0VEHYM7Y8Z.

Gómez-Valdivia, F., Parés-Sierra, A., and Laura Flores-Morales, A. (2017). Semiannual variability of the California Undercurrent along the Southern California Current System: A tropical generated phenomenon. *Journal of Geophysical Research: Oceans*, 122(2):1574–1589, DOI: 10.1002/2016JC012350.

Good, S., Fiedler, E., Mao, C., Martin, M. J., Maycock, A., Reid, R., Roberts-Jones, J., Searle, T., Waters, J., While, J., and Worsfold, M. (2020). The current configuration of the OSTIA system for operational production of foundation sea surface temperature and ice concentration analyses. *Remote Sensing*, 12(4):4, ISSN: 20724292, DOI: 10.3390/rs12040720.

Gregg, M. C., D'Asaro, E. A., Riley, J. J., and Kunze, E. (2018). Mixing Efficiency in the Ocean. *Annual Review of Marine Science*, 10(1):443–473, ISSN: 1941-1405, DOI: 10.1146/annurev-marine-121916-063643.

Gutiérrez, D., Enríquez, E., Purca, S., Quipúzcoa, L., Marquina, R., Flores, G., and Graco, M. (2008). Oxygenation episodes on the continental shelf of central Peru: Remote forcing and benthic ecosystem response. *Progress in Oceanography*, 79(2-4):177–189, ISSN: 00796611, DOI: 10.1016/j.pocean.2008.10.025.

Hales, B., Moum, J. N., Covert, P., and Perlin, A. (2005). Irreversible nitrate fluxes due to turbulent mixing in a coastal upwelling system. *Journal of Geophysical Research: Oceans*, 110(10):1–19, ISSN: 21699291, DOI: 10.1029/2004JC002685.

Hall, R. A., Huthnance, J. M., and Williams, R. G. (2012). Internal Wave Reflection on Shelf Slopes with Depth-Varying Stratification. *Journal of Physical Oceanography*, 43(2):248–258, ISSN: 0022-3670, DOI: 10.1175/jpo-d-11-0192.1.

Ham, Y. G., Kim, J. H., Kim, E. S., and On, K. W. (2021). Unified deep learning model for El Niño/Southern Oscillation forecasts by incorporating seasonality in climate data. *Science Bulletin*, 66(13):1358–1366, ISSN: 20959281, DOI: 10.1016/j.scib.2021.03.009.

Ham, Y. G., Kim, J. H., and Luo, J. J. (2019). Deep learning for multi-year ENSO forecasts. *Nature*, 573(7775):568–572, ISSN: 14764687, DOI: 10.1038/s41586-019-1559-7.

Hansingo, K. and Reason, C. J. (2009). Modelling the atmospheric response over southern Africa to SST forcing in the southeast tropical Atlantic and southwest subtropical Indian oceans. *International Journal of Climatology*, 29(7):1001–1012, ISSN: 08998418, DOI: 10.1002/joc.1919.

Hersbach, H., Bell, B., Berrisford, P., Hirahara, S., Horányi, A., Muñoz-Sabater, J., Nicolas, J., Peubey, C., Radu, R., Schepers, D., Simmons, A., Soci, C., Abdalla, S., Abellan, X., Balsamo, G., Bechtold, P., Biavati, G., Bidlot, J., Bonavita, M., De Chiara, G., Dahlgren, P., Dee, D., Diamantakis, M., Dragani, R., Flemming, J., Forbes, R., Fuentes, M., Geer, A., Haimberger, L., Healy, S., Hogan, R. J., Hólm, E., Janisková, M., Keeley, S., Laloyaux, P., Lopez, P., Lupu, C., Radnoti, G., de Rosnay, P., Rozum, I., Vamborg, F., Villaume, S., and Thépaut, J. N. (2020). The ERA5 global reanalysis. *Quarterly Journal of the Royal Meteorological Society*, 146(730):1999–2049, ISSN: 1477870X, DOI: 10.1002/qj.3803.

Hourdin, F., Ginus-Bogdan, A., Braconnot, P., Dufresne, J. L., Traore, A. K., and Rio, C. (2015). Air moisture control on ocean surface temperature, hidden key to the warm bias enigma. *Geophysical Research Letters*, 42(24):10885–10893, ISSN: 19448007, DOI: 10.1002/2015GL066764.

Hu, Z. Z. and Huang, B. (2007). Physical processes associated with the tropical Atlantic SST gradient during the anomalous evolution in the Southeastern Ocean. *Journal of Climate*, 20(14):3366–3378, ISSN: 08948755, DOI: `10.1175/JCLI4189.1`.

Hu, Z. Z., Kumar, A., Huang, B., Wang, W., Zhu, J., and Wen, C. (2013). Prediction skill of monthly SST in the North Atlantic Ocean in NCEP Climate Forecast System version 2. *Climate Dynamics*, 40(11-12):2745–2759, ISSN: 09307575, DOI: `10.1007/s00382-012-1431-z`.

Hu, Z. Z., Kumar, A., Huang, B., Zhu, J., L'Heureux, M., McPhaden, M. J., and Yu, J. Y. (2020). The interdecadal shift of ENSO properties in 1999/2000: A review. *Journal of Climate*, 33(11):4441–4462, ISSN: 08948755, DOI: `10.1175/JCLI-D-19-0316.1`.

Huang, B., Hu, Z. Z., and Jha, B. (2007). Evolution of model systematic errors in the tropical atlantic basin from coupled climate hindcasts. *Climate Dynamics*, 28(7-8):661–682, ISSN: 09307575, DOI: `10.1007/s00382-006-0223-8`.

Hummels, R., Dengler, M., Brandt, P., and Schlundt, M. (2014). Diapycnal heat flux and mixed layer heat budget within the Atlantic Cold Tongue. *Climate Dynamics*, 43(11):3179–3199, ISSN: 14320894, DOI: `10.1007/s00382-014-2339-6`.

Hutchings, L., van der Lingen, C. D., Shannon, L. J., Crawford, R. J., Verheye, H. M., Bartholomae, C. H., van der Plas, A. K., Louw, D., Kreiner, A., Ostrowski, M., Fidel, Q., Barlow, R. G., Lamont, T., Coetzee, J., Shillington, F., Veitch, J., Currie, J. C., and Monteiro, P. M. (2009). The Benguela Current: An ecosystem of four components. *Progress in Oceanography*, 83(1-4):15–32, ISSN: 00796611, DOI: `10.1016/j.pocean.2009.07.046`.

Huthnance, J. M. (1978). On coastal trapped waves: Analysis and numerical calculation by inverse iteration. *Journal of Physical Oceanography*, 8(1):74–92, https://doi.org/10.1175/1520-0485(1978)008%3C0074:OCTWAA%3E2.0.CO;2.

Huthnance, J. M. (1995). Circulation, exchange and water masses at the ocean margin: the role of physical processes at the shelf edge. *Progress in Oceanography*, 35(4):353–431, ISSN: 00796611, DOI: `10.1016/0079-6611(95)80003-C`.

Illig, S. and Bachèlery, M. L. (2023). The 2021 Atlantic Niño and Benguela Niño Events: external forcings and air–sea interactions. *Climate Dynamics*, (0123456789), ISBN: 0038202306934, ISSN: 14320894, DOI: `10.1007/s00382-023-06934-0`.

Illig, S., Bachèlery, M.-L., and Cadier, E. (2018a). Subseasonal Coastal-Trapped Wave Propagations in the Southeastern Pacific and Atlantic Oceans: 2. Wave Characteristics and Connection With the Equatorial Variability. *Journal of Geophysical Research: Oceans*, 123(6):3942–3961, ISSN: 21699291, DOI: `10.1029/2017JC013540`.

Illig, S., Bachèlery, M.-L., and Lübbecke, J. F. (2020). Why Do Benguela Niños Lead Atlantic Niños? *Journal of Geophysical Research: Oceans*, 125(9), ISSN: 21699291, DOI: `10.1029/2019JC016003`.

Illig, S., Cadier, E., Bachèlery, M.-L., and Kersalé, M. (2018b). Subseasonal Coastal-Trapped Wave Propagations in the Southeastern Pacific and Atlantic Oceans: 1. A New Approach to Estimate Wave Amplitude. *Journal of Geophysical Research: Oceans*, 123(6):3915–3941, ISSN: 21699291, DOI: `10.1029/2017JC013539`.

Imbol Koungue, R. A. and Brandt, P. (2021). Impact of Intraseasonal Waves on Angolan Warm and Cold Events. *Journal of Geophysical Research: Oceans*, 126(4):e2020JC017088, DOI: `https://doi.org/10.1029/2020JC017088`.

Imbol Koungue, R. A., Brandt, P., Lübbecke, J., Prigent, A., Martins, M. S., and Rodrigues, R. R. (2021). The 2019 Benguela Niño. *Frontiers in Marine Science*, 8(December):1–16, ISSN: 22967745, DOI: 10.3389/fmars.2021.800103.

Imbol Koungue, R. A., Illig, S., and Rouault, M. (2017). Role of interannual Kelvin wave propagations in the equatorial Atlantic on the Angola Benguela Current system. *Journal of Geophysical Research: Oceans*, 122:4685–4703, ISBN: 2169-9291, ISSN: 21699275, DOI: 10.1002/2016JC012463.

Imbol Koungue, R. A., Rouault, M., Illig, S., Brandt, P., and Jouanno, J. (2019). Benguela Niños and Benguela Niñas in forced ocean simulation from 1958 to 2015. *Journal of Geophysical Research: Oceans*, 124(8):5923–5951, ISSN: 2169-9275, DOI: 10.1029/2019jc015013.

(IPCC) Intergovernmental Panel on Climate Change (2023). *Climate Change 2021 – The Physical Science Basis: Working Group I Contribution to the Sixth Assessment Report of the Intergovernmental Panel on Climate Change*. Cambridge.

Jackson, C. R., Da Silva, J. C., and Jeans, G. (2012). The generation of nonlinear internal waves. *Oceanography*, 25(2):108–123, ISSN: 02784343, DOI: 10.1016/S0278-4343(01)00094-2.

Kämpf, J. and Chapman, P. (2016). *Upwelling Systems of the World*. ISBN: 9783319425221, DOI: 10.1007/978-3-319-42524-5.

Kaneko, H., Yasuda, I., Komatsu, K., and Itoh, S. (2013). Observations of vertical turbulent nitrate flux across the Kuroshio. *Geophysical Research Letters*, 40(12):3123–3127, ISSN: 00948276, DOI: 10.1002/grl.50613.

Karstensen, J., Stramma, L., and Visbeck, M. (2008). Oxygen minimum zones in the eastern tropical Atlantic and Pacific oceans. *Progress in Oceanography*, 77(4):331–350, ISSN: 00796611, DOI: 10.1016/j.pocean.2007.05.009.

Kirkman, S. P., Blamey, L., Lamont, T., Field, J. G., Bianchi, G., Huggett, J. A., Hutchings, L., Jackson-Veitch, J., Jarre, A., Lett, C., Lipiński, M. R., Mafwila, S. W., Pfaff, M. C., Samaai, T., Shannon, L. J., Shin, Y. J., van der Lingen, C. D., and Yemane, D. (2016). Spatial characterisation of the Benguela ecosystem for ecosystem-based management. *African Journal of Marine Science*, 38(1):7–22, ISSN: 18142338, DOI: 10.2989/1814232X.2015.1125390.

Kopte, R., Brandt, P., Claus, M., Greatbatch, R. J., and Dengler, M. (2018). Role of Equatorial Basin-Mode Resonance for the Seasonal Variability of the Angola Current at 11°S. *Journal of Physical Oceanography*, 48(2):261–281, ISSN: 0022-3670, DOI: 10.1175/JPO-D-17-0111.1.

Kopte, R., Brandt, P., Tchipalanga, P., Macueria, M., and Ostrowski, M. (2017). The Angola Current: Flow and hydrographic characteristics as observed at 11S. *Journal of Geophysical Research: Oceans*, 122:1177– 1189, DOI: doi:10.1002/2016JC012374.

Körner, M., Brandt, P., and Dengler, M. (2023a). Seasonal cycle of sea surface temperature in the tropical Angolan Upwelling System. *Ocean Science*, 19(1):121–139, DOI: 10.5194/os-19-121-2023.

Körner, M., Brandt, P., and Dengler, M. (2023b). Upper-ocean microstructure data from the tropical Angolan upwelling system. DOI: 10.1594/PANGAEA.953869.

Körner, M., Brandt, P., Illig, S., Dengler, M., Subramaniam, A., Bachèlery, M.-L., and Krahmann, G. (2024). Coastal trapped waves and tidal mixing control primary production in the tropical Angolan upwelling system. *in press, Science Advances*.

Kumar, B. P., Vialard, J., Lengaigne, M., Murty, V. S., and McPhaden, M. J. (2012). TropFlux: Air-sea fluxes for the global tropical oceans-description and evaluation. *Climate Dynamics*, 38(7-8):1521–1543, ISSN: 09307575, DOI: 10.1007/s00382-011-1115-0.

Kunze, E. (2017). The internal-wave-driven meridional overturning circulation. *Journal of Physical Oceanography*, 47(11):2673–2689, ISSN: 15200485, DOI: `10.1175/JPO-D-16-0142.1`.

Kurian, J., Li, P., Chang, P., Patricola, C. M., and Small, J. (2021). Impact of the Benguela coastal low-level jet on the southeast tropical Atlantic SST bias in a regional ocean model. *Climate Dynamics*, 56(9-10):2773–2800, ISBN: `0123456789`, ISSN: 14320894, DOI: `10.1007/s00382-020-05616-5`.

Lamb, K. G. (2014). Internal Wave Breaking and Dissipation Mechanisms on the Continental Slope/Shelf. *Annual Review of Fluid Mechanics*, 46(1):231–254, ISSN: 0066-4189, DOI: `10.1146/annurev-fluid-011212-140701`.

Latif, M. and Grötzner, A. (2000). The equatorial Atlantic oscillation and its response to ENSO. *Climate Dynamics*, 16(2-3):213–218, ISSN: 14320894, DOI: `10.1007/s003820050014`.

Laurent, L. S. and Schmitt, R. W. (1999). The contribution of salt fingers to vertical mixing in the North Atlantic Tracer Release Experiment. *Journal of Physical Oceanography*, 29(7):1404–1424, ISSN: 00223670, DOI: `10.1175/1520-0485(1999)029<1404:tcosft>2.0.co;2`.

Lazar, A., Polo, I., Arnault, S., and Mainsant, G. (2006). Kelvin waves activity in the eastern tropical Atlantic. *European Space Agency, (Special Publication) ESA SP*, (614).

Ledwell, J. R., Montgomery, E. T., Polzin, K. L., St. Laurent, L. C., Schmitt, R. W., and Toole, J. M. (2000). Evidence for enhanced mixing over rough topography in the abyssal ocean. *Nature*, 403(6766):179–182, DOI: `10.1038/35003164`.

Lee, S.-k., Lopez, H., Tuchen, F. P., Kim, D., Foltz, G. R., and Wittenberg, A. T. (2023). On the Genesis of the 2021 Atlantic Niño. *Geophysical Research Letters*, 50:e2023GL104452, DOI: `10.1029/2023GL104452`.

Legg, S. and Adcroft, A. (2003). Internal wave breaking at concave and convex continental slopes. *Journal of Physical Oceanography*, 33(11):2224–2246, ISSN: 00223670, DOI: `10.1175/1520-0485(2003)033<2224:IWBACA>2.0.CO;2`.

Lellouche, J.-M., Greiner, E., Bourdallé Badie, R., Garric, G., Melet, A., Drévillon, M., Bricaud, C., Hamon, M., Le Galloudec, O., Regnier, C., Candela, T., Testut, C.-E., Gasparin, F., Ruggiero, G., Benkiran, M., Drillet, Y., and Le Traon, P.-Y. (2021). The Copernicus Global 1/12° Oceanic and Sea Ice GLORYS12 Reanalysis. *Frontiers in Earth Science*, 9(July):1–27, ISSN: 22966463, DOI: `10.3389/feart.2021.698876`.

Li, G., Cheng, L., Zhu, J., Trenberth, K. E., Mann, M. E., and Abraham, J. P. (2020). Increasing ocean stratification over the past half-century. *Nature Climate Change*, 10(12):1116–1123, ISSN: 17586798, DOI: `10.1038/s41558-020-00918-2`.

Li, Q. P., Franks, P. J., Ohman, M. D., and Landry, M. R. (2012). Enhanced nitrate fluxes and biological processes at a frontal zone in the southern California current system. *Journal of Plankton Research*, 34(9):790–801, ISSN: 01427873, DOI: `10.1093/plankt/fbs006`.

Li, X., Hu, Z. Z., and Becker, E. (2019). On the westward shift of tropical Pacific climate variability since 2000. *Climate Dynamics*, 53(5-6):2905–2918, DOI: `10.1007/s00382-019-04666-8`.

Li, X., Tan, W., Hu, Z. Z., and Johnson, N. C. (2023). Evolution and Prediction of Two Extremely Strong Atlantic Niños in 2019–2021: Impact of Benguela Warming. *Geophysical Research Letters*, 50(12), ISSN: 19448007, DOI: `10.1029/2023GL104215`.

Lien, R. C., Sanford, T. B., Jan, S., Chang, M. H., and Ma, B. B. (2013). Internal tides on the East China Sea continental slope. *Journal of Marine Research*, 71(1-2):151–186, ISSN: 15439542, DOI: `10.1357/002224013807343461`.

Longhurst, A. (1993). Seasonal cooling and blooming in tropical oceans. *Deep-Sea Research Part I*, 40(11-12):2145–2165, ISSN: 09670637, DOI: 10.1016/0967-0637(93)90095-K.

Lübbecke, J. F., Böning, C. W., Keenlyside, N. S., and Xie, S. P. (2010). On the connection between Benguela and equatorial Atlantic Niños and the role of the South Atlantic Anticyclone. *Journal of Geophysical Research: Oceans*, 115(9):1–16, ISSN: 21699291, DOI: 10.1029/2009JC005964.

Lübbecke, J. F., Brandt, P., Dengler, M., Kopte, R., Lüdke, J., Richter, I., Sena Martins, M., and Tchipalanga, P. C. (2019). Causes and evolution of the southeastern tropical Atlantic warm event in early 2016. *Climate Dynamics*, 53(1-2):261–274, DOI: 10.1007/s00382-018-4582-8.

Lübbecke, J. F. and Mcphaden, M. J. (2014). Assessing the twenty-first-century shift in enso variability in terms of the bjerknes stability index. *Journal of Climate*, 27(7):2577–2587, ISSN: 08948755, DOI: 10.1175/JCLI-D-13-00438.1.

Lüdke, J., Dengler, M., Sommer, S., Clemens, D., Thomsen, S., Krahmann, G., Dale, A. W., Achterberg, E. P., and Visbeck, M. (2020). Influence of intraseasonal eastern boundary circulation variability on hydrography and biogeochemistry off Peru. *Ocean Science*, 16(6):1347–1366, ISSN: 18120792, DOI: 10.5194/os-16-1347-2020.

Luyten, J., Pedlosky, J., and Stommel, H. (1983). The ventilated thermocline. *Journal of Physical Oceanography*, 13(2):292–309, https://doi.org/10.1175/1520-0485(1983)013%3C0292:TVT%3E2.0.CO;2.

Mao, Z., Mao, Z., Jamet, C., Linderman, M., Wang, Y., and Chen, X. (2020). Seasonal cycles of phytoplankton expressed by sine equations using the daily climatology from satellite-retrieved Chlorophyll-a concentration (1997-2019) over global ocean. *Remote Sensing*, 12(16):2662, ISSN: 20724292, DOI: 10.3390/RS12162662.

Martín-Rey, M., Polo, I., Rodríguez-Fonseca, B., Losada, T., and Lazar, A. (2018). Is there evidence of changes in tropical Atlantic variability modes under AMO phases in the observational record? *Journal of Climate*, 31(2):515–536, ISSN: 08948755, DOI: 10.1175/JCLI-D-16-0459.1.

Martins, M. S. and Stammer, D. (2022). Interannual Variability of the Congo River Plume-Induced Sea Surface Salinity. *Remote Sensing*, 14(4):1013, ISSN: 20724292, DOI: 10.3390/rs14041013.

Mason, S. J. and Mimmack, G. M. (2002). Comparison of some statistical methods of probabilistic forecasting of ENSO. *Journal of Climate*, 15(3):8–29, ISSN: 08948755, DOI: 10.1175/1520-0442(2002)015<0008:cossmo>2.0.co;2.

Matsuno, T. (1966). Quasi-Geostrophic Motions Equatorial Area. *Journal of the Meteorological Society of Japan*, (February):25–43, DOI: 10.2151/jmsj1965.44.1_25.

McCreary, J. P. (1976). Eastern tropical ocean response to changing wind systems: with application to El Niño. *Journal of Physical Oceanography*, 6(5):632–645, https://doi.org/10.1175/1520-0485(1976)006%3C0632:ETORTC%3E2.0.CO;2.

McDougall, T. J. and Barker, P. M. (2011). Getting started with TEOS-10 and the Gibbs Seawater (GSW) oceanographic toolbox. *Scor/lapso WG*, 127(532):1–28, https://www.teos-10.org/pubs/Getting_Started.pdf.

Messié, M. and Chavez, F. P. (2015). Seasonal regulation of primary production in eastern boundary upwelling systems. *Progress in Oceanography*, 134:1–18, ISSN: 00796611, DOI: 10.1016/j.pocean.2014.10.011.

Modi, A., Roxy, M. K., and Ghosh, S. (2022). Gap-filling of ocean color over the tropical Indian Ocean using Monte-Carlo method. *Scientific Reports*, 12(1):1–11, ISBN: 4159802222, ISSN: 20452322, DOI: `10.1038/s41598-022-22087-2`.

Mohrholz, V., Bartholomae, C. H., van der Plas, A. K., and Lass, H. U. (2008). The seasonal variability of the northern Benguela undercurrent and its relation to the oxygen budget on the shelf. *Continental Shelf Research*, 28(3):424–441, ISSN: 02784343, DOI: `10.1016/j.csr.2007.10.001`.

Moisan, J. R. and Niiler, P. P. (1998). the seasonal heat budget of the North Pacific: Net heat flux and heat storage rates (1950-1990). *Journal of Physical Oceanography*, 28(3):401–421, ISSN: 00223670, DOI: `10.1175/1520-0485(1998)028<0401:TSHBOT>2.0.CO;2`.

Moore, D., Hisard, P., McCreary, J., Merle, J., O'Brien, J., Picaut, J., Verstraete, J.-M., and Wunsch, C. (1978). Equatorial adjustment in the eastern Atlantic. *Geophysical Research Letters*, 5(8):637–640, DOI: `10.1029/GL005i008p00637`.

Moore, D. W. (1968). *Planetary-gravity waves in an equatorial ocean*. Doctoral dissertation, Harvard University.

Moore, J. K., Doney, S. C., and Lindsay, K. (2004). Upper ocean ecosystem dynamics and iron cycling in a global three-dimensional model. *Global Biogeochemical Cycles*, 18(4):1–21, ISSN: 08866236, DOI: `10.1029/2004GB002220`.

Morel, A. and Antoine, D. (1994). Heating Rate within the Upper Ocean in Relation to Irs Bio-Optical State. *Journal of Physical Oceanography*, 24:1652–1665, https://doi.org/10.1175/1520-0485(1994)024%3C1652:HRWTUO%3E2.0.CO;2.

Moum, J. N., Farmer, D. M., Shroyer, E. L., Smyth, W. D., and Armi, L. (2007a). Dissipative losses in nonlinear internal waves propagating across the continental shelf. *Journal of Physical Oceanography*, 37(7):1989–1995, ISSN: 00223670, DOI: `10.1175/JPO3091.1`.

Moum, J. N., Klymak, J. M., Nash, J. D., Perlin, A., and Smyth, W. D. (2007b). Energy transport by nonlinear internal waves. *Journal of Physical Oceanography*, 37(7):1968–1988, ISSN: 00223670, DOI: `10.1175/JPO3094.1`.

Munk, W. and Wunsch, C. (1998). Abyssal recipies II: energetics of tidal and wind mixing. *Deep Sea Research Part I: Oceanographic Research Papers*, 45(1998):1977–2010, DOI: `10.1016/S0967-0637(98)00070-3`.

Nash, J. D., Kelly, S. M., Shroyer, E. L., Moum, J. N., and Duda, T. F. (2012). The unpredictable nature of internal tides on continental shelves. *Journal of Physical Oceanography*, 42(11):1981–2000, ISSN: 00223670, DOI: `10.1175/JPO-D-12-028.1`.

Nash, J. D., Kunze, E., Toole, J. M., and Schmitt, R. W. (2004). Internal tide reflection and turbulent mixing on the continental slope. *Journal of Physical Oceanography*, 34(5):1117–1134, ISSN: 00223670, DOI: `10.1175/1520-0485(2004)034<1117:ITRATM>2.0.CO;2`.

Nerem, R. S., Beckley, B. D., Fasullo, J. T., Hamlington, B. D., Masters, D., and Mitchum, G. T. (2018). Climate-change–driven accelerated sea-level rise detected in the altimeter era. *Proceedings of the National Academy of Sciences of the United States of America*, 115(9):2022–2025, ISSN: 10916490, DOI: `10.1073/pnas.1717312115`.

Nielsen-Englyst, P., Høyer, J. L., Alerskans, E., Pedersen, L. T., and Donlon, C. (2021). Impact of channel selection on SST retrievals from passive microwave observations. *Remote Sensing of Environment*, 254, ISSN: 00344257, DOI: `10.1016/j.rse.2020.112252`.

Oettli, P., Yuan, C., and Richter, I. (2021). 10 - The other coastal Niño/Niña—the Benguela, California, and Dakar Niños/Niñas. In Behera, S. K., editor, *Tropical and Extratropical Air-Sea Interactions*, pages 237–266. Elsevier, ISBN: 978-0-12-818156-0, DOI: https://doi.org/10.1016/B978-0-12-818156-0.00010-1.

Osborn, T. R. (1980). Estimates of the Local Rate of Vertical Diffusion from Dissipation Measurements. *Journal of Physical Oceanography*, 10(1):83–89, ISSN: 0022-3670, DOI: 10.1175/1520-0485(1980)010<0083:eotlro>2.0.co;2.

Ostrowski, M. (2007). Impact of equatorial Kelvin waves on aggregations of sardinellas (Sardinella spp.) in Angolan waters. *ICES Document CM 2007/G: 08*, https://www.ices.dk/sites/pub/CM%20Doccuments/CM-2007/G/G0807.pdf.

Ostrowski, M. and Bazika-Sangolay, B. (2016). On physical mechanisms controlling inshore aggregations of small pelagic fish in a tropical upwelling system. *2015 IEEE/OES Acoustics in Underwater Geosciences Symposium, RIO Acoustics 2015*, DOI: 10.1109/RIOAcoustics.2015.7473621.

Ostrowski, M., Da Silva, J. C., and Bazik-Sangolay, B. (2009). The response of sound scatterers to El Ninõ- and La Niña-like oceanographic regimes in the southeastern Atlantic. *ICES Journal of Marine Science*, 66(6):1063–1072, ISSN: 10543139, DOI: 10.1093/icesjms/fsp102.

Penland, C. (1996). A stochastic model of IndoPacific sea surface temperature anomalies. *Physica D: Nonlinear Phenomena*, 98(2-4):534–558, DOI: 10.1016/0167-2789(96)00124-8.

Perlin, A., Moum, J. N., and Klymak, J. M. (2005). Response of the bottom boundary layer over a sloping shelf to variations in alongshore wind. *Journal of Geophysical Research: Oceans*, 110(10):1–13, ISSN: 21699291, DOI: 10.1029/2004JC002500.

Petrova, D., Koopman, S. J., Ballester, J., and Rodó, X. (2017). Improving the long-lead predictability of El Niño using a novel forecasting scheme based on a dynamic components model. *Climate Dynamics*, 48(3-4):1249–1276, DOI: 10.1007/s00382-016-3139-y.

Philander, S. G. H. and Pacanowski, R. C. (1981). Response of equatorial oceans to periodic forcing. *Journal of Geophysical Research: Oceans*, 86(C3):1903–1916, DOI: 10.1029/jc086ic03p01903.

Picaut, J. (1983). Propagation of the seasonal upwelling in the eastern equatorial Atlantic. *Journal of Physical Oceanography*, 13(1):18–37, https://doi.org/10.1175/1520-0485(1983)013%3C0018:POTSUI%3E2.0.CO;2.

Pizarro, O., Shaffer, G., Dewitte, B., and Ramos, M. (2002). Dynamics of seasonal and interannual variability of the Peru-Chile Undercurrent. *Geophysical Research Letters*, 29(12):22–24, DOI: 10.1029/2002GL014790.

Poli, L., Artana, C., and Provost, C. (2022). Topographically Trapped Waves Around South America With Periods Between 40 and 130 Days in a Global Ocean Reanalysis. *Journal of Geophysical Research: Oceans*, 127(2), ISSN: 21699291, DOI: 10.1029/2021JC018067.

Polo, I., Lazar, A., Rodriguez-Fonseca, B., and Arnault, S. (2008). Oceanic Kelvin waves and tropical Atlantic intraseasonal variability: 1. Kelvin wave characterization. *Journal of Geophysical Research: Oceans*, 113(7):1–18, ISSN: 21699291, DOI: 10.1029/2007JC004495.

Polzin, K. (2004). Idealized solutions for the energy balance of the finescale internal wave field. *Journal of Physical Oceanography*, 34(1):231–246, ISSN: 00223670, DOI: 10.1175/1520-0485(2004)034<0231:ISFTEB>2.0.CO;2.

Prigent, A., Anicet, R., Koungue, I., Lübbecke, J. F., Brandt, P., Harlaß, J., and Latif, M. (2023). Future weakening of southeastern tropical Atlantic Ocean interannual sea surface temperature variability in a global climate model. *Climate Dynamics*, (0123456789), DOI: 10.1007/s00382-023-07007-y.

Prigent, A., Imbol Koungue, R. A., Lübbecke, J. F., Brandt, P., and Latif, M. (2020a). Origin of Weakened Interannual Sea Surface Temperature Variability in the Southeastern Tropical Atlantic Ocean. *Geophysical Research Letters*, 47(20):1–9, DOI: 10.1029/2020GL089348.

Prigent, A., Lübbecke, J. F., Bayr, T., Latif, M., and Wengel, C. (2020b). Weakened SST variability in the tropical Atlantic Ocean since 2000. *Climate Dynamics*, (January), DOI: 10.1007/s00382-020-05138-0.

Ray, R. D. and Mitchum, G. T. (1996). Surface manifestation of internal tides generated near Hawaii. *Geophysical Research Letters*, 23(16):2101–2104, ISSN: 00948276, DOI: 10.1029/96GL02050.

Redfield, A. C. (1934). On the Proportions of Organic Derivatives in Sea Water and their Relation to the Composition of Plankton. *University Press of Liverpool, James Johnstone Memorial Volume*, pages 176–192.

Richter, I. (2015). Climate model biases in the eastern tropical oceans: Causes, impacts and ways forward. *Wiley Interdisciplinary Reviews: Climate Change*, 6(3):345–358, ISSN: 17577799, DOI: 10.1002/wcc.338.

Richter, I., Behera, S. K., Masumoto, Y., Taguchi, B., Komori, N., and Yamagata, T. (2010). On the triggering of Benguela Niños: Remote equatorial versus local influences. *Geophysical Research Letters*, 37(20):1–6, ISSN: 00948276, DOI: 10.1029/2010GL044461.

Richter, I. and Tokinaga, H. (2020). An overview of the performance of CMIP6 models in the tropical Atlantic: mean state, variability, and remote impacts. *Climate Dynamics*, 55(9-10):2579–2601, DOI: 10.1007/s00382-020-05409-w.

Richter, I., Tokinaga, H., and Okumura, Y. M. (2022). The Extraordinary Equatorial Atlantic Warming in Late 2019. *Geophysical Research Letters*, 49(4):1–9, ISSN: 19448007, DOI: 10.1029/2021GL095918.

Roch, M., Brandt, P., Schmidtko, S., Vaz Velho, F., and Ostrowski, M. (2021). Southeastern Tropical Atlantic Changing From Subtropical to Tropical Conditions. *Frontiers in Marine Science*, 8(November):1–19, ISSN: 22967745, DOI: 10.3389/fmars.2021.748383.

Romea, R. D. and Allen, J. S. (1984). The effect of friction and topography on coastal internal Kelvin waves at low latitudes. *Tellus A: Dynamic Meteorology and Oceanography*, 36(4):384, DOI: 10.3402/tellusa.v36i4.11641.

Rouault, M. (2012). Bi-annual intrusion of tropical water in the northern Benguela upwelling. *Geophysical Research Letters*, 39(12):2–7, ISSN: 00948276, DOI: 10.1029/2012GL052099.

Rouault, M., Florenchie, P., Fauchereau, N., and Reason, C. J. C. (2003). South East tropical Atlantic warm events and southern African rainfall. *Geophysical Research Letters*, 30(5):1–4, ISSN: 00948276, DOI: 10.1029/2002GL014840.

Rouault, M., Illig, S., Bartholomae, C., Reason, C. J., and Bentamy, A. (2007). Propagation and origin of warm anomalies in the Angola Benguela upwelling system in 2001. *Journal of Marine Systems*, 68(3-4):473–488, ISSN: 09247963, DOI: 10.1016/j.jmarsys.2006.11.010.

Rouault, M., Illig, S., Lübbecke, J., and Koungue, R. A. I. (2018). Origin, development and demise of the 2010–2011 Benguela Niño. *Journal of Marine Systems*, 188(November 2016):39–48, ISSN: 09247963, DOI: 10.1016/j.jmarsys.2017.07.007.

Sakamoto, C. M., Johnson, K. S., and Coletti, L. J. (2009). Improved algorithm for the computation of nitrate concentrations in seawater using an in situ ultraviolet spectrophotometer. *Limnology and Oceanography: Methods*, 7(1):132–143, DOI: 10.4319/lom.2009.7.132.

Sandström, J. W. (1908). Dynamische Versuche mit Meerwasser. *Annalen der Hydrographie und Maritimen Meteorologie*.

Scannell, H. A. and McPhaden, M. J. (2018). Seasonal Mixed Layer Temperature Balance in the Southeastern Tropical Atlantic. *Journal of Geophysical Research: Oceans*, 123(8):5557–5570, ISSN: 21699291, DOI: 10.1029/2018JC014099.

Schafstall, J., Dengler, M., Brandt, P., and Bange, H. (2010). Tidal-induced mixing and diapycnal nutrient fluxes in the Mauritanian upwelling region. *Journal of Geophysical Research: Oceans*, 115(10):1–19, ISSN: 21699291, DOI: 10.1029/2009JC005940.

Schouten, M. W., Matano, R. P., and Strub, T. P. (2005). A description of the seasonal cycle of the equatorial Atlantic from altimeter data. *Deep-Sea Research Part I: Oceanographic Research Papers*, 52(3):477–493, ISSN: 09670637, DOI: 10.1016/j.dsr.2004.10.007.

Servain, J., Caniaux, G., Kouadio, Y. K., McPhaden, M. J., and Araujo, M. (2014). Recent climatic trends in the tropical Atlantic. *Climate Dynamics*, 43(11):3071–3089, ISSN: 14320894, DOI: 10.1007/s00382-014-2168-7.

Shannon, L. V., Agenbag, J. J., and Buys, M. E. (1987). Large- and mesoscale features of the Angola-Benguela front. *South African Journal of Marine Science*, 5(1):11–34, ISSN: 02577615, DOI: 10.2989/025776187784522261.

Shannon, L. V., Boyd, A. J., Brundrit, G. B., and Taunton-Clark, J. (1986). on the Existence of an El Nino-Type Phenomenon in the Benguela System. *Journal of Marine Research*, 44(3):495–520, ISSN: 00222402, DOI: 10.1357/002224086788403105.

Shih, L. H., Koseff, J. R., Ivey, G. N., and Ferziger, J. H. (2005). Parameterization of turbulent fluxes and scales using homogeneous sheared stably stratified turbulence simulations. *Journal of Fluid Mechanics*, 525(August 2004):193–214, ISSN: 00221120, DOI: 10.1017/S0022112004002587.

Shroyer, E. L., Moum, J. N., and Nash, J. D. (2010a). Energy transformations and dissipation of nonlinear internal waves over New Jersey's continental shelf. *Nonlinear Processes in Geophysics*, 17(4):345–360, ISSN: 10235809, DOI: 10.5194/npg-17-345-2010.

Shroyer, E. L., Moum, J. N., and Nash, J. D. (2010b). Vertical heat flux and lateral mass transport in nonlinear internal waves. *Geophysical Research Letters*, 37(8):1–5, ISSN: 00948276, DOI: 10.1029/2010GL042715.

Siegfried, L., Schmidt, M., Mohrholz, V., Pogrzeba, H., Nardini, P., Böttinger, M., and Scheuermann, G. (2019). The tropical-subtropical coupling in the Southeast Atlantic from the perspective of the northern Benguela upwelling system. *PLOS ONE*, 14(1):e0210083, DOI: 10.1371/journal.pone.0210083.

Sobral Verona, L., Silva, P., Wainer, I., and Khodri, M. (2023). Weakened interannual Tropical Atlantic variability in CMIP6 historical simulations. *Climate Dynamics*, 61(5-6):2797–2813, DOI: 10.1007/s00382-023-06696-9.

Sowman, M. and Cardoso, P. (2010). Small-scale fisheries and food security strategies in countries in the Benguela Current Large Marine Ecosystem (BCLME) region: Angola, Namibia and South Africa. *Marine Policy*, 34(6):1163–1170, ISSN: 0308597X, DOI: 10.1016/j.marpol.2010.03.016.

Stevenson, J. W. and Niiler, P. P. (1983). Upper Ocean Heat Budget During the Hawaii-to-Tahiti Schuttle Experiment. *Journal of Physical Oceanography*, 13:1894–1907, DOI: 10.1175/1520-0485(1983)013<1894:UOHBDT>2.0.CO;2.

Sylla, A., Mignot, J., Capet, X., and Gaye, A. T. (2019). Weakening of the Senegalo–Mauritanian upwelling system under climate change. *Climate Dynamics*, 53(7-8):4447–4473, DOI: 10.1007/s00382-019-04797-y.

Tang, Y., Zhang, R. H., Liu, T., Duan, W., Yang, D., Zheng, F., Ren, H., Lian, T., Gao, C., Chen, D., and Mu, M. (2018). Progress in ENSO prediction and predictability study. *National Science Review*, 5(6):826–839, ISSN: 2053714X, DOI: 10.1093/nsr/nwy105.

Taylor, G. I. (1935). Statistical theory of turbulenc. *Proceedings of the Royal Society of London. Series A-Mathematical and Physical Sciences*, 151(873):421–444.

Tchipalanga, P., Dengler, M., Brandt, P., Kopte, R., Macuéria, M., Coelho, P., Ostrowski, M., and Keenlyside, N. S. (2018a). Eastern boundary circulation and hydrography off Angola building Angolan oceanographic capacities. *Bulletin of the American Meteorological Society*, 99(8):1589–1605, ISSN: 00030007, DOI: 10.1175/BAMS-D-17-0197.1.

Tchipalanga, P. C. M., Ostrowski, M., and Dengler, M. (2018b). Physical oceanography (CTD) during Fridtjof Nansen cruise FN1998409. DOI: 10.1594/PANGAEA.887163.

Thierry, V., Treguier, A. M., and Mercier, H. (2004). Numerical study of the annual and semi-annual fluctuations in the deep equatorial Atlantic Ocean. *Ocean Modelling*, 6(1):1–30, ISSN: 14635003, DOI: 10.1016/S1463-5003(02)00054-9.

Thomas, A. C., Carr, M. E., and Strub, P. T. (2001). Chlorophyll variability in eastern boundary currents. *Geophysical Research Letters*, 28(18):3421–3424, ISSN: 00948276, DOI: 10.1029/2001GL013368.

Thomas, A. C., Ted Strub, P., Weatherbee, R. A., and James, C. (2012). Satellite views of Pacific chlorophyll variability: Comparisons to physical variability, local versus nonlocal influences and links to climate indices. *Deep-Sea Research Part II: Topical Studies in Oceanography*, 77-80:99–116, ISSN: 09670645, DOI: 10.1016/j.dsr2.2012.04.008.

Thomsen, S., Capet, X., and Echevin, V. (2021). Competition between baroclinic instability and Ekman transport under varying buoyancy forcings in upwelling systems: An idealized analog to the Southern Ocean. *Journal of Physical Oceanography*, pages 3347–3364, ISSN: 0022-3670, DOI: 10.1175/jpo-d-20-0294.1.

Thomson, R. E. and Emery, W. J. (2014). *Chapter 6 - Digital Filters*. ISBN: 9780123877826, DOI: 10.1016/B978-0-12-387782-6.00006-5.

Thorpe, S. A. (2005). *The turbulent ocean*. Cambridge University Press.

Thorpe, S. A. (2018). Models of energy loss from internal waves breaking in the ocean. *Journal of Fluid Mechanics*, 836:72–116, ISSN: 14697645, DOI: 10.1017/jfm.2017.780.

Tokinaga, H. and Xie, S. P. (2011). Weakening of the equatorial Atlantic cold tongue over the past six decades. *Nature Geoscience*, 4(4):222–226, ISSN: 17520894, DOI: 10.1038/ngeo1078.

Tseng, Y.-h., Hu, Z. Z., Ding, R., and ching Chen, H. (2017). An ENSO prediction approach based on ocean conditions and ocean–atmosphere coupling. *Climate Dynamics*, 48(5-6):2025–2044, ISBN: 0038201631, ISSN: 14320894, DOI: 10.1007/s00382-016-3188-2.

Van Haren, H. (2015). Instability observations associated with wave breaking in the stable-stratified deep-ocean. *Physica D: Nonlinear Phenomena*, 292-293:62–69, ISSN: 01672789, DOI: 10.1016/j.physd.2014.11.002.

Voldoire, A., Exarchou, E., Sanchez-Gomez, E., Demissie, T., Deppenmeier, A. L., Frauen, C., Goubanova, K., Hazeleger, W., Keenlyside, N., Koseki, S., Prodhomme, C., Shonk, J., Toniazzo, T., and Traoré, A. K. (2019). Role of wind stress in driving SST biases in the Tropical Atlantic. *Climate Dynamics*, 53(5-6):3481–3504, DOI: 10.1007/s00382-019-04717-0.

Wacongne, S. and Piton, B. (1992). The near-surface circulation in the northeastern corner of the South Atlantic Ocean. *Deep Sea Research Part A. Oceanographic Research Papers*, 39(7-8):1273–1298, ISSN: 0027-0644, DOI: 10.1016/0198-0149(92)90069-6.

Wang, D., Gouhier, T. C., Menge, B. A., and Ganguly, A. R. (2015). Intensification and spatial homogenization of coastal upwelling under climate change. *Nature*, 518(7539):390–394, ISSN: 14764687, DOI: 10.1038/nature14235.

Wang, D.-P. and Mooers, C. N. (1976). Coastal-trapped waves in a continuously stratified ocean. *Journal of Physical Oceanography*, 6(5):853 – 863, https://doi.org/10.1175/1520-0485(1976)006%3C0853:CTWIAC%3E2.0.CO;2.

Wang, W. and McPhaden, M. J. (2000). The surface-layer heat balance in the Equatorial Pacific Ocean Part II: Interannual variability. *Journal of Physical Oceanography*, 30(11):2989–3008, ISSN: 00223670, DOI: 10.1175/1520-0485(2001)031<2989:TSLHBI>2.0.CO;2.

Whalen, C. B., de Lavergne, C., Naveira Garabato, A. C., Klymak, J. M., MacKinnon, J. A., and Sheen, K. L. (2020). Internal wave-driven mixing: governing processes and consequences for climate. *Nature Reviews Earth and Environment*, 1(11):606–621, ISSN: 2662138X, DOI: 10.1038/s43017-020-0097-z.

Wolk, F., Yamazaki, H., Seuront, L., and Lueck, R. G. (2002). A new free-fall profiler for measuring biophysical microstructure. *Journal of Atmospheric and Oceanic Technology*, 19(5):780–793, ISSN: 07390572, DOI: 10.1175/1520-0426(2002)019<0780:ANFFPF>2.0.CO;2.

Wunsch, C. and Gill, A. E. (1976). Observations of equatorially trapped waves in Pacific sea level variations. *Deep Sea Research and Oceanographic Abstracts*, 23(5):371–390, ISSN: 00117471, DOI: 10.1016/0011-7471(76)90835-4.

Xu, Z., Chang, P., Richter, I., Kim, W., and Tang, G. (2014). Diagnosing southeast tropical Atlantic SST and ocean circulation biases in the CMIP5 ensemble. *Climate Dynamics*, 43(11):3123–3145, ISSN: 14320894, DOI: 10.1007/s00382-014-2247-9.

Xue, T., Frenger, I., Prowe, A. E., José, Y. S., and Oschlies, A. (2022). Mixed layer depth dominates over upwelling in regulating the seasonality of ecosystem functioning in the Peruvian upwelling system. *Biogeosciences*, 19(2):455–475, ISSN: 17264189, DOI: 10.5194/bg-19-455-2022.

Yamaguchi, R. and Suga, T. (2019). Trend and Variability in Global Upper-Ocean Stratification Since the 1960s. *Journal of Geophysical Research: Oceans*, 124(12):8933–8948, ISSN: 21699291, DOI: 10.1029/2019JC015439.

Zeng, Z., Brandt, P., Lamb, K. G., Greatbatch, R. J., Dengler, M., Claus, M., and Chen, X. (2021). Three-Dimensional Numerical Simulations of Internal Tides in the Angolan Upwelling Region. *Journal of Geophysical Research: Oceans*, 126(2):1–20, ISSN: 21699291, DOI: 10.1029/2020JC016460.

Zhang, S., Alford, M. H., and Mickett, J. B. (2015). Characteristics, generation and mass transport of nonlinear internal waves on the Washington continental shelf. *Journal of Geophysical Research: Oceans*, pages 741–758, DOI: `10.1002/2014JC010393`.

Zhao, Z., Alford, M. H., Girton, J. B., Rainville, L., and Simmons, H. L. (2016). Global observations of open-ocean mode-1 M2 internal tides. *Journal of Physical Oceanography*, 46(6):1657–1684, ISSN: 15200485, DOI: `10.1175/JPO-D-15-0105.1`.

Zuidema, P., Chang, P., Medeiros, B., Kirtman, B. P., Mechoso, R., Schneider, E. K., Toniazzo, T., Richter, I., Small, R. J., Bellomo, K., Brandt, P., De Szoeke, S., Farrar, J. T., Jung, E., Kato, S., Li, M., Patricola, C., Wang, Z., Wood, R., and Xu, Z. (2016). Challenges and prospects for reducing coupled climate model sst biases in the eastern tropical atlantic and pacific oceans: The U.S. Clivar eastern tropical oceans synthesis working group. *Bulletin of the American Meteorological Society*, 97(12):2305–2327, ISSN: 00030007, DOI: `10.1175/BAMS-D-15-00274.1`.

Publication list

Aroucha, L. C., Lübbecke, J. F, **Körner, M.**, Imbol Kongue, R.A., and Awo, F. M. (2024). The Influence of Freshwater Input on the Evolution of the 1995 Benguela Niño, *Journal of Geophysical Research: Oceans*, 129, e2023JC020241, https://doi.org/10.1029/2023JC020241.

Körner, M., Brandt, P., Illig, S., Dengler, M., Subramaniam, A., Bachèlery, M.-L., and Krahmann, G. (2024). Coastal trapped waves and tidal mixing control primary production in the tropical Angolan upwelling system, *Science Advances*, 10, eadj6686, https://doi.org/10.1126/sciadv.adj6686.

Sell, A. F., Maltitz, G. P. V., Auel, H., Biastoch, A., Bode-Dalby, M., Brandt, P., Duncan, S. E., Ekau, W., Fock, H. O., Hagen, W., Huggett, J. A., Koppelmann, R., **Körner, M.**, Lahajnar, N., Martin, B., Midgley, G. F., Rixen, T., Lingen, C. D. V. D., Verheye, H. M., and Wilhelm, M. R. (2024). Unique Southern African Terrestrial and Oceanic Biomes and Their Relation to Steep Environmental Gradients. In G. P. von Maltitz, G. F. Midgley, J. Veitch, C. Brümmer, R. P. Rötter, F. A. Viehberg, and M. Veste (Eds.), Sustainability of Southern African Ecosystems under Global Change: Science for Management and Policy Interventions, pages 23–88. Springer International Publishing, Cham, https://doi.org/10.1007/978-3-031-10948-5_2.

Brandt, P., Bordbar, M. H., Coelho, P., Koungue, R. A. I., **Körner, M.**, Lamont, T., Lubbecke, J. F., Mohrholz, V., Prigent, A., Roch, M., Schmidt, M., van der Plas, A. K., and Veitch, J. (2024). Physical Drivers of Southwest African Coastal Upwelling and Its Response to Climate Variability and Change. In G. P. von Maltitz, G. F. Midgley, J. Veitch, C. Brümmer, R. P. Rötter, F. A. Viehberg, and M. Veste (Eds.), Sustainability of Southern African Ecosystems under Global Change: Science for Management and Policy Interventions, pages 221–257. Springer International Publishing, Cham, https://doi.org/10.1007/978-3-031-10948-5_9.

Brandt, P., Alory, G., Awo, F. M., Dengler, M., Djakouré, S., Imbol Koungue, R. A., Jouanno, J., **Körner, M.**, Roch, M., and Rouault, M. (2023). Physical processes and biological productivity in the upwelling regions of the tropical Atlantic. *Ocean Science*, 19(3):581–601, https://doi.org/10.5194/os-19-581-2023.

Körner, M., Brandt, P., and Dengler, M. (2023). Seasonal cycle of sea surface temperature in the tropical Angolan Upwelling System. *Ocean Science*., 19, 121–139, https://doi.org/10.5194/os-19-121-2023.

Körner, M., Claus, M., Brandt, P., and Tuchen, F. P. (2022). Sources and Pathways of Intraseasonal Meridional Kinetic Energy in the Equatorial Atlantic Ocean. *Journal of Physical Oceanography*, 52, 2445–2462, https://doi.org/10.1175/JPO-D-21-0315.1.

Stevens, B., Bony, S., [. . .], **Körner, M.**, [. . .] (2021). EUREC4A. *Earth System Science Data*, 13, 4067–4119, https://doi.org/10.5194/essd-13-4067-2021.

Acknowledgment

First, I would like to thank my supervisor, Peter Brandt, for giving me the opportunity to conduct this thesis as a doctoral researcher within the Physical Oceanography department. I appreciate his dedicated supervision and his enormous knowledge about ocean dynamics, from which I greatly benefited. His encouragement, constructive feedback, and patience with my work kept me motivated throughout my PhD. I also want to thank him for providing me the opportunity to join numerous research cruises and conferences.

Further, I extend my thanks to my co-supervisor, Marcus Dengler, for the support during this thesis. His extensive knowledge of papers, expertise in small-scale processes, and skill in interpreting microstructure data have been of great help.

I would like to thank both Peter and Marcus for the many scientific discussion between the three of us. Working with them has been a great experience for me, and I appreciate the valuable feedback and encouragement during this time.

Special thanks go to Martin Claus for his feedback as part of my PhD advisory committee. I further appreciate his supervision of my master thesis and support during the publication of our results.

I also want to thank Stephan Juricke for accepting to examine this thesis.

A big thank you to all my friends and colleagues from the Physical Oceanography department for the many discussions, lunch breaks, coffee breaks, and overall great support. I greatly enjoyed working with you, whether on the west shore, east shore, research cruises, or at conferences. Special thanks go to Marisa, Daniel, Léo, Rodrigue, Arthur, Philip, Rebecca, Flo, and Tina for making this time both enjoyable and valuable.

Außerdem möchte ich mich bei meinen Freunden bedanken, die mich in meiner Zeit in Kiel begleitet haben. Vielen Dank für eure bedingungslose Unterstützung in allen Lebenslagen. Ihr habt Kiel für mich zu einem Zuhause werden lassen. Zudem möchte ich Momo danken, für die vielen langen Spaziergänge, die mich zu neuen Ideen inspiriert haben. Ein großer Dank geht auch an meine Eltern, meine Schwester und an meinen Opa. Vielen Dank für eure großartige Unterstützung sowie für euer Mitfiebern ab der ersten Minute.

Declaration

I hereby declare that - apart from my supervisor's guidance and acknowledged assistance - the content and design of this thesis is my own work. This thesis has not been submitted either partially or wholly as part of a doctoral degree to another examining body and has not been published or submitted for publication except for the chapters where this is explicitly stated. This thesis has been prepared in accordance with the Rules of Good Scientific Practice of the German Research Foundation. An academic degree has never been withdrawn from me.

Mareike Körner, Kiel, den 16.01.2024